LOW TEMPERATURE SYNTHESIS OF NANOGRAPHITE AND NANOQUARTZ USING SURFACTANT PHASES

PHILIP DANIEL BUCKLEY

BUCKLEY, PHILIP DANIEL (2021) LOW TEMPERATURE SYNTHESIS OF NANOGRAPHITE AND NANOQUARTZ USING SURFACTANT PHASES. Doctoral thesis, Durham University.

LOW TEMPERATURE SYNTHESIS OF NANOGRAPHITE AND NANOQUARTZ USING SURFACTANT PHASES

Philip D. Buckley

A thesis submitted for the degree of
Doctor of Philosophy at the University of
Durham

February 20, 2021

Acknowledgements

First and foremost, I would like to thank my friends Natasha Boulding, Robert Bird, Scott Bush and Jessica Andrews for their support over the past 5 years. Having such close friends to use as a sounding board and grab many a pint in the pub with has made this thesis possible. Also many thanks goes to my partner Jon Dougherty, sister Danielle Buckley, mum Susan Buckley and dad Phil Buckley for all their encouragement and aid in proof reading.

Many thanks go to Sharon Cooper for all her help and guidance during my PhD. Her excellent support has allowed a once mathematician to become a competent chemist in and out of the lab. Also included here is all members of the Cooper group, past and present for the daily collaborations and discussions.

Further, I would like to thank David Apperley and the solid-state NMR service at Durham University for running all SSNMR experiments. Final thanks are extended to Helen Riggs and Budhika Mendis for their respective SAXS and TEM training.

Statement of Copyright

Publication List

The following publication has arisen from the work presented in this thesis:

1. Buckley, P., Hargreaves, N. and Cooper, S., 2018. Nucleation of quartz under ambient conditions. Communications Chemistry, 1(1).
   Web Access: https://www.nature.com/articles/s42004-018-0049-4

List of Abbreviations

AT	Sulphuric Acid Treatment
CHN	Carbon, Hydrogen and Nitrogen
CMC	Critical Micelle Concentration
CNT	Classical Nucleation Theory
CP	Cross Polarisation
CVD	Chemical Vapour Deposition
DE	Direct Excitation
DPA	Dipicolinic Acid
EDX	Energy-Dispersive X-Ray Spectroscopy
FAT	Fuming Sulfuric Acid Treatment
FFT	Fast Fourier Transform
FTIR	Fourier-Transform Infrared Spectroscopy
FWHM	Full Width at Half Maximum
GIC	Graphite Intercalation Compounds
GIFT	Generalised Indirect Fourier Transform
GO	Graphite/Graphene Oxide
hkl	Miller Indices
HLB	Hydrophilic-Lipophilic Balance
HREM	High Resolution Transmission Electron Microscopy
NMR	Nuclear Magnetic Resonance
O/W	Oil-in-Water
pH	Power of Hydrogen
PIT	Phase Inversion Temperature
PXRD	Powder X-Ray Diffraction
Revs	Revolutions
RT	Room Temperature

SAED	Selected Area Electron Diffraction
SAXS	Small Angle X-Ray Scattering
SB	Span®80, Brij®30
SiC	Silicon Carbide
SMS	Sodium Metasilicate Nonahydrate
ssNMR	Solid-State Nuclear Magnetic Resonance
Surfactant	Surface Active Agent
TEM	Transmission Electron Microscopy
TEOS	Tetraethyl Orthosilicate
TGA	Thermogravimetric Analysis
TMS	Tetramethylsilane
TX	Triton™X-114
UHP	Ultra High Purity
W/O	Water-in-Oil
XRD	X-Ray Diffraction

List of Symbols

ΔG_m	Free Energy Change
ΔG_V	Free Energy Change due to Volume
ΔG_S	Free Energy Change due to Surface Area
ΔH_m	Enthalpy Change
ΔS_m	Entropy Change
μ	Chemical Potential
μ_i	Chemical Potential of component i
γ	Interfacial Tension & Magnetogyric Ratio
ρ	Density
η	Viscosity
σ	Supersaturation
π	3.14
θ	Angle
λ	Wavelength
$\propto$	Proportional
Å	Angstrom
$\mathbb{Z}$	Set of Integers
a_0	Optimum Surface Area of a Surfactant Head Group
A	Area
B	Magnetic Field & Mean Size of Crystallite Domains
C	Ratio of Concentrations & Capacitance
E	Wt.% of Oxyethylene Groups
F_A	Overall Mass of Acid
G	Gibbs Free Energy
h	Planks Constant
I	Quantum Spin Number & Current

$I(q)$	Intensity of Scattering Vector
J	Rate of Nucleation
K	Dimensionless Shape Factor
k	Boltzmann Constant
L	Line Broadening at Half the Maximum Intensity
l_C	Maximum Critical Radius
M_A	Mass of Acid Solutions
m_e	Mass of an electron
mL	Number of Hydrophobic Groups
M_X	Mass of Aqueous Xylose Solution
N_A	Avogadro Constant
nH	Number of Hydrophilic Groups
n_i	Number of Moles of Component i
O	Wt.& of Hydroxyl Groups
P	Pressure
$P(r)$	Pair-Distance Distribution Function
$P(q)$	Form Factor
P_C	Packing Parameter
q	Scattering Vector
R	Radius & Ideal Gas Constant
r_C	Critical Nuclei Radius
S	Entropy
$S(q)$	Structure Factor
T	Temperature
T_K	Krafft Temperature
V	Volume & Voltage
v	velocity

List of Tables

List of Figures

Contents

Chapter 1

Introduction

Over the years, the synthesis of nanocrystals and the subsequent applications have been of great interest. Their large surface area enable nanocrystals to exhibit increased bioactivity, improved material properties and greater catalytic abilities. Often the syntheses of these particles need harsh reaction conditions such as high temperatures and pressures combined with the need for harmful solvents and chemicals. This thesis challenges these traditional methods by exploring novel low temperature/ambient condition routes to both an organic and inorganic system of nanocrystallisation, namely graphite and quartz. This demonstrates the capability of eliciting thermodynamic control over both organic and inorganic crystallisation for the first time.

Previously, the theory and practice of thermodynamic control of crystallisation has been demonstrated for organic pharmaceutical and graphene-based compounds. These methods have allowed the synthesis of nanocrystals under ambient conditions by exploiting the use of microemulsions. Water-in-oil microemulsions house the water soluble precursors within a 3-D confined nanoreactor, allowing crystallisation to proceed whilst leapfrogging Ostwald's Rule of Stages in order to synthesise the relevant thermodynamically stable polymorph. The following work builds upon these routes, highlighting the significance for the need of controlled crystallisation and expanding this theory to silica-based systems for the first time. Furthermore, new routes exploiting lamellar surfactant phases are also explored. Although, the lamellar 2-D nanoconfined systems lose the ability to employ thermodynamic control of crystallisation, they allow for higher yielding products and thus may prove more fruitful in real world applications.

Currently, bottom-up methods of synthesising nm and μm-sized graphene involve graphitising carbon-based precursors at high temperatures in excess of 800 ^{o}C. These high pre-requisite temperatures have inhibited their adoption in large scale manufacture. This has inspired a new microemulsion route to nanographene/graphite production based on the classic carbon snake experiment involving sugars and sulfuric acid. These previous microemulsion syntheses have yielded products with a stable nanographitic structure.

Extending from this research, a low temperature nanographite synthesis route that exploits lamellar surfactant phases is presented in this thesis. Moving to a 2-dimensional nanoconfinement system does increase product yields, however the loss of thermodynamic control means that further treatments are also necessary to produce a nanographitic product containing polycondensed benzene rings. After treating the nanoconfined product in sulfuric acid at 250 ^{o}C, a highly aromatic rich, few layer nanographitic product was yielded. This newly synthesised material could improve the capacitance of current batteries/super capacitors due to the increased surface area seen in nanographite.

The current synthetic routes for the formation of crystalline nanoquartz also require high temperatures and/or pressures for nucleation to occur. However, this leads to fast growth rates and a loss of control over product size and morphology. The work described in this thesis proves that nanoquartz crystallisation is possible under ambient conditions, using nanoconfinement in microemulsions to elicit thermodynamic control over the precipitation of silica from sodium metasilicate, and to form its most stable polymorph, α-quartz. This finding that quartz nucleation and extraction is achievable under ambient conditions by using nanoconfinement challenges the common preconception that nanoquartz deposits are a signature of high temperature and pressure conditions. The microemulsion-extracted α-quartz nanocrystals are then used to seed hydrothermal syntheses under mild conditions of 175 °C and autogenic pressure (nominally $\approx$ 9 bar). This enables nanoquartz of defined size (<10 nm) to be obtained exclusively for the first time. These newly synthesised nanocrystals are ideal for studies aimed at minimising silicosis and other lung diseases, particularly where respiratory nanoquartz has been implicated. Furthermore, the nanocrystals of various sizes were shown to have significant catalytic effects on the formation of a β-enaminone. The two stage microemulsion-hydrothermal strategy presented in this thesis provides a novel method for the crystallisation of other inorganic nanoparticles in order to optimise their catalytic performance.

The subsequent hydrothermal treatment of these nanoquartz particles can lead to aggregation of the crystals. Further methods are presented in order to try and reduce this phenomenon, including acidified syntheses and increased droplet size within the microemulsions to produce seed crystals of a greater size. Also the coating of these seed particles with a silica shell is suggested in order to create a protective barrier during treatment.

The products and systems presented in this thesis are characterised using a number of analytical techniques including small angle X-ray scattering; Fourier-transform infra-red spectroscopy; solid state nuclear magnetic resonance spectroscopy; powder X-ray diffraction; carbon, hydrogen & nitrogen elemental analysis; transmission electron microscopy; energy-dispersive X-ray spectroscopy and thermogravimetric analysis.

Chapter 2

Background Theory

2.1 Surfactants

A **surf**ace **act**ive **a**ge**nt** (surfactant) is a substance that, when present at low concentration in a system, has the property of adsorbing onto the surfaces or interfaces of the system, altering the surface or interfacial free energies.[1] Surfactants are amphiphilic molecules consisting of a tail attached to a head group. The head group is a polar/charged compound making it hydrophilic, whilst the tail is a long alkyl chain making it lipophilic. It is this molecular arrangement that make surfactants widely applicable, especially in colloidal science.[2]

2.1.1 Classification

Surfactants are classified according to the nature of their head group. There are four main basic classes of surfactants:[3]

Anionic The hydrophilic head group is negatively charged, such as a carboxyl ($RCOO^-$), sulphonate (RSO_3^-), sulfate ($ROSO_3^-$) or phosphate ($ROPO_3^-$) group.

Cationic The hydrophile carries a positive charge, for example the quaternary ammonium halides (R_4N^+). Here the four R-groups may or may not be the same, however they will usually belong to the same general family.

Zwitterionic The head group contains both a negative and a positive charge, such as the sulphobetaines ($RN^+(CH_3)_2CH_2CH_2SO_3^-$).

Nonionic Although the hydrophile bears no charge, its water solubility is derived from containing highly polar groups, such as polyoxyethylene (R-OCH2CH2O-) or R-polyol groups (including sugars).

The hydrophobic tail groups of surfactants can also be altered *via* the addition of functional groups and the variation of chain length. This can also dictate the properties of a surfactant, such as the packing parameter (Section 2.1.2).[4]

2.1.2 Phase Behaviour

At low concentration in aqueous media, surfactants act as monomers dispersing uniformly throughout the bulk solution with a surface excess at the air-water interface. However, as the concentration increases, organised aggregates consisting of many molecules begin to form called micelles (Figure 2.1). The concentration at which this occurs is known as the critical micelle concentration (CMC). This micellisation is a consequence of the water surrounding dispersed alkyl chains being more structured, the so-called "hydrophobic effect", and desire for the hydrophilic head groups to maintain contact with the aqueous media.[2] The thermodynamics governing micellisation can be explained *via* the Gibbs-Helmholtz equation:

Figure 2.1: Free surfactant monomers in aqueous media (left) will undergo micellisation (right) at a critical concentration (CMC).

$$\Delta G_m = \Delta H_m - T\Delta S_m. \tag{2.1}$$

Here, T is the temperature of the system, ΔG_m is the free energy change, ΔH_m the enthalpy change, and ΔS_m the entropy change of micellisation. Contrary to intuition, micelle formation typically produces a small increase in the system's enthalpy whilst creating a larger decrease in entropy. Though surfactant molecules are constrained whilst in a micellar configuration, a decrease in entropy still arises due to this hydrophobic effect. To understand the hydrophobic effect, one must consider the configuration of water molecules, not the surfactant monomers. Water molecules cannot hydrogen bond with alkyl chains, so this reduces the number of configurations the water molecules can take. This leads to a cage-like structure around the alkyl chains of the monomers. Upon micellisation, this restriction is broken and entropy is increased.[5]

Micellisation does not always yield spherical formations (as depicted in Figure 2.1). In fact, there are four major structural formations a micelle can take: spherical, cylindrical, lamellar and vesicle (Figure 2.2).[1] It is known that the surfactant phase of a given system relies on the concentration of surfactant monomers. With increasing concentration micelles can undergo a transformation from free monomers to spherical micelles, to cylindrical micelles, and finally to bilayer structures (lamellar and vesicles).[6] However, it is not only the surfactant concentration which determines the resultant micelle form, shape is also a contributing factor. This is described *via* a dimensionless packing parameter, which uses a simple geometric argument to predict the phase a particular surfactant may take upon micellisation.[5] Consider a spherical micelle (Figure 2.3). Here l_c is the maximum critical

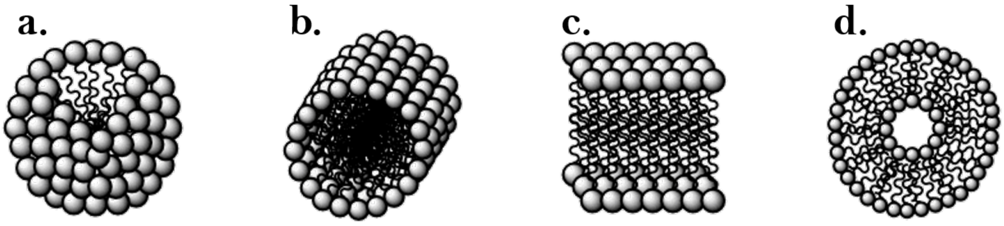

Figure 2.2: The four major structures surfactants will form upon micellisation. **a.** Spherical. **b.** Cylindrical. **c.** Lamellar. **d.** Vesicle.

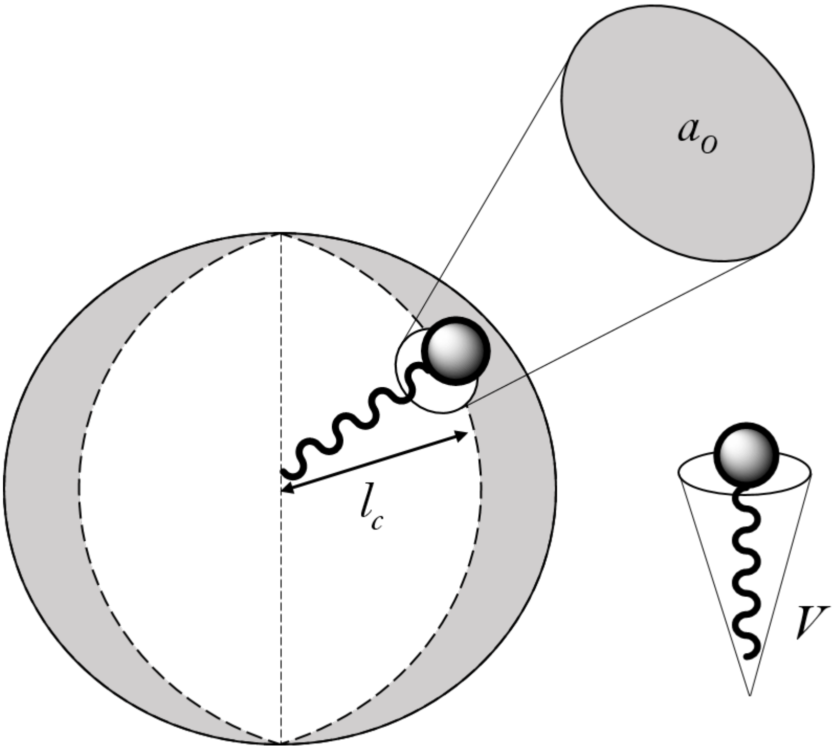

Figure 2.3: Schematic of a spherical micelle. The packing parameters for a single surfactant molecule have been defined pictorially.

radius a micelle can reach, a_0 is the optimum surface area of a surfactant head group and V is the hydrophobic tail volume. Note that this theory assumes that the surfactant head group surface areas are assumed to be close to that needed for a bilayer. Given a micelle of radius R, then for a spherical micelle:

$$\frac{V}{Ra_0} = \frac{1}{3}, \tag{2.2}$$

holds with simple geometric arguments. However since l_c has been defined to be the maximum radius a micelle can take, $R < l_c$. Thus equation (2.2) can be rearranged to

$$P_c = \frac{V}{a_0 l_c} < \frac{1}{3}, \tag{2.3}$$

where the packing parameter P_c has been defined. Equation (2.3) is known as the packing condition for spherical micelle formation. Using similar arguments, the relationships between the packing parameter and other micelle phases have been determined (Table 2.1).[7,8]

Table 2.1: Predictive relationships between the packing parameter of a surfactant molecule and the resulting micelle phase.

Micellisation Phase	Packing Parameter Condition
Spherical Micelles	$P_c < \frac{1}{3}$
Cylindrical (Worm-like) Micelles	$\frac{1}{3} < P_c < \frac{1}{2}$
Bilayers (Vesicles)	$\frac{1}{2} < P_c < 1$
Inverted Structures	$1 < P_c$

2.1.2.1 Co-surfactants

Molecules such as medium and long chain alcohols can aid surfactants in lowering the interfacial tension and help to form microemulsions. Such molecules are known as co-surfactants. They are weakly amphiphilic due to their short hydrophobic chain and hydrophilic hydroxyl group, which allows them to interfere with the primary surfactant packing, aiding stability.[9,10]

2.1.2.2 Krafft Point

The Krafft point (Krafft temperature), T_K, is a phenomenon commonly observed in ionic surfactants, however, it is also exhibited by some nonionics.[11] The Krafft point can be defined as the temperature at which the solubility of a surfactant is equal to its CMC.[12] Due to the amphiphilic nature of surfactants, their solubility in aqueous media is expected to be low when the surfactants are molecularly dispersed. This is indeed the case for temperatures below T_K. However, as the Krafft point is surpassed, surfactant solubility sharply increases due to micellisation (Figure 2.4). T_K is therefore easily attained by plotting both the CMC curve and solubility curve (with respect to temperature) for a given surfactant and considering the point of intersection. When using a particular surfactant, one must consider the Krafft point, as below T_K the surfactant is likely to be significantly less effective as micelles do not form.

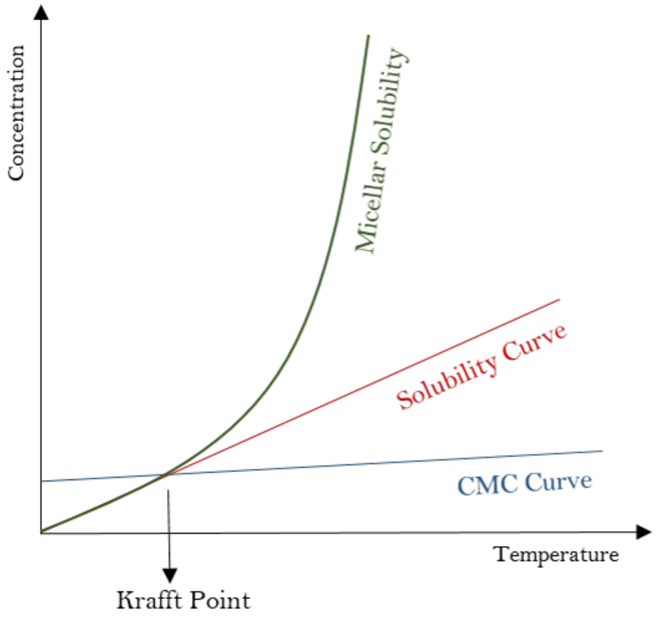

Figure 2.4: A typical surfactant CMC and solubility curve. The point of intersection is defined to be T_K, at which solubility sharply increases due to micellisation.

2.1.2.3 Cloud Point

When the temperature of a nonionic surfactant mixture is raised beyond a certain threshold, the solution separates into a surfactant-rich and surfactant-poor phase.[13] This can be observed *via* a clouding of the solution, thus this threshold is termed the cloud point. As the cloud point is approached, the hydrophilic head groups of the surfactant micelles are dehydrated because the free energy entropy penalty, $-T\Delta S$, of forming hydrogen bonds with water *via* geometric constraints becomes less favourable as temperature rises. The dehydrated head groups then begin to cluster and form micelle aggregates.[14] These micellar aggregates scatter light, which gives the solution it's cloudy appearance.[15] Contrary to the Krafft point, the cloud point is typically observed for nonionic surfactants, though some ionic systems have exhibited the behaviour.[13,16–19]

The cloud point can be affected by the concentration and structure of the surfactant as well as the presence of electrolytes or organic molecules.[14] Increasing the carbon chain length of the surfactant, for example, will decrease the temperature at which the cloud point occurs.[20] Changes in pressure as well as temperature may also result in a surfactant mixture clouding.[21,22]

2.1.2.4 Hydrophilic-lipophilic Balance

The hydrophilic-lipophilic balance (HLB) is a dimensionless scale which assigns a numerical value to a surfactant indicating the size of its hydrophobic/hydrophilic moieties. A highly hydrophobic surfactant is assigned a low HLB value (<10) and typically forms w/o emulsions, whilst hydrophilic surfactants are assigned high values (>10) and typically form o/w emulsions.[23] The expected application of a given surfactant is therefore often based on its HLB value (Table 2.2).

Table 2.2: The expected application of a surfactant and its assigned HLB value.[24]

Surfactant HLB Range	Expected Application
1 - 4	w/o emulsifier
1.5 - 3	Anti-foaming Agent
6 - 8	Wetting Agent
10 - 13	o/w emulsifier
13 - 15	Detergent
15 - 18	Solubiliser

The first empirical formula (Equation (2.4)) for working out the HLB of a surfactant was based on nonionic alkyl polyoxyethylenes,[25]

$$HLB = \frac{E+O}{5}, \tag{2.4}$$

where E and O are the weight percentages of the oxyethylene and hydroxyl groups, respectively. This formula is satisfactory for most nonionic surfactants, however a general empirical formula (Equation (2.5)) for any surfactant has been developed.[26]

$$HLB = [(nH) - (mL)] + 7. \tag{2.5}$$

Here, H and L are constants corresponding with the hydrophilic and hydrophobic groups respectively, and n, m the number of each respective group.

When multiple surfactants are used, the HLB values behave additively.[23] For example, if two surfactants are combined in a 1:3 ratio with HLB numbers 2 and 16 respectively, the resultant HLB of the blend would be $2 \times 0.25 + 16 \times 0.75 = 12.5$.

2.1.3 Interface Behaviour

Due to the amphiphilic nature of surfactants, they have affinity for oil/water interfaces. Surfactant adsorption at these interfaces is thermodynamically favourable as the interfacial tension between the two media is lowered, in turn lowering the free energy.

Molecules at an interface have reduced intermolecular interactions than the same molecules in the bulk. Due to this, work is required to pull a molecule from the bulk to the interface, as intermolecular bonds are broken; interfacial tension, γ, is a measure of this work. Interfacial tension is defined as,

$$\gamma = \frac{\partial G}{\partial A} \tag{2.6}$$

where G and A are the Gibbs free energy and interfacial area respectively.

When a surfactant is added to a water/oil system it adsorbs to the interface with its hydrophobic tail lying in the oil phase and the polar head group in the water phase. These interactions are much more favourable compared to the interactions between the immiscible oil and water molecules, and hence the surfactant lowers the interfacial tension and free energy of the system.

2.1.3.1 Emulsions

Conventionally, an emulsion is described as a dispersion of one liquid in another immiscible (or poorly miscible) liquid, typically water-in-oil (w/o) or oil-in-water (o/w). Due to the immiscibility, it is thermodynamically favourable for the two liquids to phase separate (the system wishes to reduces the total surface contact between the two liquids).[27] However, with the use of surfactants the interfacial tension between the two liquids can be reduced and thus emulsification can occur for extended time periods following sufficiently energetic mixing of the components.

The emulsion will phase separate over time as the emulsion is only metastable. Emulsion destabilisation can occur *via* creaming, droplet coalescence and Ostwald ripening. Creaming is the process of less dense droplets rising to the top of the continuous phase. (Note that if the droplets are greater in density compared to the continuous phase they would conversely sediment to the bottom.) This instability can be most notably seen in the creaming of milk, where the fat droplets cream out of the continuous media (water).

Balancing buoyancy and drag forces one can use the equation:

$$v = \frac{d^2 \Delta \rho g}{18\eta} \tag{2.7}$$

to estimate the velocity, v, at which an emulsion will cream. It can be seen from equation (2.7) that emulsions with a smaller droplet size, d, will cream at quadratically slower rates. Note that $\Delta\rho$ is the density difference of the two liquids, g is force due to gravity and η is viscosity of the continuous phase.

Due to thermal fluctuations within an emulsion, droplets commonly come into contact. If the droplets carry enough energy they can coalesce and become larger in size, causing them to cream/sediment at quicker rates.[28] Another mechanism in which an emulsion can destabilise is known as Ostwald ripening. This is the process of smaller droplets dissolving into the continuous media and then diffusing and redepositing into larger ones, again increasing the over all emulsion droplet size.[29] Like coalescence, this leads to quicker phase separation times due to creaming. Ostwald ripening occurs due to the different chemical potentials, μ, existing in different sized droplets. Smaller droplets have a higher Laplace pressure, hence a larger chemical potential,[30,31] given by:

$$\Delta P = 2\gamma \frac{1}{R} \tag{2.8}$$

where R is defined as the radius of the droplet. In order to lower the overall free energy of the system ($G = \Sigma n_i \mu_i$) molecules have a tendency to diffuse from domains of high μ to low, causing smaller droplets to shrink and larger ones to grow.

Due to the wide applications of emulsions, for example in the pharmaceutical, food and agrochemical industries, great effort has been made to try and stabilise these systems. The focus of these methods is to prevent coalescence and Ostwald ripening in order to increase the creaming time of the emulsion. One way in which the stability of emulsions can be improved is through the use of block copolymers. The amphiphilic nature of these polymers means that they migrate to oil/water interfaces and prevent coalescence of droplets through steric hindrance of the hydrophobic chains (Figure 2.5). When two droplets come into close contact the polymer chains become more restricted thus they repel one another due to entropic reasons. Also locally, the polymer concentration increases creating osmotic pressure and thus the continuous media migrates to the site repelling the droplets from one another.[32]

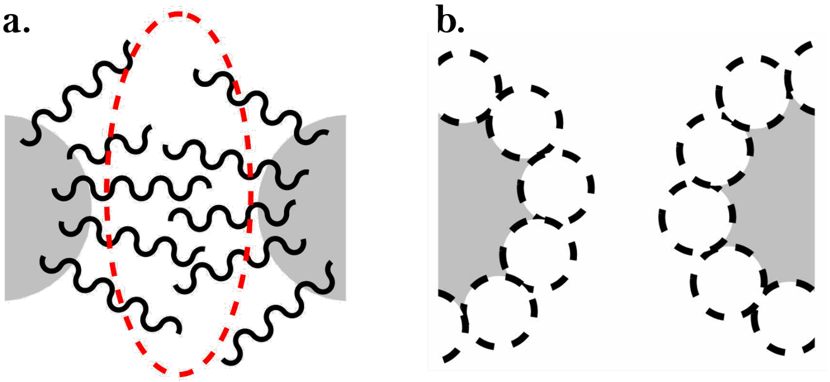

Figure 2.5: Two methods of stabilising emulsion droplets *via* block copolymers and colloidal particles. **a.** Two emulsion droplets (grey) stabilised by block copolymers (black). Steric hindrance of the polymer chains (red dash) provides repulsion by entropic and osmotic arguments. **b.** Two Pickering emulsion droplets (grey) stabilised by colloidal particles (black dash).

In a Pickering emulsion, the emulsion is stabilised by the adsorption of colloidal particles at the water-oil interface (Figure 2.5). Particles should be chosen carefully depending on whether w/o or o/w emulsions are to be stabilised. Adsorbed particles with contacts angles in the range 30° - 90° will form o/w emulsions whilst larger valued contact angles will form w/o.[33] Pickering emulsions are also thought to hinder Ostwald ripening, thus providing an extremely stable emulsion.[34]

2.1.3.2 Nanoemulsions

A nanoemulsion is a kinetically stable emulsion with droplet sizes in the order of 100 nm. They appear optically blue due to the droplets being in the size range comparable to the wavelength of blue light.[35] Having excellent kinetic stability, nanoemulsions have become increasingly important in drug delivery,[36–38] nanoparticle and polymeric material synthesis,[39,40] developing new cosmetics[41] and the crystallisation of pharmaceutical compounds.[42,43]

The synthesis of nanoemulsions can be categorised into two broad techniques: high energy methods and low energy methods.[44] High energy syntheses use ultrasonication and high-pressure homogenisation to break down the emulsion droplets to their nanometer size.[45,46] Using these brute force methods, it is possible to form nanoemulsions with large dispersed phase volume fractions (as high as 40%).[47] Low energy methods, however, can achieve similar droplet sizes seen in high energy methods with a magnetic stirrer. These approaches exploit the low interfacial tension of a system to make nanoemulsions without the need for excess shear. The emulsion inversion point, EIP, uses mixing of components in a specific order to achieve the small dispersed droplet size. For EIP synthesis to be successful, a change in the composition of a system must spontaneously change the interface curvature within it.[48] To induce this phase inversion, two methods of component addition are proposed. Method A involves the continuous addition of the dispersed phase to a mixture of the continuous phase and surfactant. Conversely, in method B it is the continuous phase that is added to a mixture of the dispersed phase and surfactant until phase inversion occurs and a nano emulsion forms.[49–51] The choice of method depends on the HLB of the surfactant; if it dislikes the continuous phase, method A should be used, if it dislikes the dispersed phase then method B should be.[52]

2.1.3.3 Microemulsions

Microemulsions are thermodynamically stable, spontaneously formed emulsions with a typical dispersed droplet size of 1-100 nm.[53–55] Macroscopically they appear as a transparent homogeneous liquid as the small droplet size minimises the scattering of light; the droplet size is smaller than the wavelength of visible light. The term “swollen micelles” or “inverse swollen micelles” can be used to describe an o/w or w/o microemulsion when the volume of the dispersed phase is decreased so much that its properties differ from that seen in its bulk phase. However, since there is no sharp transition from dispersed phase containing anisotropic core in a microemulsion and a micelle that is swollen with dispersed phase, the term microemulsion is still used throughout literature to describe systems with such low dispersed volumes.[56]

Microemulsion formation can be described using the Gibbs free energy of formation, ΔG_f,

$$\Delta G_f = \gamma \Delta A - T \Delta S. \tag{2.9}$$

The interfacial tension is denoted γ, ΔA the change in interfacial area, ΔS the change in entropy and T is the temperature of the system. If a microemulsion forms, ΔS is large and positive due to the dispersed phase having access to the whole system rather than being confined to the top/bottom. However, ΔA also increases greatly due to the formation of droplets. Therefore, if the right surfactant is used so that γ is low enough $T\Delta S > \gamma \Delta A$; a negative free energy of formation is achieved and a microemulsion will form.[57] Furthermore, the low interfacial tension required for microemulsion formation also ensures that the Laplace pressure, $\Delta P = 2\gamma/R$, remains small, even across the nanoscopic droplets. This eliminates any Ostwald ripening effects that are seen in other emulsion systems.[56]

There are four Winsor classifications of microemulsion systems when composed of water (aqueous salt), oil (organic liquid) and approximately 5-25% surfactant (Figure 2.6).[58] Winsor I and Winsor II systems are both phase separated systems consisting of an o/w microemulsion with an excess oil upper phase and a w/o microemulsion with an excess water lower phase, respectively. Winsor III is a triple phase system with a bicontinuous microemulsion phase sandwiched between phase-separated water and oil layers. A bicontinuous microemulsion, as opposed to a w/o or o/w droplet microemulsion, contains continuous domains of oil and water. Bicontinuous microemulsions can form with surfactants that have equal affinity for the oil and aqueous domains, ie. HLB values ∼ 10. The final classification of microemulsion is Winsor IV; a homogeneous system of either a w/o or o/w microemulsion or a bicontinuous microemulsion.[55]

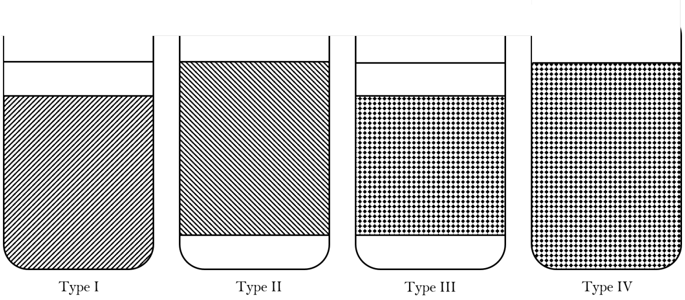

Figure 2.6: The four Winsor classifications. Winsor I: o/w microemulsion with excess oil above. Winsor II: w/o microemulsion with excess water below. Winsor III: a bicontinuous microemulsion sandwiched between oil and water layers above and below respectively. Winsor IV: a homogeneous bicontinuous, o/w or w/o microemulsion.

Due to Brownian motion, the dispersed droplets within a microemulsion have frequent collisions with one another. The most energetic of these collisions cause transient dimers to form allowing any interior content encapsulated within the droplets to be exchanged (Figure 2.7).[59] This mechanistic feature of microemulsions means that they can act as nanoreactors for the synthesis of metal nanoparticles,[60,61] quantum dots,[62] polymeric nanoparticles,[63] ceramics,[64] as wells as nanorod and core shell structured materials.[65–68]

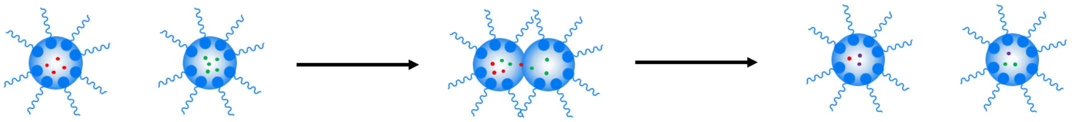

Figure 2.7: Schematic of a transient dimer forming after an energetic collision between microemulsion droplets. Upon formation any encapsulated interior reactants (red and green) can exchange between the droplets and react (purple), making microemulsions a suitable mechanism for nanoreactors.

Also due to their thermodynamic stability, optical clarity and ease of preparation, microemulsions are being used as potential drug delivery systems. Oil in water microemulsions in particular offer the ability to incorporate hydrophobic drugs into the oil phase allowing easy delivery into the body.[69]

2.1.3.4 Phase Inversion Temperature

The phase inversion temperature (PIT) is the temperature at which a nonionic surfactant system switches from an o/w emulsion to a w/o emulsion or *visa versa*.[70] Water continuous systems tend to be more stable at lower temperatures as the hydration of surfactant head groups decreases with increasing temperature.[1] The hydrophilicity of the surfactant therefore decreases at higher temperatures and an oil continuous system becomes more favourable. At the PIT, the interfacial tension is at its minimum and the surfactant has an HLB ≈ 10.[5]

2.1.4 Lyotropic Liquid Crystals

A liquid crystal is an intermediate stage of matter between that of a crystalline solid and an isotropic liquid. Liquid crystalline materials are called lyotropic if phases having long-ranged orientational order are induced by the addition of a solvent. These phases are used to describe those exhibited by amphiphilic molecules or surfactants.

In general, once the CMC of a system is reached and micelle aggregates form, a liquid crystalline I_1 phase can be obtained if the micelles are plentiful and begin to form a long range cubic order. As the concentration of amphiphilic molecules increases, these micelles grow into cylindrical aggregates which arrange on a hexagonal lattice; this is the hexagonal, H_I, phase. At higher concentrations of surfactant, the lamellar liquid crystalline, L_α, is formed. In this phase the amphiphilic molecules are arranged in bilayers separated by aqueous media. Each layer is akin to the arrangement of lipids in cell membranes. An intermediate bicontinuous, L_3, phase exists between the hexagonal and lamellar phases. In this phase channels of oil and water coexist often forming complex architectures.[71,72] The particular range of lyotropic liquid crystals formed will depend on the particular surfactant and its packing parameter.

2.1.5 Specific Surfactants

2.1.5.1 Brij®30

Polyoxyethylene(4)lauryl ether (Brij®30) is a nonionic surfactant (Figure 2.8). It has a HLB value of 10 and an approximate $P_c = 1$ (the polar head group has an area approximately equal to that of the alkyl chain).[73] This should make Brij®30 suitable for the formation of a lamellar system.

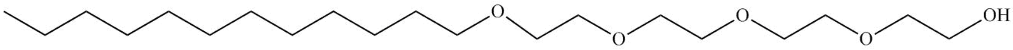

Figure 2.8: The Brij®30 molecule.

Brij®30 has been identified as the best surfactant for forming an acidified lamellar phase because the surfactant does not degrade under harsh low pH conditions. This has been confirmed with both Small Angle X-ray Scattering (SAXS) and optical microscopy (Figure 2.9). A sharp lamellar peak can be seen up to 90 °C. At greater temperatures, the lamellar phase breaks down into a disordered L_3 bicontinuous liquid crystalline phase. Though only one peak is able to be resolved in the X-ray data, the presence of Maltese crosses in micrographs taken under crossed polarisers indicates the formation of a lamellar surfactant phase.[74]

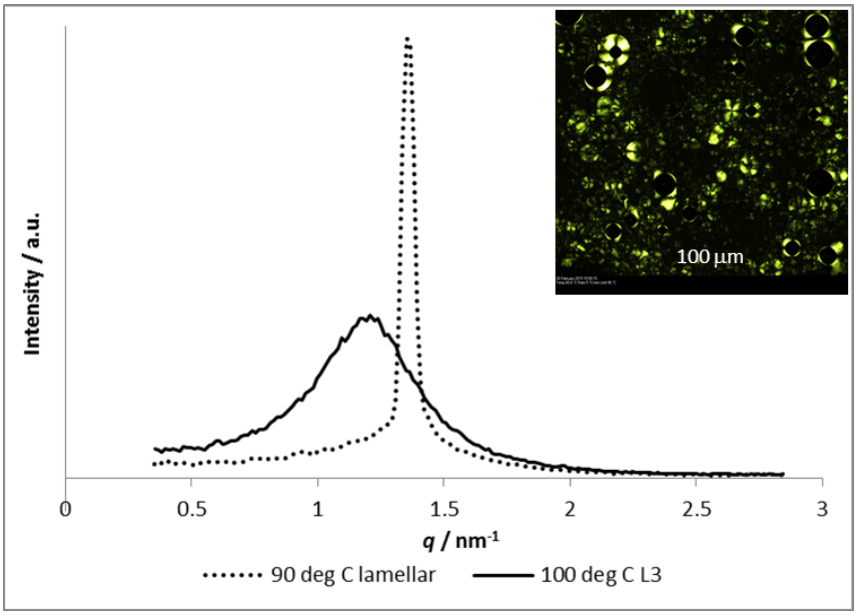

Figure 2.9: SAXS data of the Brij® 30 lamellar system. The system breaks down at temperatures above 90 °C to a disordered L_3 phase. Optical micrograph of the lamellar phase displays Maltese crosses under cross polarisers (inset). Data is collected by Janet Berry of Dr Cooper's Research group.

2.1.5.2 Span®80

[(2R)-2-[(2R,3R,4S)-3,4-dihydroxyoxolan-2-yl]-2-hydroxyethyl] (Z)-octadec-9-enoate (Span®80) is a viscous, water soluble nonionic surfactant (Figure 2.10). It is a lipophilic molecule with a HLB of 4.3, making it suitable as a water-in-oil emulsifier.[73] It has been shown that a system with a 1:1 ratio of Span®80 and Brij®30, water and heptane can form a water-in-oil microemulsion, with the droplet size easily tunable by varying the weight percentage of water.[124]

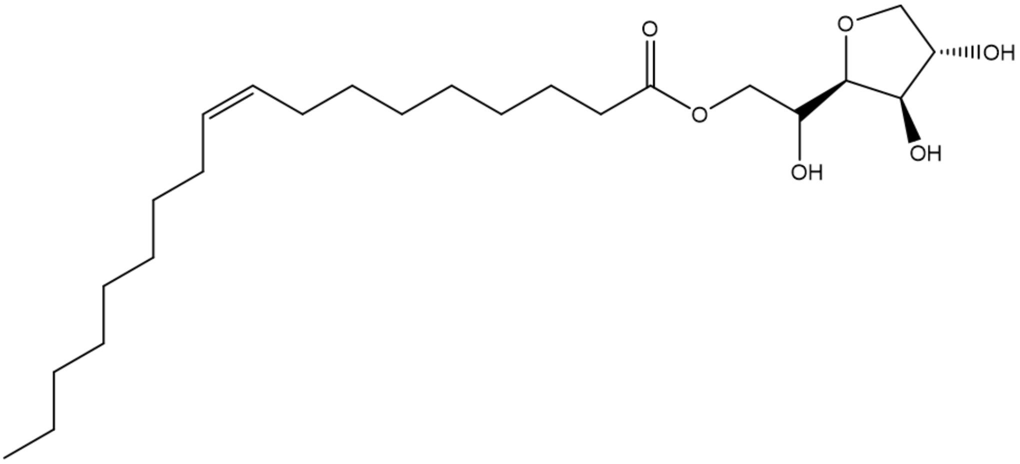

Figure 2.10: The Span®80 molecule.

2.1.5.3 Triton™X-114

(1,1,3,3-Tetramethylbutyl)phenyl-polyethylene glycol, Polyethylene glycol tert-octylphenyl ether (Triton™X-114) is a nonionic surfactant that has a hydrophilic polyethylene oxide chain (7.5 units long on average) and an aromatic, hydrocarbon hydrophobic group (Figure 2.11). Having a HLB of 12.4, usually Triton™X-114 is used as an oil-in-water emulsifier.[73] However, when cyclohexane is used as a continuous oil phase, w/o microemulsions can be formed using this surfactant.[124]

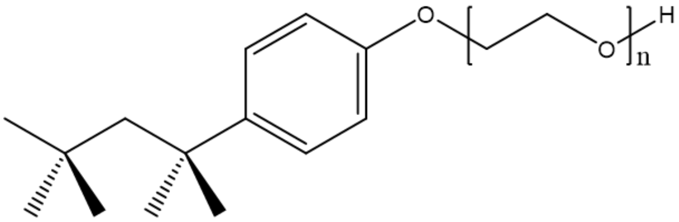

Figure 2.11: The Triton™X-114.

2.2 Crystallisation

A crystal is characterised by a periodically repeating regular array of atoms, known as a unit cell. Therefore a crystalline solid exhibits long-range order throughout the system; knowledge of the physical properties within any arbitrary unit cell implies knowledge within any other unit cell. This differs from amorphous solids where long-range order is destroyed and only short-range order may exist on a local microscopic level.[75]

2.2.1 Crystal Classification

Crystals are classified on the basis of space group symmetries. These symmetries comprise of translations, rotations, reflections, inversions or a combination of these. In $\mathbb{R}^3$ there are 230 of these distinct symmetries. Space groups exhibiting similar symmetries are classified into seven crystal systems. These systems are defined by length of the axis vectors of a crystal's unit cell and the angle they make with each other (Table 2.3).

Table 2.3: The seven crystal systems and the criteria for a crystal's unit cell dimensions to belong to each.

System	Lengths	Angles
Cubic	$a = b = c$	$\alpha = \beta = \gamma = 90^o$
Trigonal	$a = b = c$	$\alpha = \beta = \gamma \neq 90^o$
Hexagonal	$a = b \neq c$	$\alpha = \beta = 90^o, \gamma = 120^o$
Tetragonal	$a = b \neq c$	$\alpha = \beta = \gamma = 90^o$
Orthorhombic	$a \neq b \neq c$	$\alpha = \beta = \gamma = 90^o$
Monoclinic	$a \neq b \neq c$	$\alpha = \beta = 90^o \neq \gamma$
Triclinic	$a \neq b \neq c$	$\alpha \neq \beta \neq \gamma$

The axis vectors $\vec{a}$, $\vec{b}$ and $\vec{c}$ of a unit cell can also be used to index planes of a crystal. This is done *via* Miller indices, (hkl), which denotes the plane orthogonal $\vec{g}$ such that

$$\vec{g} = \mathrm{h}\vec{a} + \mathrm{k}\vec{b} + \mathrm{l}\vec{c} \tag{2.10}$$

is satisfied. Note that by convention h,k and l are integers, the greatest common divisor between all three should be one, and negative values are denoted $\bar{\mathrm{h}}$ etc. Furthermore {hkl} denotes the set of all planes equivalent to (hkl) by symmetry.[76]

2.2.2 Supersaturation

In order for crystals to form spontaneously, a supersaturated solution of its constituent molecules must be present.[77] Supersaturation, σ, can be described *via* a change in chemical potentials akin to that of a one-component vapour at the vapour-solid phase boundary (equation 2.11).

$$\sigma = \frac{(\mu_{ss} - \mu_0)}{kTN_A} \tag{2.11}$$

Here, the chemical potentials of the supersaturated state (supersaturated solution) and the equilibrium state (crystalline solid) are denoted μ_{ss} and μ_0 respectively, N_A is Avogadro's constant, k is the Boltzmann constant and T is the temperature of the system. If the solution is assumed to be ideal (activity coefficient is one), supersaturation can then be expressed as a ratio of concentrations, C, which is termed the supersaturation ratio.[78] (equation 2.12).

$$\sigma = ln\left(\frac{C_{ss}}{C_0}\right) \tag{2.12}$$

The simplest way to achieve the conditions needed to generate a supersaturated solution is to utilise the temperature dependence of solubility. Generally, as the temperature of a solute/solvent system increases so does the solubility of the solute. Therefore if the saturation limit of a system is reached at high temperature and the solution is cooled at a rate faster than the rate of precipitation, a supersaturated solution is formed.[79] Similar manipulations of the pressure and volume of a system can also result in a supersaturated state.[80]

A supersaturated solution is in a higher free energy state than a regular saturated solution, and therefore crystallisation/precipitation occurs to allow the solution to reach a lower free energy state. Depending on the system conditions, it can lie within one of three zones within a supersaturated state: precipitation, nucleation and metastable (Figure 2.12). Crystallisation can only occur within the nucleation zone. As the precipitation zone is reached the solute precipitates out as an amorphous solid. Within the metastable zone, a new crystallite may not form for a long period of time, however crystal growth on added seeds can still occur. To grow large well-ordered crystals one can therefore hold the system in the nucleation zone for a short time to activate a few nucleation sites, before returning the solution to metastable zone to allow the crystals to grow.[81]

2.2.3 Nucleation

Supersaturation alone is not enough to initiate crystallisation of a system. Before crystals can grow there must exist stable clusters (nuclei) of minute solid bodies that act as centres of crystallisation. The term nucleation is used to describe the point at which there

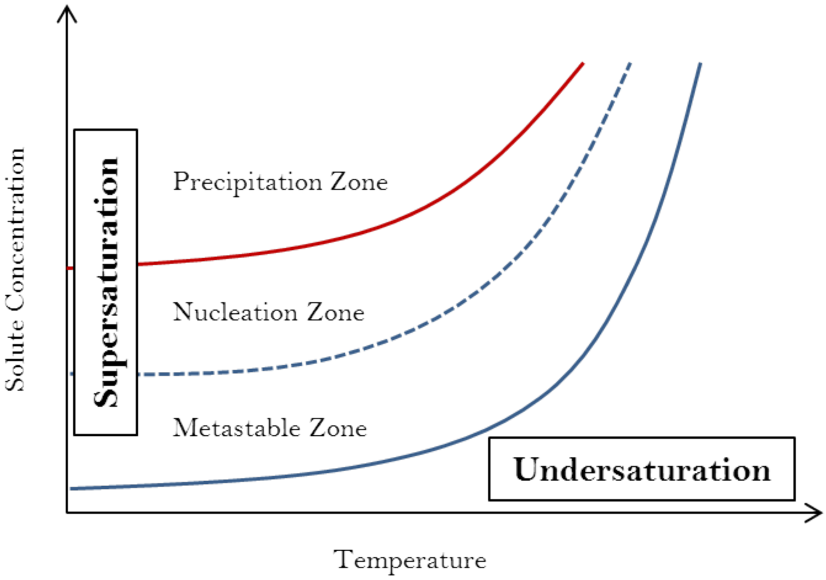

Figure 2.12: Schematic of a hypothetical solubility curve for a solute (solid blue curve). As the dashed blue curve/solid red curve is surpassed the supersaturated state enters the nucleation/precipitation zone.

are sufficient bodies within nuclei to induce irreversible growth of the crystal.[76] Often, nucleation can be induced by mechanical shock, agitation and extreme pressures.[82,83]

2.2.3.1 Classical Nucleation Theory

Classical nucleation theory (CNT) describes the process in which clusters of constitute molecules grow above a critical size by overcoming the tendency to redissolve and thereby form a stable solid particle.

Consider a supersaturated solution of solutes in which a small spherical solid particle of radius r is formed *via* homogeneous nucleation (Figure 2.13). The formation of a solid

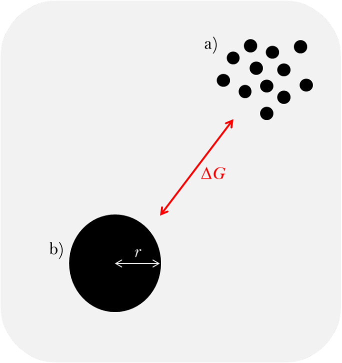

Figure 2.13: Schematic of a supersaturated solution of constitute solutes (a) homogeneously nucleating to form a solid body of radius r (b). A difference in free energy ΔG is observed.

particle creates an interface between itself and the surrounding supersaturated solution, hence a difference in free energy, ΔG, is observed in the system. This total change in free energy can be expressed as the sum of the free energy change due to volume and surface area changes, denoted ΔG_V and ΔG_S respectively (Equations 2.13).

$$\begin{aligned} \Delta G_V &= \frac{4}{3}\pi r^3 \Delta G_v \\ \Delta G_S &= 4\pi r^2 \gamma \end{aligned} \tag{2.13}$$

Where γ is the interfacial tension between the developing crystalline solid and the surrounding supersaturated solution, and ΔG_v is the free energy change of the liquid-solid transition per unit volume.When creating a solid/liquid interface work must be done. This results in a positive ΔG_S which is proportional to r^2, whilst ΔG_V depends on r^3. Note that in a supersaturated solution, molecular interactions in the bulk solid phase have a large enthalpic gain, hence a negative ΔG_V is seen. The total free energy change is given in equation 2.14.

$$\Delta G = \frac{4}{3}\pi r^3 \Delta G_v + 4\pi r^2 \gamma \tag{2.14}$$

The two terms that contribute to the total free energy change have opposing signs and differing dependencies on r. Therefore ΔG will pass through a maximum at a critical nuclei radius, r_c, which corresponds to the activation energy needed for homogeneous nucleation, $\Delta G_{critical}$ (figure 2.14). The values of r_c and $\Delta G_{critical}$ can be calculated by setting the derivative of the free energy of formation, ΔG, to zero and solving (equations 2.15).

$$\begin{aligned} \frac{d\Delta G}{dr} &= 4\pi r_c^2 \Delta G_v + 8\pi r_c \gamma = 0 \\ r_c &= \frac{-2\gamma}{\Delta G_v} \\ \Delta G_{critical} &= \frac{16\pi\gamma^3}{3\left(\Delta G_v\right)^2} = \frac{4\pi\gamma r_c^2}{3} \end{aligned} \tag{2.15}$$

For nuclei to form, the activation energy barrier must be surpassed (*via* energy fluctuations within the system) such that the radius of solid phase exceeds r_c, at which point the crystallite becomes stable and can continue to grow decreasing the free energy of formation. Clusters that are smaller in size than r_c are likely to re-dissolve back into solution as growth is energetically unfavourable.[76,84–87]

Although the energy of a solution is constant at a fixed temperature and pressure, for any fluid system there will be a localised statistical distribution of energy in the constitute molecules. It is the regions in the system that are most supersaturated that will carry the

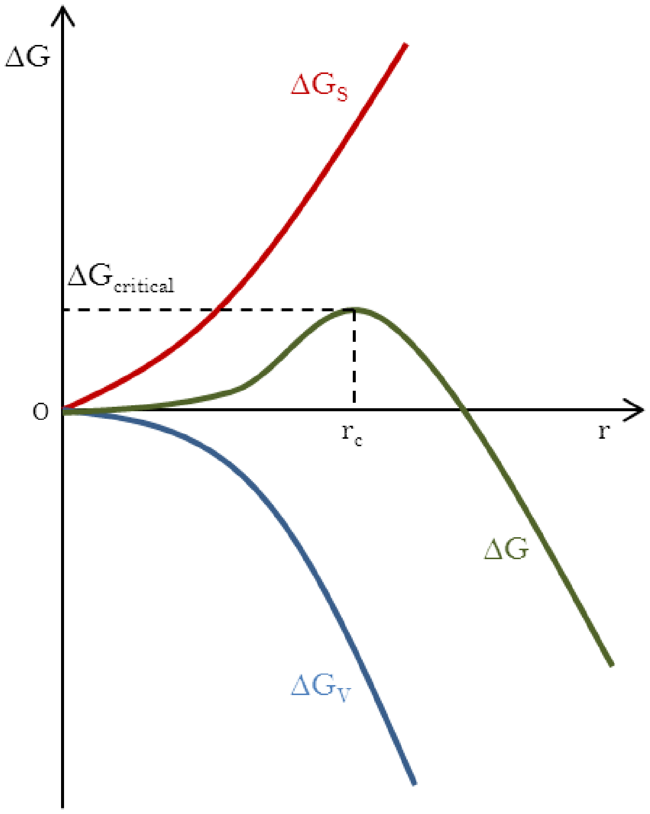

Figure 2.14: Hypothetical free energy curves: a positive ΔG_S (red curve) and a negative ΔG_V (blue curve) will sum to give ΔG (green curve) which will reach a maximum at r_c. This denotes the critical radius size whose free energy of formation corresponds to the activation energy needed for homogeneous nucleation, $\Delta G_{critical}$.

most energy and favour nucleation. The rate of nucleation, J, can then be described by the Arrhenius equation (equation 2.16).

$$J = Aexp\left(-\frac{\Delta G_{critical}}{k_B T}\right) \tag{2.16}$$

Where the exponential factor describes the probability of the energy fluctuation. The relationship between the size and solubility of a nucleating particle is given by the Gibbs-Thompson equation relation (equation 2.17).

$$lnS = \frac{2\gamma v}{k_B T r_c} \tag{2.17}$$

Here, v is the molecular volume whilst S is the degree of supersaturation and is given by $S = C/C^*$, where C and C^* are the concentrations of the solution and the saturated state, respectively. Rearranging for r_c and substituting into equation 2.15 leads to an expression for the activation energy required for nucleation in terms of the degree of supersaturation,

S (equation 2.18).

$$\Delta G_{critical} = \frac{16\pi\gamma^3 v^2}{3\left(k_B T ln S\right)^2} \tag{2.18}$$

Substituting this expression of ΔG into equation 2.16 leads to a final equation for the rate of nucleation (equation 2.19).

$$J = exp\left(-\frac{16\pi\gamma^3 v^2}{3k_B^3 T^3 \left(lnS\right)^2}\right) \tag{2.19}$$

The rate of nucleation is therefore determined by the interfacial tension, temperature and degree of supersaturation of the system.[76,88]

In practice, systems tend to have foreign bodies such as solid impurities and container walls present. It is much more common for these bodies to seed nucleation rather than for spontaneous homogeneous nucleation to occur. This is due to the presence of a surface catalysing the process and is known as heterogeneous nucleation. Heterogeneous nucleation has a lower activation energy than that of homogeneous, thus allowing nuclei to form more rapidly (equation 2.20).

$$\Delta G_{critical}(\text{Homogenous}) = f(\theta)\Delta G_{critical}(\text{Heterogenous}) \tag{2.20}$$

Here, the activation energy factor in which heterogeneous nucleation is lowered by is denoted $f(\theta)$. At the simplest level, consider the contact angle, θ, between the three planar interfacial tensions between the solid surface of a foreign body and the liquid and nucleating crystal phases (figure 2.15). Resolving the interfacial tensions, Young's equation

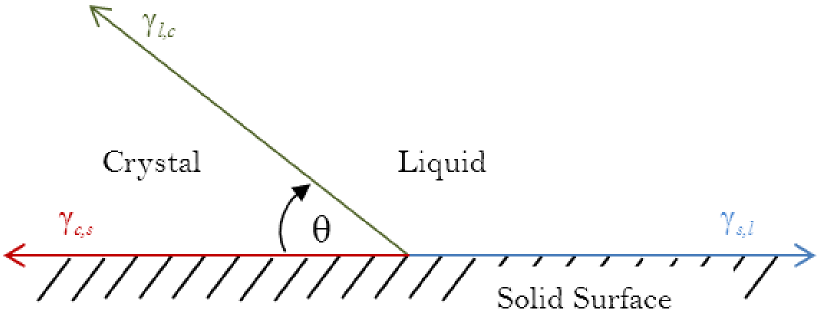

Figure 2.15: Schematic identifying the contact angle between the three heterogeneous nucleation phases. The three interfacial tensions are $\gamma_{l,c}$ (green), $\gamma_{s,l}$ (blue) and $\gamma_{c,s}$ (red), which are the tensions of the interfaces between the nucleus of the crystal and the liquid phase, the liquid phase and the solid surface, and the crystal and the solid surface, respectively.

is derived with which the contact angle can be determined (equation 2.21).

$$cos\theta = \frac{\gamma_{c,s} - \gamma_{s,l}}{\gamma_{l,c}} \tag{2.21}$$

The function $f(\theta)$ is then constructed to have a range between zero and one for $0 < \theta < \pi$ (equation 2.22).

$$f(\theta) = \frac{1}{2} - \frac{3}{4}cos(\theta) + \frac{1}{4}cos^3(\theta) \tag{2.22}$$

In the limit $\theta \to \pi$ the nucleating crystal detaches itself from the foreign surface and becomes a solid sphere. This is known as drying and is analogous to homogeneous nucleation discussed above.[89]

Thus far, only primary (spontaneous) nucleation has been discussed. As $\theta \to 0$, $f(\theta) \to 0$ in equation 2.22 and the nucleation barrier disappears. The supersaturated solution will completely wet the solid surface and is akin to seeding the system with a crystal of the solute; this is known as secondary nucleation.[89]

2.2.3.2 Non-Classical Nucleation and Crystallisation

Classical nucleation theory adequately describes a molecule-by-molecule assembly process to form stable nuclei, however negates to explain the alternative mechanism of aggregation of larger particles to form close-packed crystalline domains.[90] The occurrence of metastable intermediates in protein crystallisation has led to development of a different type of crystallisation theory.[91,92] Treating proteins as spheres with short-range interactions, experimental and computational evidence provides an alternative two-step nucleation mechanism for the solution to crystal phase transition. The first step involves the formation of dense liquid droplets, termed clusters, which have no long-range order. These then transform into crystal nuclei in the second step due to structural ordering of the constitute molecules.[93,94]

This ideal has been adopted to explain the nanoparticle-mediated crystallisation of mesocrystals and is referred to as non-classical crystallisation. Initially simultaneous nucleation events take place to form nanoparticles which then aggregate to form a mesocrystal; a highly ordered crystalline macrostructure where the constitute nanoparticles remain visible as discrete units (Figure 2.16).[95]

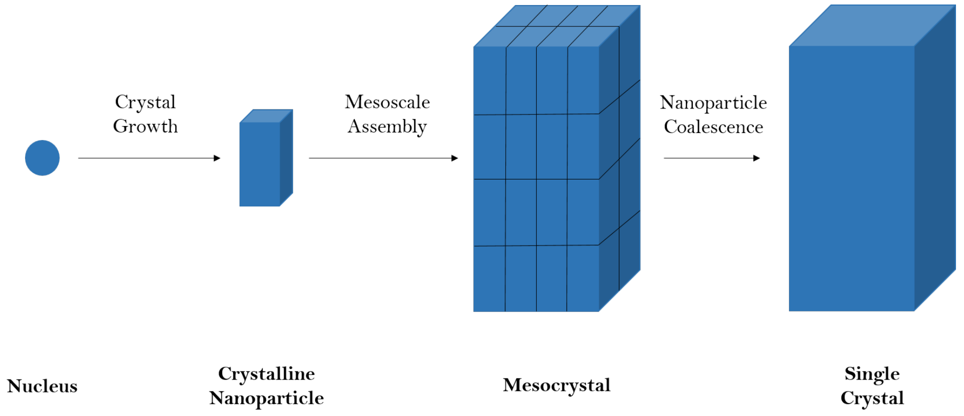

Figure 2.16: Schematic describing the mesocrystal mediated pathway to crystal formation.

2.2.4 Crystal Growth

Once nucleated, a crystal will begin to grow by continuously incorporating the constitute molecules from solution into the lattice until the surrounding supersaturation is relieved. The widely accepted crystal growth mechanisms that have been proposed are based on the crystal surface structure first suggested by Kossel.[96] In this simplified model, each crystal surface comprises of monatomic cubic units which form layers. Incomplete layers contain steps and kink sites (Figure 2.17). According to the two dimensional growth mechanism, constitute molecules are most easily bound to the crystal lattice at a kink site as it is most energetically favourable. This kink addition process continues until the row is complete, and then the next molecule must bind to a less favourable step site building up a monolayer of steps along the surface. The surface continues to grow in this fashion until the new crystal layer is complete, decreasing the total surface energy.[97] Molecules then have to take up more unfavourable sites in order for a new surface layer to grow. This can be

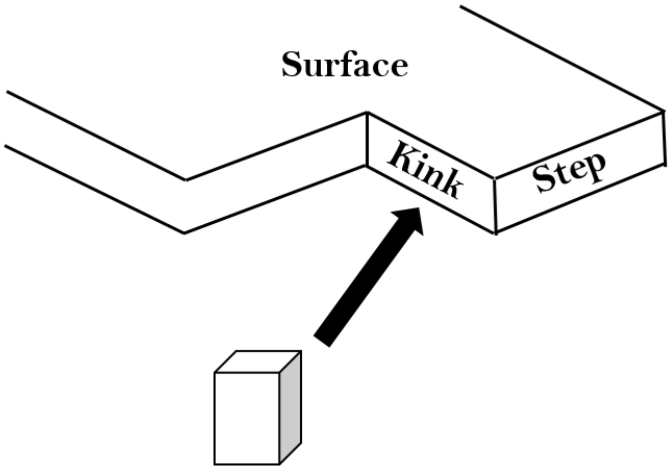

Figure 2.17: Schematic of a step and a kink on a growing crystal surface. A new constitute molecule incorporates at a kink.

achieved by the formation of a 2-D nucleus on the flat surface of the crystal, which aids further growth by then supplying steps and kinks that promote molecule attachment.[98]

Kinetic roughening can occur when sufficiently high supersaturation levels are reached. Here, multiple 2-D nuclei are formed, termed polynucleation, meaning that the growth of the crystal no longer proceeds layer-by-layer. Instead multiple surfaces begin to grow at the same time inducing a roughening which can be observed using microscopy.[99]

However, the energy required to form 2-D nuclei is prohibitive at very low supersaturations. The presence of surface defects and dislocations allow crystal growth to still proceed under these very low supersaturation conditions. Dislocations are defined as the boundary between undeformed and deformed regions within a crystalline structure. In particular, a screw dislocation is created by cutting a crystal along the plane and slipping one half across the other.[100] This dislocation provides a permanent step along the face of the crystal resulting in a constant lower energy site for molecule attachment. Hence, 2-D nucleation on a perfectly flat crystal face is no longer required for crystal growth. Thus the crystal begins to grow from the dislocation propagating in a spiral (Figure 2.18), with each addition providing a new step surface.[101,102]

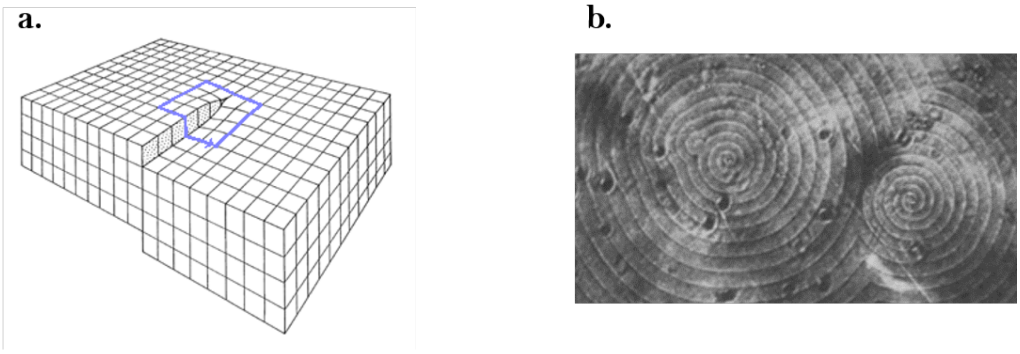

Figure 2.18: Evidence for screw dislocations inducing spiral growth patterns in crystals. **a.** Schematic of a crystalline structure exhibiting a screw dislocation.[103] **b.** Experimental evidence for spiral growth in crystals of silicon carbide.[104]

2.2.5 Polymorphism

A compound is termed polymorphic if it has the ability to exhibit multiple crystal structures, whilst keeping the same molecular composition.[105] Polymorphism is commonly observed in organic, inorganic and polymeric materials,[106–112] with each polymorph in a given system exhibiting different physical properties including: solubility, colouration, melting point and bioavailability.[113] For a given crystal system, polymorphic transitions can be induced *via* mechanical grinding, variation of temperature/pH and the introduction of additives such as surfactants.[114–117]

Within the classical nucleation framework, the factors that dominate rate of nucleation are interfacial tension, temperature and the degree of supersaturation (equation 2.19). This indicates that a relationship exists between the solubility of a particular polymorph and its rate of nucleation. Consider a dimorphic system in which two polymorphs, A and B, exist. At a particular temperature, polymorph A is the stable form and hence has a lower free energy (equation 2.23).

$$G_A < G_B \tag{2.23}$$

The chemical potential of the species in the solid phase of form A is therefore lower than that in the solid phase of form B. When equilibrium is reached such that the crystallite is in contact with its supersaturated solution, the chemical potentials for each species in the solid and solution phases are identical. It is therefore possible to rewrite equation 2.23 in terms of a standard chemical potential, μ_0, and the activities, a_A and a_B, of the supersaturated solutions of form A and B respectively (equation 2.24).

$$\mu^0 + RTln\left(a_A\right) < \mu^0 + RTln\left(a_B\right) \tag{2.24}$$

In the above, the temperature of the system is denoted T whilst R represents the ideal gas constant. At a given temperature, all terms except the solution activities remain constant. As such, the activity of form A is less than the activity of form B. Since activity and concentration are related by the activity coefficient, which will be the same for form A and form B, and the polymorphic system is identical in all other states other than the solid state, the above relation holds for concentration (equation 2.25).

$$C_A < C_B \tag{2.25}$$

Thus, the thermodynamically stable polymorph will always have the lowest solubility in any surrounding solvent.[76] Simple solubility experiments can therefore be used to determine the stability of polymorphs at given temperatures.[118] Solubility determinations can also allow one to learn if a polymorphic system is monotropic or enantiotropic. A monotropic system exhibits just one stable polymorph across all temperatures below the highest melting point of all the solid phases. On a solubility curve, the stable polymorph will remain the least soluble with no intersections with other polymorphs present (Figure 2.19). Intersecting solubility curves of different polymorphs indicate the presence of

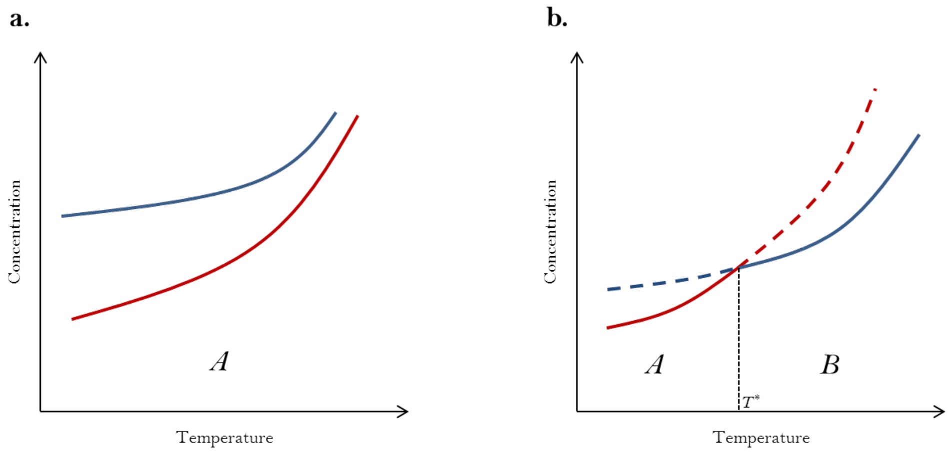

Figure 2.19: Theoretical solubility curves for a dimorphic system consisting of polymorphs A (red curve) and B (blue curve). **a.** A monotropic system: polymorph A is less soluble over all temperatures and is the only stable polymorph exhibited by the system. **b.** An enantiotropic system: below a transition temperature, T^*, polymorph A is less soluble and hence stable. As T^* is surpassed B becomes the less soluble and stable polymorph.

a enantiotropic system. Here, as a transition temperature, T^*, is surpassed a different polymorph becomes the least soluble. Therefore many stable polymorphs can exist over a range of temperatures in an enantiotropic system.[76]

At specified temperatures and pressures, only one thermodynamically stable polymorph of a crystal system may exist. All other polymorphs are deemed metastable and have the capability of transforming into the stable form. In fact, crystallisation is typically a kinetically driven process with metastable polymorphs crystallising initially before transforming to the stable form. This is described by Ostwald's rule of stages which states that a system will not necessarily tend towards equilibrium but towards the metastable state closest in free energy to the original state.[119,120]

The solubility and stability of different polymorphs has never been more clearly highlighted than in the case for the drug Ritonavir. Ritonavir was prescribed in 1992 by Abbot Laboratories as an anti-HIV/aids drug administered *via* oral solutions and soft gelatine tablets. After two years on the market, several batches of the drug failed quality control dissolution tests. Over time a more stable, less soluble, polymorph of Ritonavir had formed leading to a decrease in dissolution rates and hence bioavailability of the marketed drug. Consequently it was removed from the market and redeveloped at the cost of several hundred million US dollars.[121,122]

2.3 Crystallisation In Microemulsions

As stated previously, microemulsions can be used as nanoreactors for the synthesis of a wide range of nanomaterials. This transient dimer mechanism can also be exploited to allow the crystallisation of materials to proceed (Figure 2.20). The crucial mechanism is the formation of a transient dimer between a droplet containing a crystal nucleus and another nucleus-free droplet containing a supersaturated solution of constitute molecules. The crystal nucleus then gains access to more growth material from this supersaturated solution, thus crystallisation continues. Interest in this method has grown since the ability to elicit thermodynamic control over crystallisation in microemulsions was shown recently.[123]

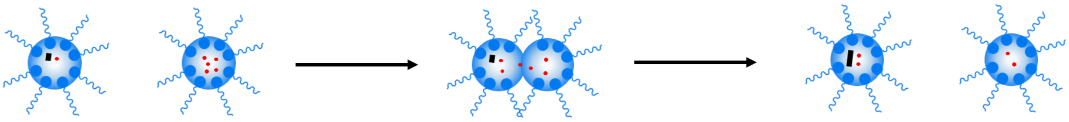

Figure 2.20: Schematic of how transient dimers can also allow crystallisation to proceed. Upon collision, and droplet containing a crystal nucleus (black) gains access to more growth material (red) from a nucleus-free droplet containing a supersaturated solution of the constitute molecules.

Crystallisation in the bulk, i.e. on the macroscopic scale, contains a large reservoir of constitute supersaturated solution. Any critical nuclei that form will therefore have access to a large amount of growth material and grow to large μm and mm sizes. A large substantial decrease in free energy is seen as crystallisation proceeds until a minimum is reached in which the crystal is now surrounded by a saturated solution. This large decrease in free energy (due to the crystal being able to grow to large sizes) means that crystallisation in the bulk is irreversible. Crystallisation confined to microemulsion system, however, contains only small quantities of the constitute supersaturated solution. This is due to the small nm confinement of the droplets, with any crystal nuclei that exist only getting access to more growth material *via* transient dimer formation. This 3-D nanoconfinement ensures that any critical nuclei can only grow to nm sizes, causing a considerably smaller decrease in free energy than that seen in the bulk (Figure 2.21).

In accordance with Ostwald's rule of stages, where crystallisation tends to be under kinetic control, a metastable polymorph from a polymorphic system has a lower nucleation barrier than the stable one. It will therefore irreversibly crystallise out first to large sizes in bulk solution (Figure 2.22). The contrary holds true if the stable polymorph has the lowest nucleation barrier. In bulk crystallisation, it is therefore entirely system dependant on which polymorph will crystallise out first. This lack of control means it is difficult

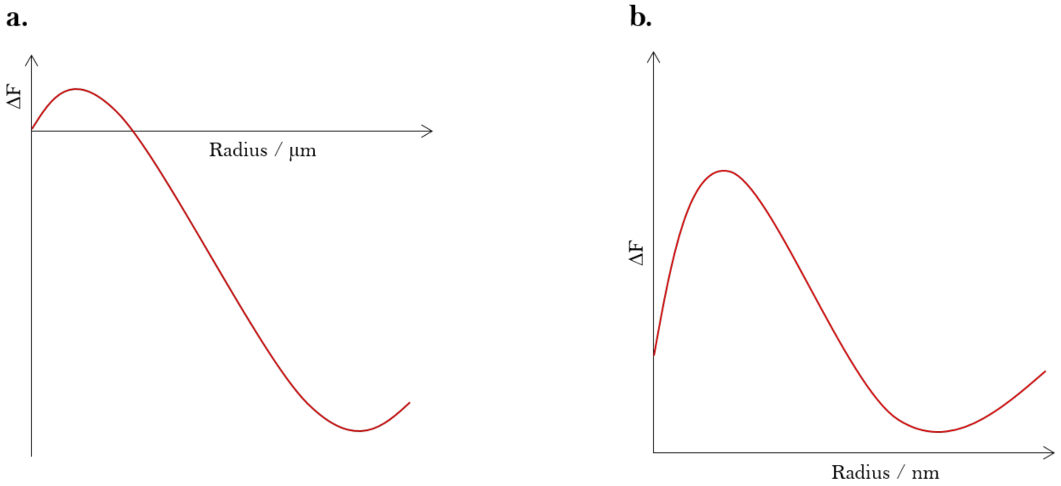

Figure 2.21: Theoretical free energy curves for crystallisation in the bulk and crystallisation under 3-D nanoconfinement in microemulsion droplets. **a.** Crystallisation in the bulk: due to the large amount of growth material in the surrounding supersaturated solution, nucleated crystals can irreversibly grow to μm and mm sizes. **b.** Crystallisation under 3-D nanoconfinement: Crystal nuclei can only grow to nm sizes until repeated transient dimers form.

to predict crystallisation outcomes a priori and there is no certainty in finding the most stable polymorph.

When confined to a microemulsion, the fall in free energy is not sufficient for irreversible crystallisation and the nucleation barrier is surmountable in both directions. This reversibility of crystallisation means that the persistent nuclei are now determined by their long term stability rather than their critical size. Since the stable polymorph is always the least soluble, these nuclei can grow to larger sizes and therefore persist over time. Thermodynamic control of crystallisation is thereby achieved. However, the above mechanism only holds under certain supersaturation conditions. In particular, for a dimorphic system, if both minima in the free energy curves ($\Delta F_{\mathrm{min,A,B}}$) are much greater than kT then the supersaturation of the confined solution is too low. Crystallisation is stabilised due to the 3-D nanoconfinement of the microemulsion droplets and cannot proceed for either polymorph because long-lived nuclei cannot be achieved as ΔF_{min} is too large relative to kT, so the population of such nuclei is negligible. (Figure 2.23). If the stable polymorph A (red curve) can form stable nuclei ($\Delta F_{\mathrm{min,A}} < kT$) but the metastable polymorph B (blue curve) cannot ($\Delta F_{\mathrm{min,B}} > kT$), then thermodynamic control is achieved and crystals of the stable polymorph will form (Figure 2.23). However, raise the supersaturation level too high and both polymorphs can form stable nuclei ($\Delta F_{\mathrm{min,A,B}} < kT$) and irreversible grow so that crystallisation will then be under kinetic control with the metastable crys-

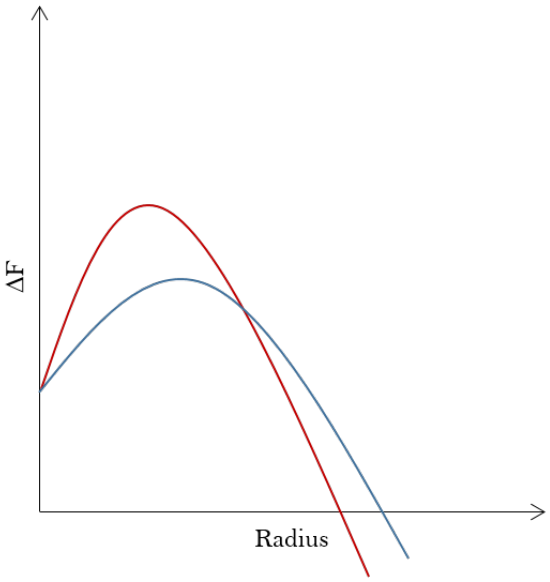

Figure 2.22: Theoretical free energy curves of a stable (red curve) and metastable (blue curve) polymorph. The metastable form has the lowest nucleation barrier, thus these crystals will irreversible crystallise out first to large sizes.

tals forming predominantly due to their lower nucleation energy barrier and more rapid crystallisation rate (Figure 2.23). Therefore, to elicit thermodynamic control of crystallisation, the supersaturation of the confined phase should be gradually increased to a level when crystallisation is only just possible. This ensures we are in the regime where only the stable polymorphs nuclei can persist and grow.

This methodology has been proven experimentally for polymorphic organic crystals such as glycine, mefenamic acid and ROY..[123–125] Given that this approach provides a generic route to finding the most stable polymorph for any compound, it should be of significant use in the screening process of drugs within the pharmaceutical industry. This could prevent future large scale crises such as was seen for the drug Ritonavir.

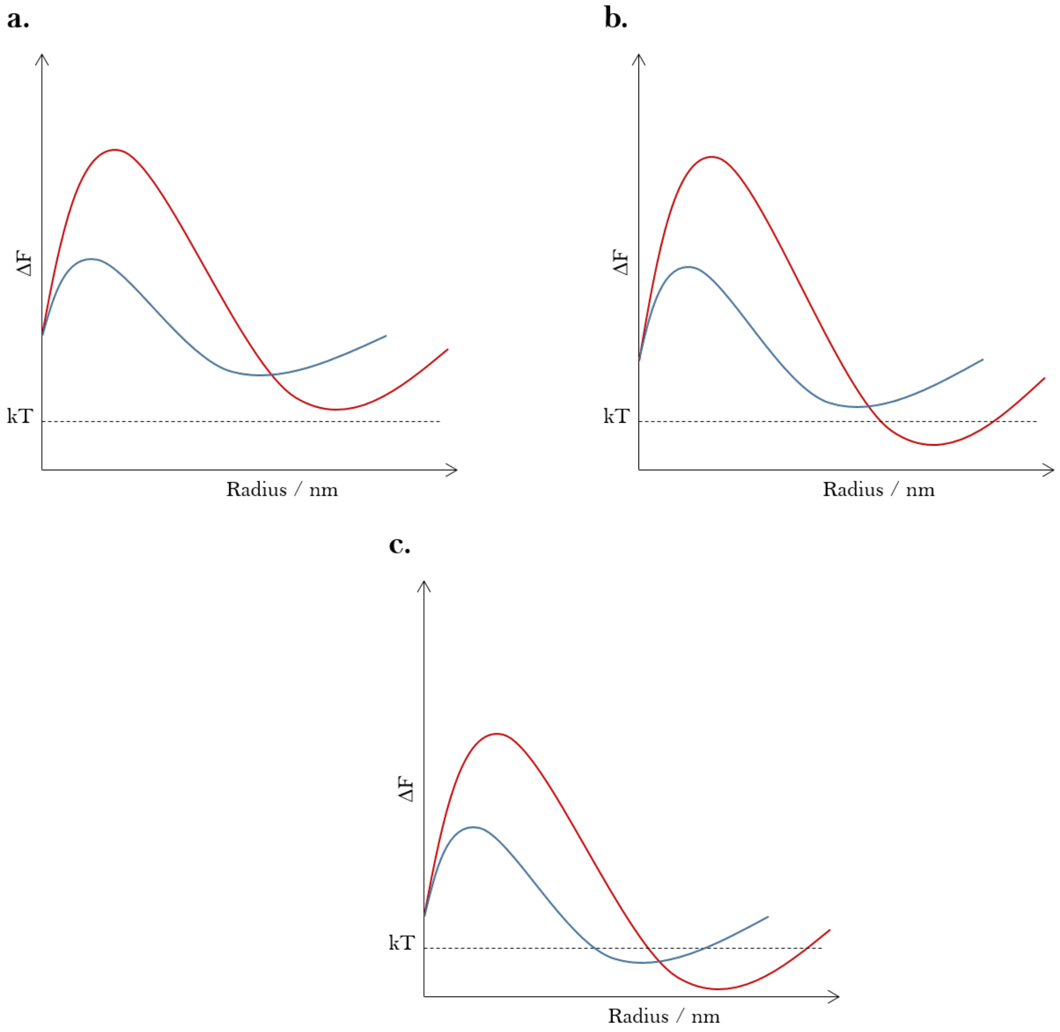

Figure 2.23: Theoretical free energy curves of a dimorphic crystal system consisting of a stable polymorph A (red curve) and a metastable polymorph B (blue curve). **a.** Both minima have free energies greater than kT: supersaturation level is too low, the system is stabilised due to 3-D nanoconfinement and no crystallisation proceeds. **b.** The minima in free energy of the stable polymorph is less than kT whilst the metastable's is greater than: the stable polymorphs nuclei can persist, the system is under thermodynamic control and polymorph A crystallises out. **c.** Both polymorphs have free energy minima less than kT: the supersaturation level is too high, the system is under kinetic control and polymorph B will crystallise out.

Chapter 3

Experimental Techniques

3.1 X-ray Scattering

X-ray scattering uses X-ray radiation to probe the structure of a material. X-rays interact and are scattered by electrons. In weak scattering theory (which is assumed in this case), the X-rays are scattered once by the electrons, with multiple scattering events being ignored. This theory can be best described using wave vector $\vec{k}$, where

$$|\vec{k}| = \frac{2\pi}{\lambda} \tag{3.1}$$

and λ is the wavelength of the X-ray radiation used. The difference between the initial wave vector, $\vec{k_0}$, and the scattered wave vector, $\vec{k_1}$, is defined to be the scattering vector q (Figure 3.1). Prescribing the angle between these two wave vectors as θ, leads to

$$|\vec{q}| \equiv q = \frac{4\pi}{\lambda} sin\left(\frac{\theta}{2}\right) \tag{3.2}$$

by simple geometric arguments.

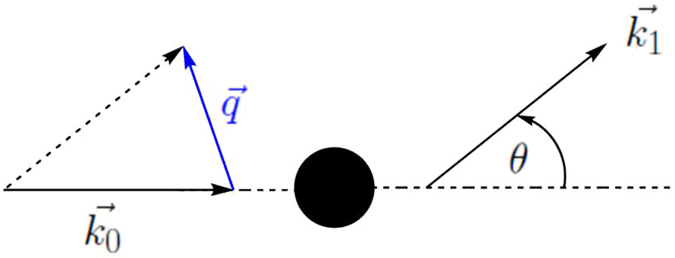

Figure 3.1: The scattering vector q is defined as the difference between the initial wave vector, $\vec{k_0}$, and the scattered wave vector, $\vec{k_1}$.

In X-ray diffraction, only elastic (Bragg) scattering is considered. Here there is no transfer of energy between the electron and X-ray photons during the scattering event. This results in the X-rays being scattered in phase. The diffraction pattern results from the sum of all independent, in phase scattered photons. By considering the scattering vector, $\vec{q}$, normal to the equidistant crystal lattice planes (Figure 3.2), one can use the Bragg equation

$$2dsin\left(\theta\right) = n\lambda, \quad n \in \mathbb{Z} \tag{3.3}$$

to calculate the lattice spacing, d, from the diffracted photon angle, θ.

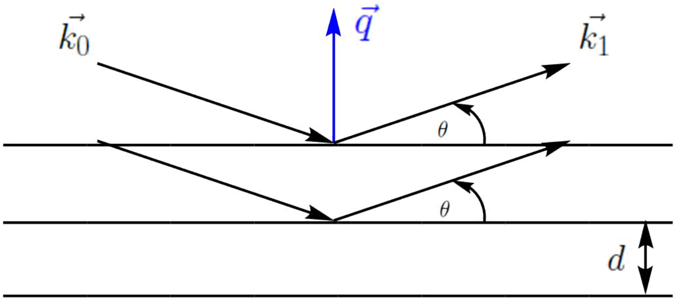

Figure 3.2: Reflected wave vectors, $\vec{k_1}$, reflect of crystal lattice planes with spacing, d, at an angle, θ, when the scattering vector, $\vec{q}$, is normal to the planes. This diffraction picture leads to the formulation of the Bragg equation (3.3).

3.1.1 Small Angle X-ray Scattering

Small Angle X-ray Scattering (SAXS) was utilised to confirm the existence of lamellar phases *via* a sharp peak in the X-ray scattering pattern. The scattering vector q at which this peak is positioned is used to give the d spacing of the lamellar system. This is the length scale of repeating surfactant lamellar blocks (Figure 3.3).

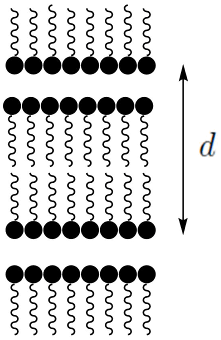

Figure 3.3: A lamellar surfactant system. The d spacing of the system has been indicated and is the length between the repeated lamellar blocks.

SAXS data was obtained from a Brucker Nanostar SAXS machine operated at 40 kV and 35 mA to produce Cu Kα radiation with a wavelength of 1.54 Å. The machine is fitted with a Hi-star 2-D detector, and has cross-coupled Gobel mirrors and pinhole collimation for point focus geometry. The samples were contained in a 2 mm quartz capillary and inserted into a sample chamber, which was evacuated to a pressure of 10^{-1} mbar to minimise air scatter. To ensure the capillary was positioned for maximum scatter to occur, the Gadds program Radiography/nanography was run with the attenuator dropped. The attenuator was then lifted before data collection. The SAXS experiments were run for one hour as sufficient data was attained in this time frame.

3.1.1.1 Generalised Indirect Fourier Transform Analysis

Generalised Indirect Fourier Transform (GIFT) analysis was used to transform SAXS microemulsion scattering curves to a pair-distance distribution function, $p(r)$. From this distribution the average droplet size within the microemulsion could be determined. Firstly, a Porod extrapolation is applied to the scattering function $I(q)$ in order to remove background signals, ensuring that the resultant $p(r)$ function has a value ≈ 0, at $r = 0$.

The intensity of the scattering signal, I(q), at scattering vector q is comprised of two components; a form factor, P(q), and a structure factor, S(q) (Equation 3.4).

$$I(q)\ \alpha\ P(q) \cdot S(q) \tag{3.4}$$

The form factor is a representation of the intraparticle scattering and thus dominates in dilute samples where the particle size is much smaller than the particle-particle distance. The structure factor is a representation of the interparticle scattering, and thus is observed for concentrated particle systems. For the microemulsion systems the structure factor of the dispersed droplets were modelled assuming hard sphere interactions within the GIFT software.

Pair-distance distribution function curves are then calculated by the GIFT software by applying a Fourier transform to $I(q)$ (equation 3.5)

$$P(r) = \frac{1}{2\pi^2} \int I(q) \cdot qr \cdot sin(qr)\ dq \tag{3.5}$$

These curves are generated by a combination of software-derived Lagrange multipliers (a method of determining local maxima and minima of a function) and user-inputted maximum particle sizes. The most suitable fit of these curves is determined through identifying the Lagrange multiplier in which the function has a turning point. Typically, for a spherical particle system (akin to the microemulsion systems), the $P(r)$ function takes the form of a bell curve. The GIFT software then uses the corresponding r value at the maximum value of P to calculate the mean hydrophilic core radius of the droplets.[126]

3.1.2 Powder X-ray Diffraction

Powder XRD data was obtained from a Bruker D8 Advance operated at 40 kV and 40 mA to produce Cu K_α radiation with a wavelength of 1.54 Å. The experimental set up was conducted within the DIFFRAC.SUITE software. Samples were thoroughly dried and ground before being applied to a glass slide. The sample was subjected to a 6 mm X-ray beam width and was continuously rotated 60° to reduce preferential orientation effects. Angles were scanned between $2\theta = 10 - 70°$ at increments of 0.02° with the beam exposed at each angle for 1 s.

3.2 Nuclear Magnetic Resonance

Nuclear Magnetic Resonance (NMR) uses electromagnetic radiation (typically in the radio frequency range) to excite nuclei. Samples must first be placed into an external magnetic field to align the nuclei to an equilibrium spin state. The pulse frequency needed to excite a nucleus from its equilibrium spin state, v_x, depends on the magnetic field at the nucleus, B, and the magnetogyric ratio, γ, which is specific to each nucleus (Equation (3.6)).

$$v_x = \frac{\gamma B}{2\pi}. \tag{3.6}$$

The spin quantum number, I, of the nucleus must be non-zero; the nucleus must be spin active to be observed by NMR. This prerequisite depends on the isotope of the element to be observed. For example, ^{12}C has $I = 0$ and cannot be observed, though ^{13}C, ^{1}H and ^{29}Si have $I = \frac{1}{2}$ and can be.

The frequencies needed to excite nuclei are affected by the surrounding chemical environments. The deshielding effects for a particular chemical environment are denoted with a corresponding constant, δ, which is measured in parts per million and is termed the chemical shift (Equation (3.7)).

$$\delta_x = \frac{v_x - v_{ref}}{v_{ref}}. \tag{3.7}$$

Where v_{ref} is the NMR frequency of a reference material. The frequency needed to excite a particular nucleus, x, is compared to a reference sample in order to calculate δ. A typical reference sample for both protons and ^{13}C measurements is tetramethylsilane (TMS),

$SiMe_4$, since it is inert and produces a sharp signal that does not often interfere with sample resonances. The position of the peaks in a ^{13}C NMR spectra can therefore be used to identify the particular carbon chemical environments that exist in the sample.[127,128]

3.2.1 Solid State Nuclear Magnetic Resonance

In solution NMR, the active random movement of the atoms lead to the anisotropic NMR interactions being averaged out, resulting in sharp spectra peaks. Solids cannot exhibit such behaviour and broad peaks that are difficult to assign are observed. To overcome this, solid state nuclear magnetic resonance (SSNMR) utilises a technique called magic angle spinning. Here the sample is spun quickly at 54.75° to the external magnetic field, introducing artificial solution-like behaviour by cancelling out the dipolar, chemical shift anisotropy and quadrupolar interactions seen in the condensed phase. Using this technique, high resolution spectra can be obtained.[129]

SSNMR spectra were obtained from the Solid State NMR Service at Durham University on a Bruker Advance III HD spectrometer with a 9.4 T magnet (operating at 100 MHz for ^{13}C, 400 MHz for ^{1}H and 79.44 MHz for ^{29}Si nuclei). Spectra were obtained *via* Cross Polarisation (CP) or Direct Excitation (DE) with magic angle spinning and TMS as the reference.

Due to the poor abundance of ^{13}C isotopes, DE can be a timely and costly experiment, therefore CP is typically favoured. Cross polarisation experiments also tend to give better signal to noise ratios. In CP, magnetisation is built up in abundant proton sources and is then transferred to the dilute ^{13}C nuclei. Once this carbon signal is detected, the protons are decoupled. For CP experiments to be possible, the abundant and dilute nuclei must fulfil the Hartmann-Hahn condition.[130] For ^{1}H and ^{13}C nuclei the Hartmann-Hahn match (Equation (3.8)) can be achieved by inducing an external magnetic field that is 4 times stronger when exciting protons than that used to excite ^{13}C nuclei.[131,132]

$$\gamma_H B(^1H) = \gamma_C B(^{13}C). \tag{3.8}$$

If CP experiments emit low signals due to the lack of protons or due to electrical conductivity, DE must be used at the expense of signal to noise, increased time.

3.3 Fourier-Transform Infrared Spectroscopy

Fourier-Transform Infrared Spectroscopy (FTIR) is a technique that uses the absorbance or transmittance of infrared radiation to characterise materials. A FT-IR spectrometer (Figure 3.4) produces an infrared beam containing the full spectrum of frequencies of light, which is then passed through an interferometer. Here, a configuration of mirrors, one of which moves, alters the distribution of light. The beam then passes through the sample before hitting the detector to produce an interferogram, a signal of light output as a function of mirror position. As the mirror moves, constructive and destructive interference periodically transmits and blocks each wavelength of light, meaning the radiation has a different spectrum each time it leaves the interferometer and hits the sample. As this process is repeated many times the computer infers what the infrared absorbance/transmittance is at each position. It then performs a Fourier transform to produce a spectra from the interferogram, light output as a function of infrared wavelength (or wavenumber).[134]

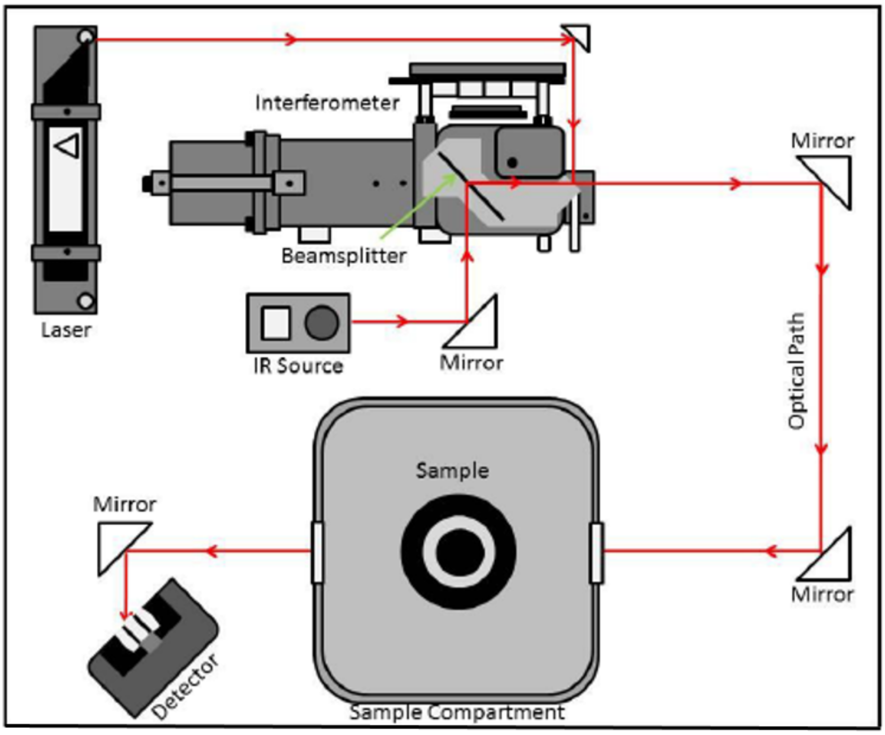

Figure 3.4: Schematic of a FT-IR spectrometer.[133]

FTIR exploits the fact that molecules have vibration modes. When a particular bond vibration matches the wavelength of the passing beam, the radiation is absorbed and a peak observed in the spectra. In order for a vibrational mode to be infrared active, the dipole moment of the molecule must change during the vibration, hence simple homonuclear diatomics aren't infrared active and cannot be characterised with FT-IR.[135] As different bonds exhibit different vibrations, they each present characteristic peaks in the FT-IR spectrum enabling the studied material to be identified.

FTIR spectra were recorded on a Perkin-Elmer Frontier FT-IR spectrometer equipped with a U-ATR sampling accessory and caesium iodide optics. 16 scans were collected for each sample at a resolution of 2 cm^{-1} over a wavenumber region of 4000 cm^{-1} to 380 cm^{-1}.

3.4 Thermogravimetric Analysis

Thermogravimetric Analysis (TGA) is a technique in which the mass of a substance is monitored as a function of temperature or time as the sample specimen is subjected to a temperature increase/decrease (most commonly at a constant rate) in a controlled atmosphere. A typical TGA instrument consists of a sample pan that is supported by a precision balance. The sample pan is contained within a furnace and is heated or cooled during the experiment with the change in mass of the sample recorded. A purge gas (air, inert gases) is flowed over the sample to control the sample environment (Figure 3.5).

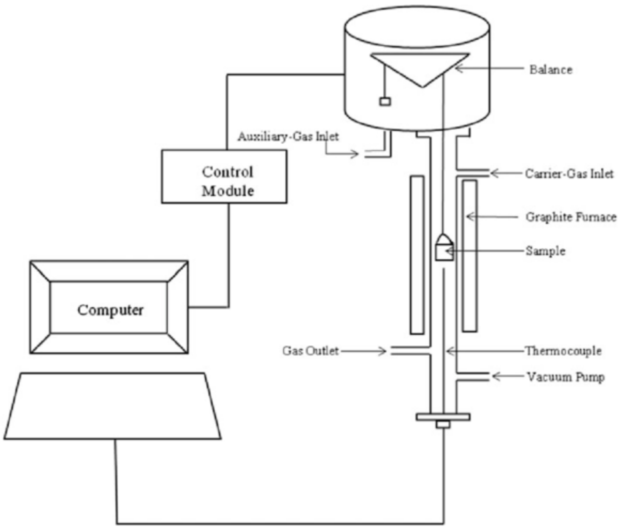

Figure 3.5: Schematic of a TGA instrument.[136]

The TGA data collected from an experiment is compiled into a plot of mass or percentage of initial mass on the y axis versus either temperature or time on the x-axis. This curve (TGA curve) is then smoothed, and the first derivative of the curve may also be plotted to determine the inflection points to aid interpretation.[137]

Thermogravimetric analysis (TGA) curves were collected using a Perkin-Elmer Pyris 1 TGA using air as the carrier gas. Samples were heated at a rate of 10 °C min^{-1} to 800 °C, where they were held for 60 min.

3.5 Transmission Electron Microscopy

Transmission Electron Microscopy (TEM) uses a high energy beam of electrons to probe the structure of nm-sized materials, providing information such as crystal structure, size and shape of the sample material. The electron beam is focussed on the sample, and is scattered due to interactions with the atomic nuclei and electrons in the material. The transmitted electron beam is then passed through a series of intermediate lenses to focus and magnify the resultant image, allowing it to be viewed on a phosphor screen or on photographic film (Figure 3.6).

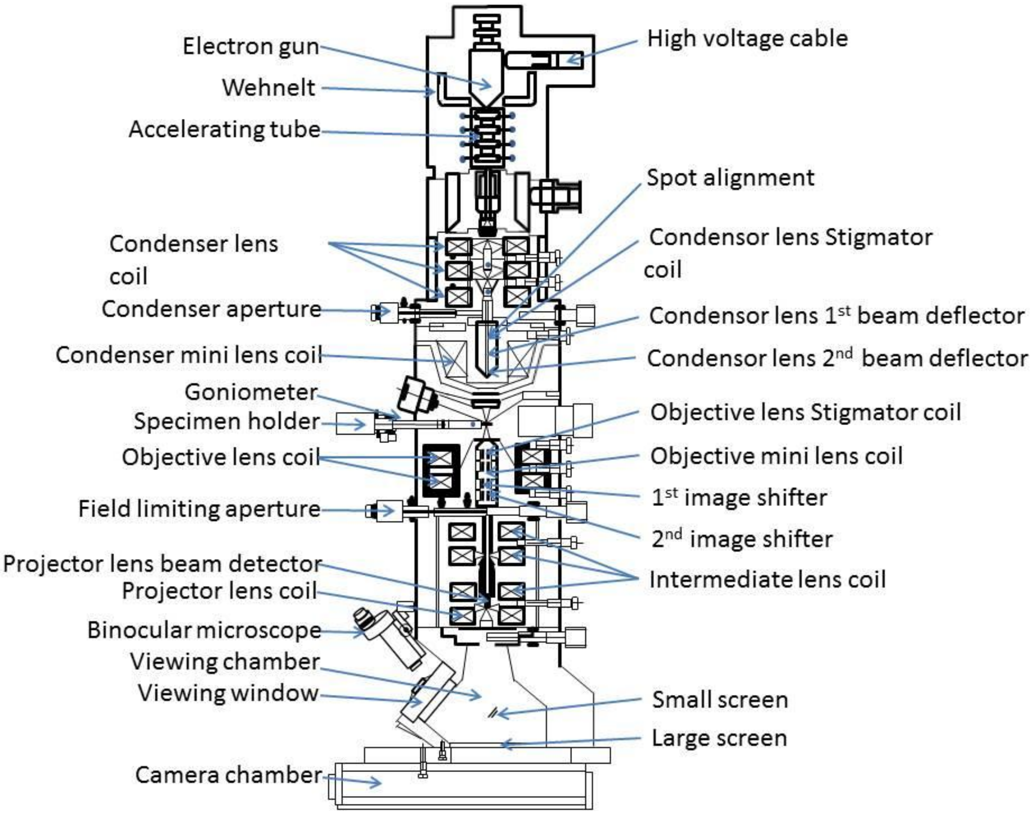

Figure 3.6: Schematic of a transmission electron microscope.?

The resolution of TEM is much higher than that for an optical microscope due to the small de Broglie wavelength of electrons (Equation 3.9) compared to that of light.

$$\lambda = \frac{h}{m_e v} \tag{3.9}$$

Here, λ is the wavelength, h is Plancks constant, m_e the mass of an electron and v the velocity of the electron beam. Typically TEM uses a wavelength of of $\approx$ 0.02 Å. The theoretical resolution limit of TEM can therefore be calculated to be $\approx$ 0.1-0.2 Å. This means that even individual rows of atoms can be seen in high-resolution TEM (HREM).

Furthermore, transmitted electrons are scattered (due to the crystallinity of a material) which leads to the observation of a series of fringes. These fringes can be fast Fourier transformed (FFT) to give a diffraction (SAED) pattern. The spacing between these reflections can then be measured to obtain the d-spacing of the nm-sized crystalline sample.

TEM analysis was performed using a JEOL 2100 field emission gun TEM (FEG TEM) operating at 200 kV, a ZrO/W (100) Schottky Field Emission analytical emission microscope, in combination with an Oxford INCAx-Sight Si(Li) detector for Energy-Dispersive X-ray (EDX) spectroscopy and a Gatan Orius CCD camera. Phase contrast high resolution electron microscopy (HREM) was used to image nm-sized crystals. The structure of an individual nanocrystal was determined by indexing the fast Fourier transform and selected area diffraction patterns. Sample particles were dispersed in UHP water *via* sonication in an ultrasound water bath for 30 min. The dispersion was pipetted onto holey carbon, 300 copper mesh TEM grids. The TEM grids were left to dry completely before examination.

3.6 Energy-Dispersive X-Ray Spectroscopy

Energy-Dispersive X-Ray (EDX) Spectroscopy is commonly used in conjunction with TEM analysis. The high energy interactions between electrons and a sample described in section 3.5 are elastic; the interactions result in a change of direction of the incident electron beam without any associated energy change. However, there are also interactions that result in inelastic scattering in which an incident electron will lose energy. These interactions also result in secondary emissions of X-ray energy. In short, when an incident electron interacts with the sample, a localised electron within that sample may be “knocked out”. This results in an outer electron within the sample falling into vacancy and emitting an X-ray photon of energy equivalent to the difference between these two excited states (Figure 3.7). This energy is characteristic of an individual atomic species, thus a SiLi detector can capture and interpret these X-ray photons to provide information on the chemical composition of the sample.

3.7 Carbon, Hydrogen and Nitrogen Elemental Analysis

Carbon, Hydrogen and Nitrogen (CHN) elemental analysis measures the carbon, hydrogen and nitrogen elemental content of samples with accuracy and precision.

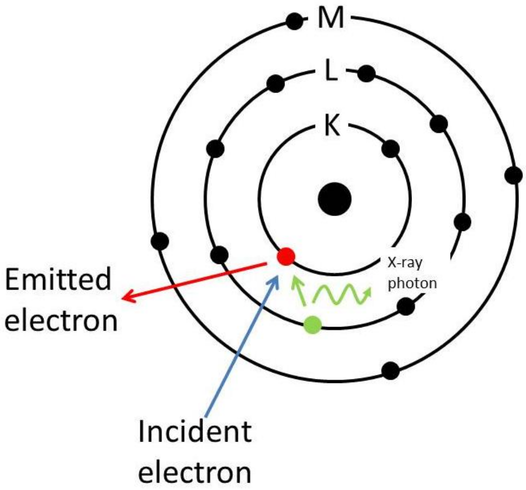

Figure 3.7: Schematic of an inelastic interaction between a electron and a sample atom. Upon collision an X-ray photon is emitted. microscope.[133]

The sample to be analysed is weighed precisely to one millionth of a gram inside a small tin capsule. The capsule is then introduced to a furnace (combustion tube), which is at a temperature of 950 °C. At this temperature, the tin capsule combusts in a high oxygen environment, forming tin oxide and elevating the temperature to above 1800 °C. At this temperature, the sample is vaporised and undergoes complete combustion, to form CO_2, N_2, N_xO_y, H_2O. Undesirable by products are removed from the system by 'scrubbing' chemicals inside the combustion tube. After combustion, the sample gases flow through a reduction tube to remove any unused oxygen, and convert nitrogen oxides to N_2. A small portion of the sample gas mixture is then flowed through a series of thermal conductivity cells, where the percentages of each gas; CO_2, H_2O, N_2 and He carrier gas, is recorded and the % C, H and N is calculated.

CHN elemental analysis experiments were performed on an Exeter Analytical CE-440 elemental analyser under static combustion, with a horizontal furnace and calibrated with acetanilide.

Chapter 4

Low Temperature Synthesis of Nanographite

4.1 Introduction

The element carbon has received much interest due to the ability for it to exist in various polymorphs.[138] Carbon atoms have the electron configuration $1s^2 2s^2 2p^2$, with the four valence electrons existing in 3 hybridisation states: sp^3, sp^2 and sp^1 (Figure 4.1).[139]

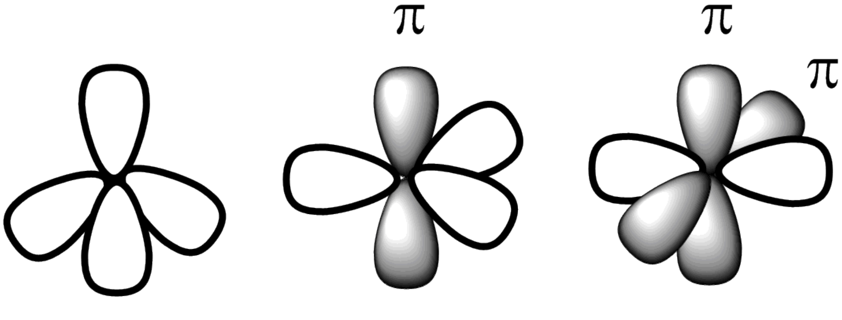

Figure 4.1: The hybridised states of carbon atoms. From left to right: sp^3, sp^2 and sp^1 states.

It is these three hybridised states that give rise to the number of carbon allotropes, including diamond, graphite, graphene, fullerenes and amorphous carbons. Though each display interesting properties in their own right, here the focus lies with graphite and graphene.

4.1.1 Graphite

Graphite involves the sp^2 (trigonal) hybridisation of carbon atoms and is the thermodynamically stable form of carbon under ambient conditions. This hybridisation state creates a structure of individual carbon layers in which the atoms are arranged in a hexagonal pattern (graphene). These sheets are then held together by weak van der Waals interactions (arising from the de-localised π-orbitals) to create a hexagonal close-packed crystal structure.[138] The graphene sheets are known to stack in three common ways to produce natural graphite: hexagonal (AA), Bernal (AB) and rhombohedral (ABC) stacking (Figure 4.2).[140] The most abundant (80%) and stable form of graphite is Bernal stacking.

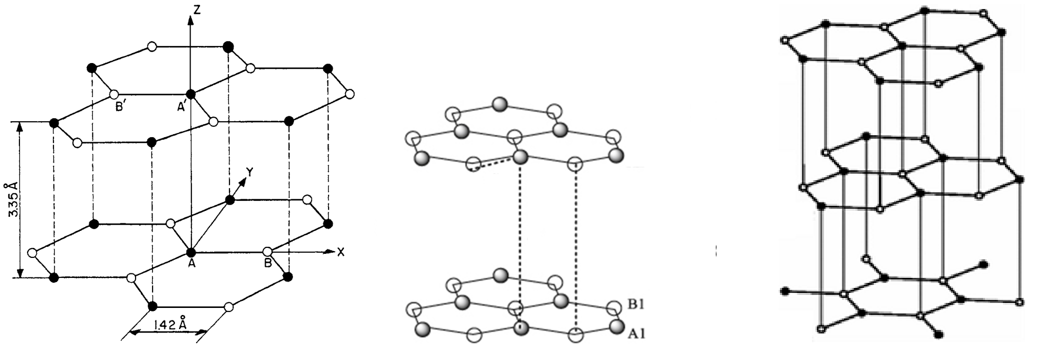

(a) Bernal Stacking.[138] (b) Hexagonal Stacking.[140] (c) Rhombohedral Stacking.[141]

Figure 4.2: The three stacking arrangements of graphite.

Here, the graphene sheets stack 3.35 Å apart with a 60° perpendicular rotation, resulting in a 4 atom unit cell (A, A', B, B' in Figure 4.2a). In adjacent graphene planes, the atoms A and A' have neighbours directly above and below, whereas the atoms B and B' do not.[142–144] Hexagonal stacking involves perfect alignment of the graphene sheets, such that every carbon atom has a neighbour both above and below in adjacent planes. This stacking is rarely observed in nature due to the steric hindrance arising between sheets. It is this hindrance that inhibits the de-localisation of electrons (observed in Bernal stacking), which in turn makes the hexagonal stacking arrangement unstable.[145] Rhombohedral stacking of graphite involves three graphene layers A,B, C and can be introduced by grinding.[138] Both A and B layers are Bernal stacked whilst C lies in the same orientation as B but is translated parallel to the plane.[142]

The close-packed crystal structure of graphite provides a unique powder X-ray diffraction pattern. A diffraction peak at $2\theta = 26.5°$ with Cu K_α radiation corresponds to the inter layer spacing of graphite (002) plane of crystallinity, $d = 3.4$ Å, whilst a weak peak at $2\theta = 44.3°$ is that of the (004) plane.[146] Secondary and ternary peaks at $2\theta = 44.3$ and 42.6° correspond to the (101) and (100) planes of crystallinity, respectively.[147] One must note that the relative intensity of the (100) plane of crystallinity is extremely low and may not be seen.

4.1.2 Graphene

Mono layer graphene (Figure 4.3) is the sp^2 hybridisation of carbon, with a unit cell containing two carbon atoms progressing into two sub-lattices. These 2-dimensional latices can bulk stack to form graphite (section 4.1.1), or stack sparingly to form bilayer and few layer (typically <10 layers) graphene.[148]

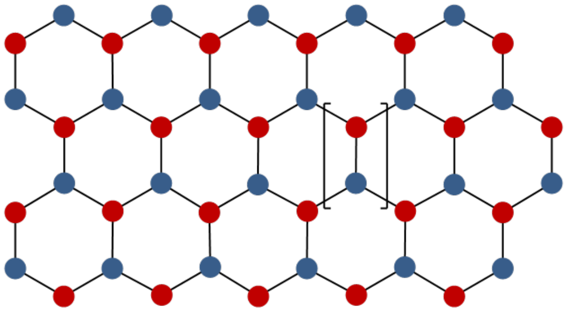

Figure 4.3: Mono layer graphene consisting of two sub-lattices denoted in red and blue. The individual unit cell is bracketed.

4.1.2.1 Properties

Due to its unique structure, graphene exhibits extraordinary properties lending itself to a multitude of possible applications. At only one atom thick, graphene has an extremely large surface area, despite this it is stronger than steel, has a Young's modulus of 1 TPa and is impermeable to gases.[149,150] It also displays remarkable thermal conductivity, up to approximately 5000 W m^{-1} K^{-1},[151] due to strong C-C bonds and high phonon speeds.[152] Graphene is also transparent absorbing only approximately 2.3% of white light.[153]

Graphene's partially filled π-orbitals above and below the plane gives rise to a unique band structure and its remarkable electronic properties. A valence band is formed from π bonding states whilst π^* anti-bonding states form a conduction band.[148] These bands touch at six single points, known as Dirac points, which are approximated as touching symmetrical cones (Figure 4.4). Graphene, therefore, does not have a band gap.[152] Consequently, freely suspended graphene can display charge carrier mobilities in excess of 200 000 cm^2 V^{-1} s^{-1}.[156] This incredible electrical conductivity also results from the ballistic propagation of electrons through the graphene lattice; the electrons can travel sub-micron distances without scattering.[157] Graphene's electrons can also be described as massless fermions, governed by the Dirac equation rather than the conventional Schrödinger equation. These combined, allow electron quantum effects to survive at room temperature.[154,158] These electron properties also hold under the reversible folding of graphene.[153]

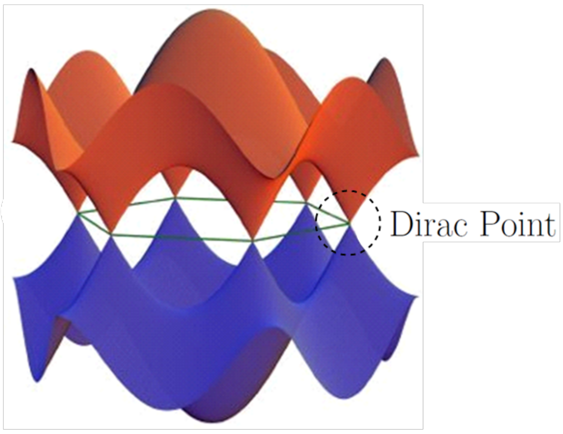

Figure 4.4: The band structure of graphene. A valence band (blue) and conduction band (red) touch at 6 Dirac points.[154,155]

4.1.3 Current Synthesis Methods

In general, the synthesis of graphene can be categorised as either a bottom-up or top-down method. Bottom-up methods involve the production of graphene directly from carbon based precursors, whilst top-down methods are based on the isolation of a single/few layers of graphite. The latter requires the breaking of the Van der Waals forces between the graphitic layers either mechanically or chemically.[159]

4.1.3.1 Bottom-Up Methods

An epitaxial graphene layer can nucleate and grow on a silicon carbide (SiC) substrate due to the preferential sublimation of silicon and subsequent graphitisation of the excess carbon atoms. Synthesis routes usually involve growing the graphene on a hexagonal phase SiC substrate, under high temperatures and ultra-high vacuum conditions.[160] Early methods resulted in defected products as the high temperatures needed (> 1000 °C) for quality graphene growth induced intolerable silicon sublimation rates.[159] However, growth in argon atmospheres or in the presence of disilane has been shown to reduce the rate of sublimation,[161–163] thus higher temperatures are now used and the quality of graphene has increased. Lower temperatures (700-800 °C) can be used to synthesise high quality graphene using a nickel catalyst; a thin layer of nickel is deposited on the SiC surface before graphitisation.[164–167] Epitaxial growth on SiC has applications in electronic devices/electronic components as it is not necessary to remove the graphene from the underlying substrate. However, graphene can successfully be transferred from the underlying SiC.[168,169] As well as the extreme conditions needed for this synthesis, SiC is expensive and so its use is hindered in commercial applications.

Chemical vapour deposition (CVD) involves synthesising graphene by the high temperature pyrolysis of carbon-containing gases. Transition metals are used to provide a substrate for graphene sheets to grow. CVD graphene growth can be achieved *via* two mechanisms: surface catalysed growth and segregation methods.[159] Copper substrates are used to grow graphene through the former mechanism, where the copper surface is used as a nucleation site for graphene islands to form and grow. Since this method uses the substrate as a catalyst for nucleation, surfaced catalysed growth is self-limiting to mono layer graphene independent of reaction conditions.[170–172] Nickel is used as a substrate to grow few layer graphene through the segregation method. This involves carbon-based gases diffusing into the bulk of the metal with the carbon atoms then segregating and precipitating to the surface.[173,174] CVD methods are disadvantaged due to the high temperatures needed, and in some cases (growth on copper), ultra-high vacuum conditions.

Graphene has also successfully been synthesised (bottom-up) substrate free, negating the need to purchase specific substrates as well as increasing the ease of product extraction. These methods use CVD of methanol using a microwave plasma reactor.[175,176] More recently large quantities of graphene have been yielded from using the thermal decomposition of sodium ethoxide in ethanol.[177] These methods use high temperatures (∼900 °C), a general trend across all bottom-up methods.

4.1.3.2 Top-Down Methods

The first mechanical exfoliation of graphene flakes from graphite was demonstrated in 2004 using adhesive tape to cleave the layers apart. Unfortunately, these flakes tend to be several to tens of microns at best as well as having irregular shape and orientation.[178] As such, the extraordinary properties associated with large sheet graphene are not seen and this method of synthesis has been disregarded commercially.[178]

Bulk graphene powder can be synthesised *via* the electrochemical exfoliation of graphite electrodes. Electrodes are placed in an electrolyte of water and surfactant, or sulfuric acid,[179] and a voltage is applied. After time, a mixture of mono and few layer graphene is suspended in the electrolyte which can be isolated after centrifuging.[180]

The exfoliation of natural flake graphite can also be achieved *via* sonication in particular solvents.[181,182] The solvents have been identified to give the highest percentage of mono layer graphene and highest absolute percentage of graphene, respectively. There is a general increasing trend between the boiling point of the solvent used and the percentage of graphene produced. This can lead to problems in product extraction, as well as problems associated with the use of harmful solvents.[183] Thus, other techniques have been explored in order to try and increase yield. Simply increasing sonication time and using a sonic probe rather than a water bath has been successful, however, this has been detrimental to the flake size and quality of the sheets produced.[184,185] Another strategy to reduce the use of harmful solvents, is to use an aqueous surfactant solution. This has the advantage of preventing self-aggregation of the sheets once exfoliated,[186] however the yield is lower than when high boiling point solvents are used and residual surfactant can be problematic during product extraction.[187,188]

Graphene can also be produced from graphite intercalation compounds (GICs). The formation of GICs between graphitic layers can increase the inter plane distance and force the sheets apart. This again can be solvent-assisted such that the intercalated material expels gas and exfoliates the graphite. This has been demonstrated with alkali metals with water and ethanol to expel H_2 and metal ethoxide.[189,190] Exfoliation can also occur when GICs are thermally expanded, for example when supercritical carbon dioxide is used (sCO_2). Upon rapid depressurisation, the sCO_2 readily expands forcing the graphitic sheets apart.[191,192] This, however, requires high temperatures and pressures in order for CO_2 to reach its supercritical fluid state. GICs (often graphite bisulfate) are commonly formed by exposing graphite to strong acids. Exfoliation then occurs with rapid thermal heating or microwave radiation.[193] Note that graphene produced via GICs is known as exfoliated graphite and although applications exist in composite materials and thermal insulators, it has recently been considered as a precursor for graphene.[159,194]

A scalable approach to producing single layer graphene is that of the reduction of graphite oxide (GO). Firstly, graphite is oxidised *via* the Hummer's method in which potassium permanganate is added to a solution of graphite, sodium nitrate and sulfuric acid.[195] This creates an AB stacked graphitic network with larger inter planer distances as hydroxyl and epoxy groups exist within each basal plane. It is these hydrophilic oxygenated groups that allow single sheets of GO to disperse upon the addition of water. The single layered GO can then be reduced with addition of hydrazine, or by initially dispersing the GO sheets directly in hydrazine rather than water.[196] Note that this reduction step requires great care as hydrazine is highly toxic and potentially explosive.[197] This GO method has received attention due to the ease of GO exfoliation relative to that of graphite.[159] This exfoliation can be achieved by sonication or thermal treatment.[198] However, complete reduction of the GO sheets has not yet been achieved and the yielded product is known as reduced graphene oxide or functionalised graphene. Defects can result due to the harsh reduction as well as the formation of wrinkles due to the residual epoxy groups applying strain on the surrounding carbon atoms.[199]

4.1.3.3 Other Methods

Graphene nanosheets have also been produced by a number of different methods. A well-known example of this is the flash pyrolysis of the solvothermal synthesised product of sodium and ethanol. The resulting graphene consists of individual sheets held together in a porous foam-like structure. The sheets of graphene can be then separated with several minutes sonication in ethanol.[200] Graphene nanosheets can also be synthesised *via* a combination of both a bottom-up and a top-down approach. First, the formation of graphite is achieved by the carbonisation of metal phthalocyanine using microwave radiation at 450 °C. This is then exfoliated to graphene upon rapid cooling.[201]

A synthesis route that defies the convention of needing high temperatures and pressures to produce graphene is through the use of microemulsions. Here high quality few layer nano-graphite has been grown under ambient conditions. Unfortunately, the extremely low product yield and small nm-size of the product produced using this route currently blocks any commercial up scaling.[133,202]

4.1.4 Applications

Due to the exceptional properties of graphene, there are a vast array of potential applications. It has been utilised in polymer composites,[203] electrodes,[204,205] transistors,[206] sensors, conductive inks and energy storage devices to name several.[207–209]

The synthesis route taken to produce graphene influences the resulting application. For example, CVD routes that use metal substrates are not suitable for electronic devices, as the graphene film would need to be transferred to an insulating substrate. Here, epitaxial graphene growth on SiC substrates is favoured, due to the resulting graphitic wide-band gap semiconductor material.[210–212] Growth on metals, however, is readily utilised for field emission applications as good ohmic contact is achieved.[213]

The large surface area of graphene has led to applications in fillers for polymer composites due to the considerable surface contact between the polymer matrix and graphene. This produces conducting plastics with increased mechanical strength. Unfortunately, the low solubility of graphene means that it must first be functionalised to graphene oxide and then reduced within the matrix. The residual oxygen containing functionalities can cause defects within the sp^2 hybridisation, degrading the physical properties of the graphene.[203,214]

Although much of the research into graphene is relatively new, and large scale applications have not reached the commercial market, interest from the scientific community and advances in technologies continue to grow.

4.1.5 Synthesis of Carbon Products From Sugars

The dehydration of sugars using acids has been demonstrated in many papers.[215–219] Sulfuric acid, for example, donates protons to form hydronium ions in the presence of water, and therefore can used as a strong dehydrating agent (Scheme 4.1).[220]

$$\begin{gathered} H_2SO_4 + H_2O \longrightarrow H_3O^+ + HSO_4^- \\ HSO_4^- + H_2O \longrightarrow H_3O^+ + SO_4^{2-} \end{gathered}$$

Scheme 4.1: The hydration of sulfuric acid *via* formation of hydronium ions.

4.1.5.1 Sucrose

Take the classic “carbon snake” experiment, in which bulk quantities of sucrose are dehydrated by concentrated sulfuric acid to yield amorphous carbon products and humins absent of any layered structure. This simple experiment was utilised to synthesis nanographite under ambient conditions. A microemulsion system was used in order to provide a 3-D nanoconfinement to exert thermodynamic control over the reaction. Although dehydration of sugar is essentially irreversible, the nano confinement provided control over the stacking of graphene sheets to a stable nanographitic structure over humins. However, this method yields very little product due the tiny confinement of microemulsion droplets. Further, low concentrations of the sucrose precursor must be used to ensure the growth of sheets is slow and complete dehydration is achieved.[133,202]

Initial work to tackle these low yields has been conducted. This has been achieved by moving to a lamellar surfactant system in which the same dehydration takes place. Though this does increase the yield of the carbonaceous product, thermodynamic control is lost, complete dehydration does not occur and a highly furanic product results.

4.1.5.2 Xylose

The synthesis of humins from xylose has also been well documented. The most notable being that of producing furfural from the dehydration of xylose.[221] A proposed mechanism for this reaction initiates the dehydration of xylose at position 2. (Scheme 4.2).[219] Although furfural is not the sp^2 hybridisation of carbon that is desired for graphitic products, this mechanism does provide a promising route to do so if nano confinement is evoked to aid complete dehydration.

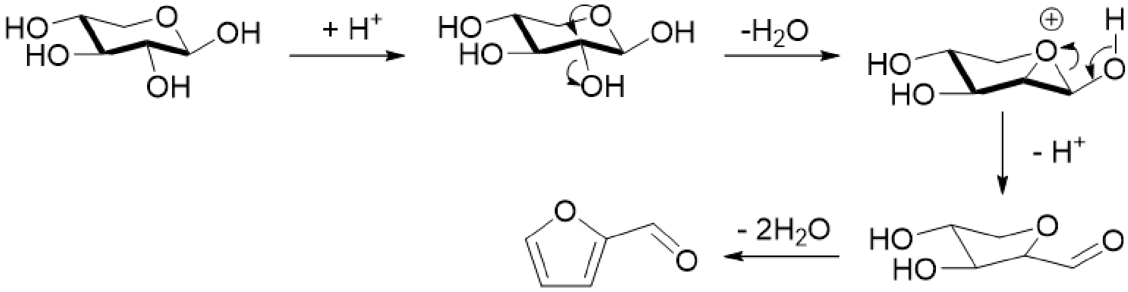

Scheme 4.2: The proposed reaction pathway for the dehydration of xylose to furfural, initiated by the dehydration of xylose at position 2.[219]

4.1.6 Project Outline

Bottom-up routes of graphene involve graphitising carbon based precursors at high temperatures in excess of 800 °C. The high pre-requisite temperatures needed for graphene production have inhibited its growth in large scale manufacture. This has inspired a new route to nanographene/graphite production based on the classic "carbon snake experiment", where microemulsions have been exploited previously in order to exert thermodynamic control over the reaction, controlling the stacking of graphene sheets to yield a stable nanographitic structure.[202]

This chapter discusses a low temperature nanographite/graphene synthesis route that exploits lamellar surfactant phases. Moving to a 2-dimensional nanoconfinement system does increase product yields, however the loss of thermodynamic control means that further treatment are needed to produce a nanographitic product containing polycondensed benzene rings.

The synthesis route presented consists of two stages. The first stage involves a mixed lamellar phase synthesis in which xylose is bathed in excess sulfuric acid at 80 °C for 3 days. Reaction of the sugar occurs within the nanoconfinement of the lamellar system to promote dehydration into polycondensed sp^2 hybridised carbon domains, although a largely furanic product is yielded. After this synthesis the products undergo acid treatment in which they are subjected to bulk excess >95% or fuming sulfuric acid and heated. This promotes complete dehydration of any humins present in the products after the first stage whilst also removing residual surfactant, yielding a few layered nanographitic product. This synthesis route provides a novel, low temperature bottom-up approach to the formation of nanographite exploiting the use of lamellar surfactant phases.

4.2 Experimental

4.2.1 Materials

Surfactants and solvents were of a laboratory grade (unless otherwise stated). The materials used were as follows: xylose (≥99.9%, Aldrich), furfural (99%, Sigma-Aldrich), hexadecane (99%, Sigma-Aldrich) Brij®30 (Acros Organics), sulfuric acid (>95%, Fisher Scientific), fuming sulfuric acid (20% SO_3, Sigma-Aldrich), acetone (wash, Banner) and methanol (99.9%, Fisher Scientific). Ultra high purity (UHP) water with a resistivity of 18.2 MΩ cm was obtained from a Sartorius arium® comfort water purifier system.

4.2.2 Mixed Lamellar Phase Nanographite Synthesis

The formation of a stable lamellar surfactant phase when Brij®30, hexadecane and aqueous xylose solution (40 wt.%) are combined has been achieved. A stable lamellar acid phase consisting of Brij®30 and a 75 wt.% sulfuric acid aqueous solution or >95% sulfuric acid has also been achieved. The xylose and acid lamellar phases were then mixed in a sample vial *via* thorough stirring and vortexing to create a homogeneous gel. The mixed lamellar phase consists of alternating 2-dimensional confined layers consisting of the xylose & acid solutions and the hexadecane. This 2-dimensional nanoconfinement is hoped to aid the 2-D growth of nanographite (Figure 4.5).

The masses of both the xylose (1.2 g - 2.4 g) and acid (2.4 g - 4.8 g) solutions were varied in the recipe, and were stored at temperatures of 80, 100 and 120 °C for 3 days to facilitate xylose dehydration.

For the fuming sulfuric acid mixed lamellar phase synthesis, fuming sulfuric acid (50 ml) and UHP water (8 ml) were combined to produce a 96.6% fuming sulfuric acid solution (using Equation (A.2)). The nanographite synthesis proceeded as above with sulfuric acid substituted with the fuming acid solution. The masses of both the xylose aqueous solution

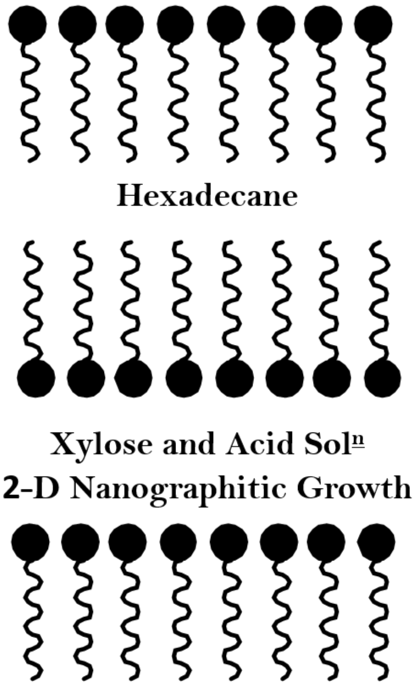

Figure 4.5: Schematic showing the mixed lamellar phase consists of alternating 2-dimensional confined layers consisting of the xylose & acid solutions and the hexadecane.

(0.8 g - 2.4 g) and fuming sulfuric acid solution (2.8 g - 4 g) were varied in the recipe, and were stored at a temperature of 80 °C for 3 days.

For product extraction, up to 3 sample vials were diluted with methanol (300 ml) and thoroughly washed. An intermediate product was recovered *via* Büchner filtration, with the filtrate retained for carbon dot analysis. To remove residual surfactant, this washing/recovery process was repeated with the intermediate product using a solution of methanol (150 ml) and acetone (150 ml). One final washing/recovery procedure using acetone (300 ml) was conducted to yield the final product, which was left to dry under vacuum.

4.2.3 Sulfuric Acid Treatment

The yielded product from the mixed lamellar phase synthesis (1 g) was added to sulfuric acid/fuming sulfuric acid (30 ml) and left to sonicate in a water bath for 1 hour. It was then heated (RT-250°C) for 1-5 hours before allowing to naturally cool to room temperature.

The acidic solution was diluted with UHP water (200 ml) and centrifuged using a Hettich Universal 32, mid bench centrifuge at 9000 rpm for 10 minutes. The resultant supernatant was discarded, replenished with UHP water and repeated until pH 7 was achieved. Residual solvent was removed under vacuum to yield the graphitic product.

4.2.4 Nanographite Characterisation

Small Angle X-ray Scattering (SAXS) measurements were performed on the lamellar phases using the Cooper Group's in-house Bruker Nanostar, with cross-coupled Göbel mirrors and pin-hole collimation, using a sealed tube X-ray source operated at 40 kV and 35 mA to produce the Cu Kα radiation with a wavelength of 1.54 Å. The SAXS camera was fitted with a Hi-star 2-D multiwire detector. Samples were contained in 2 mm glass capillaries. The optics and sample chamber were under vacuum to minimise air scatter. Scattering files were integrated to give the one-dimensional scattering intensity function I(q). The sample to detector distance was 650 mm, which provided a q range of 0.2-3.2 nm^{-1}. Samples were made up to the mixed lamellar recipes with the xylose aqueous solution substituted with UHP water. This was to avoid the synthesis taking place whilst inside the machine and causing potential blockage of the sample capillary.

Solid-state ^{29}Si Nuclear Magnetic Resonance (ssNMR) spectra of the nanographite were recorded at 100 MHz for ^{13}C and 400 MHz for ^{1}H nuclei using a Varian VNMRS spectrometer and a 6 mm (rotor o.d.) magic-angle spinning probe. They were obtained using cross polarisation (CP) or direct excitation (DE) with a 300 s recycle delay at ambient probe temperature ($\sim$25 °C) and at a sample spin-rate of approximately 6 kHz. Between 200 and 240 repetitions were accumulated. Spectral referencing was with respect to an external sample of neat tetramethylsilane (carried out by setting the high-frequency signal from tetrakis(trimethylsilyl)silane to -9.9 ppm).

Powder X-ray Diffraction (XRD) was performed on the nanoquartz using a Bruker D8 Advance operated at 40 kV and 35 mA to produce Cu Kα radiation. The experimental set-up was conducted within the DIFFRAC.SUITE software. Samples were thoroughly dried and ground with a spatula before being applied to a glass XRD slide. The sample was subjected to a 6 mm X-ray beam width and was continuously rotated through 360° to reduce preferential orientation effects. Angles were scanned between 2θ = 10-70° at increments of 0.02° with the beam exposed at each angle for 1 s.

CHN elemental analysis experiments were performed on the nanographite samples with an Exeter Analytical CE-440 elemental analyser under static combustion, with a horizontal furnace and calibrated with acetanilide.

4.3 Results

4.3.1 Mixed Lamellar Phase Nanographite Synthesis

The prepared samples as described in section 4.2.2 were kept for 3 days at 80, 100 and 120 °C (Table 4.1). During this time the samples turned from a colourless gel to a black gel.

Table 4.1: Review of the mixed lamellar phase synthesis recipes. Each corresponding acid and xylose phase was formed individually before being combined to start the reaction.

Variant	Lamellar Phase	Brij®30	Hexadecane	Acid Solution	Xylose Solution
1	Acid	6 g	-	2.4 g	-
	Xylose	4 g	1 g	-	1.2 g
2	Acid	6 g	-	3.6 g	-
	Xylose	4 g	1 g	-	1.8 g
3	Acid	6 g	-	4.8 g	-
	Xylose	4 g	1 g	-	2.4 g

As the concentration of acid and xylose solutions increased in each sample, so did the rate of colouration. This trend was also seen with increasing temperatures. Although there was no direct visual indication of product formation, since the product remained in the gel and did not sediment, the colour change was taken to be a sign that the reaction had taken place. The recovered yields were all dull brown in colour and fluffy in texture (Figure 4.6). Representative yields of 0.33 g (68.75%), 0.71 g (98.61%) and 0.91 g (94.79%) for variant 1, 2 and 3 respectively were obtained. Yields increased as xylose solution masses increased as expected, with higher masses of acid solution also producing increased yields. This is due to higher acid concentrations driving sugar dehydration closer to completion. It must be noted however, that it is unlikely these yields are solely a result of the desired product, the resulting "fluffy" appearance indicates residual surfactant likely remains.

Figure 4.6: Product after mixed lamellar phase synthesis with 3.6 g acid solution and 1.8 g xylose solution at 100°C. A dull brown fluffy powder can be seen. All recovered samples above at all temperatures were visually identical. Product is pictured in a 28 ml squat vial.

4.3.1.1 SAXS

To ensure a lamellar surfactant phase had been established, SAXS experiments were conducted at 80, 100 and 120 °C (Figure 4.7). A sharp lamellar peak is seen in the scattering curves for all variants at all temperatures, with the exception of variant 1 at 100 and 120 °C. In these cases, a broad peak is seen indicating the break down of the lamellar system into a disordered bicontinuous phase.

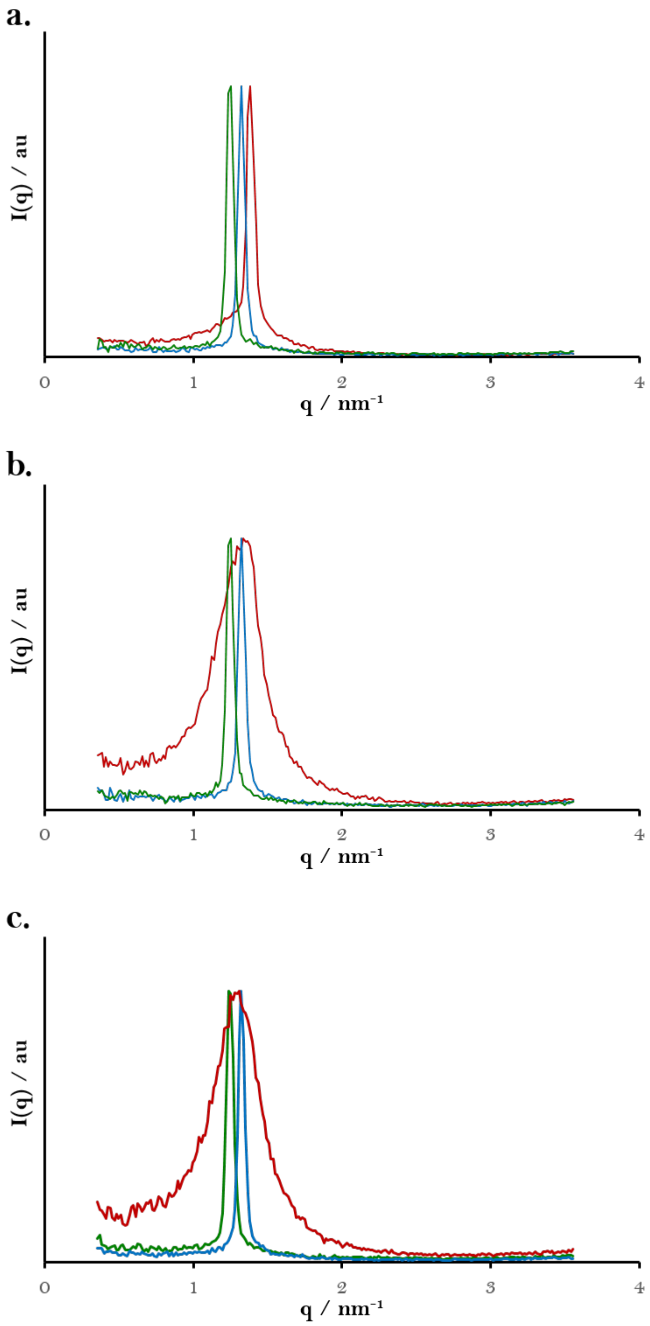

Figure 4.7: Mixed lamellar phase nanographite synthesis SAXS scattering curves from variant 1 (red lines), variant 2 (blue lines) and variant 3 (green lines). **a.** 80 °C synthesis. **b.** 100 °C synthesis. **c.** 120 °C synthesis.

SAXS data is collected in inverse Fourier space, as such, smaller values of q in the patterns indicate a larger lamellar d-spacing (Equation 4.1).

$$d = \frac{2\pi}{q} \tag{4.1}$$

For example, the d-spacing of the lamellar phase for variant 1 at 80°C is calculated to be 4.49 nm. The aqueous channel d-spacing, $\mathrm{d_{aq}}$, is calculated *via* $\mathrm{d_{aq}} = \phi\mathrm{d}$, where ϕ is the volume fraction of the hydrophilic components. This has been outlined for variant 1 (Equation 4.2).

$$\begin{aligned}
&\text{Mass fraction of aq. phase:} && \text{mass fraction} = \frac{1.2 + 2.4}{14.6} = 0.247 \\
&\text{Density of aq. phase:} && \rho = \frac{(1.2 \times 1) + (2.4 \times 1.84)}{3.6} = 1.56 \text{ g / ml} \\
&\text{Volume fraction of aq. phase:} && \phi = \frac{\text{mass fraction}}{\rho} = 0.16 \\
&\text{Aqueous Channel d Spacing :} && \mathrm{d_{aq}} = 0.16 \times 4.49nm = 0.72 \text{ nm}
\end{aligned} \tag{4.2}$$

As the total mass of the aqueous phase is increased so does the d-spacing which is expected, with exception of disordered bicontinuous phases. Furthermore, perhaps counterintuitively, all peaks are shifted to higher q values as the temperature is increased, indicating the channel width narrows. One possible explanation is at higher temperatures, the surfactant tails begin to intercalate with each other narrowing the repeated d-spacing. Though this is desirable, the potential breakdown of the lamellar phases indicates syntheses at these temperatures should be avoided.

4.3.1.2 XRD

Although recovered products from the mixed lamellar phase synthesis were thought to be largely amorphous, powder XRD was used to determine the interlayer spacing, the (002) plane, of the carbonaceous product as well as any in plane (100) or 3-D (101) crystallinity that may be present (Figure 4.8). All products exhibit similar XRD patterns. Broad peaks or humps are seen over sharp peaks due to the lack of long range crystallinity in the samples. However, this broadening may arise due to the fact that few layered nanographitic products would have crystalline regions limited to only a few nm or 10's of nm at best. This is best described by the Scherrer equation (Appendix B), where a broadening of this

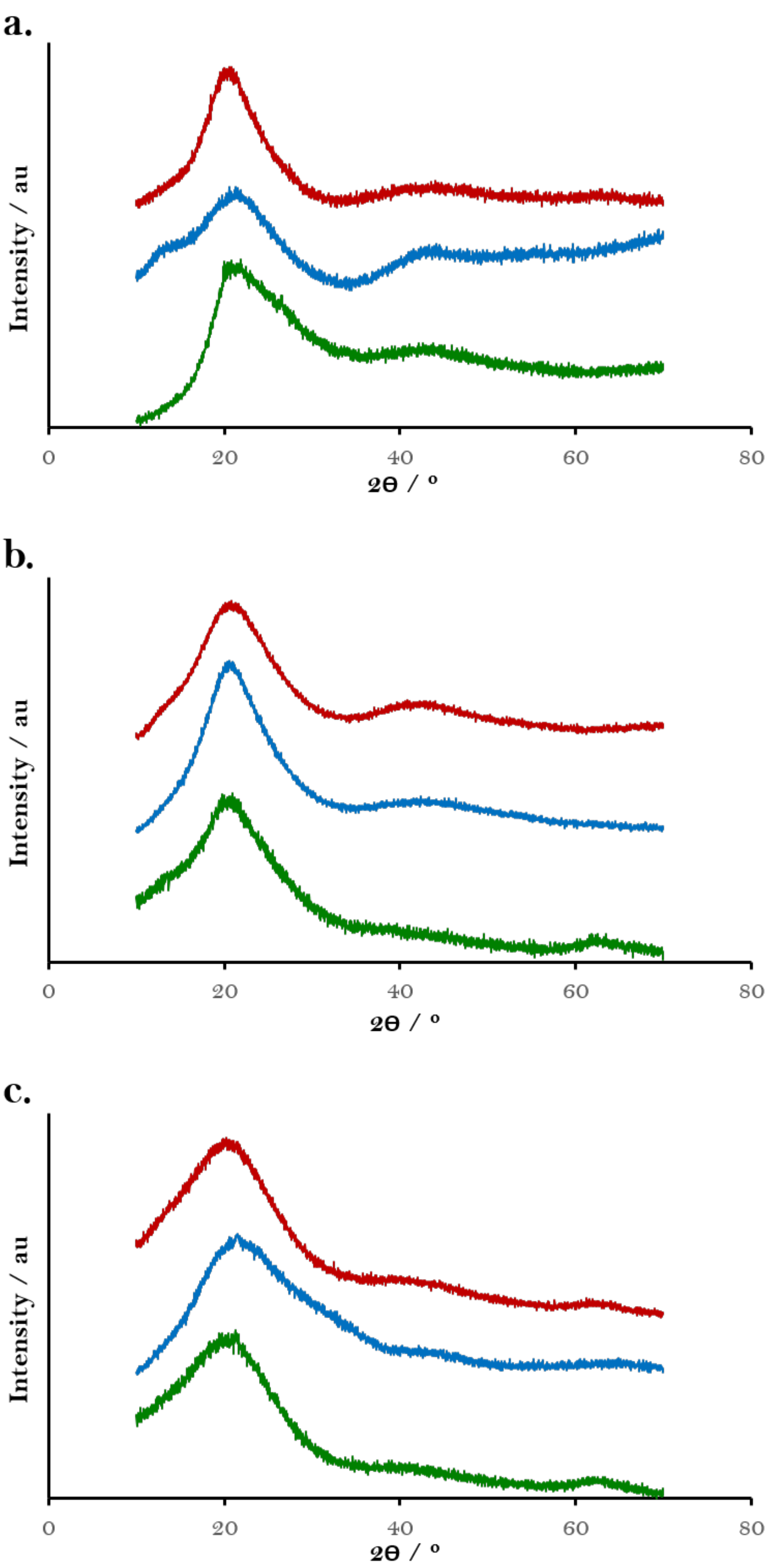

Figure 4.8: Mixed lamellar phase nanographite products XRD patterns from variant 1 (red lines), variant 2 (blue lines) and variant 3 (green lines). **a.** 80 °C synthesis. **b.** 100 °C synthesis. **c.** 120 °C synthesis.

degree indicates 3-4 layer nanographite (~1.26 nm).

At 80 and 100 °C, the predominant peak is seen at $2\theta = 21.3^\circ$ and $2\theta = 20.9^\circ$ (corresponding d-spacings of 4.2 Å and 4.2 Å), respectively. Unlike the lower temperatures, the 120 °C products have varying inter layer spacings. These distances are larger than that of graphite's (002) interlayer spacing, 3.4 Å, due to impurities and functional groups in the products inhibiting close stacking of the sheets. There is little evidence of any in plane crystallinity in any of the samples except for variant 1 at 100 °C. This may be due to lack of polycondensed benzene rings in the products, however this cannot be confirmed with XRD alone.

4.3.1.3 ssNMR

^{13}C (CP) SSNMR was utilised to determine the chemical nature of the carbon atoms present in the samples (Figure 4.9). All spectra are similar with typically the same 4 peaks present. The signal to noise ratio is good due to the use of CP, however this may indicate a substantial presence of hydrogen in the samples.

At 80 and 100 °C, the spectra are dominated by peaks at 30.2 and 70.7 ppm. These are assigned to $\mathbf{C}H_2$, alkyl groups and $\mathbf{C}OH$, hydroxyl groups respectively. This indicates that residual Brij$^{®}$30 is present in the samples. Additional washing was performed, however the surfactant remained suggesting that side reactions have occurred to create impurities in the product. The weak peak at 113.5 ppm is assigned to furanic rather than just sp^2 hybridised carbons due to the existence of the other furanic peak at $\sim$ 150 ppm. In addition, it is more likely that the products contain furan rings rather than aromatics due to the up field position of this peak. Ideally the peak would show around 126 ppm to confidently conclude sp^2 hybridisation.

At 120 °C all of the 4 peaks above are again present. The peak at 114 ppm has broadened and intensities can now be seen around 126 ppm. Though encouraging, an indication that a furanic rich product still exists is the occurrence of the two evenly intense peaks around 113 and 150 ppm. The samples synthesised at 120°C are therefore likely to contain more furanic carbons than the sought after sp^2 polycondensed benzene rings of nanographite.

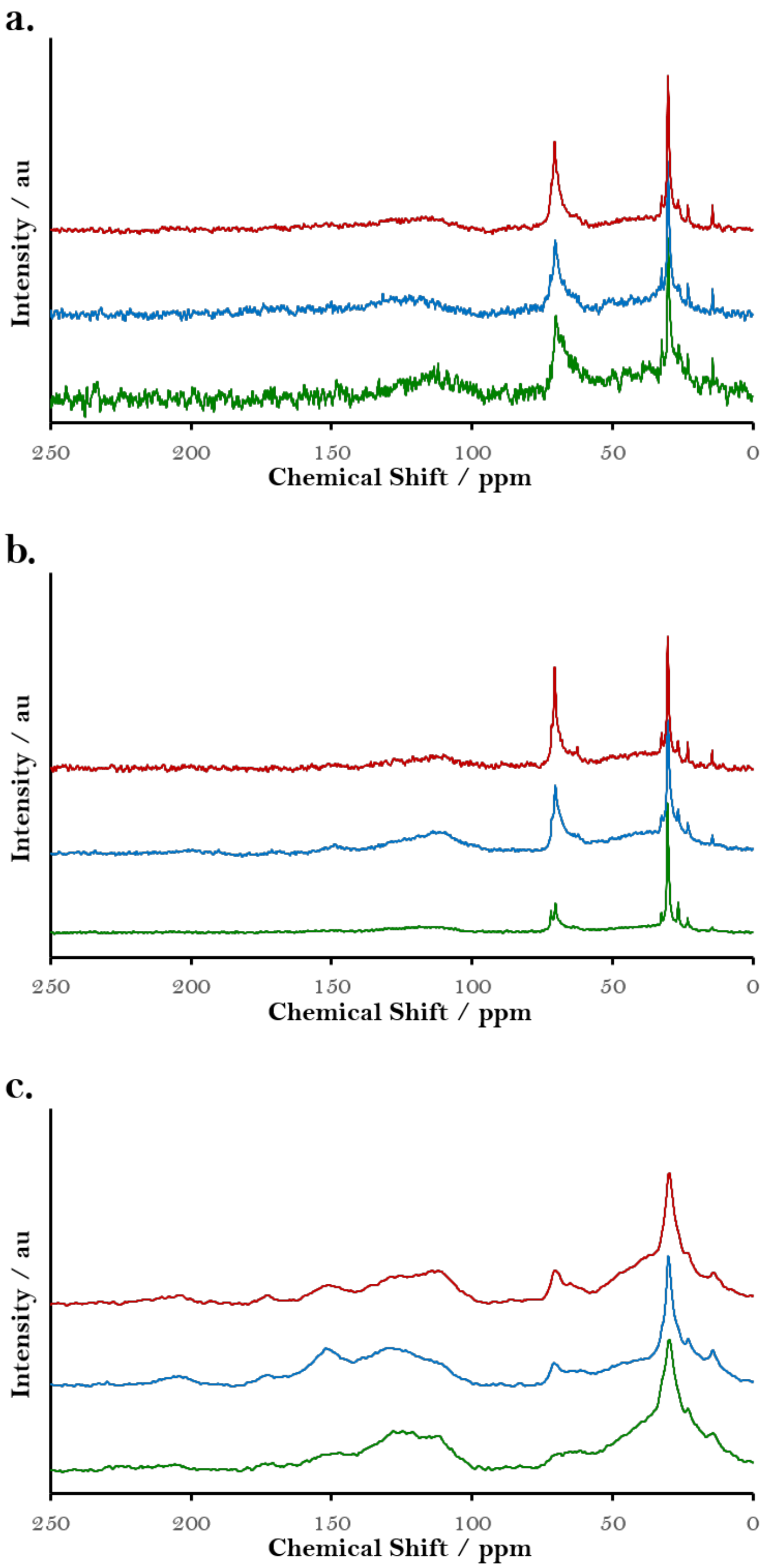

Figure 4.9: Mixed lamellar phase nanographite products ssNMR spectra from variant 1 (red lines), variant 2 (blue lines) and variant 3 (green lines). **a.** 80 °C synthesis. **b.** 100 °C synthesis. **c.** 120 °C synthesis.

4.3.1.4 Increasing Acid Concentration

The effect of increasing the ratio of sulfuric acid solution to aqueous xylose solution was studied to yield a more desirable product. At 120 °C, SAXS samples had started to turn brown in the quartz cuvette whilst experiments were performed. This is attributed to degradation of the surfactant, hence this temperature was no longer considered. There is little to distinguish the samples *via* ssNMR at 80 and 100 °C and therefore the XRD patterns were used to progress the synthesis recipes. Although all the patterns are similar (Figure 4.8), at 100 °C the variant 1 recipe shows promise exhibiting a potential (100) broad peak. This recipe was therefore adapted. In order to achieve a similar lamellar spacing during synthesis, the mass of the aqueous phase was kept constant, however the ratio of acid to xylose solution was changed (Table 4.2). Using equation (A.1), the total acid concentration of the aqueous phase in this syntheses is 64% compared to an acid concentration of 58% in the previous syntheses (Appendix A).

Table 4.2: Review of the mixed lamellar phase synthesis recipe with increase acid concentration. The total aqueous phase mass was kept to be 3.6 g. The acid and xylose phases was formed individually before being combined.

Lamellar Phase	Brij®30	Hexadecane	Acid Solution	Xylose Solution
Acid	6 g	-	2.8 g	-
Xylose	4 g	1 g	-	0.8 g

SAXS experiments confirm the channel width is similar to that of the previous variant 1 recipe (Figure 4.10). A broad peak can be seen at $q = 1.4$ nm^{-1}, corresponding to a d-

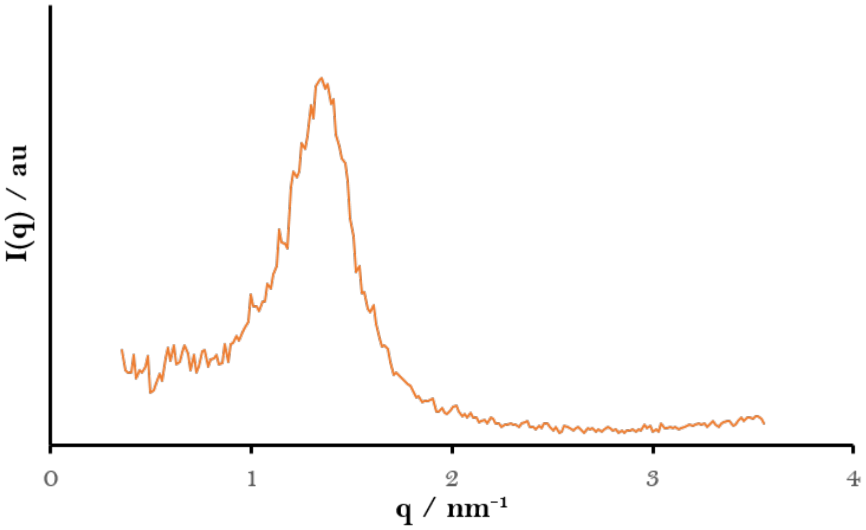

Figure 4.10: SAXS scattering curve of the mixed surfactant phase recipe consisting of 2.8 g sulfuric acid solution and 0.8 g xylose aqueous solution at 100 °C. A L_3 bicontinuous phase is observed.

spacing of 4.65 nm. This is identical to the previous variant 1 recipe as expected, with the lamellar structure breaking down into a L_3 bicontinuous phase at 100 °C. Consequently, in future high acid concentration recipes will be synthesised at 80 °C and not 100 °C to ensure the lamellar phase is retained.

XRD and SSNMR were used to characterise the yielded product as before (Figure 4.11). The XRD pattern is similar to those previously. A peak at $2\theta = 20.9°$ is lower than those previously reported. This is perhaps counter intuitive as the increased concentration should remove more unwanted functional groups and allow closer sheet packing. The increased acid concentration may be degrading the surfactant more severely creating more impurities than before (supported by the degradation of the lamellar phase at this tem-

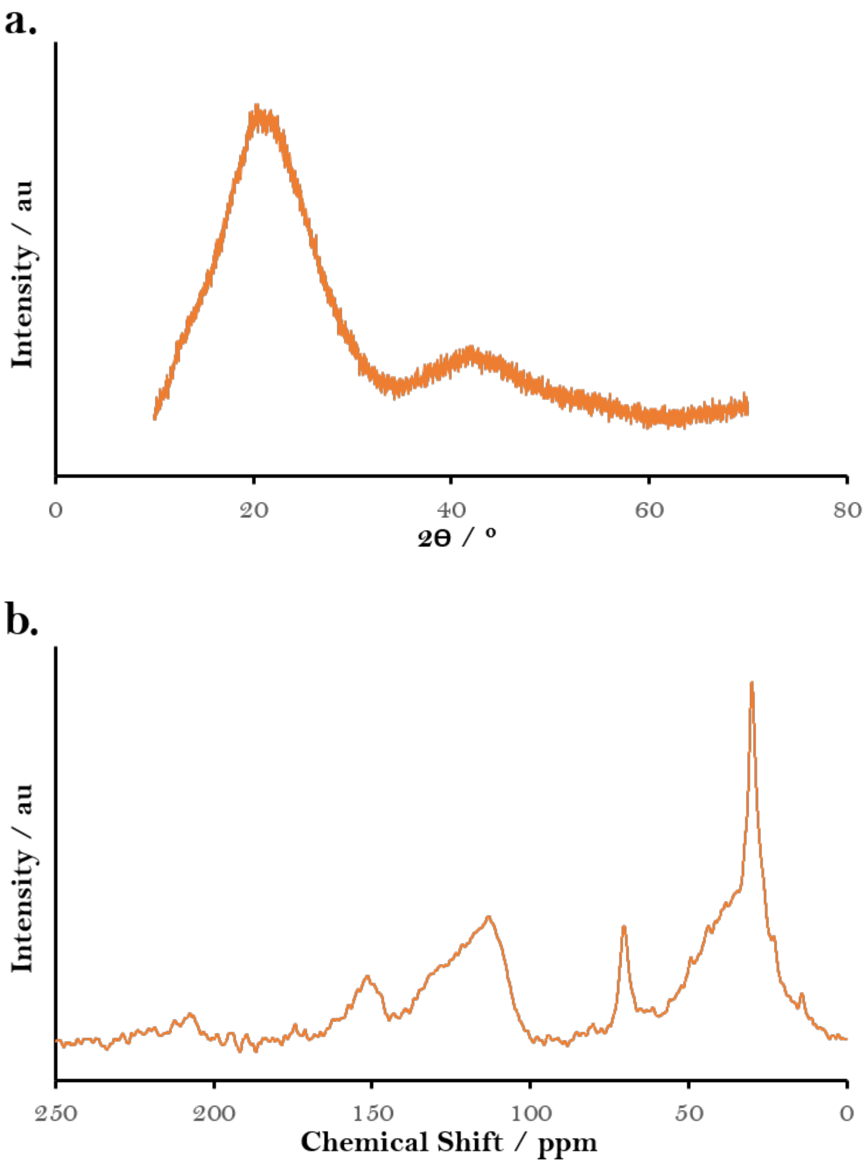

Figure 4.11: Analysis of the mixed surfactant phase recipe consisting of 2.8 g sulfuric acid solution and 0.8 g xylose aqueous solution at 100 °C. **a.** XRD. **b.** ssNMR. A mixed furanic and aromatic product is seen with an interlayer spacing greater than that of graphite.

perature), and hence inhibiting close stacking to a greater extent. Up field surfactant peaks once again dominate the SSNMR spectra, however peak intensities have increased at 113.2 and 151.6 ppm assigned largely to furanic carbons. The peak at 113.2 ppm however has a broad shoulder extending beyond 125 ppm, indicating the presence of sp^2 hybridised aromatic carbons. This is a significant improvement compared to the lower acid concentration syntheses, indicating that higher acid concentrations may result in a more desirable product containing polycondensed benzene rings.

4.3.1.5 >95% Sulfuric Acid Synthesis

Increasing the total sulfuric acid concentration in the aqueous phase has produced a product with an increased number of aromatic carbons. To optimise the synthesis, the affect of increasing the acid concentration further was explored. Here, the same synthesis route is followed identically as described in section 4.2.2 with the acid aqueous solution substituted with >95% sulfuric acid.

First, it must be checked that a stable acid lamellar system can be formed when using >95% sulfuric acid. Upon combining Brij®30 (6 g) and >95% acid (2.4 g), a homogeneous gel is formed, however, slight discolouration is seen (Figure 4.12). This discolouration is

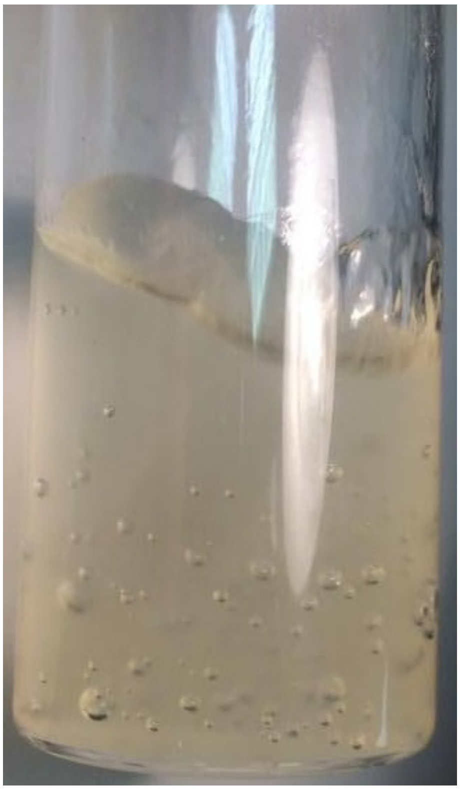

Figure 4.12: Upon combining Brij®30 (6 g) and >95% acid (2.4 g), a homogeneous lamellar phase gel is formed. Slight discolouration is seen. Gel is pictured in a 28 ml squat vial.

attributed to surfactant degradation upon contact with the harsh acidic environment. To ensure a lamellar system is still evident, SAXS was utilised (Figure 4.13). The sharp peak at q = 1.6 nm confirms, despite any discolouration, that a stable sulfuric acid lamellar system is able to be formed at room temperature. Thus >95% sulfuric acid was taken forward for the mixed lamellar nanographite synthesis.

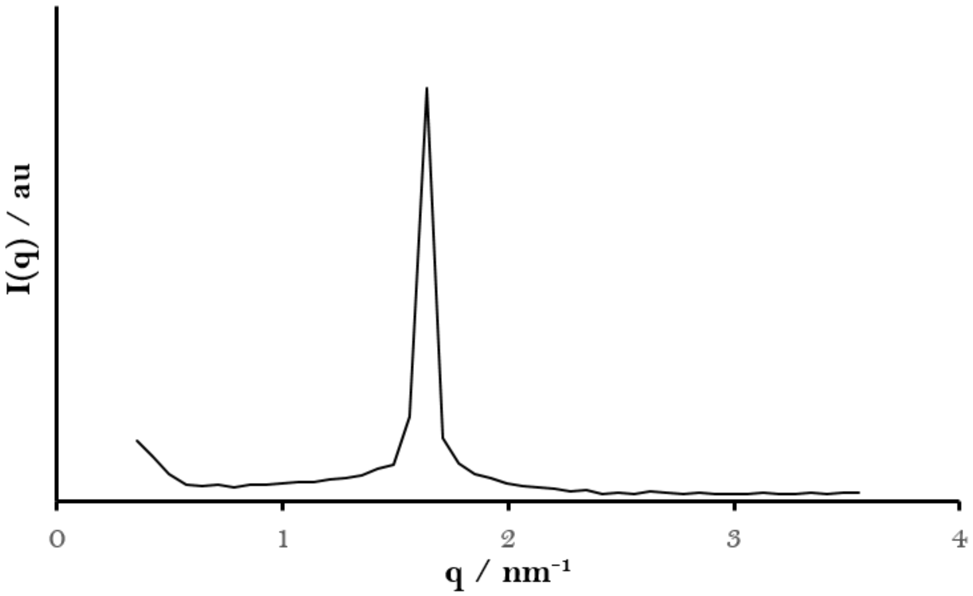

Figure 4.13: SAXS scattering curve of a mixed surfactant phase consisting of 2.4 g sulfuric acid and 6 g Brij®30. A sharp lamellar peak can be seen confirming the existence of an acidic lamellar phase.

Samples were prepared as described in section 4.2.2 with the sulfuric acid aqueous solution substituted with >95% sulfuric acid (Table 4.3) and were kept for 3 days at 80 °C. The temperature was kept at 80 °C due to the much harsher acidic conditions >95% sulfuric acid brings, and the previous recipe forming a disordered L_3 liquid crystalline phase at 100 °C rather than the sought after lamellar. The previous recipe was adapted (due to the improved SSNMR spectra of the product), with all masses staying identical. This recipe has been denoted the narrow channel width variant due its previous 1.47 nm d-spacing (this value of d being the original variant 1 recipe at 80 °C). A 4 g/2.4 g acid/sugar

Table 4.3: Review of the mixed lamellar phase synthesis recipes with >95% sulfuric acid. Each corresponding acid/xylose phase was formed individually before being combined.

Variant	Lamellar Phase	Brij®30	Hexadecane	Acid Solution	Xylose Solution
Narrow	Acid	6 g	-	2.8 g	-
	Xylose	4 g	1 g	-	0.8 g
Wide	Acid	6 g	-	4 g	-
	Xylose	4 g	1 g	-	2.4 g

recipe (wide channel width variant) has also been developed at 80 °C to produce a higher yielding product, as well as to investigate the affect of an increased aqueous channel d-spacing. The overall % acid in the aqueous phase for these syntheses is 81% and 70% for the narrower and wide channel width, respectively (the concentrated acid is assumed to be 95%). Both samples turned to a black gel quicker than previously due to the increased rate of dehydration seen in the harsher acidic environments. Although the wide channel width product was recovered as a brown fluffy powder (as before), the narrow channel width product was recovered as a harder shiny black powder (Figure 4.14). This more familiar graphitic appearance is attributed to the increased dehydration of xylose due to the increased acidic aqueous environment, meaning less functionalities/impurities are present in the yielded product.

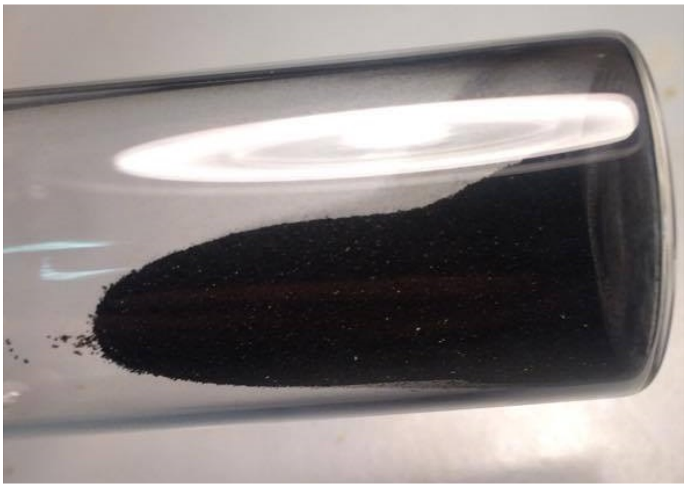

Figure 4.14: Product after mixed lamellar >95% sulfuric acid phase synthesis with 2.8 g >95% sulfuric acid and 0.8 g xylose solution at 80 °C. A hard shiny black powder can be seen. Product is pictured in a 14 ml squat vial.

Lamellar surfactant phases were formed at 80 °C for both >95% sulfuric acid recipes (Figure 4.15). Sharp peaks are observed at $q = 1.48$ nm^{-1} and $q = 1.32$ nm^{-1} (d_{aq} values of 0.68 nm and 1.15 nm) for the narrow and wide channel variant recipes respectively, confirming that a lamellar surfactant system has been formed at 80 °C. The corresponding d-spacings for the respective narrow and wide channel recipes are 4.25 nm and 4.80 nm.

The interlayer stacking of the products observed by XRD were similar to that of previous samples (Figure 4.16). Amorphous humps are once again seen, indicating that long range crystallinity is absent in the products. The primary peaks are at smaller values of 2θ than the desired 26.5° of graphite; $2\theta = 20.6°$ and $2\theta = 21.6°$ for the narrow and wide channel variants, respectively. This is perhaps surprising. With the higher acid concentration and shiny black appearance, one may think that less functional groups

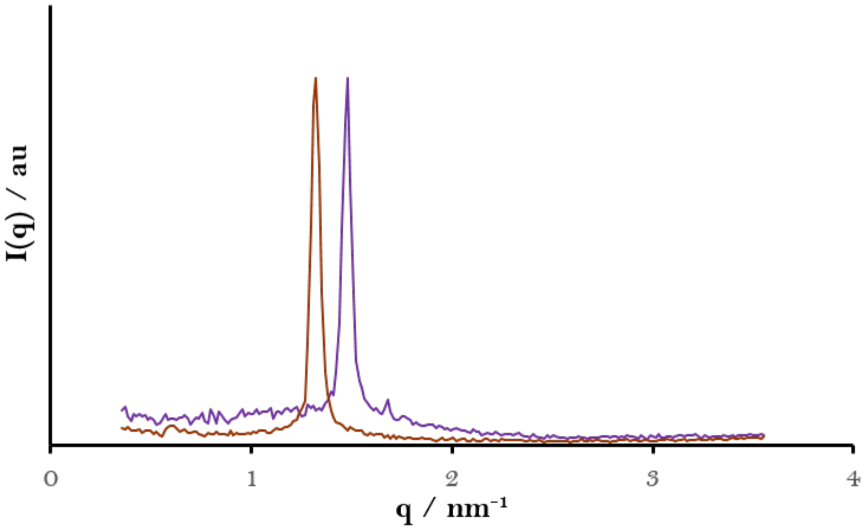

Figure 4.15: SAXS scattering curves from narrow channel variant (purple line) and wide channel variant (brown line) >95% sulfuric acid mixed lamellar phase nanographite syntheses at 80 °C. Sharp lamellar peaks can be seen at $q = 1.48$ nm^{-1} and $q = 1.32$ nm^{-1} respectively, confirming the existence of a lamellar phase.

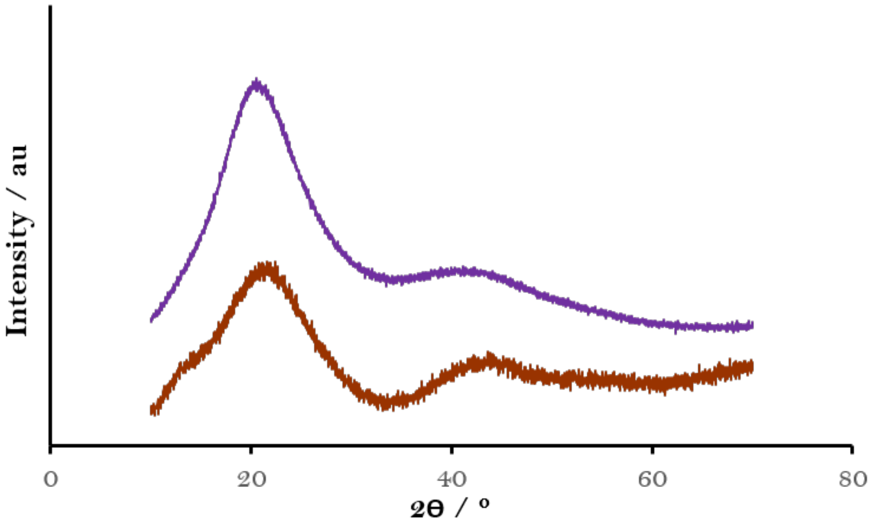

Figure 4.16: XRD patterns from narrow channel variant (purple line) and wide channel variant (brown line) >95% sulfuric acid mixed lamellar phase nanographite products at 80 °C. Interlayer distances, (002) plane, are larger than that seen for graphite.

would be present in the narrow channel width product, thus allowing better stacking of the sheets and a smaller interlayer spacing. A broad shoulder can be seen in the pattern for the wide channel width variant. Due to the texture of the product, samples had to be ground with greater force before XRD analysis was possible. This may have induced structural changes within the nanographite causing the extra peaks to appear in the XRD analysis.

CP ssNMR spectra were also obtained from both yielded products (Figure 4.17). Residual surfactant peaks are present in both spectra, indicating that Brij®30 is taking part in the synthesis and residing in the products. Both spectra look similar with evenly intense peaks at 113.0/150.7 ppm and 114.8/151.6 ppm for the narrow and channel products respectively. This is characteristic of furanic carbons, indicating both syntheses yield furans. Encouragingly, however, both spectra have broad peaks around high 120 ppm values assigned to sp^2 hybridised carbons. These are more pronounced than the shoulder seen previously, indicating that increased acid concentrations within the aqueous phase is indeed yielding a more graphitic material.

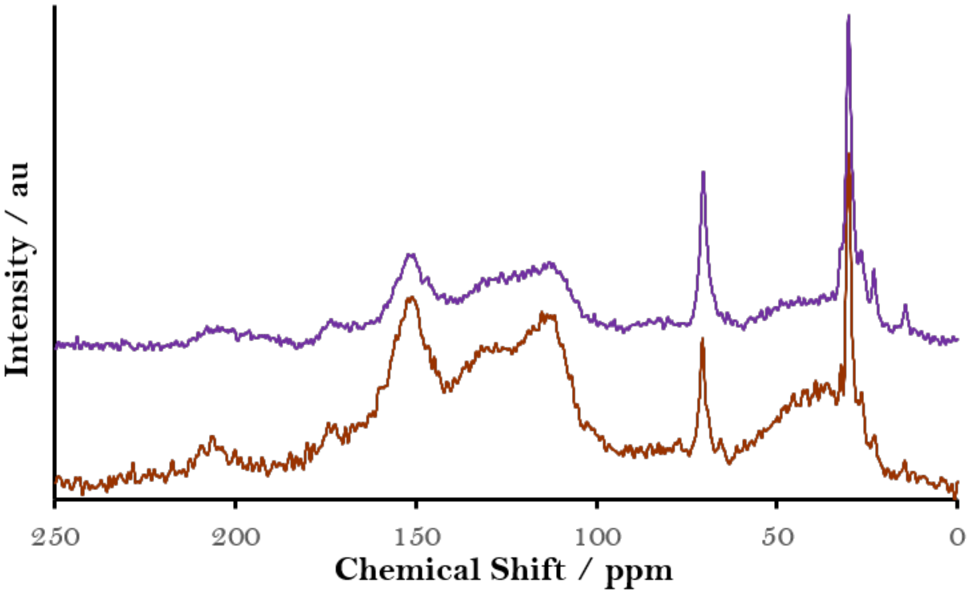

Figure 4.17: CP ssNMR spectra from narrow channel variant (purple line) and wide channel variant (brown line) >95% sulfuric acid mixed lamellar phase nanographite products at 80 °C. All products contain residual surfactant, and furans. The emergence of peaks at high 120 ppm values on both spectra infer sp^2 hybridised aromatic carbons are also present.

CHN analysis also confirms the existence of residual surfactant within the narrow channel product, with a low % C (41.84%) and noticeable % H (5.62%) composition (Table 4.4).

Table 4.4: CHN analysis of the >95% sulfuric acid narrow channel width product, 2.8 g acid and 0.8 g xylose solution. Note that a negative value for % N is seen due to the elemental signal being smaller than the background measurements.

Variant	% C	% H	% N
Narrow	41.84	5.62	-0.32

4.3.1.6 Fuming Sulfuric Acid Synthesis

In attempt to increase the sp^2 hybridisation of the synthesised products, the total acid % in the aqueous phase was again increased. Here, fuming sulfuric acid was used, ie. sulfuric acid containing 20% free $S0_3$ gas. However, in order to use fuming sulfuric acid, an initial stable acid lamellar phase must be achieved. Due to fuming sulfuric acid being highly corrosive, SAXS experiments were not conducted with this reagent. To check for surfactant stability, colouration of the resulting gel was analysed. Upon addition of fuming sulfuric acid (2.4 g) to Brij®30 (6 g) the colour changed immediately to black suggesting complete surfactant degradation (Figure 4.18). The acid was therefore diluted with UHP water at different concentrations and added to the surfactant (6 g) until minimal discolouration was seen, indicating a stable lamellar phase was formed (Table 4.5). A stable system was achieved when 160 μl of UHP water was added to 1 ml of fuming sulfuric acid whilst keeping dilution minimal. Using Equation (A.2), the resulting % of the fuming acid solution was calculated to be 96.6%.

Figure 4.18: Upon addition of fuming sulfuric acid (2.4 g) to Brij®30 (6 g), the gel turned immediately black, indicating complete surfactant degradation. Gel is pictured in a 28 ml squat vial.

Samples were prepared as described in section 4.2.2 with the sulfuric acid aqueous solution substituted with the new formulated fuming acid solution and were kept for 3 days at 80 °C (Table 4.6). The same recipes used in the >95% sulfuric acid synthesis

Table 4.5: Review of the fuming acid dilution recipes with UHP water and whether a stable lamellar phase was created upon addition of surfactant.

Volume of Fuming H_2SO_4	Volume of UHP Water	Stable Phase Achieved?
1000 μl	200 μl	✓
1000 μl	180 μl	✓
1000 μl	170 μl	✓
1000 μl	160 μl	✓
1000 μl	150 μl	x

Table 4.6: Review of the mixed lamellar phase synthesis recipes with 96.6% fuming sulfuric acid solution. Each corresponding acid/xylose phase was formed individually before being combined.

Variant	Lamellar Phase	Brij®30	Hexadecane	Acid Solution	Xylose Solution
Narrow	Fuming Acid	6 g	-	2.8 g	-
	Xylose	4 g	1 g	-	0.8 g
Wide	Fuming Acid	6 g	-	4 g	-
	Xylose	4 g	1 g	-	2.4 g

were adapted in order to directly compare the affect of increasing the acid concentration further. The overall sulfuric acid concentrations within the aqueous phase for these recipes when using fuming sulfuric acid was 82% and 71% for the narrow and wide channel variants respectively. Again, the wide channel product was recovered as a brown fluffy powder whilst the narrow channel product was recovered as a hard shiny black powder. The appearance of the yielded product looks like it is associated with the overall acid concentration; the higher the concentration, the harder and shinier the appearance. After mixing the xylose and acid lamellae, samples started to change colour at room temperature and both turned black within 15 minutes once incubated at 80 °C.

The room temperature colour change inspired an identical synthesis at 50 °C in order to try and minimise the temperature required. These, however, took days to turn black in colour (rather than tens of minutes) and thus were left for 7 days before recovery. The recovered products showed no improvement to the desired properties in either the XRD or ssNMR data. Hence, syntheses at temperatures lower that 80 °C were not explored further.

Due to fuming sulfuric acid being highly corrosive, SAXS experiments were not conducted with this reagent. As such, colouration of the lamellar gel was used to check for surfactant phase stability. Increasing the total % acid in the aqueous phase *via* increasing the initial acid solution has resulted in minimal changes in the SAXS data previously. Thus, SAXS data from the >95% sulfuric acid recipes has been assumed for the fuming sulfuric samples to give a d-spacing of 4.25 nm and 4.80 nm for the narrow and wide channel recipes respectively.

XRD was utilised to see if the use of fuming sulfuric acid had affected the sheet spacing in the yielded products (Figure 4.19). Again amorphous humps are seen indicating a lack of long range crystallinity. The diffraction patterns look similar to their predecessors with both exhibiting main peaks at $2\theta = 20.7°$.

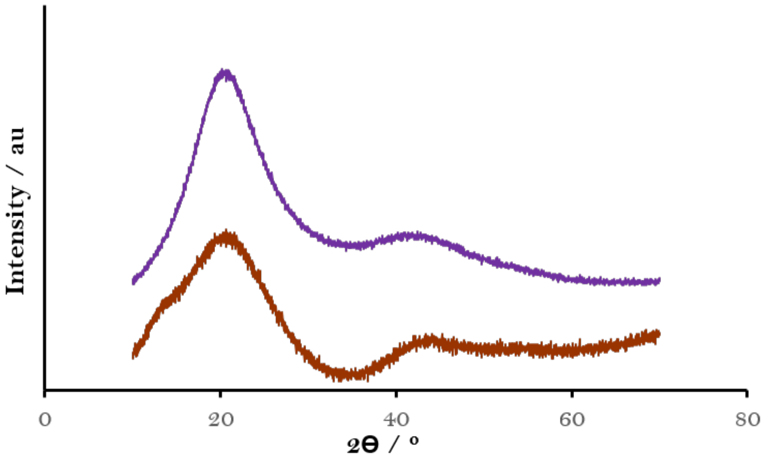

Figure 4.19: XRD patterns from narrow channel variant (purple line) and wide channel variant (brown line) fuming sulfuric acid solution mixed lamellar phase nanographite products at 80 °C. Interlayer distances, (002) plane, are larger than that seen for graphite.

Increasing the concentration of acid in the aqueous phase has resulted in a greater sp^2 carbon hybridised product thus far. CP SSNMR was utilised to see if this trend continued when using fuming sulfuric acid (Figure 4.20). As expected, surfactant peaks are present up field. Both products show peaks at 113.1 and 151.9/152.2 ppm for the narrow/wide

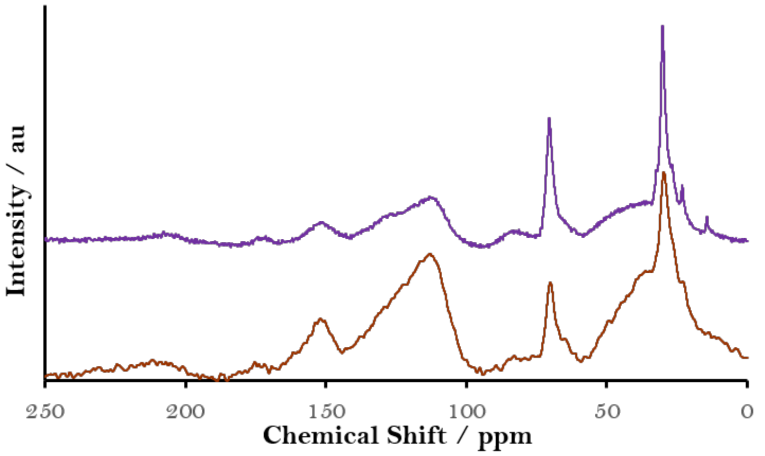

Figure 4.20: CP ssNMR spectra from narrow channel variant (purple line) and wide channel variant (brown line) fuming sulfuric acid solution mixed lamellar phase nanographite products at 80 °C.

channels, with broad peaks at high 120 ppm values on both spectra.

Using fuming sulfuric acid for the mixed lamellar phase synthesis of nanographite hasn't yielded improved results in either the XRD or ssNMR data. As a result, future developments will use variants from the >95% sulfuric acid recipes.

4.3.1.7 Effect of Hexadecane

Hexadecane has been used in the previously as a viscosity modifier in order to ensure the resultant lamellar gel was workable and not too viscous. This is important when both the acid and xylose phases are mixed together to ensure a homogeneous mixture. However, hexadecane is an expensive reagent,[222] and as such it would be advantageous to remove it from the synthesis. Furthermore, unnecessary ingredients in a formulative synthesis should be removed to decrease complexities in understanding the system.

The >95% acid narrow channel variant recipe was adapted by simply removing hexadecane (table 4.7). The viscosity of both the xylose lamellar phase and the mixed lamellar phase were unchanged in viscosity (estimated by hand stirring). Thus mixing of the two initial phases was not inhibited. The samples was incubated at 80 °C for 3 days before being recovered as a hard shiny black powder.

Table 4.7: Review of the mixed lamellar phase synthesis recipe with >95% sulfuric acid and no hexadecane. The corresponding acid/xylose phase was formed individually before being combined.

Variant	Lamellar Phase	Brij®30	Acid Solution	Xylose Solution
Narrow	Acid	6 g	2.8 g	-
	Xylose	4 g	-	0.8 g

SAXS pattern confirm the existence of an acidified lamellar phase without the assistance of hexadecane (Figure 4.21). However, the scattering peak appears at a higher value of q, 1.59 nm^{-1}, as would be expected. The removal of hexadecane from the system has decreased the d spacing from 4.25 nm to 3.95 nm (a $\mathrm{d_{aq}}$ value of 0.63 nm).

Furthermore, Powder XRD (Figure 4.22) and SSNMR (Figure 4.23) corroborate findings that hexadecane is not needed for nanographite synthesis. Both patterns/spectra are almost identical to that of the 2.8 g fuming acid solution and 0.8 g xylose solution recipe. A more intense broad peak at the high 120 ppm values can be seen in the SSNMR data, indicating a more aromatic carbon rich product. As hexadecane provides no support to the synthesis and possibly yields a more desirable product when negated, hexadecane will be no longer be used for the mixed lamellar phase nanographite synthesis herein.

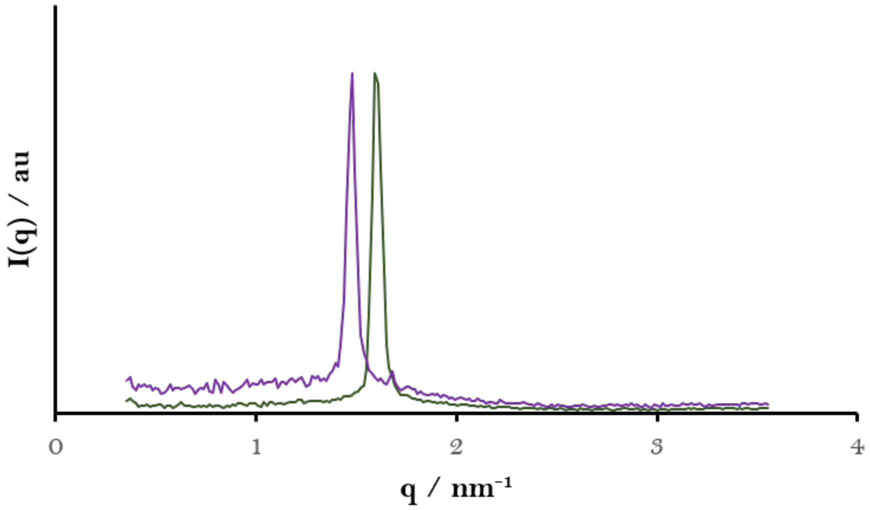

Figure 4.21: SAXS scattering curves from the narrow channel variant containing hexadecane (purple line) and narrow channel variant containing no hexadecane (dark green line) >95% sulfuric acid mixed lamellar phase nanographite products at 80 °C. Sharp lamellar peaks can be seen at $q = 1.48$ nm^{-1} and $q = 1.59$ nm^{-1}

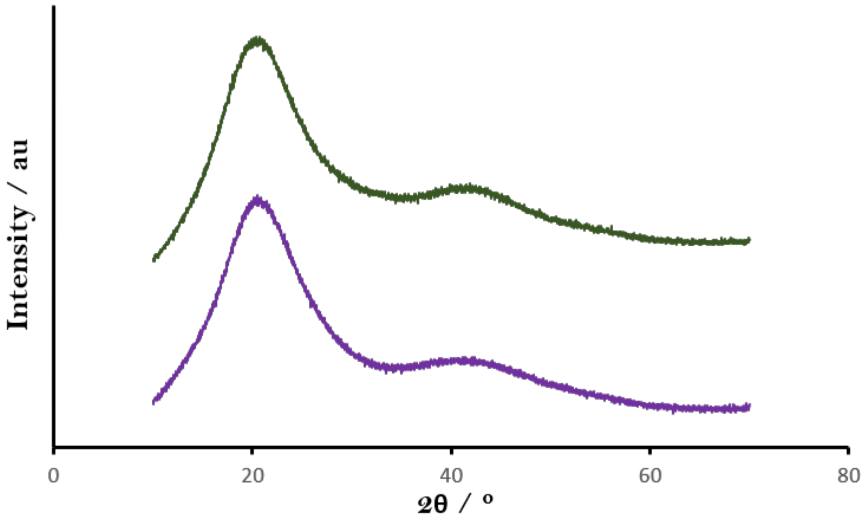

Figure 4.22: XRD patterns from narrow channel variant containing hexadecane (purple line) and narrow channel variant containing no hexadecane (dark green line) >95% sulfuric acid mixed lamellar phase nanographite products at 80 °C. Both patterns are identical.

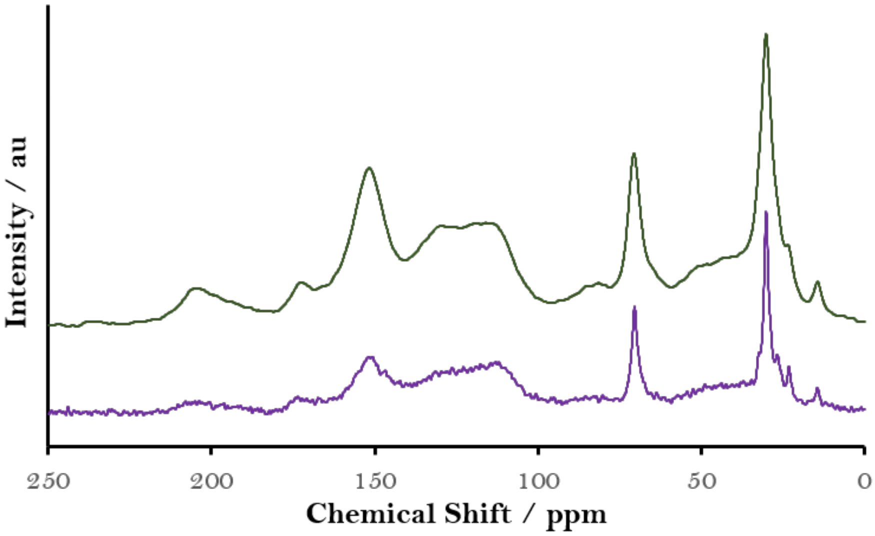

Figure 4.23: CP ssNMR spectra from narrow channel variant containing hexadecane (purple line) and narrow channel variant containing no hexadecane (dark green line) >95% sulfuric acid mixed lamellar phase nanographite products at 80 °C.

4.3.1.8 TEM Analysis

Unfortunately, TEM analysis was not able to be performed on the nanographite samples due to the unavailability of 80 KeV training on the Transmission electron Microscope.

4.3.1.9 Conclusions

A novel, bottom-up, low-temperature synthesis of nanographite has been developed using mixed lamellar phases. Although the resulting product is carbonaceous with a predominantly furanic structure, this method provides a promising route to producing a nanographitic material.

A structure containing increased aromatics can be achieved through increasing the concentration of sulphuric acid in the acidic lamellar phase, with >95% sulfuric acid yielding the best results. Although fuming sulfuric acid can be used for this synthesis, the dilution required to ensure that a stable lamellar phase is formed produces a product that is similar to when >95% sulfuric acid is used. Therefore, at this stage it is recommended that fuming sulfuric acid is not used.

Moreover, it is shown that hexadecane (a reagent used as a viscosity modifier) is not needed to form a homogeneous mixed lamellar phase. It is also thought that the narrower channels produced when hexadecane is negated from the synthesis, produces a more favourable 2-D nanoconfined environment which helps promote sugar dehydration and hence resulting in a more aromatic product. Herein, hexadecane will therefore be omitted from all mixed lamellar phase syntheses.

Finally, XRD patterns reveal that the (002) graphitic spacing is seen at lower diffraction angles than what would be expected for a nanographitic material. This is thought to be due to the intercalation of residual oxygen containing groups that are present between the graphitic layers (akin to graphene oxide) due to incomplete dehydration. Further additional steps are needed to be explored to help promote this dehydration and reduce the interlayer graphitic distance.

Sulfuric acid can be used as a catalyst to dehydrate epoxy, hydroxyl and C-H groups, similar to that of the dehydration of sugars discussed above. The heat produced during dehydration is also enough to decompose carboxyl groups to CO_2.[223] This is seen in top-down syntheses with the reduction of graphene oxide. Heating carbonaceous precursors in fuming sulfuric acid for two hours at 105 °C and elevated pressures has been shown to produced products containing polycondensed aromatics.[224]

Acid treatment can therefore be utilised to remove any furans and undesired functionalities in order to yield a product with the desired sp^2 hybridisation. Since this treatment no longer needs the role of a surfactant, higher temperatures can be used. However, this will be limited to the boiling point of sulfuric acid (290 °C) and fuming sulfuric acid (141 °C),[225,226] depending upon whether concentrated sulfuric acid or fuming sulfuric acid is used.

4.3.2 Sulfuric Acid Treatment

It is evident that increasing the total acid concentration in the aqueous phase during the mixed lamellar phase synthesis is not sufficient to remove residual functionalities and impurities from the yielded product. Here, sulfuric acid treatment (AT) in which the product yielded from the mixed lamellar phase synthesis (1 g) is heated in >95% sulfuric acid (30ml) for 1 hour is explored. The >95% sulfuric acid narrow channel width product, 2.8 g acid and 0.8 g xylose solution, without the addition of hexadecane is treated at 200 °C and 250 °C (Table 4.8). This precursor has been selected due to it exhibiting more

Table 4.8: Review of the sulfuric acid treatment recipes. AT200 and AT250 variants correspond to treating the product yielded from the narrow channel >95% sulfuric acid mixed lamellar synthesis at 200 °C and 250 °C respectively.

Variant	Precursor Mass	>95% Sulfuric Acid	Treatment Temperature/Time
AT200	1 g	30 ml	200 °C / 1 Hr
AT250	1 g	30 ml	250 °C / 1 Hr

aromatic structures than the others in the initial mixed lamellar phase synthesis. Both treatments yielded a hard shiny grey/black powder. Significant mass loss was seen in the yield (75±4% and 51±11% for AT200 and AT250, respectively) indicating the potential loss of impurities and functional groups from the samples.

Powder XRD was again used to characterise the products post acid treatment (Figure 4.24). Amorphous humps are once again seen in the power XRD patterns, indicating that there is no large range crystallinity and a nm-sized product remains. However, a shift in the main (002) peak to $2\theta = 25.7°$ and $2\theta = 26.4°$ is evident for the products treated at 200 °C and 250 °C respectively. This indicates that a sulphuric acid treatment at 250 °C yields a graphitic material that has an inter-layer spacing of that of graphite. This is attributed to the loss of impurities and functional groups from the precursor material allowing the graphitic stacking to be no longer inhibited.

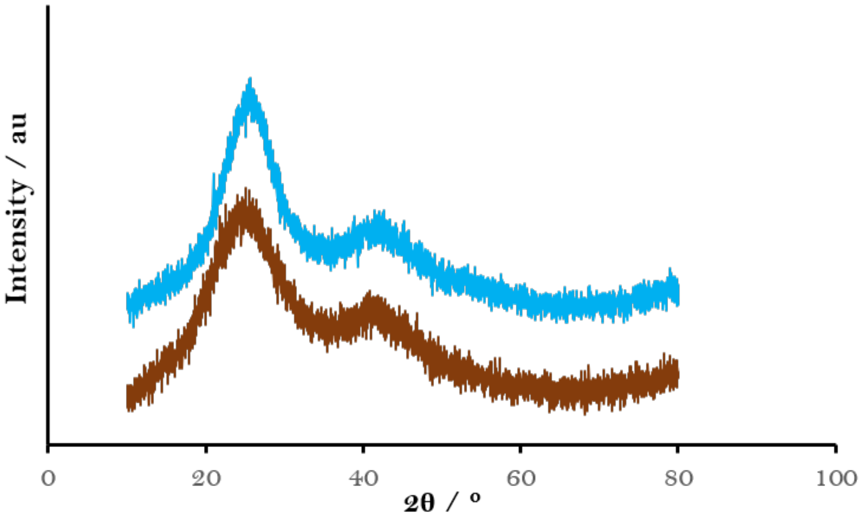

Figure 4.24: XRD patterns of AT200 (brown line) and AT250 (light blue line) >95% sulfuric acid treated nanographite products.

An acid treatment mediated transition to a graphitic structure is also corroborated by CP ssNMR data (Figure 4.25). Both spectra are dominated by a single peak at 124.6 ppm, assigned to aromatic sp^2 hybridised carbons. However, a furanic shoulder signal can be seen for the 200 °C sulfuric acid treated product at 150.6 ppm. No furan signals are present for the 250 °C treated product indicating that at this temperature, sulfuric acid treatment can successfully convert furans to aromatics. The majority of up field surfactant peaks have been lost for both samples, however, some signal is present at 28.2 ppm. Again, this is assigned to residual surfactant, though due to the loss of all other peaks, the products are thought to be free from most surfactant impurities and functional

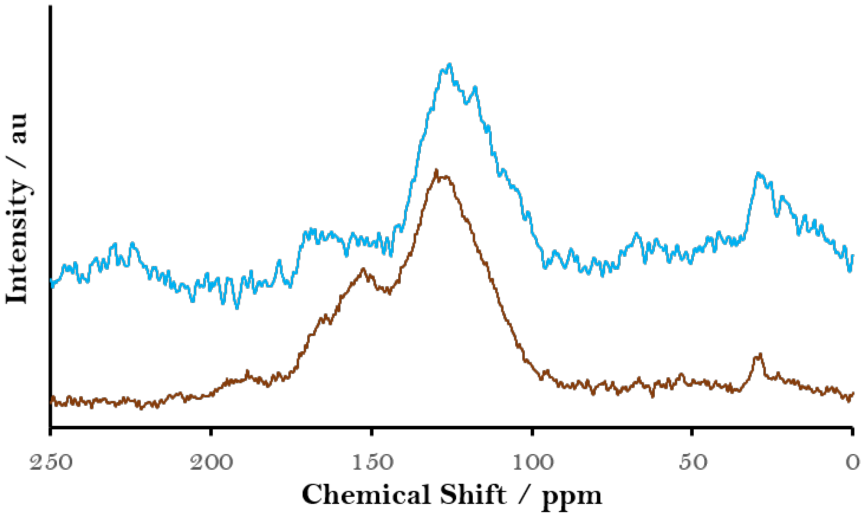

Figure 4.25: CP ssNMR spectra of AT200 (brown line) and AT250 (light blue line) >95% sulfuric acid treated nanographite products.

groups.

As CP ssNMR was used, the poor signal to noise ratio seen in the 250 °C spectra may be explained *via* the lack of hydrogen present in the sample. This is confirmed in the CHN analysis of AT250, where only 2.87% H is observed (Table 4.9). However, a large increase in % C is observed (+ 24.52%) compared to that of the >95% sulfuric acid narrow channel width product, 2.8 g acid and 0.8 g xylose solution, indicating significant furan to aromatic conversion. The remaining ∼ 30% elemental composition is most likely to be sulphur and oxygen from residual adsorbed sulfuric acid and oxygen-containing residual groups that remain in the product. X-ray photoelectron spectroscopy would be needed to confirm this.

Table 4.9: CHN analysis of AT250. Note that a negative value for % N is seen due to the elemental signal being smaller than the background measurements.

Variant	% C	% H	% N
AT250	66.36	2.87	-0.30

4.3.2.1 Fuming Sulfuric Acid Treatment

Due to the strong dehydration properties of fuming sulfuric acid, fuming acid treatment (FAT) is explored where >95% sulfuric acid is substituted with fuming sulfuric acid in the treatment process. One must note that the use of fuming sulfuric acid restricts the treatment temperature to a maximum of 141 °C. Again the >95% sulfuric acid narrow channel width product, 2.8 g acid and 0.8 g xylose solution, without the addition of hexadecane is treated at RT, 100 °C and 125 °C (Table 4.10). Here, the treatment temperature was also varied to see if the use of fuming sulfuric acid allowed for successful treatment at lower temperatures. Although all samples were sonicated for one hour prior to treatment (Section 4.2.3), the room temperature samples were left to sonicate for the entirety of the treatment. Again, all treatments yielded a hard shiny grey/black powder with significant mass loss with a yield of 78±4%, 58±4% and 52±11% for FATRT, FAT100 and FAT125 respectively.

Table 4.10: Review of the fuming sulfuric acid treatment recipes. FATRT, FAT100 and FAT125 variants correspond to treating the product yielded from the narrow channel >95% sulfuric acid mixed lamellar synthesis at RT, 100 °C and 125 °C respectively.

Variant	Precursor Mass	>95% Sulfuric Acid	Treatment Temperature/Time
FATRT	0.5 g	30 ml	RT / 5 Hr
FAT100	0.5 g	30 ml	100 °C / 2 Hr
FAT125	0.5 g	30 ml	125 °C / 2 Hr

In order to see if a graphitic inter-layer spacing was achieved through fuming sulfuric acid treatment (akin to >95% sulfuric acid treatment at 250 °C), powder XRD experiments were conducted (Figure 4.26). Broad peaks are again seen in all samples, where the predominant (002) peaks shows a shift to $2\theta = 25.7°$. However, fuming sulfuric acid treatment has not been successful in fully achieving the inter layer spacing seen in graphite ($2\theta = 26.5°$). This indicates that impurities/functionalities still exist in the products intercalating between the sheets and inhibiting the capability of graphitic stacking.

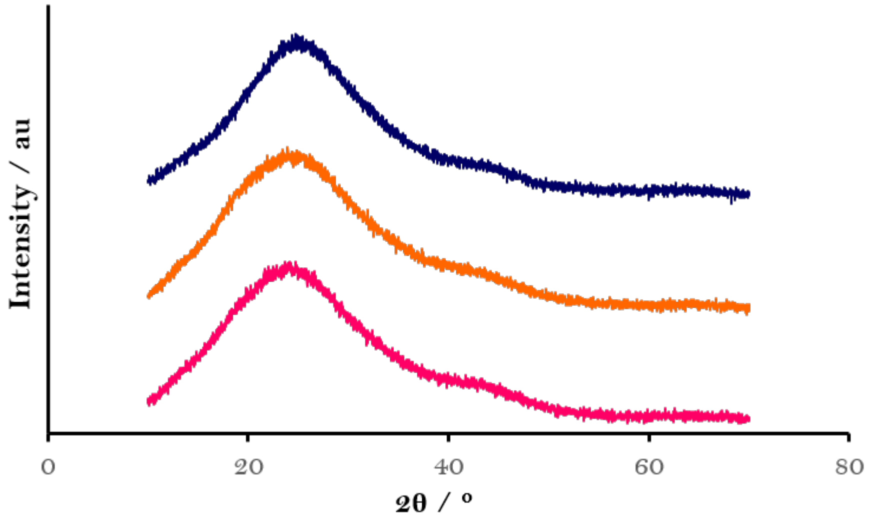

Figure 4.26: XRD patterns of FATRT (pink line), FAT100 (orange line) and FAT125 (dark blue line) fuming sulfuric acid treated nanographite products.

This is also seen in the CHN elemental analysis of FAT125 (Table 4.11). Although a

Table 4.11: CHN analysis of FAT125.

Variant	% C	% H	% N
FAT125	49.58	4.23	0.01

loss in % H is seen from the original (attributed to potential surfactant loss) only a small increase (+ 7.74%) is seen in the % C compared to that of the >95% sulfuric acid narrow channel width product, 2.8 g acid and 0.8 g xylose solution. This is also indicative that other intercalated species are present in the product.

To investigate the capability of furan to aromatic carbon conversion in the fuming sulfuric acid treatments, CP ssNMR was used (Figure 4.27). Though strong peaks at 150.5, 151.8 and 152.5 ppm are present for the room temperature, 100 and 125 °C treatments, the lack of an equally intense peak ∼ 110 ppm indicates some furan to aromatic conversion has taken place. The 150-155 ppm peaks are assignable to phenyl groups as well as furans. A broad down field peak is seen, which decreases in intensity as the temperature is increased. These are again assigned to residual surfactant in the product, with the higher temperatures having a greater effect at degrading these impurities as expected. All spectra, however, contain an intense peak at 128.4 ppm which is assigned to the desired sp^2 hybridisation of carbon, indicating that a polycondensed aromatic product may have been yielded.

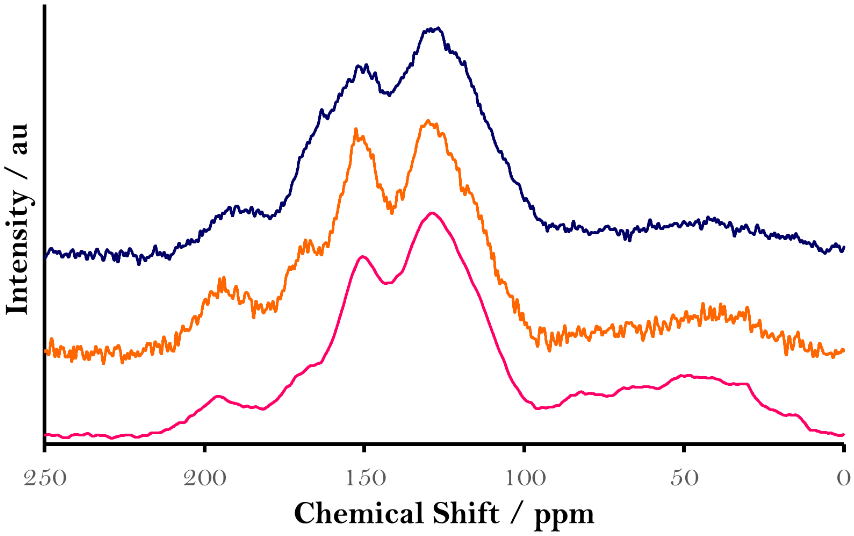

Figure 4.27: CP ssNMR spectra of FATRT (pink line), FAT100 (orange line) and FAT125 (dark blue line) fuming sulfuric acid treated nanographite products.

4.4 Discussion

Since 2004 and the successful isolation of a single layer, potential applications of graphene have received much attention, due to its extraordinary properties. As a consequence of this, various synthesis methods have been developed in order to obtain high quality graphene sheets. Unfortunately, bottom-up methods need unfavourable high temperatures in order to achieve high levels of graphitisation. Top-down approaches are usually laborious, result in defected graphene and use graphite as a precursor; a finite natural resource. Although graphite can be produced synthetically, these methods also use high temperatures. A bottom-up, ambient condition, synthesis route exploited the use of microemulsions in order to gain thermodynamic control and produce pristine graphene. The yields produced *via* this method, however, were too little for practical applications.

This chapter detailed a low temperature synthesis route towards the production of few layer nanographite/graphene. This methodology exploited the use of lamellar surfactant phases in hope that the 2-D nanoconfinement exhibited by these systems was able to inhibit stacking of defected graphene sheets, allowing them to be bathed in sulfuric acid for longer periods of time, and hence resulting in pristine few-layer stacked graphene sheets. Though this method yielded much larger quantities of product than that seen in microemulsion syntheses, the loss of thermodynamic control has largely resulted in the formation of furans.

Increasing the total concentration of acid in the aqueous channel of the system resulted in the formation of polycondensed benzene rings. Although furans were still present, the emergence of these aromatic regions inspired further increases in acid concentration. This was done two ways: increasing the mass ratio of acid to aqueous components and changing the type of acid used. Using diluted fuming sulfuric acid (96.6% total H_2SO_4) in the mixed lamellar synthesis yielded the product with the most polycondensed sp^2 hybridised carbons.

Two variants in particular were studied: a narrow and wide channel width recipe. SAXS experiments were conducted to confirm the existence of a lamellar phase with d-spacings 4.25 nm and 4.80 nm, respectively. Both recipes yielded similar products after the first mixed lamellar synthesis.

Powder XRD was utilised to confirm the existence of graphitic crystallinity in the products. All patterns exhibited broad peaks or humps indicating the lack of long range crystallinity, however this was expected due to the small regions of few layer graphitic material being produced. The primary peak was seen at values of 2θ lower than that of the (002) plane in graphite, indicating a larger inter layer spacing is present in the products. This is thought to be due to functional groups and impurities inhibiting the graphitic stacking. Bragg peaks corresponding to the (101) plane are not seen signifying that only small regions of polycondensed benzene rings have been produced.

To improve the product after the mixed lamellar synthesis, the samples were sulfuric acid treated. Sulfuric acid treatment at 250 °C for one hour has yielded a highly aromatic rich, few layer carbonaceous product with the sought after polycondensed sp^2 hybridised carbons and an inter layer spacing the same as graphite.

Although fuming sulfuric acid treatments have been shown to convert furanic carbon rich products to aromatic rich graphitic products, there is still evidence for residual functional groups, impurities and furans. Although we are limited by temperature, a better product conversion could be achieved with increasing the treatment time. In addition, the highest temperature studied for the wide channel lamellar product was 125 °C, thus far. Hydrothermal treatments may result in a predominantly furan-free, aromatic product, since the furans only comprise a minor component in the 125 °C spectra.

The nanographitic material synthesised from these bottom-up methods maybe of use in batteries/super capacitor applications. It is suggested that higher capacitance could arise from anodes made of nanographitic material, due to the increased surface area and therefore increased storage of Li ions on the surface of the anode. Electrochemical studies would need to be employed to confirm this.[227]

Furthermore, this nanographitic material could prove useful in the application of carbon quantum dots, where they are used in medicine, bioimaging, chemical sensors, solar lights and LEDs.[228] The controlled synthesis of these particles is paramount to obtain a narrow size distribution of particles.

Chapter 5

Nucleation of Quartz Under Ambient Conditions

5.1 Introduction

Crystalline silicon dioxide (SiO_2), also known as crystalline silica, exhibits many polymorphs with α-quartz being the stable form under ambient conditions. Under elevated temperatures and pressures other metastable polymorphs such as β-quartz, cristobalite, tridymite, coesite and stishovite persist as the dominant phase (Figure 5.1).[229] Crystalline silica is derived from the interlinking of SiO_4 tetrahedra at the oxygen sites. Each oxygen

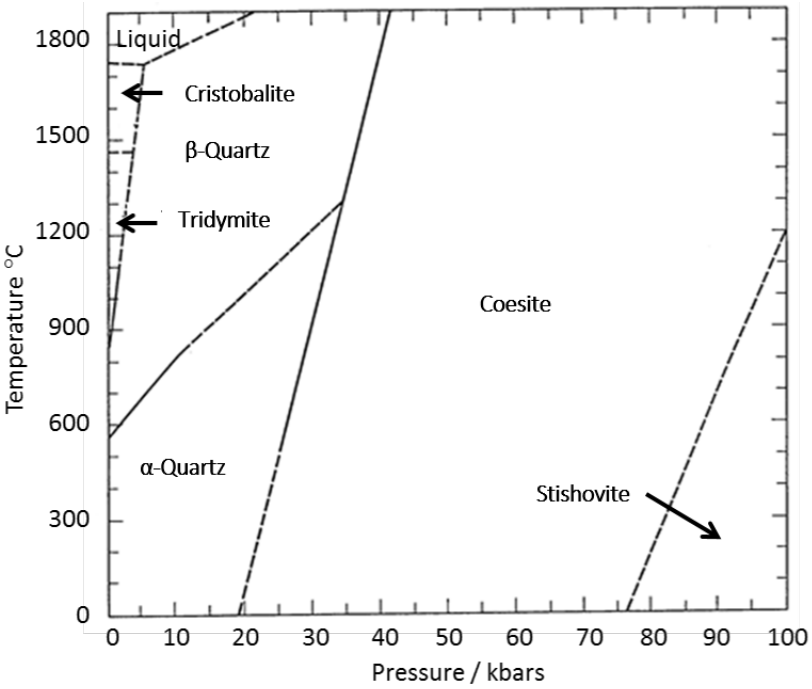

Figure 5.1: Thermodynamic phase diagram for the polymorphs of crystalline silicon dioxide.[133]

atom is therefore linked to two tetrahedra to form 6, 8 and even 12 membered rings depending on the polymorph. In ^{29}Si SSNMR Q^n notation has been developed in order to describe a compound's structure locally, where n is a number (0-4) denoting the number of Si units attached through the oxygen to an individual silicon atom (Figure 5.2).[230]

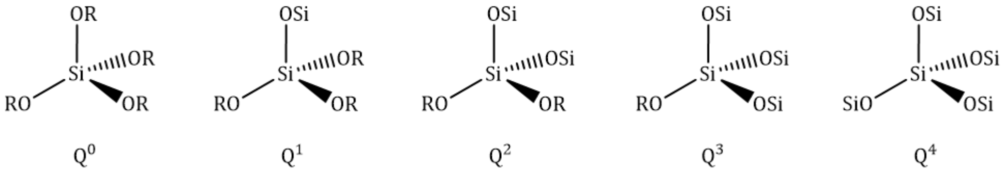

Figure 5.2: Local structure of Q^0, Q^1, Q^2, Q^3 and Q^4 silica.

5.1.1 Quartz

Quartz is an abundant material in the Earth's soil and crust, forming molten magmas at 800 °C and hydrothermal veins at temperatures of 250 to 450 °C. Two forms of quartz exist, the thermodynamically stable α-quartz and the high-temperature β-quartz, both of which are chiral. The transition temperature in which α-quartz transforms to β-quartz takes place abruptly at 573 °C.[231] Herein, any reference to quartz will refer to the stable α-quartz form.

α-Quartz belongs to the trigonal crystal system (space group $P3_121$ or $P3_221$ depending on chirality), taking the form of a six-sided prism terminating with six-sided pyramids at each end (Figure 5.3).[232] In nature, quartz crystals can form massive (cm and mm) single crystals but are often twinned (contains both right-handed and left-handed quartz

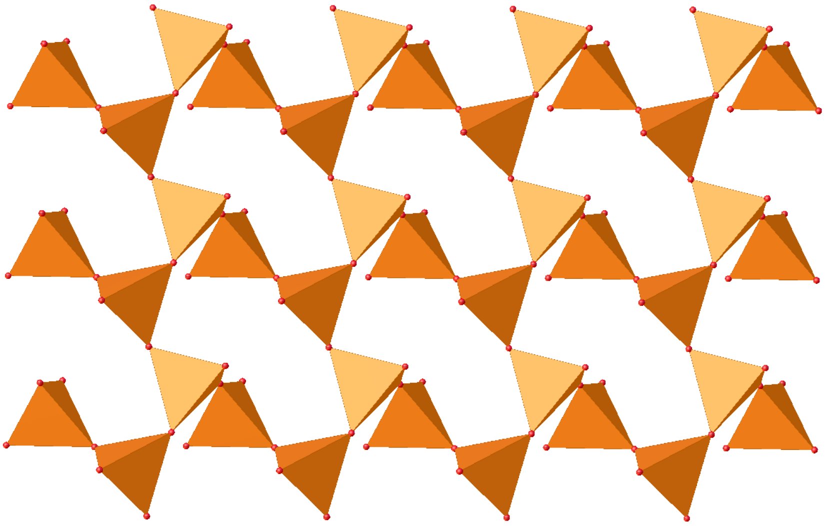

Figure 5.3: Crystal structure of α-quartz. Red balls denote oxygen, whilst orange pyramids represent silicon tetrahedra.

helices), distorted and intergrown with other mineral crystals. As such, routes to produce synthetic quartz have been developed, however, these methods typically result in polydisperse populations that are μm and nm in size.

5.1.1.1 Current Synthesis Methods

Many routes have been taken to synthesise nanoquartz crystals. However, challenges in the typical harsh conditions required for quartz nucleation, as well controlling the size and perfection of crystals, remain.

The chemical synthesis of nm-sized α-quartz is a recent area of study, with the first synthesis published in 2003.[233] It was found that dissolving dry amorphous silica in 0.1 M NaOH, and subjecting the solution to harsh hydrothermal conditions of 300 °C and 8.58 MPa produces polydisperse 10-100 nm quartz. However, strict work up and dialysis methods are needed to produce crystals in this range. Dialysis was pH controlled (pH 8) as, although basic solutions favour the dissolution of solid phase silica, it was found that acidic conditions would coagulate the silica and block filters. At this pH, the smallest isolated fraction of quartz nanocrystals had an average size of 18±5 nm. However, the basic conditions led to product dissolution resulting in poor yields of <5 mg. Also it was found that metal impurities (aluminosilicates) could be transferred into the final product from the metal autoclaves required to achieve the elevated temperatures/pressures. This can be quite simply overcome, though, with the use of more modern hydrothermal units with PTFE cup inserts. Furthermore, this study found that pure phase quartz only precipitated at elevated temperatures (>250 °C) under basic conditions. At lower temperatures and solutions with pH's towards neutrality, the products formed included cristobalite and unreacted fumed silica.

Monodisperse quartz nanoparticles were synthesised in 2011 again *via* hydrothermal methods.[234] Milder conditions of 200 °C and 15 atm were achieved by using NaCl and alkali hydroxide in a PTFE lined hydrothermal unit under stirring to devitrify an amorphous silica precursor (Scheme 5.1). Basic conditions and an excess of NaCl were used to suppress silica solubility and eliminate secondary quartz nucleation and growth as well as Ostwald ripening. Under these conditions, the resulting nanocrystals take on the size and shape of

$$\text{Hydrated amorphous silica} \longrightarrow \text{Anhydrous amorphous silica} \longrightarrow \alpha\text{-quartz}$$

Scheme 5.1: Synthesis pathway to α-quartz nanoparticles templated from uniform amorphous silica precursor the precursor template. By using high purity, uniform, hydrated fumed silica (prepared from tetraethyloxysilane), monodisperse α-quartz nanoparticles in the order of 10s of nm can be synthesised. Although monodisperse, crystals smaller in size would be preferred in the application areas of nanoquartz.

Solvothermal syntheses (similar to that of hydrothermal methods, however the primary solvent used is not water) have also been employed to produce nanoquartz. One such method reports a reverse-micelle solvothermal methodology for synthesising high-purity, single-crystal, hexagonally faceted, quartz nanorods.[235] Toluene, oleic acid, ethanol, tetraethylorthosilane and KOH were mixed. The KOH solution and oleic acid forms an emulsion creating discrete precursor domains to aid the templating of particle size. The addition of NaF also aided the chemical templating of particle shape and growth through weak hydrogen bonding and coordination to the quartz surfaces, respectively. The solutions were heated in a fused silica lined autoclave to 300 °C and 78-90 bar before the precipitated nanocrystals were recovered through centrifugation and ethanol rinses. Although the reported emulsion produced in this system aids with size control, whether or not the emulsion still persists when exposed to harsh solvothermal conditions casts doubts on this methodology. Nonetheless this proposed method shows some promise, however the harsh conditions required akin to those seen in hydrothermal methods are expensive and hinders the commercialisation/scale up of this process.

A prevalent route to producing silica-based nanoparticles is the sol-gel methodology due to its ability to create particles with a narrow size distribution under mild conditions. These methodologies take a dispersion of a precursor material (a sol) which is then transformed into a gel *via* a series of chemical/thermal reactions. The constitute molecules in the precursor then react to form networks of metal-oxygen bonds. Whilst these methods are common in the route to silica nanoparticle production, the near ambient conditions employed results in either an amorphous or poorly crystalline product. Consequently, subsequent thermal treatments are required for the conversion into crystalline silica forms.[236,237] Piezoelectric α-quartz thin films have synthesised using this method however with Sr^{2+}/Ba^{2+} flux (a melt or solvent) being embedded into mesoporous amorphous silica.[238] This homogeneous dispersion of metal in silica was then used as a precursor for epitaxial growth of α-quartz onto Si(100) substrates. More recently this was adapted in a synthesis where $LiNO_3$ and $LiNO_3^-$ saturated furfuryl alcohol was introduced to a colloidal crystal consisting of monodispersed silica nanospheres. After thermal treatment at 870 °C under the flow of argon, the furfural alcohol carbonised alongside the crystallisation of the silica nanospheres. This quartz-carbon composite then underwent calcination at 550 °C to remove the carbon framework resulting in a single-crystalline mesoporous quartz superlattice.[239]

5.1.1.2 Syntheses Under Ambient Conditions

Due to the harsh conditions necessary to nucleate and grow α-quartz (outlined above), obtaining quartz under ambient conditions is exceedingly difficult.

Crystalline silica has been produced by a biological route involving the fungus *Fusarium oxysporum*, but the nanocrystals contained significant quantities of occluded proteins.[240]

Primary nucleation of quartz under ambient conditions by non-biological routes has never been reported in the literature before this study. Indeed, even secondary nucleation and growth on existing α-quartz crystals under ambient conditions is exceedingly slow, requiring yearly timescales.[241] Instead, the main silica phase precipitating under ambient temperature and pressure is amorphous silica, exemplified by natural biosilification processes and the Stöber reaction, which can produce nearly monodisperse amorphous silica spheres.[242,243]

A novel approach of eliciting thermodynamic control over crystallisation has been outline previously to selectively synthesis α-quartz under ambient conditions *via* the 3-D nanoconfinement of silica precursors in microemulsions.[133] Under ambient conditions, the predominant crystallised silica phase was α-quartz when the microemulsion dispersed phase volume was 5 μl g^{-1} and the sodium meta silicate (SMS) precursor concentration was <10 wt.%. When the dispersed phase volume and SMS concentration exceeded these limits, cristobalite and amorphous silica emerged as the predominant silica phase. However, due to the small yields these crystals were unable to be extracted from the dispersed microemulsions. As such, only TEM analysis could be conducted on the dispersions.

5.1.1.3 Applications

The inhalation of crystalline silica dust (containing both μm and nm-sized quartz) has been attributed to several health complications, which often affect those who work in industrial settings. The most prominent is a form of fibrotic lung disease known as Silicosis. Silicosis is a potentially fatal and progressive condition that occurs through the growth of nodules and scarring around silica particles present in lung tissue making breathing difficult.[244] Other serious pathologies attributed to the inhalation of silica (primarily quartz) include lung cancer, chronic obstructive pulmonary disease and pulmonary tuberculosis.[245] Although the affect of μm-sized particle on these conditions has been well studied, the unique kinetics and bioactivity of nm-sized particles have not. It is becoming increasingly important that synthetic nanoquartz of a controllable size and structure can be synthesised for these studies, especially given recent reports stating that surface disorder and surface activity is correlated to cell toxicity and sustained lung damage.[235,246]

Piezoelectricity is a phenomena where an electric potential is produced when a mechanical stress is applied to a crystal. The reverse is also true; when a voltage is applied to opposing faces of a piezoelectric crystal, it will deform due to the mechanical stress created. This induced stress produces oscillations at a characteristic frequency dependent on the size, shape and type of material used.[247] Quartz is an example of a piezoelectric material. Quartz oscillators are used in microbalances,[248] quartz clocks, mobile phones, military radars and many other digital systems. If piezoelectricity in quartz could be translated to the nanoscale, developments in nanotechnology in the application of small-scale actuators and motors could progress.[233] Unfortunately, such piezoelectric studies are currently hindered due to the difficulties in producing well-controlled nm-sized quartz.

It is also feasible that nanoquartz could be used in the development of nanoscale optical sensors for biological applications.[248] Biological systems contain a vast amount of nanoscale entities including enzymes, membranes and proteins. The manufacture of biological sensors on the nanoscale could vastly improve their detection rate.

Furthermore, the structure and phase transition of quartz is of great interest to fundamental chemists. Quartz displays two distinct forms depending on its chirality: α-quartz and β-quartz which display trigonal and hexagonal crystal structures, respectively. The phase transition between these two forms is first-order, meaning that nucleation events of the new form occur at the high energy defects in the crystal. As the new form grows, new defects can easily form, increasing the number of nucleation sites which results in complicated transformation kinetics to study. As nanoquartz contains fewer defect sites, it is believed that phase transitions take place from single nucleation sites.[249] It has been reported that the first order character of the α-β phase transition is greatly reduced in nm-sized quartz compared to that of μm-sized.[250] However, this study was conducted on milled nanoquartz taken from that of larger crystals. Therefore, if nanoquartz (free from impurities) could be synthesised bottom-up in a controlled manner, improved studies could be conducted on the α-β phase transition on the nm-scale.

5.1.2 Project Outline

In this chapter the bulk formation of α-quartz nanocrystals of size 1-5 nm is reported from water-in-oil microemulsions under ambient conditions within 14 days using aqueous sodium metasilicate (pH 12-13) as the silica precursor. As shown previously, microemulsions can induce thermodynamic control of crystallisation in organic crystals.[123–125,202,251] It is shown here that microemulsions can elicit the same thermodynamic control in crystallising silica, a giant covalent structure, even though this requires the creation and breaking of much stronger covalent bonds compared to the intermolecular bonds in organic crystals. These crystals are allowed to grow for 14 days to allow easy extraction of bulk nanoquartz synthesised under ambient conditions for the first time. Si-O bond cleavage/formation is catalysed at high/low pH. Consequently, it is hypothesized that it is the diversity of the local pH environment arising from the presence or absence of hydroxyl and far rarer hydronium ions in the isolated droplets that enables both Si-O bond cleavage and formation to occur repeatedly on the 14-day timescale of the microemulsion experiments. This helps ensure near-equilibration and hence thermodynamic control. This finding that quartz nucleation and extraction is achievable under ambient conditions by using nanoconfinement challenges the common preconception that nanoquartz deposits are a signature of high temperature and pressure conditions.

The microemulsion-extracted α-quartz nanocrystals are then used to seed hydrothermal syntheses under mild conditions of 175°C and autogenic pressure (nominally ≈ 9 bar). This enables nanoquartz of defined size (<10 nm) to be obtained exclusively for the first time. Shorter hydrothermal synthesis times produce nanoquartz crystals with a perturbed α-quartz structure and more surface and interior defects, which dissolve and anneal out, respectively, after longer hydrothermal times of up to 7 days to produce the expected α-quartz structure. Such nanocrystals will be ideal for studies aimed at minimising silicosis and other lung diseases where respiratory nanoquartz has been implicated, particularly given recent suggestions that it is surface disorder on quartz nanocrystals that helps induce cell toxicity.[246]

Amorphous silica is known to catalyse the reaction of β-diketones and amines to form β-enaminones, which are important organic intermediates. The nanocrystals are used to affect the yield of the β-enaminone, 4-(phenylamino)-pent-3-en-2-one, produced from acetylacetone and aniline. Contrasting results are obtained dependent on the nanoquartz structure. Nanoparticulate catalysts are vital in heterogeneous catalysis. This two-stage microemulsion-hydrothermal synthesis methodology can provide significant control over the size and surface structure of nanocrystals to help optimise their catalytic performance.

5.2 Experimental

5.2.1 Materials

Surfactants and solvents were of analytical laboratory grade (unless otherwise stated). Chemicals were used as supplied and were as follows: sodium metasilicate nonahydrate (SMS) (≥98%, Aldrich), Span® 80 (sorbitan monooleate) (Sigma-Aldrich), Brij® 30 (polyoxyethylene (4) lauryl ether) (Acros Organics), Triton X-114 (polyoxyethylene tert-octylphenyl ether, $C_{14}H_{22}O(C_2H_4O)n$, n∼7.5) (Sigma-Aldrich), heptane (≥99% Acros Organics), cyclohexane (99% GLC Specified, Fisher Scientific), methanol (99.99%, Fisher Scientific), acetone (99.98%, Fisher Scientific), ethyl acetate (99.92%, Fisher Scientific), sodium hydroxide (>97% Laboratory reagent grade, Fisher Scientific), chloroform-deuterated (>99.8 atom % D, Apollo Scientific), acetylacetone (>99 %, Acros Organics), aniline (99%, Sigma-Aldrich), 7 nm fumed silica (Sigma-Aldrich), 200-300 nm fumed silica (Sigma-Aldrich) and quartz standard certified reference material BCR® - 068 (Sigma-Aldrich). Ultra-high purity (UHP) water with a resistivity of 18.2 MΩ cm was obtained from a Sartorius arium® comfort water purifier system.

5.2.2 Nanoquartz Synthesis in Microemulsions

The microemulsions used either a surfactant combination of 1:1 wt.% Span® 80 and Brij® 30 in heptane at a surfactant:heptane ratio of 40:60 wt.%, or a surfactant solution comprising of 30 wt.% Triton X-114 in cyclohexane. The microemulsions using Span® 80 and Brij® 30 are denoted with the prefix SB whilst the microemulsions using Triton X-114 have the prefix TX. Microemulsions were prepared by adding 2.5 wt.% sodium metasilicate (SMS) aqueous solutions to the surfactant solutions followed by thorough mixing by vigorous hand-shaking to achieve a single transparent, homogeneous phase.

Further 2 g additions of 2.5 wt % SMS solution were added to the microemulsions after 2 and 4 days. After 2 weeks, the precipitated nanoquartz was washed in a 1:1 solution of methanol and ethyl acetate (300 ml) *via* sonication in an ultrasound water bath for

30 minutes to remove residual surfactant and impurities. The purified nanoquartz was extracted by centrifugation at 9418 G (9000 revs per minute) for 10 min and left to dry in an oven at 60 °C for 24 h.

5.2.3 Nanoquartz Characterisation

Transmission Electron Microscopy (TEM) analysis was performed on the nanoquartz samples using a JEOL 2100 field emission gun TEM (FEG TEM) operating at 200 kV, a ZrO/W (100) Schottky Field Emission analytical emission microscope, in combination with an Oxford INCAx-Sight Si(Li) detector for Energy-Dispersive X-ray (EDX) spectroscopy and a Gatan Orius CCD camera. Phase contrast high resolution electron microscopy (HREM) was used to image nm-sized crystals. The structure of an individual nanocrystal was determined by indexing the fast Fourier transform (FFT) and selected area diffraction patterns. Extracted nanoquartz was dispersed in UHP water *via* sonication in an ultrasound water bath for 30 min. The dispersion was pipetted onto holey carbon, 300 copper mesh TEM grids. The TEM grids were left to dry completely before examination using TEM.

Small Angle X-ray Scattering (SAXS) measurements were performed on the microemulsions using the Cooper Group's in-house Bruker Nanostar, with cross-coupled Göbel mirrors and pin-hole collimation, using a sealed tube X-ray source operated at 40 kV and 35 mA to produce the Cu Kα radiation with a wavelength of 1.54 Å. The SAXS camera was fitted with a Hi-star 2-D multiwire detector. Samples were contained in 2 mm glass capillaries. The optics and sample chamber were under vacuum to minimise air scatter. Scattering files were background subtracted using a capillary filled with the microemulsions' continuous phase and were integrated to give the one-dimensional scattering intensity function I(q). The sample to detector distance was 650 mm, which provided a q range of 0.2-3.2 nm^{-1}.

Powder X-ray Diffraction (PXRD) was performed on the nanoquartz using a Bruker D8 Advance operated at 40 kV and 35 mA to produce Cu Kα radiation. The experimental set-up was conducted within the DIFFRAC.SUITE software. Samples were ground with a spatula and placed on a glass XRD slide. The sample was subjected to a 6 mm X-ray beam width and was continuously rotated through 360° to reduce preferential orientation effects. Angles were scanned with the knife edge in place between 2θ = 3-80° at increments of 0.02° with the beam exposed at each angle for 1 s.

Thermogravimetric analysis (TGA) was performed on the nanoquartz using a Perkin-Elmer Pyris 1 TGA using air as the carrier gas. Samples were heated at a rate of 10 °C min^{-1} to 800 °C, where they were held for 60 min.

Fourier Transform Infrared (FTIR) spectra of the nanoquartz were recorded on a Perkin-Elmer Frontier FT-IR spectrometer equipped with a U-ATR sampling accessory and caesium iodide optics. A total of 16 scans were collected for each sample at a resolution of 2 cm^{-1} over a wavenumber region of 4000 cm^{-1} to 380 cm^{-1}.

Solid-state ^{29}Si Nuclear Magnetic Resonance (ssNMR) spectra of the nanoquartz were recorded at 79.44 MHz using a Varian VNMRS spectrometer and a 6 mm (rotor o.d.) magic-angle spinning probe. They were obtained using direct excitation with a 300 s recycle delay at ambient probe temperature ($\sim$25 °C) and at a sample spin-rate of approximately 6 kHz. Between 200 and 240 repetitions were accumulated. Spectral referencing was with respect to an external sample of neat tetramethylsilane (carried out by setting the high-frequency signal from tetrakis(trimethylsilyl)silane to -9.9 ppm).

^{1}H Nuclear Magnetic Resonance spectra of the catalysis reaction mixture containing acetylacetone, aniline and 4-(phenylamino)-pent-3-en-2-one in chloroform were recorded on a Bruker Avance III spectrometer with operating frequency of 400.13 MHz. Chemical shift values were expressed in ppm, using residual protic solvent as an internal standard.

5.2.4 Hydrothermal Synthesis Experiments

Hydrothermal synthesis experiments were conducted at 175 °C for 1-7 days using 237.4 mg of fumed silica in 0.1 M SMS aqueous solution together with 57.4 mg of seeds consisting of either (i) the nanoquartz synthesised from the microemulsions or (ii) fumed silica for the control experiments. The 237.4 mg of fumed silica in 0.1 M SMS solution was heated to 90 °C to dissolve the fumed silica before adding to the seeds in the hydrothermal unit, sealing the unit and then heating to 175 °C. After the hydrothermal unit had cooled, acetone was added to the hydrothermal product, present as a sedimented hydrated cake, to aid extraction from the hydrothermal unit. This was followed by centrifugation at 9418 G (9000 revs per minute) for 10 minutes to recover the product. The sediment was dried in an oven at 60 °C for 24 h, producing a cake that was then ground with a spatula to give the resulting nanoquartz powders.

5.2.5 Catalysis Studies

Acetylacetone (3 mmol), aniline (3 mmol), and 18 mg of nanoquartz particles (10 mol%) were placed in a glass vial and sonicated in an ultrasonic bath for 6 h, during which time the water bath temperature was naturally raised to 55 °C. The resulting reaction mixture (10 μl) was pipetted into 750 μl of deuterated chloroform for ^{1}H NMR analysis. The yield of the product, 4-(phenylamino)-pent-3-en-2-one, was determined at 4, 5 and 6 h from the ratio of the reactant, aniline, triplet of triplets at 6.76 ppm and the product, 4-(phenylamino)-pent-3-en-2-one, singlet at 5.19 ppm, since both these signals correspond to one proton.

^{1}H NMR (400 MHz, $CDCl_3$) characterisation data. Aniline: δ 3.60 (brs, 2 H), 6.69 (dt, 2 H), 6.76(tt, 1 H), 7.16 (td, 2 H). Acetylacetone: δ 2.05 (s, 6 H), 2.24 (s, 6 H), 3.59 (s, 2 H), 5.50 (s, 1 H). 4-(phenylamino)-pent-3-en-2-one: δ 1.99 (s, 3 H), 2.10 (s, 3 H), 5.19 (s, 1H), 7.10-7.36 (m, 5 H), 12.47 (brs, 1 H).

5.3 Results

5.3.1 Nanoquartz From Microemulsions

The nucleation of quartz under ambient conditions has been previously observed within two different microemulsion systems both using a 5 μl g^{-1} dispersed phase concentration.[133,252] These systems were adopted here in the hope that bulk powders of nanoquartz could be extracted for the first time (Tables 5.1 and 5.2). Compositions containing 3 wt.% and 7.5 wt.% SMS solution for the SB microemulsions were also prepared for TEM analysis.

Table 5.1: Composition of the 2.5 wt.% SMS aqueous solution Span®80/Brij®30 (SB) microemulsions.

	Heptane	Span®80	Brij®30	SMS Aqueous Solution	Total
Mass / g	1.200	0.400	0.400	0.010	2.010
No. Moles	0.0120	9.32x10^{-4}	1.10x10^{-3}	5.49x10^{-4}	0.0146
Mass Fraction	0.580	0.199	0.199	4.97x10^{-3}	1.00
Volume Fraction	0.687	0.154	0.154	4.46x10^{-3}	1.00
Mole Fraction	0.823	0.0640	0.0759	0.0377	1.00

Small Angle X-ray Scattering (SAXS) and GIFT analysis was used to size the microemulsion droplets (Figure 5.4 and Table 5.3).[253] The droplets' mean hydrophilic core radius measured 1.5 nm at 5 μl g^{-1} SMS solution volume for the SB microemulsions.

Table 5.2: Composition of the 2.5 wt.% SMS aqueous solution Triton$^{\text{TM}}$X-114 (TX) microemulsions.

	Cyclohexane	Triton$^{\text{TM}}$X-114	SMS Aqueous Solution	Total
Mass / g	1.400	0.600	0.010	2.010
No. Moles	0.0166	$1.20\text{x}10^{-3}$	$5.49\text{x}10^{-4}$	0.0183
Mass Fraction	0.697	0.299	$4.97\text{x}10^{-3}$	1.00
Volume Fraction	0.759	0.237	$4.22\text{x}10^{-3}$	1.00
Mole Fraction	0.909	0.0611	0.0300	1.00

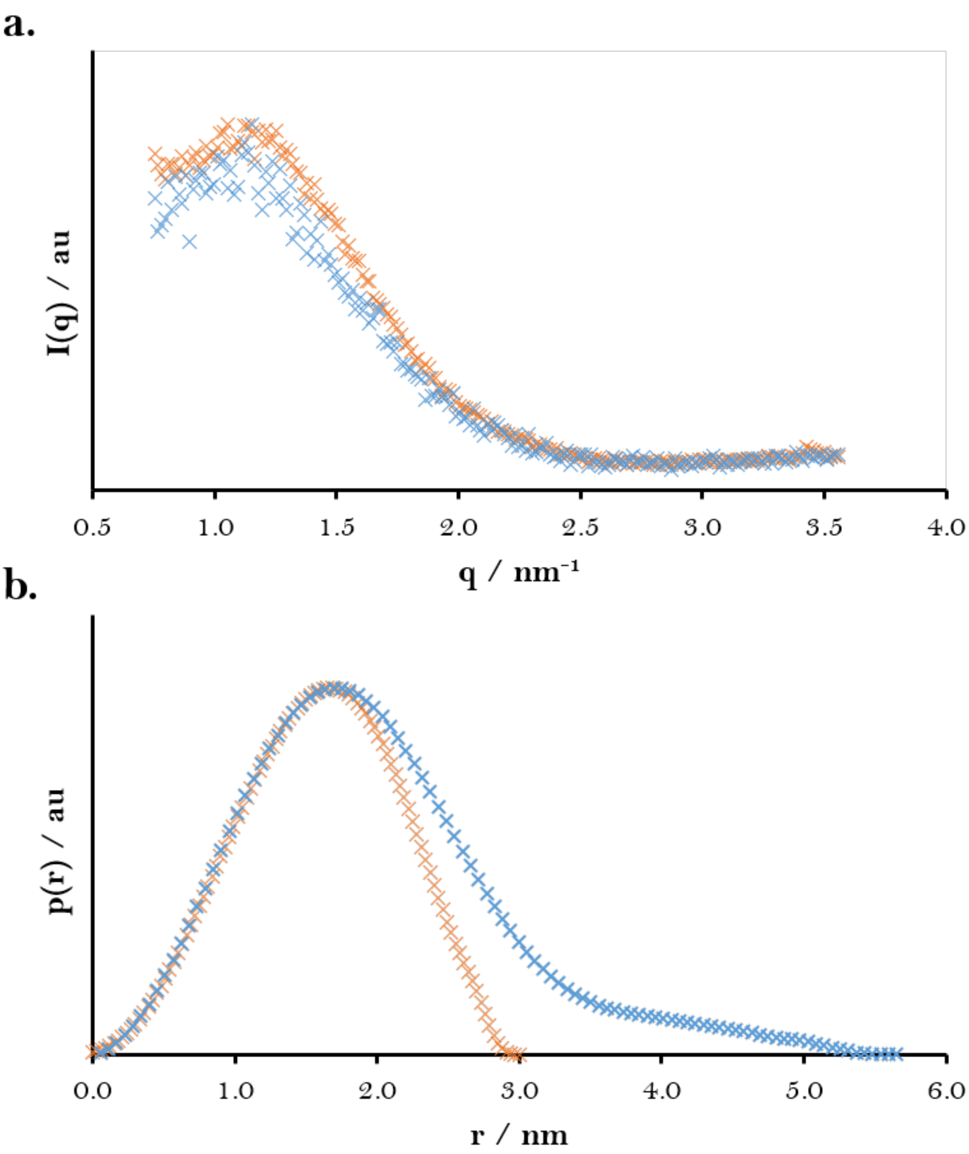

Figure 5.4: Microemulsion SAXS data. **a.** SAXS Scattering curves I(q) vs. q for microemulsions containing 5 μl g^{-1} aqueous SMS (2.5 wt.%) as the dispersed phase. Orange: SB microemulsions and blue: TX microemulsions. **b.** Pair-distance distribution curves p(r) vs. r for microemulsions containing 5 μl g^{-1} aqueous SMS (2.5 wt.%) as the dispersed phase. Orange: SB microemulsions and blue: TX microemulsions.

Table 5.3: Properties of the 2.5 wt.% SMS aqueous solution microemulsions.

	SB Microemulsions	TX Microemulsions
Dispersed Volume / μlg^{-1}	5.0	5.0
Mean Hydrophilic Core Radius ($\pm$0.3 nm) / nm	1.5	2.0
Approximate Number of Droplets per Gram of Microemulsion / 10^{18}	9.9	5.7
Mean Number of Water Molecules per Droplet	17	29
Mean number of Surfactant Molecules per Droplet	61	59
$W_O = \frac{[H_2O]}{[\text{Surfactant}]}$	0.28	0.49

These values are consistent with those of other SB microemulsions.[123,124] For the TX microemulsions, the droplets' mean hydrophilic core radius measured 2.0 nm at 5 μl g^{-1} SMS solution volume. These droplet sizes suggest that the nanoquartz were confined within the droplets during their nucleation and growth.

On this 2-gram microemulsion scale, the maximum quantity of α-quartz nanocrystals that could be obtained was 0.025 mg, given that 2.5 wt.% aqueous SMS was used to produce α-quartz. Consequently, large scale 400 g microemulsions were prepared containing 2.5 wt.% SMS solution (Appendix D) to extract sufficient α-quartz nanocrystals for TEM, XRD, FTIR and ^{29}Si ssNMR analysis (Table 5.4). On this larger scale, a slight cloudiness in the SB microemulsions was often evident due to solid impurities (soluble in a 1:1 solution of methanol and ethyl acetate) in the surfactants. This cloudiness dissipated as the impurities precipitated after 2 days. Centrifuging at 9418 G was ineffective at sedimenting the 1–5 nm nanoquartz particles from the microemulsions. Instead, the SB microemulsions were left for 2 weeks for nanoquartz aggregation and subsequent sedimentation to occur.

Table 5.4: Composition of 400g scale 2.5 wt.% SMS aqueous solution Span®80/Brij®30 (SB) microemulsions.

	Heptane	Span®80	Brij®30	SMS Aqueous Solution	Total
Mass / g	240	80.0	80.0	2.00	402
No. Moles	24.0	0.186	2.20	0.110	2.92
Mass Fraction	0.580	0.199	0.199	4.97x10^{-3}	1.00
Volume Fraction	0.687	0.154	0.154	4.46x10^{-3}	1.00
Mole Fraction	0.823	0.0640	0.0759	0.0377	1.00

There was no observed precipitation of nanoquartz from the large scale 400 g TX microemulsions, and therefore only SB microemulsions were taken forward in this study. It is believed that the small quantity of solid impurities present in the SB surfactants aids the precipitation of the nanoquartz.

5.3.1.1 TEM

TEM studies on the microemulsion derived nanoquartz established the formation of α-quartz nanocrystals as the majority silica phase present (Figure 5.5). The size of the nanocrystals after 14 days ranged from 1–5 nm, with a mean size of 2.0 ± 0.7 nm, based

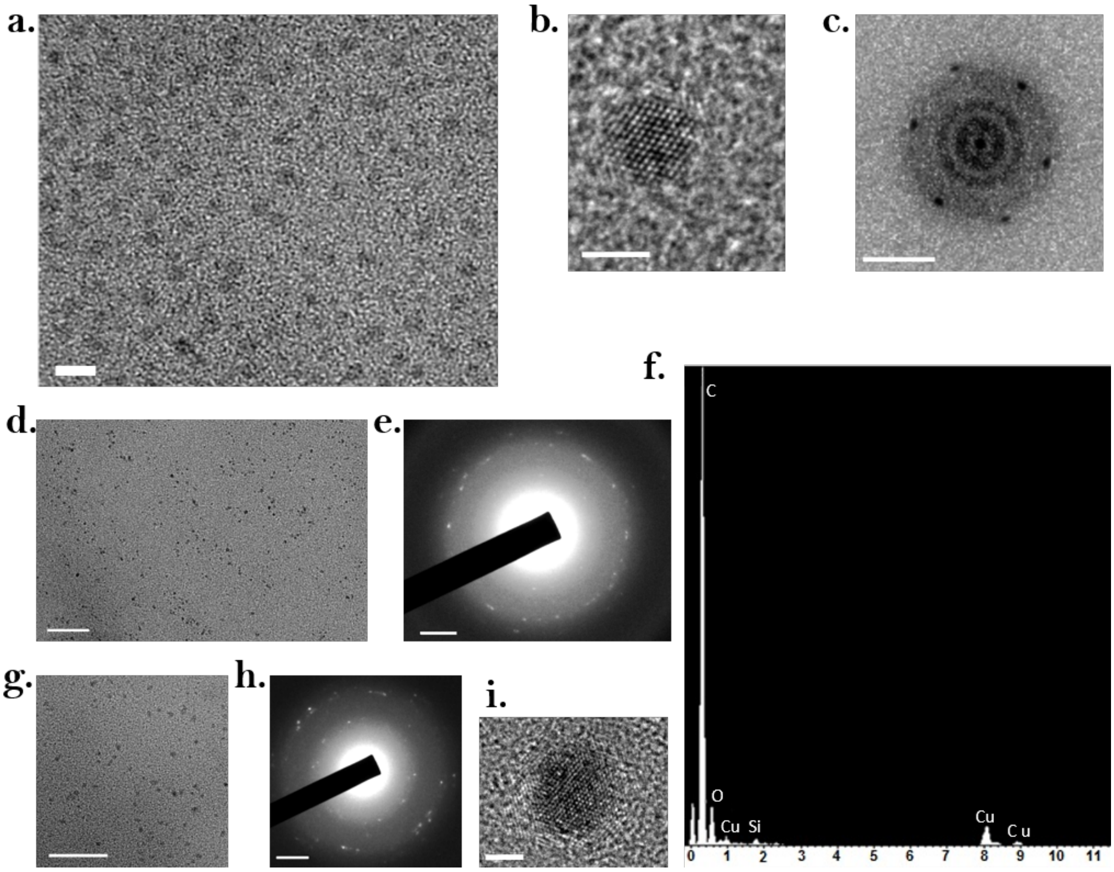

Figure 5.5: Representative TEM data of the nanoquartz synthesised from SB microemulsions using 5 μl g^{-1} of a 2.5 wt.% (**a.-c.**), 3 wt.% (**d.-e.**) and 7.5 wt.% (**g.-i.**) aqueous SMS solution. **a.**, **d.**, **g.** Bright field images of 1-5 nm microemulsion-derived nanoquartz particles. **b.**, **i.** High resolution image (HREM) of 2.5 wt.% and 7.5 wt.% nanoquartz particles respectively. **c.** FFT of the image **b.**, which indexes on the $\langle 212 \rangle$ zone axis of α-quartz. **e.**, **h.** Electron diffraction patterns of the regions shown in **d.** and **g.** respectively, revealing diffraction spots attributed to α-quartz and silicon (Table 5.5). Scale bars are 5 nm in **a.**, 2 nm in **b.** and **i.**, 5 nm^{-1} in **c.**, 50 nm in **d.** and **g.**, and 2 nm^{-1} in **e.** and **h.** **f.** Representative EDX spectra of the microemulsion-synthesised nanoquartz TEM micrographs. The oxygen peak is larger than expected from SiO_2 alone, suggesting that there is residual surfactant present on the grid. Note that there is no signal due to sodium (expected at 1.04 keV), showing that the silica phase present does not contain any sodium silicate.

on the sizing of 550 particles in TEM micrographs (Figure 5.6). Upon increasing the

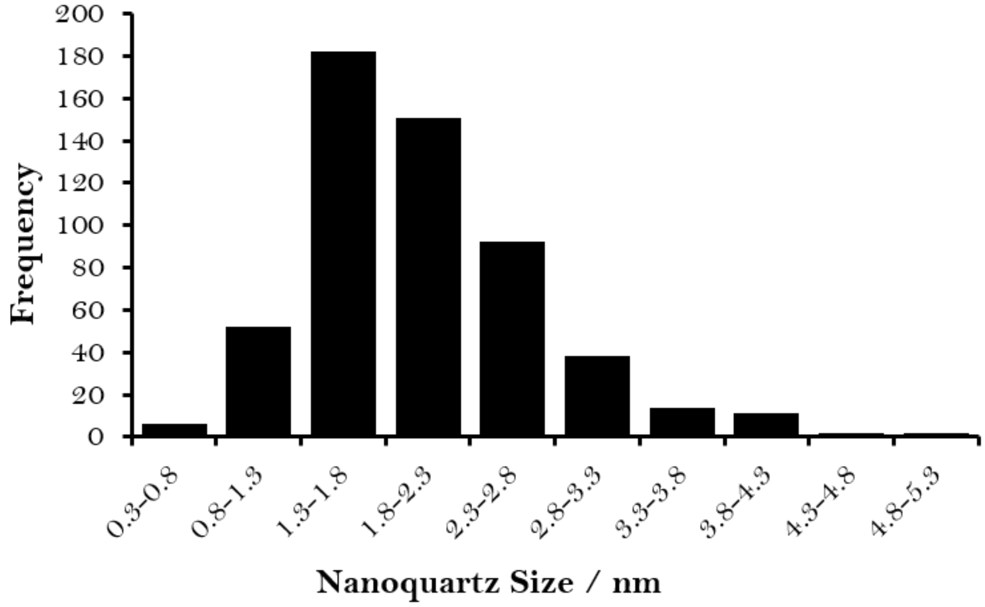

Figure 5.6: Histogram showing the particle size distribution for the microemulsion-synthesised nanoquartz obtained by sizing 550 particles from TEM micrographs.

concentration of aqueous SMS (up to 7.5 wt.%), the increased quantity of nanocrystals provided sufficient crystallinity to enable electron diffraction patterns to be observed, albeit weakly, above the diffuse rings of the amorphous holey carbon grid background. Silicon and oxygen peaks were present in the EDX patterns but there was no sodium peak, confirming that the nanocrystals were not sodium silicate.

Analysis of the diffraction patterns revealed spacings of 0.34, 0.24, 0.20, and 0.17 nm, consistent with diffraction from $\{\bar{1}01\}$, $\{1\bar{2}0\}$, $\{02\bar{1}\}$, and $\{\bar{2}02\}$ α-quartz planes, respectively, which are all part of the $\langle 212\rangle$ zone axes. The presence of the 0.34 nm spacing established that there must be nanoquartz present since silicon and cristobalite have no interplanar distances close to this spacing. In addition, 0.31 and 0.19 nm spacings were observed, attributable to the $\{111\}$ and $\{220\}$ strongest diffracting planes of silicon, since it is known that α-quartz can beam damage and reduce to silicon under even relatively low intensity electron beams (Table 5.5).[254]

Fast Fourier Transforms (FFTs) from high resolution nanocrystal images revealed the same diffraction spacings of 0.20 and 0.17 nm attributable to the α-quartz $\langle 212\rangle$ zone axes (Table 5.6). The $\langle 212\rangle$ zone axes correspond to the quartz nanocrystals lying on, or close to, the low energy rhombohedral $\{101\}$ faces. The $\{101\}$ faces have a large proportion of Q^3 Si–OH silanol surface sites, i.e. a silicon atom bonded to three 3 bridging oxygen atoms and one Si-OH surface bond, rather than Q^2 Si-$(OH)_2$ sites.[255] This aids their

Table 5.5: Diffraction spacings and assignments for diffraction patterns. † These spacings are slightly larger than the bulk α-quartz spacings. This may just reflect the uncertainty in the measurements or it may be indicative of a slightly perturbed quartz structure for the nanocrystals. The latter would be in agreement with our hydrothermal studies, where XRD analysis shows the nanoquartz obtained after 1-5 days also contained perturbed structures, with $\{101\}$ spacings of 0.340 nm.

Electron diffraction from 3.0 wt.% aqueous SMS microemulsion		Electron diffraction from 7.5 wt.% aqueous SMS microemulsion	
Measured d-spacing (nm)	Assignment	Measured d-spacing (nm)	Assignment
0.172†	α-quartz $\{\bar{2}02\}$ at 0.167 nm	0.172†	α-quartz $\{\bar{2}02\}$ at 0.167 nm
		0.192	Silicon $\{220\}$ at 0.192 nm
0.197	α-quartz $\{02\bar{1}\}$ at 0.198 nm	0.200	α-quartz $\{02\bar{1}\}$ at 0.198 nm
0.311	Silicon $\{111\}$ at 0.314 nm	0.311	Silicon $\{111\}$ at 0.314 nm
		0.339†	α-quartz $\{\bar{1}01\}$ at 0.334 nm

thermodynamic stability and is consistent with the proposed model of the crystallisation being under thermodynamic control.

Table 5.6: $\langle 212\rangle$ zone axis of quartz.

Zone axis	d-spacings (nm)			Angles (°)		
$\langle 212\rangle$	0.198 $\{02\bar{1}\}$	0.198 $\{\bar{2}21\}$	0.167 $\{\bar{2}02\}$	72.6 $\angle\{02\bar{1}\}$ $\{\bar{2}21\}$	53.7 $\angle\{\bar{2}21\}$ $\{\bar{2}02\}$	53.7 $\angle\{02\bar{1}\}$ $\{\bar{2}02\}$

5.3.1.2 XRD

XRD analysis on the precipitated nanoquartz reveals a broad hump at $2\theta = 22^o$ which appears to be more consistent with amorphous silica than a crystalline phase (Figure 5.7). The breadth of the hump suggests the broadening arises not only from the small 1-5 nm crystallite size, but from variations in the lattice positions, i.e. the nanoquartz has a slightly perturbed bulk α-quartz structure and may contain surface defects. This is expected of crystals in this size range due to their large surface area contribution.

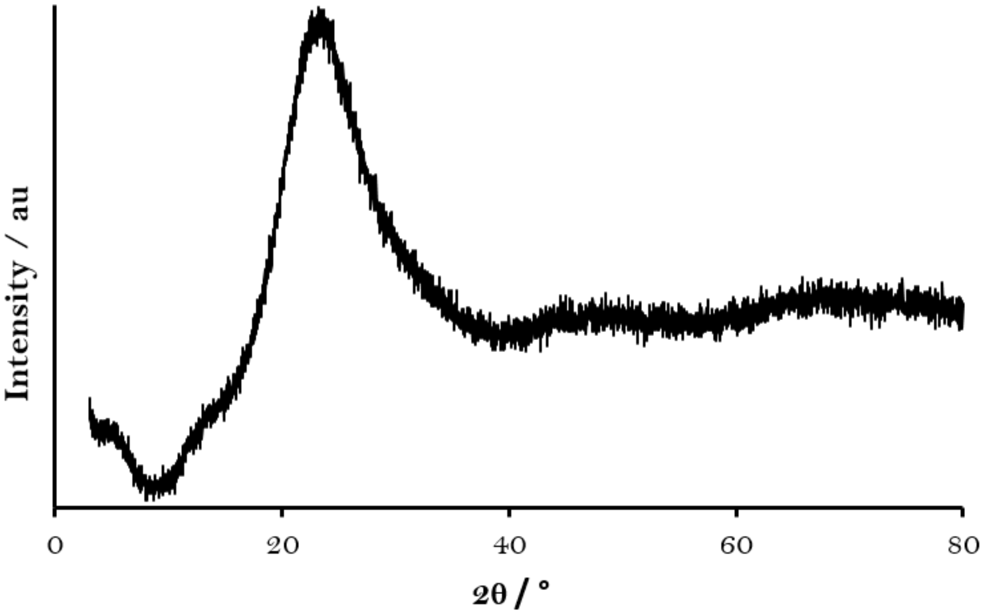

Figure 5.7: XRD pattern of the microemulsion-synthesised nanoquartz.

5.3.1.3 FTIR

FTIR analysis shows a significant Si–OH peak at 958 cm^{-1} along with prominent Si-O-Si peaks at 1064 cm^{-1}, 808 cm^{-1} and 448 cm^{-1} and a broad OH stretch centred at 3350 cm^{-1} (Figure 5.8). The major peaks at 1064 cm^{-1} (Si-O-Si antisymmetric stretch), 808 cm^{-1} (Si-O-Si symmetric stretch) and 448 cm^{-1} (rocking of oxygen atoms) correspond to silica structures containing Si-O-Si bonds exclusively. However, the signals at 958cm^{-1} (Si-OH Stretch) and 553cm^{-1} (Si-O bending in non-bridging Si-OH) are characteristic of

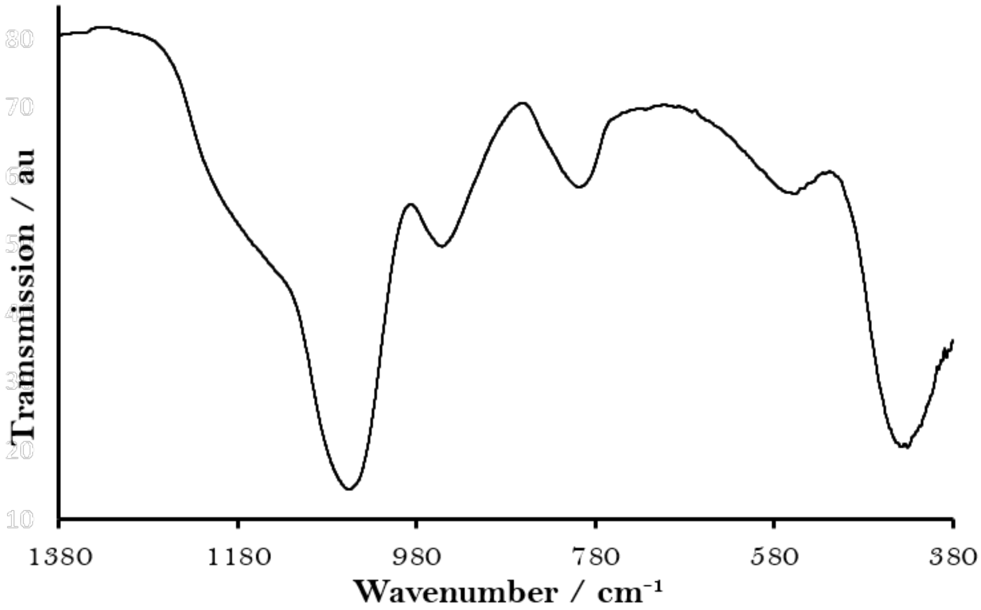

Figure 5.8: FTIR spectrum of the microemulsion-synthesised nanoquartz.

Si-OH bonding arising from the surface silanol groups expected in nanoquartz.

5.3.1.4 ssNMR

^{29}Si ssNMR revealed peaks at -92, -101 and -110 ppm attributable to 4.7% Q^2 $Si(OH)_2$, 35.3% Q^3 Si(OH), and 60.0% Q^4 Si (Figure 5.9). Nanocrystals of size 2.0±0.7 nm nm would be expected to have a large proportion of Q^3 Si(OH) sites due to their large surface to volume ratios, whilst the low proportion of Q^2 $Si(OH)_2$ is consistent with the nanocrystals having many surfaces along, or close to, low energy {101} planes. However, the breadth of all the ^{29}Si ssNMR peaks indicates variations in Si-O-Si angles arising from distortions of the bulk quartz structure. Note though, the Q^3 and Q^4 peaks are still narrower than that of the 7 nm fumed silica, which, being amorphous, has larger variations in the Si-O-Si angles.

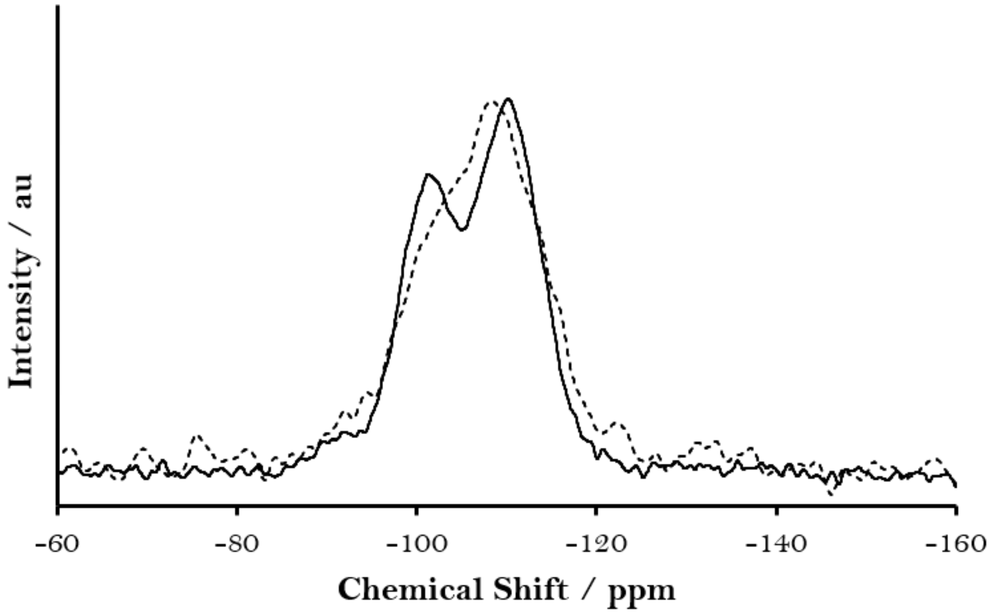

Figure 5.9: ssNMR spectra of the microemulsion-synthesised nanoquartz (solid line) and the 7 nm fumed silica (dashed line).

5.3.1.5 TGA

TGA analysis (Figure 5.8) reveals the nanocrystals lose 27% of their mass upon heating to 800 °C; 10% is due to surface water loss before 100 °C and the remaining 17% corresponds to removal of Si-OH bonds both on the nanocrystal surface and at any defect sites within the nanocrystals.

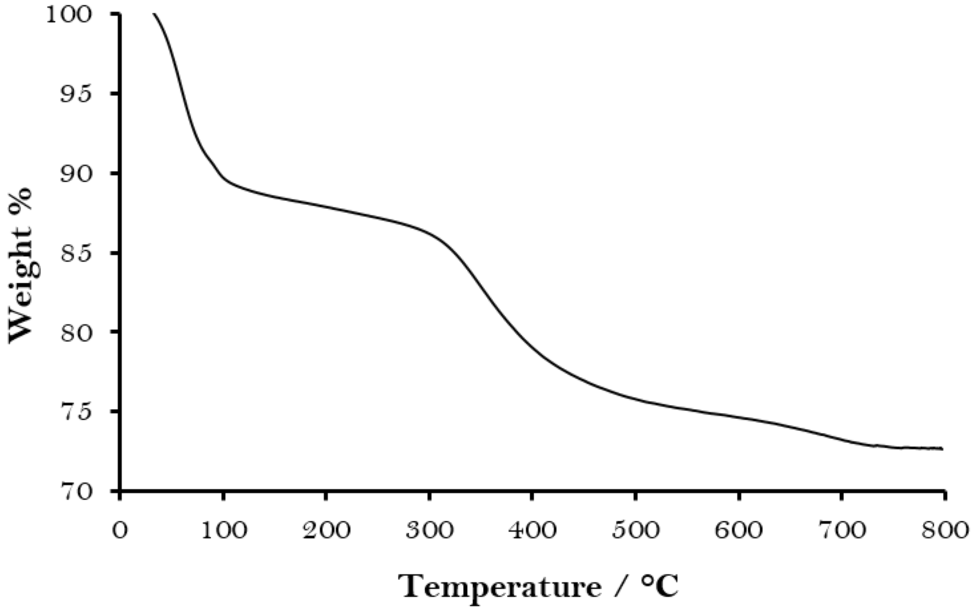

Figure 5.10: TGA analysis of the microemulsion-synthesised nanoquartz.

5.3.1.6 Conclusions

It is clear from the lattice fringes and electron diffraction in the TEM studies that quartz-like crystallinity is present in the microemulsion-derived nanoparticles, notwithstanding the perturbations. Moreover, the formation of these 1-5 nm particles from the 2.5 wt.% SMS solution, a solution undersaturated with respect to amorphous silica, definitively establishes these nanoparticles are less soluble than amorphous silica, despite their small size, indicating improved interior bonding over amorphous silica. Solubility tests in 0.1 M NaOH corroborated this (Section 5.3.3).

Addition of further aliquots (2 g) of 2.5 wt.% SMS solution to existing 400 g scale 2.5 wt.% SMS microemulsions produced more quartz nanocrystals. This process could be repeated up to ≈ 12 times before the nanocrystal yield reduced significantly, presumably because of the increasing alkalinity favouring dissolution over growth.

5.3.2 Hydrothermal Syntheses

Hydrothermal synthesis under mild conditions of 175 °C and autogenic pressure (nominally ≈ 9 bar) was used to anneal and grow the nanoquartz obtained from the microemulsions to obtain quartz nanocrystals of controllable size and structure.

5.3.2.1 TEM

TEM analysis shows there is slight growth of the nanocrystals as the crystals anneal (Figure 5.11). After 7 days, most of the crystals were still <5 nm in size; the mean size being 4.4 nm ± 0.9 nm; based on the sizing of 461 particles in TEM micrographs (Figure 5.12). This mean value is entirely consistent with a process involving only growth and annealing of existing particles (Section 5.3.2.4). Hence, the microemulsion-derived nanoquartz particles are indeed crystalline and can act as effective seeds.

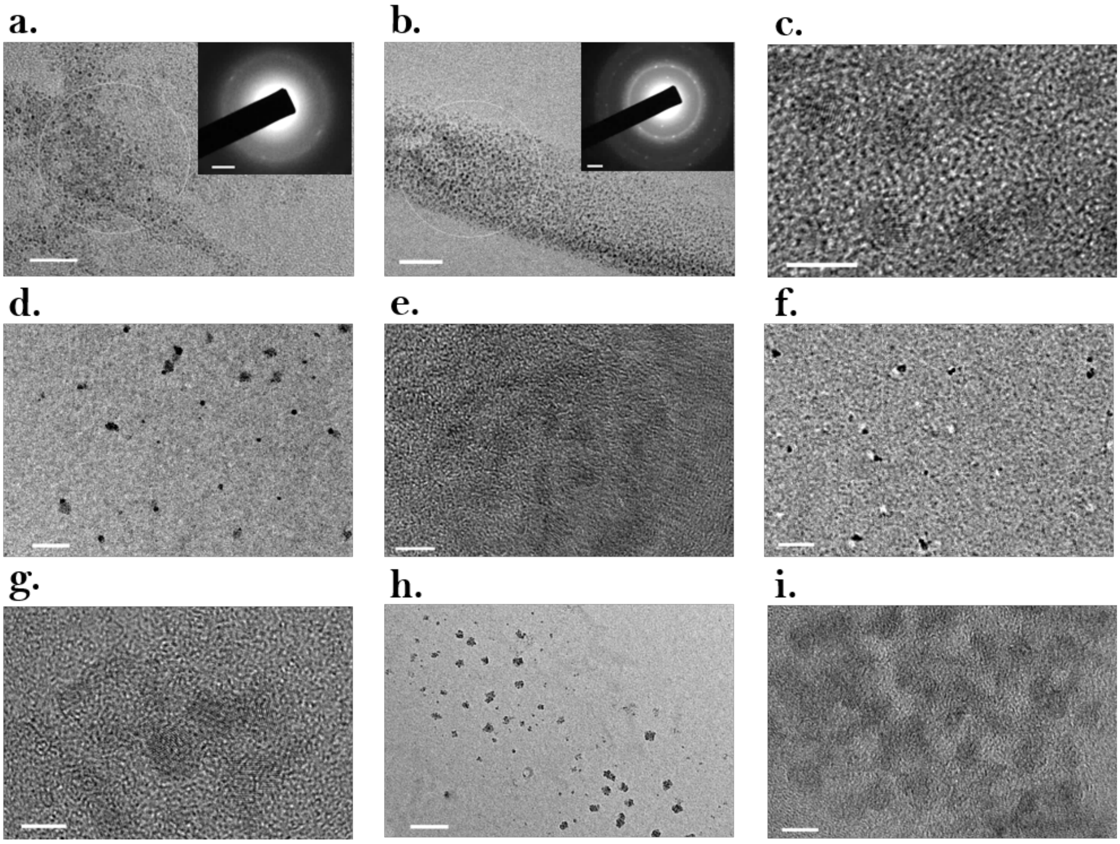

Figure 5.11: Representative TEM images of the nanoquartz. **a.** Microemulsion-synthesised nanoquartz. **b.**, **c.**. 2-day hydrothermal product. **d.**, **e.** 5-day hydrothermal product. **f.**, **g.** 6-day hydrothermal product. **h.**, **i.** 7-day hydrothermal product. The scale bars are 50 nm in **a.** and **b.**, 5 nm in **c.**, **e.**, **g.** and **i.**, 100 nm in **d.**, **f.** and **h.**, and 2 nm^{-1} in the insets to **a.** and **b.** The insets to **a.** and **b.** show the electron diffraction pattern from the circled regions. The diffraction ring in **a.** corresponds to 0.2 nm, consistent with the electron diffraction patterns shown in (Figure 5.5). The diffraction pattern in **b.** has a ring pattern commensurate with quartz and inner hexagonal diffraction spots that index (003) on a doubled quartz cell, consistent with a slightly perturbed quartz structure.

Note that aggregation of the nanocrystals into larger ≈ 20–70 nm aggregates was common after 2 days of hydrothermal treatment. Performing the hydrothermal experiments under stirring would be expected to reduce the number of these aggregates. The (101) XRD full width at half maximum (FWHM) peak breadth for the 5-7 day hydrothermal

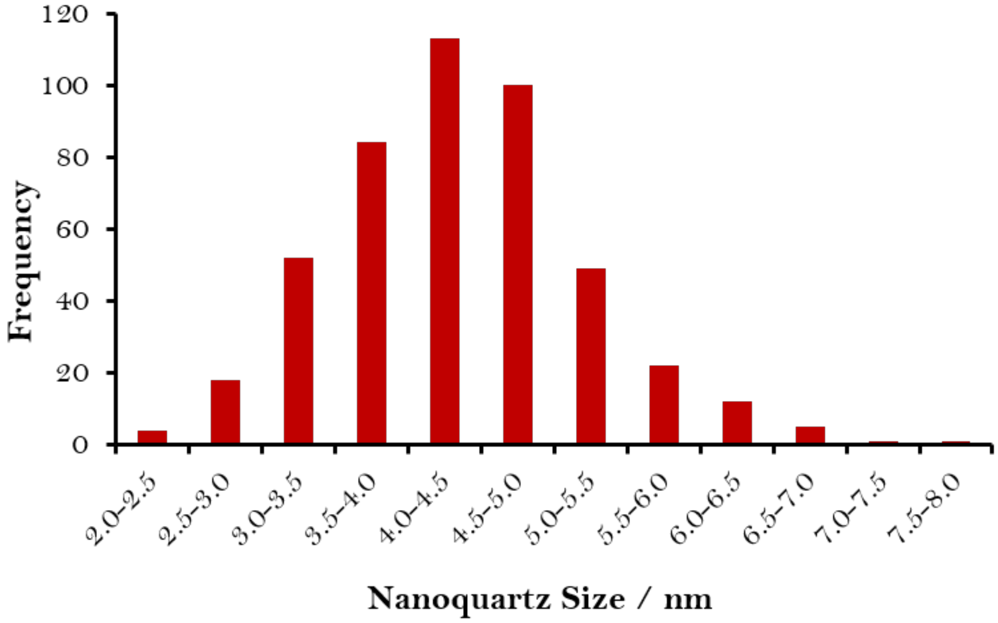

Figure 5.12: Histogram showing the particle size distribution for the 7-day hydrothermal product obtained by sizing 461 particles from TEM micrographs.

products gave crystallite sizes $\approx$ 50 nm based on the Scherrer equation (Appendix B). This is significantly larger than the 4.4 nm mean crystallite size obtained from TEM images; rather it is more consistent with the observed 20-70 nm crystal aggregate size. This is attributed to a substantial degree of scattering from aggregates that have either undergone oriented attachment or have intergrown and then annealed to largely remove the grain boundaries. HREM images reveal aggregates of size $\approx$ 40 nm containing many $\approx$ 5 nm crystals (Figure 5.13). The $\approx$ 5 nm crystals have approximately the same crystallographic orientation, as shown by their similar FFTs, and so the entire aggregate acts more like a coherent scattering domain than a collection of individual nanocrystals. Annealing of grain boundaries would occur concomitantly with the observed increase in crystal perfection, so this finding is not unexpected. In addition, the nanocrystals typically lie on the same zone axis $\langle 212 \rangle$ owing to the expression of stable $\{101\}$ faces, so the misalignment of neighbouring crystals will not, in any case, be as significant as in randomly orientated nanocrystals. This, combined with extended times of up to 7-days, allows the original grain boundaries to almost disappear.

It can be stated with confidence that the structure of non-aggregated and less-aggregated particles that remain dispersed match those of the larger sedimented aggregates, from the following:

1. Samples enriched with isolated particles were obtained by evaporating the supernatants acquired after centrifuging at 3316 G for 8 minutes the aqueous dispersions

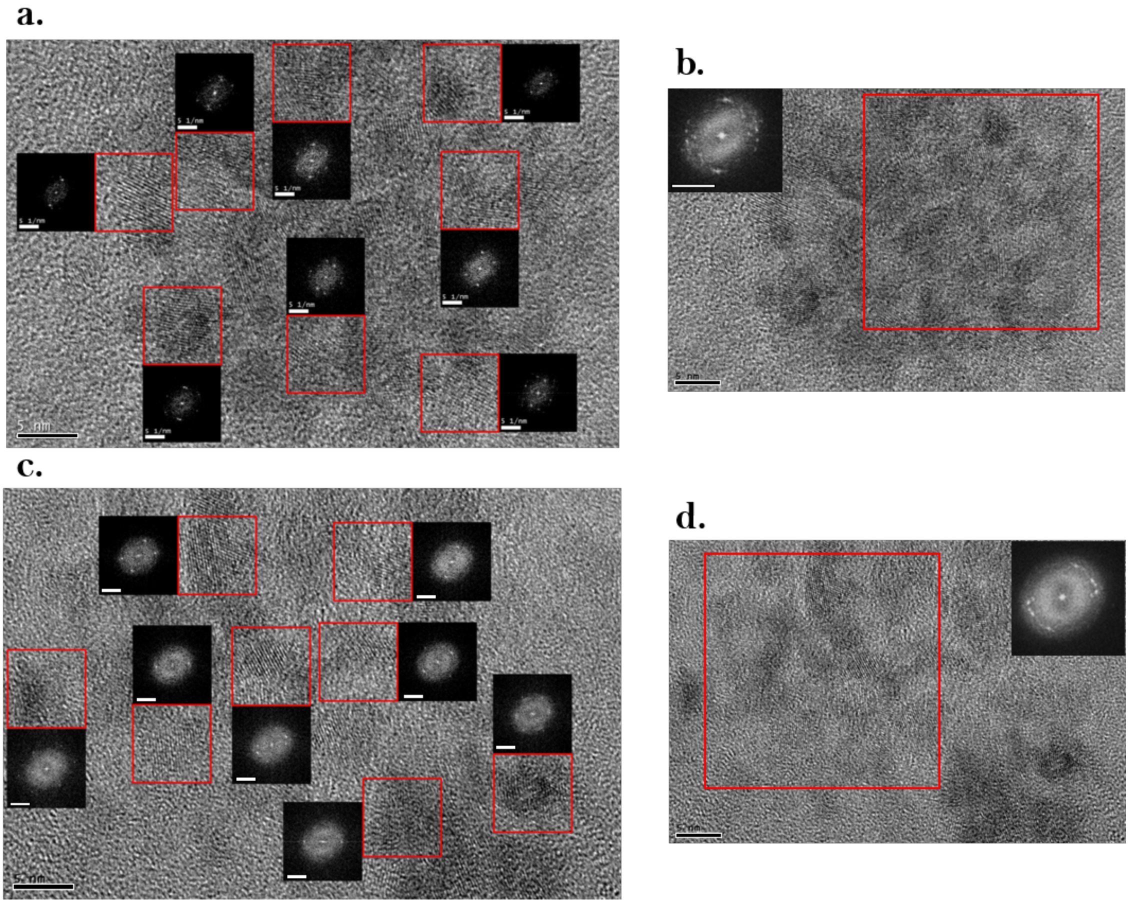

Figure 5.13: TEM data of two 7-day hydrothermal nanoquartz aggregates of size ≈40 nm. Annealing of the grain boundaries has produced nanocrystals that show similar orientation, close to the [001] zone axis. Consequently, (110) diffraction spots are prominent in the FFTs and have similar orientation. **a.** HREM image of a ≈40 nm aggregate containing several 5 nm nanoquartz particles. **c.** HREM of a different ≈40 nm aggregate containing several 5 nm nanoquartz particles. The red boxes in **a.** and **c.** show selected nanocrystals with their accompanying FFTs alongside. **b.** HREM image of the same aggregate shown in **a.** **d.** HREM image of the same aggregate shown in **c**. The larger red boxes in **b.** and **d.** enclose several nanocrystals with the insets showing the associated FFTs. The dominant (110) peak positions are evident in theses FFTs. The scale bars are 5 nm in the HREM images and 5 nm^{-1} in the FFTs.

of the 5-7 day hydrothermal nanoquartz. The supernatants contained between 4-12% of the original nanoquartz by mass. This quantity was insufficient for XRD analysis but allowed FTIR spectra to be obtained (Figure 5.14). The FTIR spectra of these samples, enriched with isolated particles, matched those of corresponding non-centrifuged nanoquartz samples.

2. XRD was performed on a 7-day hydrothermal powder obtained from an evaporated acetone dispersion that had been bath sonicated for 1 hour and then centrifuged at 29 G for 1 minute, resulting in 60% by mass of the sample sedimenting (Figure 5.15). This XRD pattern, characteristic of smaller aggregates and isolated particles, gave

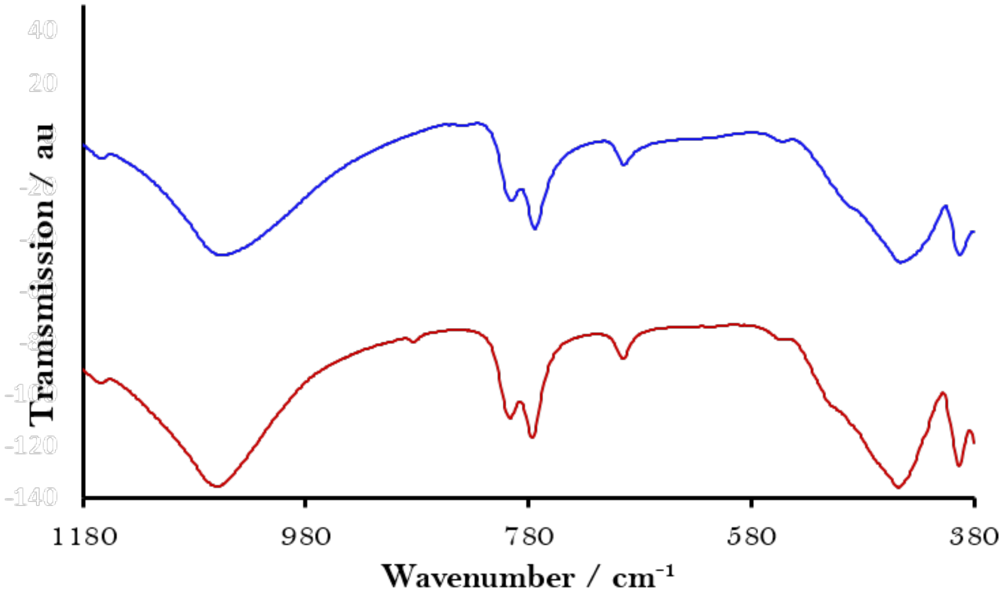

Figure 5.14: Representative FTIR data of the isolated nanoquartz particles. FTIR analysis of the nanoquartz particles isolated from the 7-day hydrothermal product by centrifugation (dark blue line), and the 7-day hydrothermal product (red line).

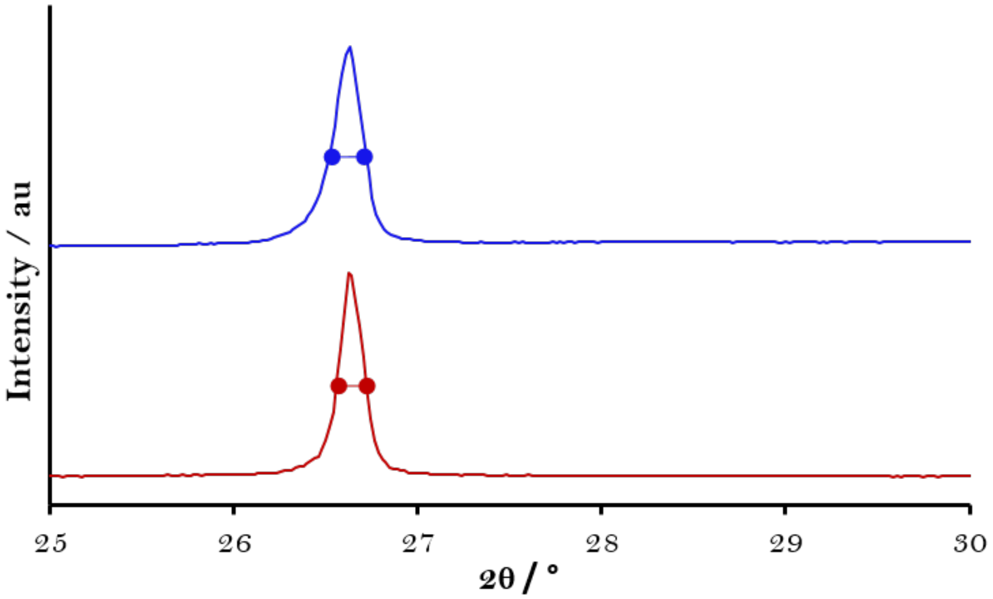

Figure 5.15: XRD analysis of the nanoquartz particles isolated from the 7-day hydrothermal product by centrifugation (dark blue line), and the 7-day hydrothermal product (red line). For the isolated particles, the FWHM for the dominant (101) quartz peak observed at $2\theta = 26.68$ has widened by a factor of 1.57.

the same XRD pattern as the corresponding non-centrifuged nanoquartz sample except that the peaks had broadened.

5.3.2.2 XRD

After 1 day of hydrothermal treatment, sharper peaks appeared in the XRD pattern of the extracted nanocrystals (Figure 5.16). However, the peaks at θ values of 26.0°, 27.9°,

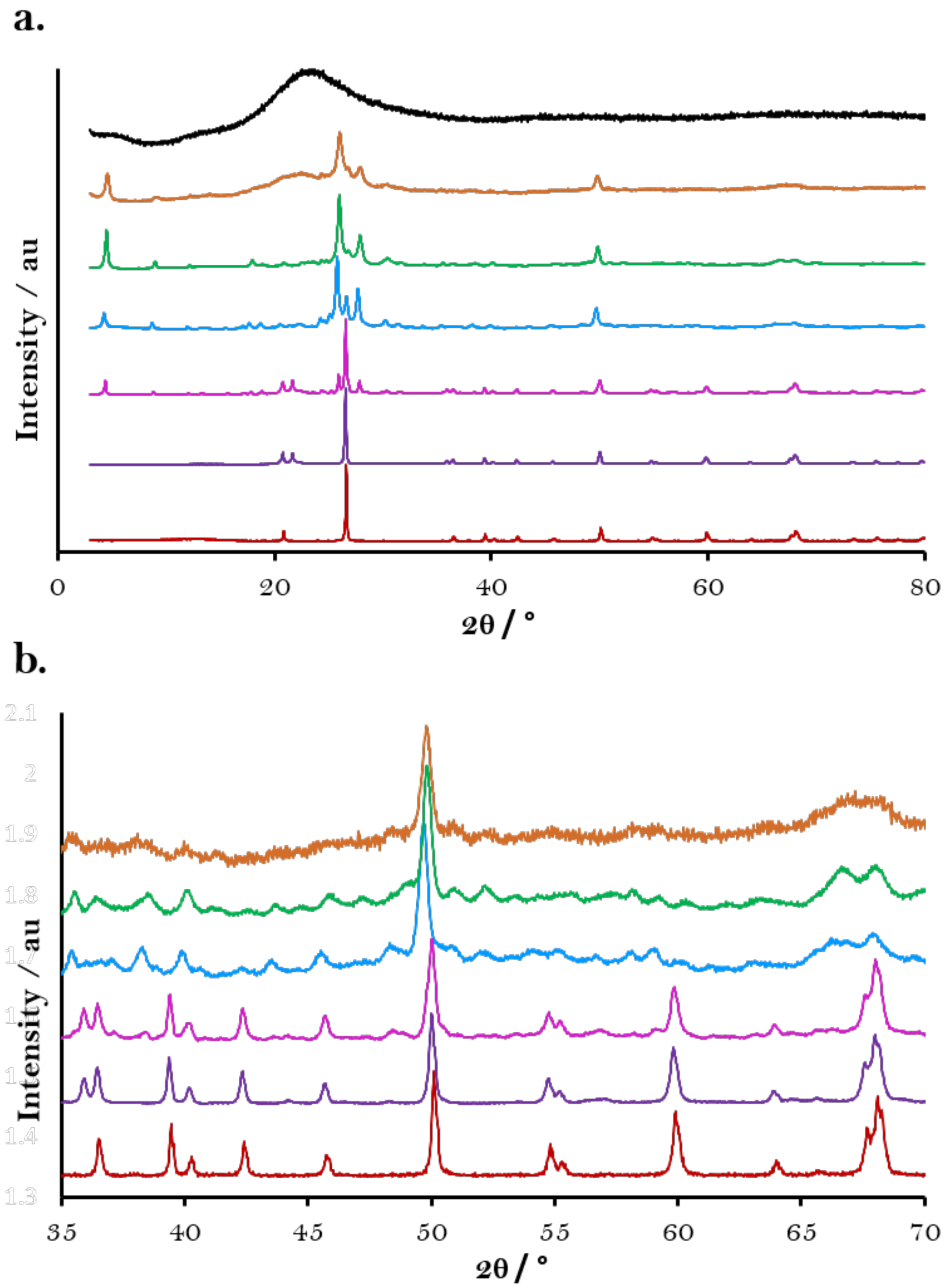

Figure 5.16: XRD analysis of the microemulsion-synthesised nanoquartz (black lines) and the products from 1-day (brown lines), 2-day (green lines), 3-day (blue lines), 5-day (pink lines), 6-day (purple lines), and 7-day (red lines) hydrothermal synthesis at 175 °C. **b.** Provides a more-detailed view of the 1-7 hydrothermal XRD data between $2\theta = 35 - 70^o$, to better show the weaker peaks.

and 30.4° (corresponding to d-spacings of 0.34 nm, 0.32, and 0.29 nm, respectively) are more consistent with the moganite phase of silica rather than a bulk α-quartz structure.[256] Quartz has its main (101) diffraction peak at $2\theta = 26.7^o$ (d = 0.33 nm) and has no other peaks in the $2\theta =$ 26–35^o region. Moganite consists of alternating (101) layers of left and right-handed α-quartz helices, and therefore represents the extreme form of quartz Brazil twinning occurring on the unit cell length-scale.[256] The low angle peak at $2\theta = 4.6^o$ (d = 2.1 nm) and its second order peak are consistent with a quartz supercell structure containing 6 α-quartz (101) planes. Accordingly, this suggests that the nanocrystals at this stage contained both left and right-handed α-quartz helices, leading to a perturbed α-quartz supercell structure with features similar to moganite. It is likely that the left and right-handed α-quartz helices were also present in the microemulsion-synthesized nanoquartz given the broadness of its XRD peak.

Note that the location of the low angle XRD peak at $2\theta = 4.6^o$ and its second order observed from 1-5 days correspond to low angle peaks attributed to the silica polymorph named "phase X2" by Schäf *et al* in their low temperature (125-220 °C), high pressure (103 bar) hydrothermal synthesis of quartz, although their X2 phase had significantly broader XRD peaks.[257] It is not believed that there is a distinct X2-type phase here that then dissolves as α-quartz nucleates. Rather, it is considered that quartz nucleation under ambient conditions, followed by nanoquartz growth at 175 °C, proceeds through a defect-containing and perturbed α-quartz structure that gradually perfects, as the defective sites tend to anneal and dissolve and are replaced with the bulk α-quartz structure.

After 2 days of hydrothermal treatment, pre-existing peaks sharpen slightly and additional weak, relatively sharp XRD peaks appear, again consistent with a perturbed quartz supercell that contains both left and right-handed α-quartz helices. An emerging peak at $2\theta = 26.7^o$ signals that the bulk α-quartz structure is now developing. From 3-6 days, there is an increase in the XRD peaks associated with the bulk α-quartz structure, whilst the peaks due to the perturbed supercell are decreasing. After 7 days of hydrothermal treatment, only the bulk α-quartz structure is evident.

5.3.2.3 FTIR and ssNMR

FTIR and ^{29}Si ssNMR fully corroborated the XRD findings. FTIR peaks associated with defective quartz and moganite at $\approx$ 660, 615, 575, and 545 cm^{-1} are apparent from 1-5 days (Figure 5.17).[258] The α-quartz doublet at 780 and 800 cm^{-1} and the so-called "crystallinity peak" at 700 cm^{-1} emerges at 2 days. At 6 and 7 days, only the bulk α-quartz spectrum with its prominent doublet and crystallinity peak is evident.

The ^{29}Si ssNMR spectrum after 1 day shows significant narrowing of the Q^3 Si-OH peak at -100 ppm and the Q^4 Si peak has split into three components at -108, -111, and -113; the peak at -108 ppm represents the emerging bulk α-quartz structure, and the -111

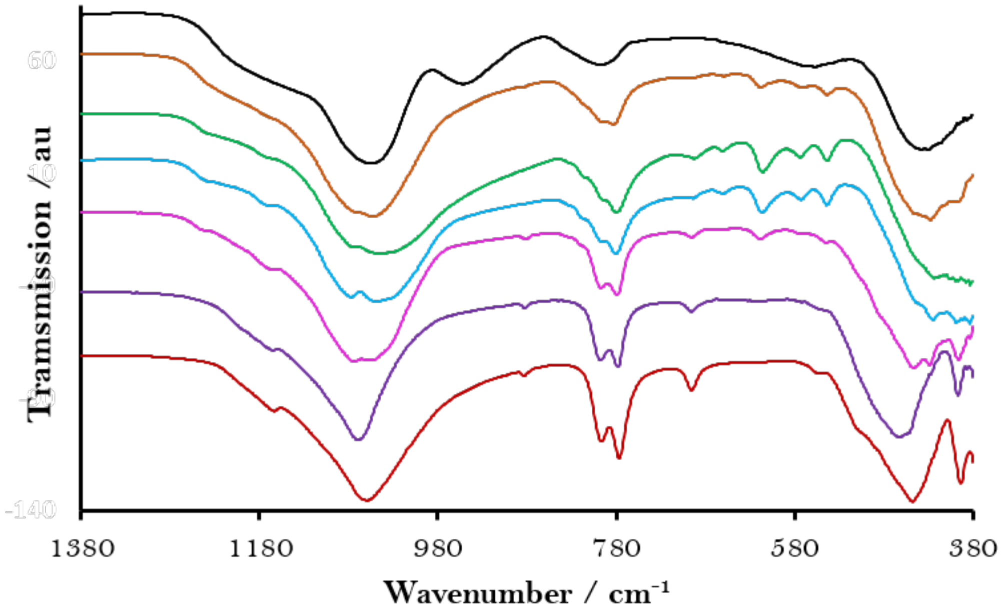

Figure 5.17: FTIR analysis of the microemulsion-synthesised nanoquartz (black line) and the products from 1-day (brown line), 2-day (green line), 3-day (blue line), 5-day (pink line), 6-day (purple line), and 7-day (red line) hydrothermal synthesis at 175 °C.

and -113 ppm peaks, the perturbed α-quartz structure (Figure 5.18). In comparison, the

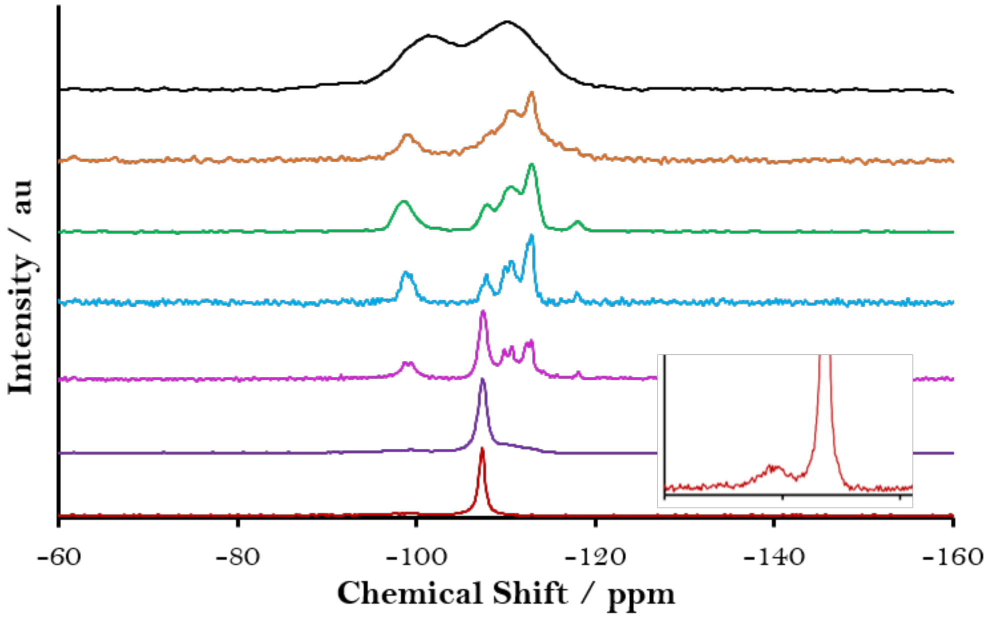

Figure 5.18: ssNMR analysis of the microemulsion-synthesised nanoquartz (black line) and the products from 1-day (brown line), 2-day (green line), 3-day (blue line), 5-day (pink line), 6-day (purple line), and 7-day (red line) hydrothermal synthesis at 175 °C. The inset shows an expanded view of the 7-day ^{29}Si ssNMR spectrum, revealing the small, broad Q^3 Si-OH peak at -99 ppm. Q^4 Si-O peaks appear at -107 to -118 ppm, Q^3 Si-OH peaks at -99 to -101 ppm and Q^2 Si(OH)$_2$ peaks at -92 ppm.

^{29}Si ssNMR peaks for moganite occur at -106 and -110 ppm.[259] There is no longer a Q^2 Si-(OH)$_2$ peak in the 1-day spectrum. At 2 days, a sharper Q^3 Si-OH peak at -99 ppm and 4 sharper Q^4 Si peaks at -108, -111, -113, and -118 ppm are seen. The small -118 ppm peak is most likely due to a minority of highly-strained 4-membered silica rings. From 3-5 days, the peaks sharpen and the α-quartz signal increases in intensity and shifts slightly to -107 ppm. The 6-day sample contains only 1 sharp bulk α-quartz peak at -107 ppm, together with a weak broad Q^3 Si-OH peak at -98 ppm mainly due to surface silicons, and a weak broad Q^4 Si peak at -109 ppm reflecting the remaining perturbations to the bulk quartz structure. At 7 days, only the sharp -107 ppm bulk α-quartz signal is evident, showing that the nanocrystals had (largely) annealed. Note, however, there remains a small, broad Q^3 Si-OH peak at -99 ppm after 7 days (Figure 5.18 inset), which accounts for 7.9% of the silicon atoms, consistent with their nm-size.

5.3.2.4 Hydrothermal Synthesis Yields

The measured yield of the hydrothermal products ranged from 144.2 mg for the 1-day hydrothermal experiment to 232.3 mg for the 7-day run; these yields being consistent with their relative solubilities. Furthermore, the relative size increase of the microemulsion seeds from 2.0 ± 0.7 nm to 4.4 ± 0.9 nm for the 7-day product is also consistent with these yields. In particular, TGA establishes $\approx$ 10% water in the microemulsion seeds compared to $\approx$ 2% for the 7-day hydrothermal product (Figure 5.19). Excluding this surface water gives a SiO_2 mass increase from 51.7 to 227.7 mg in 7 days, i.e. by a factor

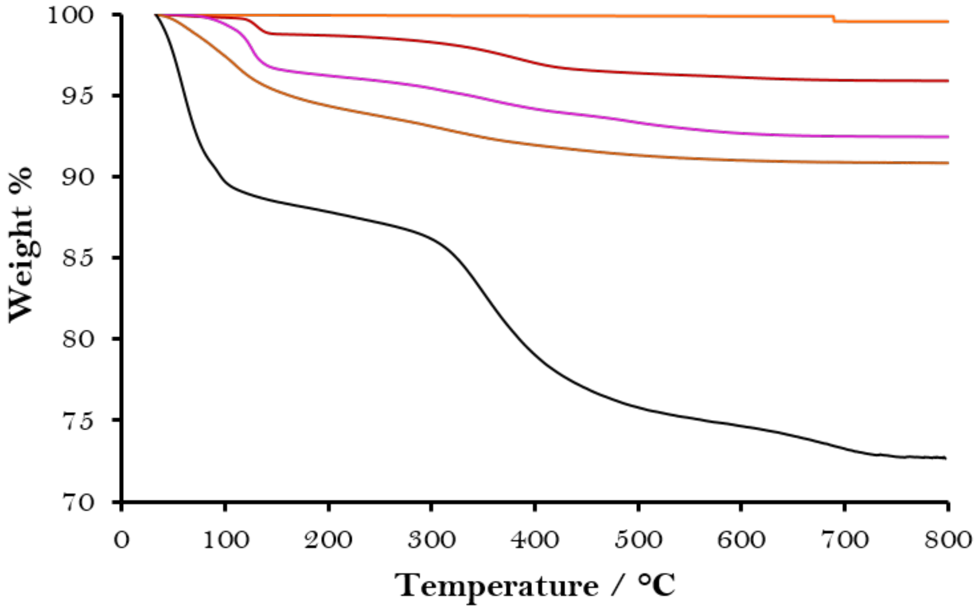

Figure 5.19: TGA data obtained from the nanoquartz. Micron-sized quartz standard (orange line), microemulsion-synthesised nanoquartz (black line), and the 1-day (brown line), 5-day (pink line), and 7-day (blue line) products from the hydrothermal synthesis at 175 °C.

of 4.4. The particle size should increase by $\approx 4.41/3 \approx 1.6$ for isotropic 3-D growth and by $\approx 4.41/2 \approx 2.1$ for mainly 2-D growth. These values are in good agreement with our observed mean size increase of 2.2, particularly given that after 7 days, Ostwald ripening would have led to dissolution of the smallest crystals and growth of the largest. This provides further proof that the nanoquartz hydrothermal product occurs *via* annealing and growth of the microemulsion-derived nanoquartz seeds; a mechanism reliant on new particle nucleation and growth is certainly not occurring.

5.3.2.5 Quartz Nucleation and Growth at Low Temperature

It is well-known that the critical nucleus can possess a structure that differs from the bulk crystal phase; the structures that minimise the free energy on the nm-scale and bulk scale vary (sometimes markedly) due to the large surface contributions to the former. It is considered that this happens here. However, the perturbations to the bulk quartz structure are relatively minor once the nanocrystals reach >2 nm, given the electron diffraction patterns can be indexed using the bulk quartz structure and major XRD peaks of the product remain at $2\theta = 26.0$-26.7°, 49.7-50.2°, and 67.8-67.9° throughout the hydrothermal 1-7 day experiments (Figure 5.16).

A concomitant quartz nucleation-nanocrystal dissolution mechanism can be categorically ruled out because the nucleation rate under the hydrothermal conditions proceeds at too low a rate compared to crystal growth. A low quartz nucleation rate would result in the final product mainly consisting of fewer, but larger (μm-sized) quartz particles as previously observed.[233–235] This is borne out by control hydrothermal experiments at 175 °C and autogenic pressure using 7 nm fumed silica rather than the microemulsion nanoquartz seeds (Section 5.3.3). In these control systems, the majority of the quartz crystals were μm-sized, even after 2 days (Figure 5.21). These results highlight the effectiveness of this two-stage microemulsion-hydrothermal synthesis strategy in obtaining selective crystallisation of nanoquartz of size range <10 nm.

5.3.3 Control Hydrothermal Syntheses

In our control experiments (using fumed silica as seeds), after 1 day at 175 °C and autogenic pressure (nominally ≈ 9 bar), a predominantly amorphous product was obtained due to the excess fumed silica. However, the XRD of this product did contain some weak sharper peaks showing some limited nucleation had occurred (Figure 5.20). As expected, the FTIR and ^{29}Si ssNMR spectra of this 1-day control were similar to that of the 7 nm fumed silica, though TEM analysis confirmed the presence of some tiny <5 nm nanocrystals amongst this amorphous product (Figure 5.21). After 2 days, the relatively low nucleation rate meant that these nanocrystals had grown to μm-sized crystals, whilst nucleation events in the interim had led to some smaller nm-sized crystals; hence a polydisperse product was obtained. The XRD, FTIR and ^{29}Si ssNMR data revealed that the crystals possessed a similar perturbed bulk quartz structure to our 1–2 day hydrothermal nanoquartz crystals.

The perturbed bulk structure was still evident in the product from the 5-day hydrothermal control experiment, with most crystals now being >2 μm in size. This demonstrated that, as expected, the growth process was similar to that of our nanoquartz-seeded hydrothermal experiments, albeit the growth was somewhat delayed due to the nucleation time-lag, and this low nucleation rate then meant that fewer but much larger, μm-sized crystals developed. The much larger crystal sizes resulted in reduced solubilities compared to the analogous nanoquartz-seeded experiments after 6 and 7 days (Table 5.7).

After 7 days in the control experiments, the bulk quartz crystal structure was observed using XRD, FTIR, and ^{29}Si ssNMR but by this stage, most crystals were ≥ 3 μm in size (Figure 5.20, 5.21) and had a solubility 61% lower than the 7-day hydrothermal nanoquartz-seeded sample.

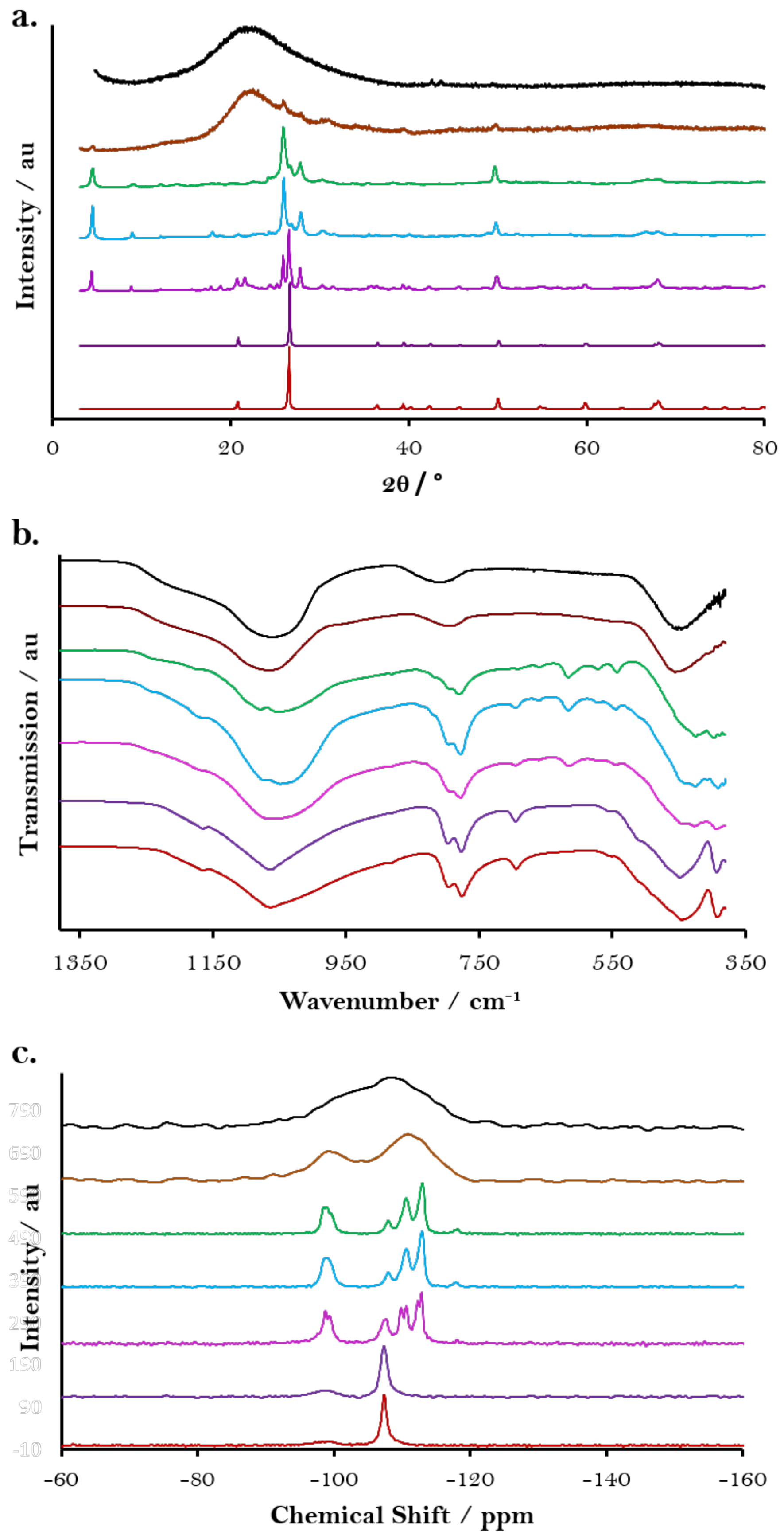

Figure 5.20: Analysis of the 7 nm fumed silica and the control hydrothermal products. **a.** XRD, **b.** FTIR, and **c.** ^{29}Si ssNMR of the 7 nm fumed silica (black lines) and the products from 1-day (brown lines), 2-day (green lines), 3-day (blue lines), 5-day (pink lines), 6-day (purple lines) and 7-day (blue lines) control hydrothermal synthesis at 175 °C.

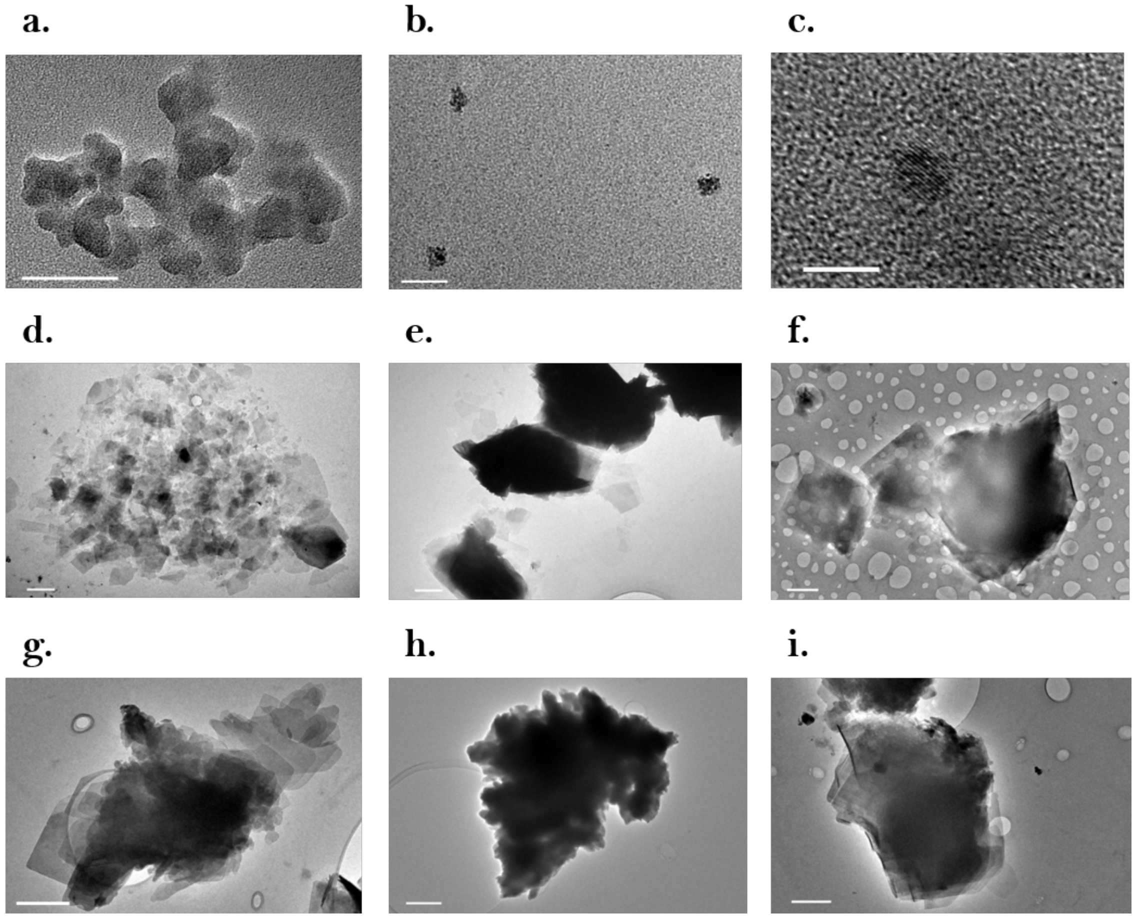

Figure 5.21: Representative TEM images of fumed silica and product from control experiments. **a.** 7 nm fumed silica and **b**-**i.** the product obtained from the control fumed silica seeded hydrothermal syntheses. **b.**, **c.** Control 1-day hydrothermal product containing mainly **b.** fumed silica and **c.** rarer quartz nanocrystals; **d.**, **e.** control 2-day hydrothermal product; **f.** control 3-day hydrothermal product; **g.** control 5-day hydrothermal product; **h.** control 6-day hydrothermal product and **i.** control 7-day hydrothermal product. The scale bars are 50 nm in **a.** and **b.**; 5 nm in **c.** and 1 μm in **d**-**i**.

Table 5.7: Solubility of the nanoquartz in 0.1 M NaOH at 90 °C. 45.3 mg of the nanoquartz was added to 5.5 ml of 0.1 M NaOH and the solubilities were determined after heating to 90 °C for 24 days. †These solubility values represent an upper bound for the particles size, since as the particles start to dissolve, their solubility will increase further due to their reduced size. A lower and slightly more accurate solubility value for the particle sizes would be obtained by adding a large excess of particles to the 0.1 M NaOH, however there were insufficient particles for this.

Nanoquartz Sample	Solubility† in 0.1 M NaOH at 90 °C after 24 days (mg/ml)
Microemulsion-Synthesised	8.02
1-day Hydrothermal Synthesis	5.50
2-day Hydrothermal Synthesis	4.63
3-day Hydrothermal Synthesis	3.47
5-day Hydrothermal Synthesis	2.56
6-day Hydrothermal Synthesis	2.05
7-day Hydrothermal Synthesis	0.89
7 nm Fumed silica	8.24
1-day Hydrothermal Control	7.95
2-day Hydrothermal Control	4.09
3-day Hydrothermal Control	3.93
5-day Hydrothermal Control	2.60
6-day Hydrothermal Control	0.96
7-day Hydrothermal Control	0.35
Quartz Standard with Mean Crystal Size ≈ 50 μm	0.02

5.3.4 Catalyst Performance

Amorphous silica is known to catalyse the formation of β-enaminones, an important class of synthons for the production of various heterocyclic and pharmaceutical compounds. The effect of fumed silica and quartz nanoparticles on the reaction between acetylacetone and aniline to form the β-enaminone, 4-(phenylamino)-pent-3-en-2-one was investigated (Table 5.8).[260,261] Experiments showing standard deviations had been repeated at least twice; values without standard deviations were from single experiments. The 7 nm fumed silica and no catalyst experiments were performed in each batch of experiments to ensure reproducibility of results. Note that acetylacetone exists as enol and keto tautomeric forms in equilibrium, with the ratio of these two forms essentially unchanged within experimental error (enol:keto approximately 9:2, see peaks H and J in Figure 5.22) throughout the experiments. The 7 nm fumed silica was an effective catalyst, in agreement with previous studies in which the catalytic ability was linked to absorption of acetylacetone onto silanol sites.[260,261] This facilitates the nucleophilic attack of the amine to generate the imine intermediate followed by tautomerization to the corresponding β-enaminone. The

Table 5.8: Product yields for the reaction between acetylacetone and aniline

Silica phase added as a potential catalyst	% Yield of product, 4-(phenylamino)-pent-3-en-2-one		
	4 h	5 h	6 h
7 nm Fumed Silica	70±1	76±2	81±2
200-300 nm Fumed Silica	59	67	74
Microemulsion-Synthesised Nanoquartz	45±5	54±4	60±4
Microemulsion-Synthesized Nanoquartz, Excess (100 μl) SB Surfactant Mixture	47.4	54.9	61.3
Quartz Standard with Mean Crystal Size ≈350 μm	31.9	42.4	53.8
None	31±2	42±4	52±5
1-day Hydrothermal Nanoquartz	8±1	12±4	16±6
5-day Hydrothermal Nanoquartz	11±4	15±4	19±6
6-day Hydrothermal Nanoquartz	18±1	25±1	32±1
7-day Hydrothermal Nanoquartz	3.9±0.1	5.2±0.2	7.1±0.5
7-day Hydrothermal Nanoquartz, 300% excess aniline	10.5	11.3	13.1
7-day Hydrothermal Nanoquartz, 300% excess acetylacetone	25.4	40.5	53.2
Control 1-day Hydrothermal Quartz	9.2	13.5	17.6
Control 5-day Hydrothermal Quartz	12.9	19.3	26.1
Control 6-day Hydrothermal Quartz	15.8	26.5	38.3
Control 7-day Hydrothermal Quartz	24.7	36	47.6

microemulsion-synthesised nanoquartz, with its perturbed quartz structure, only weakly catalysed the reaction. This is surprising, given it contained comparable amounts of silanol groups to the 7 nm fumed silica. Furthermore, a strong inhibitory effect was observed for the hydrothermal nanoquartz crystals, with the annealed 7-day hydrothermal nanoquartz causing extreme inhibition. The precise origin of this inhibition requires further study and residual alkalinity (at a level too low to impact the 9:2 enol:keto ratio) in the hydrothermal quartz samples may play a part. Nevertheless, given that reaction rates for the 7-day hydrothermal nanoquartz system are increased significantly when excess acetylacetone is used, but markedly less so with excess aniline, this suggests adsorption of the acetylacetone onto the annealed nanoquartz occurs in a manner discordant with subsequent β-enaminone formation. In comparison, the control 5–7 day hydrothermal quartz

a.

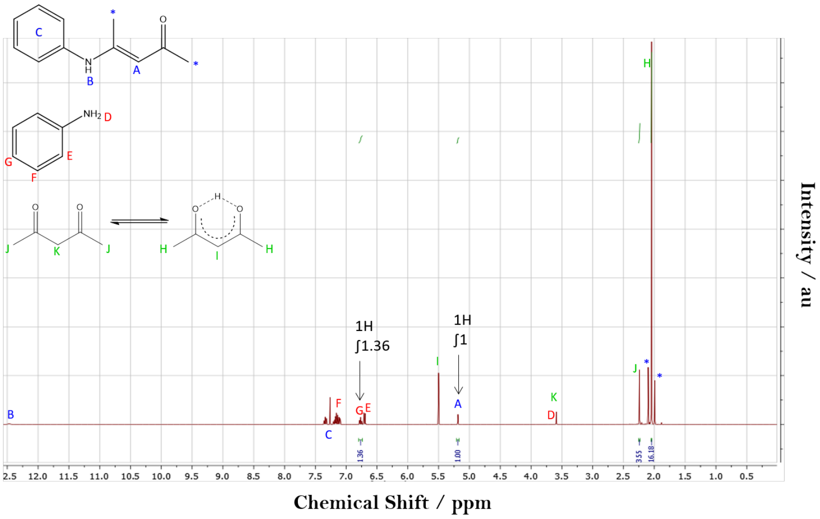

No Catalyst 5 hours. Product Yield of (1/(1+1.36))x100% = **42.3 %**.

b.

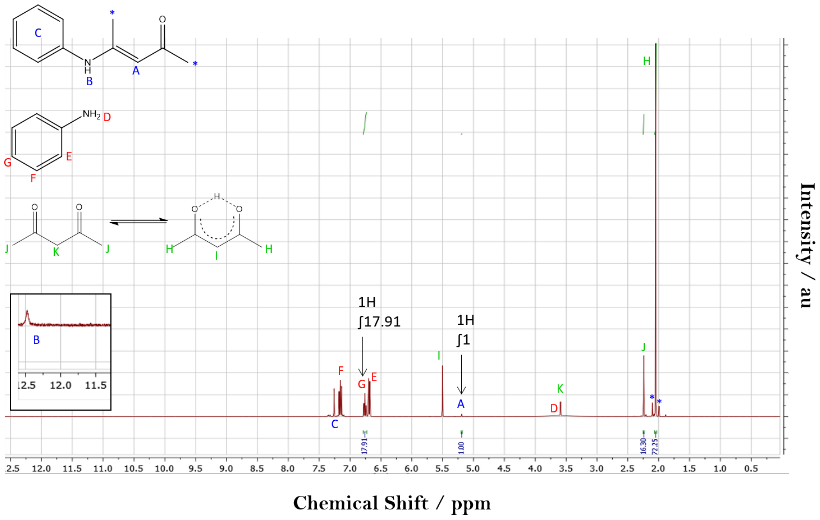

7 Day Catalyst 5 hours. Product Yield of (1/(1+17.91))x100% = **5.29 %**.

c.

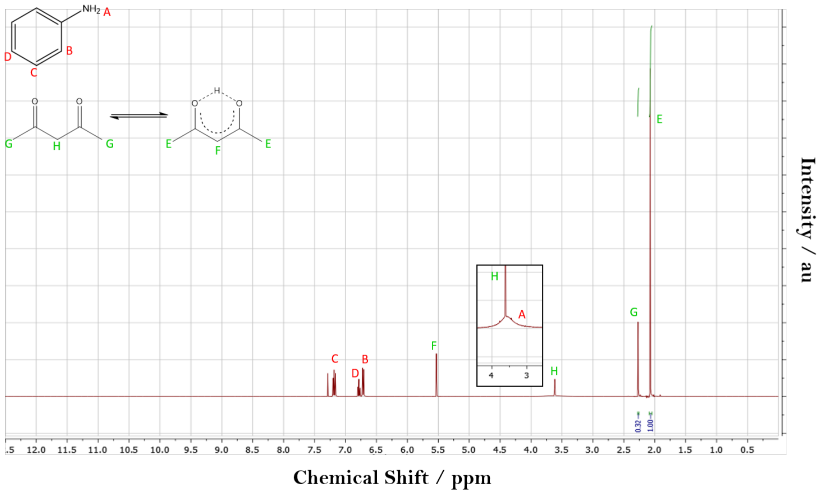

Mixed Reagents at Time = 0. **No Product**.

Figure 5.22: Representative ^{1}H NMR data from the catalyst reaction. ^{1}H NMR data of **a.** no catalyst reaction mixture after 5 hours, **b.** 7-day hydrothermal nanoquartz reaction mixture after 5 hours and **c.** mixed reactants at zero hours.

crystals had a more limited inhibitory effect, owing to their μm size and reduced surface area. Accordingly, the catalyst performance findings are consistent with inhibition increasing as the perturbed nanoquartz structure anneals to that of α-quartz. This finding emphasizes the need for careful control over the synthesis of nanoparticulate catalysts to ensure effective performance.

5.4 Discussion

α-Quartz nanocrystals have been produced in 14 days at ambient temperature by using a microemulsion-mediated methodology. Previous studies have demonstrated the ability of microemulsions to elicit thermodynamic control over crystallisation for organic molecular crystals,[123–125,202,251] but this is the first time thermodynamic control and subsequent extraction of crystals has been achieved for a 3-D giant covalent structure. The theory underlying this thermodynamic control has been detailed previously (Section 2.3). Factors that favour silica dissolution events over silica formation, particularly low SMS concentrations and high alkalinity, would be expected to induce thermodynamic control and thus produce α-quartz nanocrystals. The striking difference between organic molecule crystallisation in microemulsions and the system presented here is that the silica nanoparticle growth and dissolution occur *via* the creation and breaking of covalent bonds rather than weaker intermolecular interactions. Adventitiously, the required Si-O bond breakage and formation is facilitated by the large fluctuations in alkalinity in the droplets as they exchange hydroxyl and (much more rarely) hydronium ions during energetic droplet collisions that produce transient dimers (See Appendix C). The large fluctuations in alkalinity result in repeated nanocrystal growth and dissolution steps, aiding thermodynamic control. Hence α-quartz nanocrystals are selectively obtained. Note that the sodium cations and effects arising from water confinement may also impact on the nanocrystal growth and dissolution steps; elucidating the significance of these factors requires further study.

It is well-known that ≈2 nm amorphous silica particles can be formed by acidifying high pH silica solutions.[262–264] In stark contrast, the microemulsion methodology presented here enables the crystallisation of 1-5 nm α-quartz under ambient conditions from low concentration SMS solutions without the need for added acid. This is the first time nanoquartz has been synthesised and extracted from a non-biological route under ambient conditions.

The 1–5 nm nanocrystals synthesised from the microemulsions have a perturbed bulk-quartz structure but nonetheless have sufficient crystallinity to act as effective seeds for the hydrothermal synthesis of larger quartz nanocrystals under mild conditions of 175 °C and autogenic pressure. The nanocrystals slowly grow and anneal over time, readily enabling nanoquartz of defined size and structure to be obtained exclusively by changing reaction times for the first time. This detailed study of the crystallisation pathway from a perturbed α-quartz structure for the 2 nm-sized nanoquartz through to the bulk α-quartz structure for the 4 nm-sized nanoquartz is important theoretically. It establishes 4 nm as the effective cut-off point at which the surface no longer influences the interior structure.

It was shown that the yield of 4-(phenylamino)-pent-3-en-2-one (a β-enaminone and key organic intermediate) is increased by adding catalytic amounts of amorphous silica, and the microemulsion-derived nanoquartz. The yield increase for the microemulsion-derived nanoquartz, however, was smaller than that for the 7 nm amorphous silica further evidencing the superior crystallinity of the nanoquartz over fumed silica. In contrast, a remarkably strong inhibition occurred for the more structurally perfect hydrothermal nanoquartz. Consequently, adopting a similar microemulsion-hydrothermal strategy for other inorganic nanocatalytic systems will provide far greater control over the size and structure of the crystals aiding catalytic performance.

These nanocrystals, free from growth modifiers or other contaminants, will be ideal for studies aimed at elucidating the harmful role that silica crystallinity plays in inducing lung diseases such as silicosis. Furthermore, it is noted that nanoquartz deposits are common in North Sea Danian chalk, with one hypothesis suggesting that the nanoquartz may have crystallised in the sea during sedimentation of the chalk rather than it being formed by burial diagenesis.[265] However, the slow rate of quartz growth, let alone nucleation, has meant that this type of crystallisation is usually assumed to be too slow at ambient temperature to be of any significance.[266] These findings provide a tantalising indication that perhaps the quartz nucleation could have been facilitated by confinement in nanopores.

Chapter 6

Large Droplet, Acidified and TEOS Shell Coating Synthesis of Nanoquartz

6.1 Introduction

It has been shown previously that quartz crystals within microemulsion droplets can be grown to a size greater than 2-5 nm, through both growing the crystals in larger droplets and by acidifying the microemulsion.[133,252] Although these crystals were not able to be extracted from the microemulsions, TEM analysis clearly indicated the presence of up to ~400 nm sized crystals, providing a possible route for the growth and extraction of larger quartz crystals.

6.1.1 Microemulsion Syntheses with a Larger droplet size

Thermodynamic control of crystallisation is dependant on there being a relatively small number of constitute molecules present within the microemulsion droplets, so they can reversibly change between a crystallite and a supersaturated solution. This has been shown previously in this thesis for the crystallisation of quartz, the thermodynamically stable polymorph of SiO_2, when sodium metasilicate (SMS) was entrapped in 5 μl g^{-1} dispersed phase concentration. However, upon increasing the dispersed phase amount and hence the droplet size, more molecules are required to be present in order for the droplet to become supersaturated, which in turn may cause crystallites to form irreversibly preventing thermodynamic control.

For instance, although α-quartz particles have been synthesised previously in microemulsions that contain 50 μl g^{-1} of the dispersed phase (Figure 6.1),[133] these α-quartz crystals were still of a small size (~2 nm) and were a minority phase. The predominant phase formed at these larger droplet sizes was that of cristobalite, a metastable polymorph of SiO_2. This was akin to the results seen when the concentration of the precursor SMS was increased to 10 and 14 wt.%

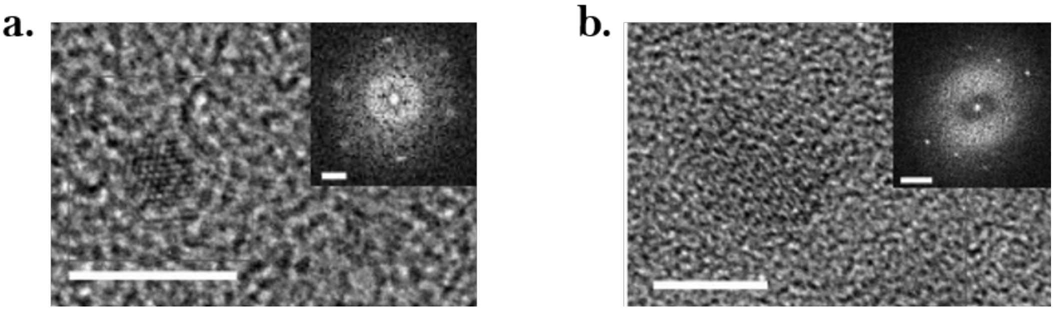

Figure 6.1: Representative TEM data of crystalline silica from larger-sized SB microemulsions. The crystalline silica was synthesized from SB (Span® 80 and Brij® 30) microemulsions using 50 μl g^{-1} of a 1 wt.% aqueous SMS (sodium metasilicate) solution. **a.** HREM image of a 2 nm particle. The inset shows the FFT, which indexes on the $\langle 212 \rangle$ zone axis of α-quartz. **b.** HREM image of a 5 nm particle. The inset shows the FFT, which indexes on the $\langle 110 \rangle$ zone axis of cristobalite. The scale bars are 5 nm in **a.** and **b.** d and 2 nm^{-1} in the insets.

6.1.2 Microemulsion Syntheses with the Addition of Acid

Recently, the effect of the addition of hydrochloric acid to microemulsion derived precipitates has been studied for a dipicolinic acid (DPA) system.[251] Typically a shift towards neutrality is observed within microemulsion droplets compared to macroscopic acid solutions, which in this case causes DPA to form metal salts as anionic protolytic forms of DPA persist at neutral pHs (Figure 6.2) Therefore, without the addition of HCl, the

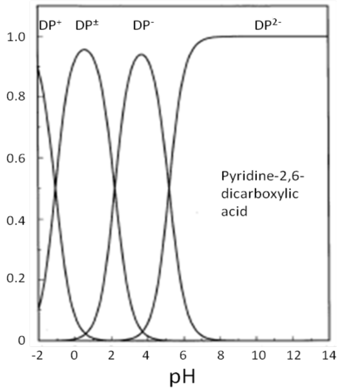

Figure 6.2: Distribution curves for the different protolytic species of DPA that exist in aqueous solution.[267]

precipitation of DPA metal salts was observed from this microemulsion system. Based on earlier work, it was postulated that this was caused not only due to the metal binding ability of DPA but the pH dependent self-assembly behaviour of DPA.[268,269] Upon the addition of 2 M HCl, TEM studies showed that nanocrystals of DPA, and larger mesocrystal structures of DPA could form, highlighting the effect of pH on thermodynamic control within nanoconfinement.

These acidified microemulsion syntheses were extended to silica systems, where the effect upon the addition of HCl was studied in the formation of α-quartz crystals. Like DPA, the formation of silica-based anionic species when SMS is in solution is heavily pH dependant (Figure 6.3).[270] Similarities between the two distribution curves exist. Basic conditions favour silica bond dissolution. Consequently, the addition of HCl, causes larger fluctuations between acid/basic conditions present within the microemulsion droplets, and should aid the formation of larger α-quartz crystals.

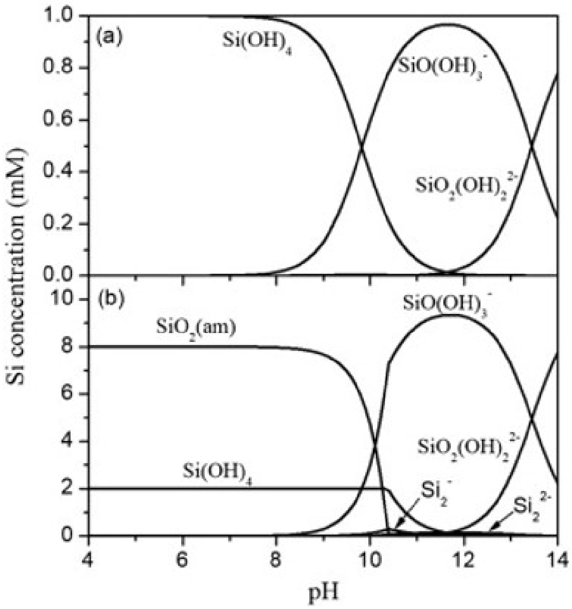

Figure 6.3: Distribution curves showing the effect of concentration and pH upon the distribution of silicate anions in solution.[270]

These larger α-quartz crystals were in fact seen. Span-Brij microemulsions containing a dispersed phase concentration of 50 μl g^{-1} of 1 wt.% SMS solution in addition to 50 μl g^{-1} 1.5 M HCl (an overall dispersed phase concentration of 100 μl g^{-1}), were successful in producing ~400 nm triangular shaped α-quartz nanocrystals (Figure 6.4). These larger crystals, however, did form a minority phase with smaller ~2 nm α-quartz crystals persisting.

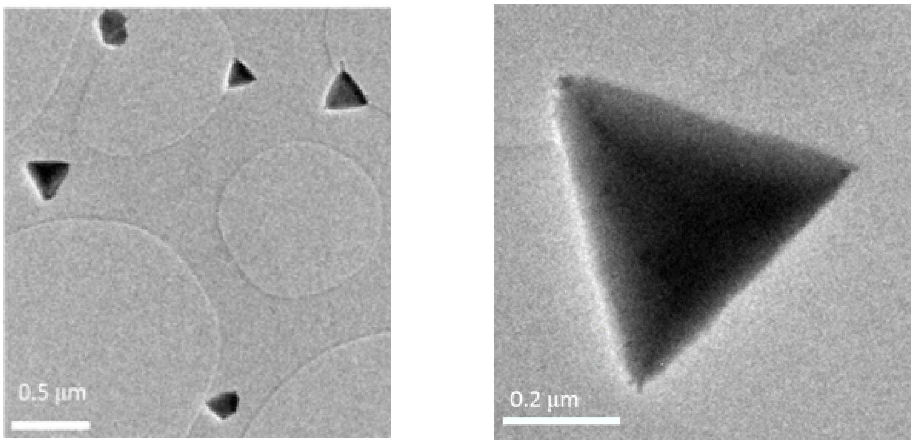

Figure 6.4: Representative TEM of ~ 400 nm α-quartz crystals synthesised from SB microemulsions containing a dispersed phase concentration of 50 μl g^{-1} of 1 wt.% SMS solution in addition to 50 μl g^{-1} 1.5 M HCl.[133]

6.1.3 Tetraethyl Orthosilicate

Tetraethyl orthosilicate (TEOS) has been used as an effective precursor to synthesis amorphous silicon dioxide. This is exemplified most by the production of monodisperse amorphous silica spheres in the Stöber process which involves the hydrolysis of TEOS followed by condensation and oligomerisation of silicic acid to form silica (Scheme 6.1)

Hydrolysis: $Si(OC_2H_5)_4 + 4H_2O \longleftrightarrow Si(OH)_4 + 4C_2H_5OH$
Condensation: $Si(OH)_4 \longleftrightarrow SiO_2 + H_2O$

Overall Reaction: $Si(OC_2H_5)_4 + 2H_2O \longleftrightarrow SiO_2 + 4C_2H_5OH$

Scheme 6.1: Scheme outlining the hydrolysis and condensation reactions in which TEOS transforms into silica.

However, utilising TEOS as a precursor in the formation of α-quartz from w/o microemulsions is difficult as TEOS is immiscible with water. Therefore, an aqueous dispersed phase that contains TEOS must be homogenised with an alcohol such as ethanol, however this would make the dispersed phase partially miscible with the continuous phase. Conversely TEOS can be added to the oil containing continuous phase, however the formation of α-quartz would be dependent on the TEOS molecules penetrating the surfactant interface to the aqueous droplet in order to undergo hydrolysis.[271,272]

Although it may be difficult to use TEOS as a precursor in w/o microemulsions, it has been used successfully in order to create a silica barrier around nanoconfined crystals within a w/o microemulsion. Metal nanoparticles have successfully been coated in a silica shell to form metal-silica based nanoparticles.[273] Firstly the metal nanoparticles were sonicated in a aqueous phase to uniformly disperse them. The nanoparticle solution was then added to a surfactant in oil mixture to form a w/o solution followed by the addition of TEOS into the continuous oil phase. After undergoing stirring for 5 days, the metal nanoparticles were extracted and analysed to show the existence of a silica shell around the nanoparticles.

6.1.4 Project Outline

In the previous chapter, the successful formation and extraction of 1-5 nm α-quartz nanocrystals was reported from water-in-oil microemulsions under ambient conditions within 14 days using aqueous sodium metasilicate (pH 12-13) as the silica precursor. These nanocrystals seeded subsequent hydrothermal syntheses under mild conditions to enable nanoquartz of a defined size to be obtained. After 7 days hydrothermal treatment, the quartz crystals had grown and perfected, however, they had also begun to aggregate into larger ~40 nm sized groups.

In this chapter, two further methods are outlined in which the bulk formation of α-quartz nanocrystals can be produced under ambient conditions, utilising again the thermodynamic control seen in microemulsions. Firstly, microemulsions containing a dispersed phase concentration of 50 μl g^{-1} were used. Secondly acidified microemulsions containing HCl were used. Both methods resulted in the successful bulk formation of α-quartz akin to the microemulsion derived nanoquartz reported in the previous chapter. These successful syntheses were used to seed mild hydrothermal syntheses. It was hoped that these microemulsion-derived nanoquartz crystals would be larger in size than those previously reported. In turn, hydrothermal treatment times would be reduced and hopefully aggregation would be minimised.

In addition, the shell coating of the microemulsion derived nanoquartz with a silica shell derived from TEOS is explored. Rather than attempting to increase the size of the nanoquartz seeds prior to hydrothermal treatment, it is hoped that these silica shells will provide a protective barrier during the hydrothermal syntheses inhibiting the aggregation of the crystals.

6.2 Experimental

6.2.1 Materials

Surfactants and solvents were of analytical laboratory grade (unless otherwise stated). Chemicals were used as supplied and were as follows: tetraethyl orthosilicate (≥98%, Acros Organics), sodium metasilicate nonahydrate (SMS) (≥98%, Aldrich), Span® 80 (sorbitan monooleate) (Sigma-Aldrich), Brij® 30 (polyoxyethylene (4) lauryl ether) (Acros Organics), hydrochloric acid solution (5 M, Pure Bench Reagent, Fisher Scientific), heptane (≥99% Acros Organics), methanol (99.99%, Fisher Scientific), acetone (99.98%, Fisher Scientific) and ethyl acetate (99.92%, Fisher Scientific). Ultra-high purity (UHP) water with a resistivity of 18.2 MΩ cm was obtained from a Sartorius arium® comfort water purifier system.

6.2.2 Nanoquartz Synthesis in Microemulsions

The microemulsions used a surfactant combination of 1:1 wt.% Span® 80 and Brij® 30 in heptane at a surfactant:heptane ratio of 40:60 wt.%. The microemulsions using Span® 80 and Brij® 30 are denoted with the prefix SB. Microemulsions were prepared by adding 0.5 wt.%, 1.25 wt.% or 2.5 wt.% sodium metasilicate (SMS) aqueous solutions to the surfactant solutions followed by thorough mixing by vigorous hand-shaking to achieve a single transparent, homogeneous phase.

For the acidified microemulsions, the SMS and acidic phases were formed separately before mixing the two microemulsions with vigorous hand-shaking.

For the large droplet, silica encapsulated microemulsions, the microemulsion was first formed without the addition of TEOS as above. After 4 days, TEOS was added directly to the microemulsion. The system was left under stirring for the remainder of the time.

After 2 weeks, the precipitated nanoquartz/encapsulated nanoquartz was washed in a 1:1 solution of methanol and ethyl acetate (300 ml) *via* sonication in an ultrasound water bath for 30 minutes to remove residual surfactant and impurities. The purified nanoquartz was extracted by centrifugation at 9418 G (9000 revs per minute) for 10 min and left to dry in an oven at 60 °C for 24 h.

6.2.3 Nanoquartz Characterisation

Transmission Electron Microscopy (TEM) analysis was performed on the nanoquartz samples using a JEOL 2100 field emission gun TEM (FEG TEM) operating at 200 kV, a ZrO/W (100) Schottky Field Emission analytical emission microscope, in combination with an Oxford INCAx-Sight Si(Li) detector for Energy-Dispersive X-ray (EDX) spectroscopy and a Gatan Orius CCD camera. Phase contrast high resolution electron microscopy (HREM) was used to image nm-sized crystals. The structure of an individual nanocrystal was determined by indexing the fast Fourier transform (FFT) and selected area diffraction patterns. Extracted nanoquartz was dispersed in UHP water *via* sonication in an ultrasound water bath for 30 min. The dispersion was pipetted onto holey carbon, 300 copper mesh TEM grids. The TEM grids were left to dry completely before examination using TEM.

Powder X-ray Diffraction (PXRD) was performed on the extracted nanoquartz using a Bruker D8 Advance operated at 40 kV and 35 mA to produce Cu Kα radiation. The experimental set-up was conducted within the DIFFRAC.SUITE software. Samples were ground with a spatula and placed on a glass XRD slide. The sample was subjected to a 6 mm X-ray beam width and was continuously rotated through 360° to reduce preferential orientation effects. Angles were scanned with the knife edge in place between 2θ = 3-80° at increments of 0.02° with the beam exposed at each angle for 1 s.

Fourier Transform Infrared (FTIR) spectra of the nanoquartz were recorded on a Perkin-Elmer Frontier FT-IR spectrometer equipped with a U-ATR sampling accessory and caesium iodide optics. A total of 16 scans were collected for each sample at a resolution of 2 cm^{-1} over a wavenumber region of 4000 cm^{-1} to 380 cm^{-1}.

Solid-state ^{29}Si Nuclear Magnetic Resonance (ssNMR) spectra of the nanoquartz were recorded at 79.44 MHz using a Varian VNMRS spectrometer and a 6 mm (rotor o.d.) magic-angle spinning probe. They were obtained using direct excitation with a 300 s recycle delay at ambient probe temperature ($\sim$25 °C) and at a sample spin-rate of approximately 6 kHz. Between 200 and 240 repetitions were accumulated. Spectral referencing was with respect to an external sample of neat tetramethylsilane (carried out by setting the high-frequency signal from tetrakis(trimethylsilyl)silane to -9.9 ppm).

6.2.4 Hydrothermal Synthesis Experiments

Hydrothermal synthesis experiments were conducted at 175 °C for 3 days using 237.4 mg of fumed silica in 0.1 M SMS aqueous solution together with 57.4 mg of seeds consisting of either (i) the nanoquartz synthesised from the 50 μl g^{-1} microemulsions, (ii) the nanoquartz synthesised from the acidified microemulsions or (iii) the silica coated shell nanoquartz synthesised from the microemulsions with added TEOS. The 237.4 mg of fumed silica in 0.1 M SMS solution was heated to 90 °C to dissolve the fumed silica before adding to the seeds in the hydrothermal unit, sealing the unit and then heating to 175 °C. After the hydrothermal unit had cooled, acetone was added to the hydrothermal product, present as a sedimented hydrated cake, to aid extraction from the hydrothermal unit. This was followed by centrifugation at 9418 G (9000 revs per minute) for 10 minutes to recover the product. The sediment was dried in an oven at 60 °C for 24 h, producing a cake that was then ground with a spatula to give the resulting nanoquartz powders.

6.3 Results

6.3.1 Large Droplet Synthesis of Nanoquartz

The nucleation of quartz under ambient conditions has been previously observed within SB microemulsion systems using a 50 μl g^{-1} dispersed phase concentration, although these α-quartz phases were a minority.[133,252] The predominant phases were that of cristobalite and amorphous silica, with these phases persisting further at higher SMS wt.% concentrations. These systems were adopted here with low SMS concentrations, namely 0.5 and 1.25 wt.%, to promote the synthesis of α-quartz within microemulsions that contain an aqueous dispersed droplet phase of a larger size.

Although no SAXS data on these microemulsions was able to be obtained (due to downtime of the x-ray tube), the 50 μl g^{-1} microemulsions are expected to contain larger droplets due to the increased volume of the aqueous dispersed phase. This is corroborated by previous studies (from SAXS and GIFT analysis) in which the average measured droplet radius was 2.7 nm for the 50 μl g^{-1} microemulsions (1.8X that of the 5 μl g^{-1} microemulsions).[133]

6.3.1.1 0.5 wt.% Synthesis

In order to obtain sufficient material for analysis, large scale (420 g) microemulsions were made up containing 0.5 wt.% SMS solution (Table 6.1). As before, the microemulsions were left for 2 weeks to promote nanoquartz aggregation and sedimentation.

Table 6.1: Composition of the 0.5 wt.% SMS aqueous solution large droplet SB microemulsions.

	Mass / g
Heptane	240
Span®80	80
Brij®30	80
SMS Aqueous Solution	20
Total	420

FTIR analysis shows similar peaks to that of the 5 μl g^{-1} microemulsion derived nanoquartz; a significant Si–OH peak at 958 cm^{-1} along with prominent Si-O-Si peaks at 1064 cm^{-1}, 808 cm^{-1} and 448 cm^{-1} (Figure 6.5) and a broad OH stretch centred at 3350 cm^{-1}. Again, the major peaks at 1064 cm^{-1} (Si-O-Si antisymmetric stretch), 808 cm^{-1} (Si-O-Si symmetric stretch) and 448 cm^{-1} (rocking of oxygen atoms) correspond to silica structures containing Si-O-Si bonds exclusively. However, the signals at 958cm^{-1} (Si-OH Stretch) and 553cm^{-1} (Si-O bending in non-bridging Si-OH) are characteristic of Si-OH bonding arising from the surface silanol groups expected in nanoquartz.

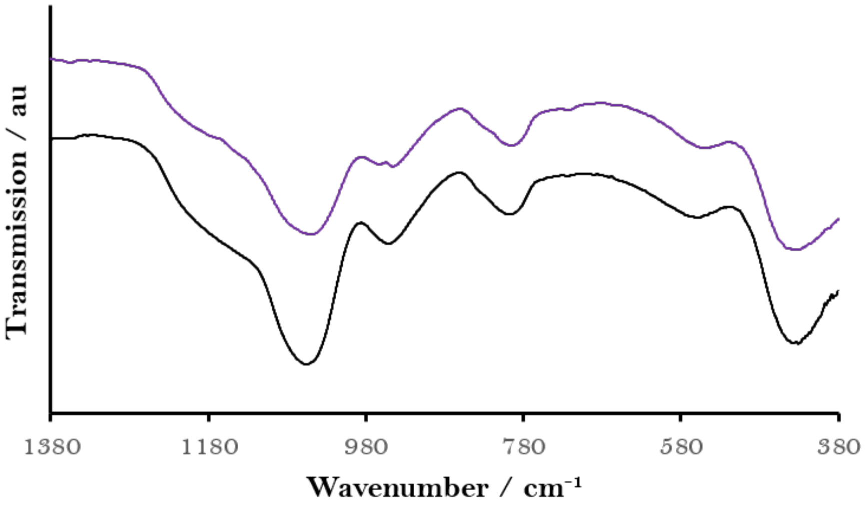

Figure 6.5: FTIR analysis of the 5 μl g^{-1} microemulsion-synthesised nanoquartz (black line) and the large droplet (0.5 wt.%) microemulsion-synthesised nanoquartz (purple line).

^{29}Si ssNMR revealed peaks at -92, -101 and -110 ppm attributable to 4.7% Q^2 Si(OH)$_2$, 35.3% Q^3 Si(OH), and 60.0% Q^4 Si (Figure 6.6). As before, small nanocrystals of α-quartz would be expected to have a large proportion of Q^3 Si(OH) sites due to their large surface to volume ratios. Note though, the Q^3 and Q^4 peaks present have narrowed slightly compared to that of the 5 μl g^{-1} microemulsion-derived nanoquartz. This is perhaps an indication that the large droplet microemulsion derived nanoquartz is sufficiently larger in size to show less distortions of the bulk α-quartz structure.

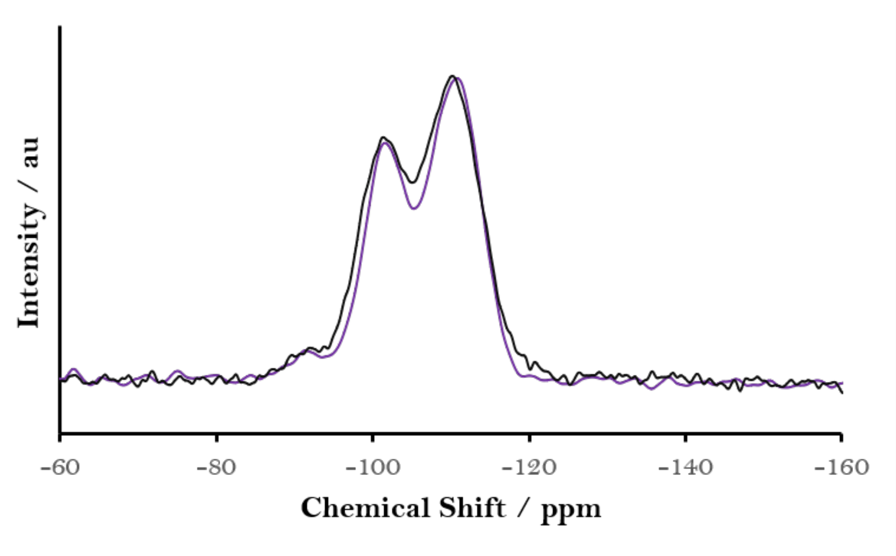

Figure 6.6: ssNMR analysis of the 5 μl g^{-1} microemulsion-synthesised nanoquartz (black line) and the large droplet (0.5 wt.%) microemulsion-synthesised nanoquartz (purple line).

6.3.1.2 1.25 wt.% Synthesis

Although multiple large scale microemulsions were formed, there was not enough extracted large droplet microemulsion-derived nanoquartz for XRD analysis using 0.5 wt.% SMS solution. As a result the SMS concentration was increased to 1.25 wt.% whilst noting that any further increase would promote cristobalite/amorphous silica formation and not the desired α-quartz nanocrystals (Table 6.2). After increasing the SMS wt.% concentration, there was still insufficient nanoquartz extracted for XRD analysis. Instead FTIR and

Table 6.2: Composition of the 1.25 wt.% SMS aqueous solution large droplet SB microemulsions.

	Mass / g
Heptane	240
Span®80	80
Brij®30	80
1.25 wt.% SMS Aqueous Solution	20
Total	420

ssNMR was utilised once again.

FTIR spectrum of the large droplet, 2.5 wt.% microemulsion-derived nanoquartz is similar to the previous spectra (Figure 6.7). Peak analysis is the same as that described on section 6.3.1.1.

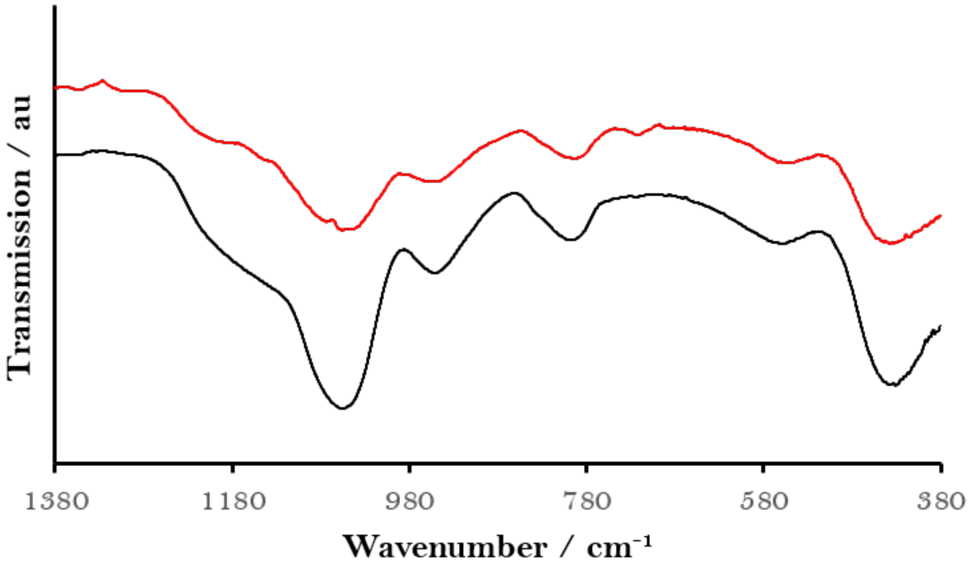

Figure 6.7: FTIR analysis of the 5 μl g^{-1} microemulsion-synthesised nanoquartz (black line) and the large droplet (1.25 wt.%) microemulsion-synthesised nanoquartz (red line).

ssNMR spectrum of the large droplet, 2.5 wt.% microemulsion-derived nanoquartz exhibits the two same broad Q^3 and Q^4 peaks at -101 and -110 ppm respectively (Figure 6.8). Note that the Q^3 peak at -92 ppm has broadened and the Q^3 and Q^4 peak

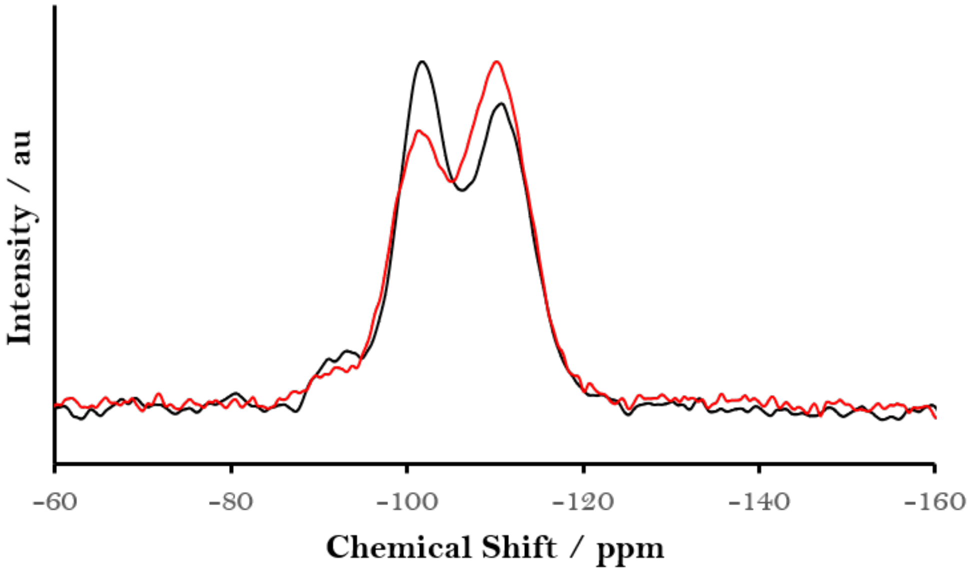

Figure 6.8: ssNMR analysis of the 5 μl g^{-1} microemulsion-synthesised nanoquartz (black line) and the large droplet (1.25 wt.%) microemulsion-synthesised nanoquartz (red line).

has significantly decreased and increased respectively when compared to the 5 μl g^{-1} microemulsion-synthesised nanoquartz. This may indicate that the resultant α-quartz are larger in size but TEM analysis is needed to confirm this.

6.3.1.3 TEM

TEM studies on the large droplet (0.5 and 1.25 wt.%) microemulsion-derived nanoquartz established the formation of α-quartz nanocrystals as the majority silica phase present (Figure 6.9). A diffraction ring at a spacing of 0.24 nm is clearly visible, consistent with diffraction from $\{1\bar{2}0\}$ α-quartz planes which is part of the $\langle 212 \rangle$ zone axes. As

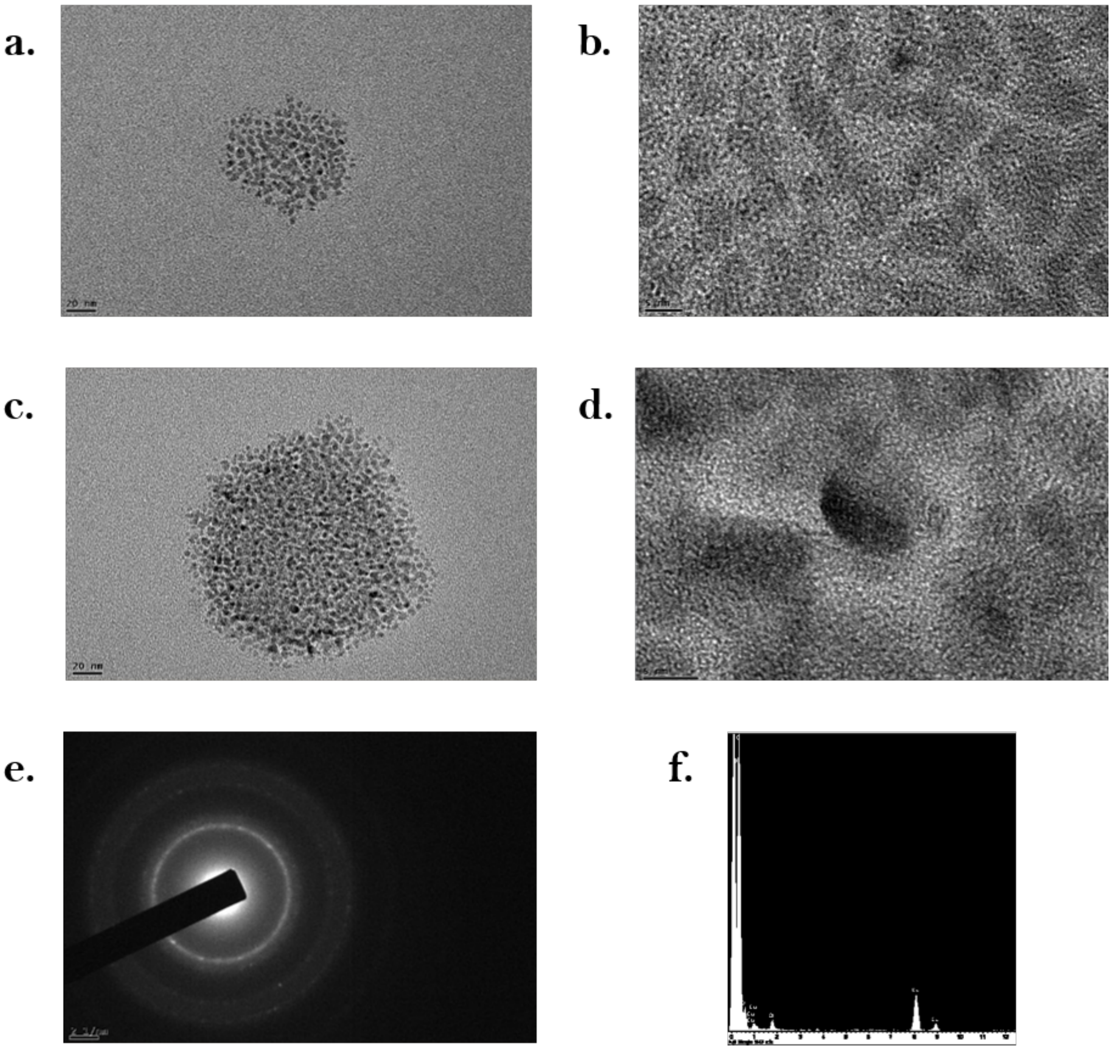

Figure 6.9: Representative TEM data of the nanoquartz synthesised from SB microemulsions using 50 μl g^{-1} of a 0.5 wt.% (**a.**-**b.**) and 1.25 wt.% (**c.**-**e.**) aqueous SMS solution. **a.**, **c.** Bright field images of 5 nm large droplet microemulsion-derived nanoquartz particles. **b.**, **d.** High resolution image (HREM) of 0.5 wt.% and 1.25 wt.% nanoquartz particles respectively. **e.** Electron diffraction pattern of the region shown in **c.** revealing a diffraction ring at a spacing of 0.24 nm. Scale bars are 20 nm in **a.** **c.**, 5 nm in **b.** and **d.**, and 2 nm^{-1} in **e.** Representative EDX spectra of the large droplet microemulsion-synthesised nanoquartz TEM micrographs. There is no signal due to sodium (expected at 1.04 keV), showing that the silica phase present does not contain any sodium silicate.

expected from the ssNMR analysis, both large droplet syntheses have yielded larger α-quartz nanocrystals (~5 nm). This is thought to be a result of the larger diameters of droplets seen in these microemulsions allowing the crystals to grow to ~5 nm until being restricted by the surfactant layer.

6.3.1.4 Hydrothermal Studies

The larger ~5 nm crystals yielded from the large droplet microemulsions were used to seed hydrothermal syntheses under 175 ^{o}C and autogenic pressure in order to grow and anneal the nanoquartz. It is hoped that using seeds that are larger in size will allow the nanoquartz to grow and anneal to a bulk α-quartz structure without needing a treatment time of 7 days. This should yield isolated nanoquartz particles without aggregation.

After 3 days of hydrothermal treatment, FTIR spectra of the 0.5 wt.% (Figure 6.10) and 1.25 wt.% (Figure 6.11) of the large droplet-derived nanoquartz show peaks associated with defective bulk quartz and moganite at $\approx$ 660, 615, 575, and 545 cm^{-1}.

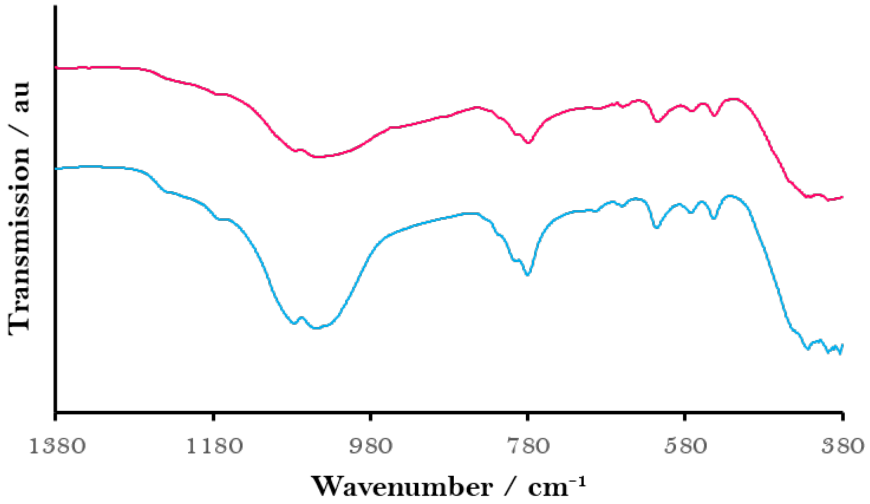

Figure 6.10: FTIR analysis of the 3-day hydrothermally treated 5 μl g^{-1} microemulsion-synthesised nanoquartz (light blue line) and the 3-day hydrothermally treated large droplet (0.5 wt.%) microemulsion-synthesised nanoquartz (pink line).

Focussing on the signature ”quartz doublet” which appears at 780 and 800 cm^{-1}, we see that it is clearly apparent for the 3-day hydrothermally treated 5 μl g^{-1} microemulsion-synthesised nanoquartz. However the definition of this doublet decreases for the 3-day hydrothermally treated large droplet (0.5 wt.%) microemulsion-synthesised nanoquartz and decreases further for the 3-day hydrothermally treated large droplet (1.25 wt.%) microemulsion-synthesised nanoquartz.

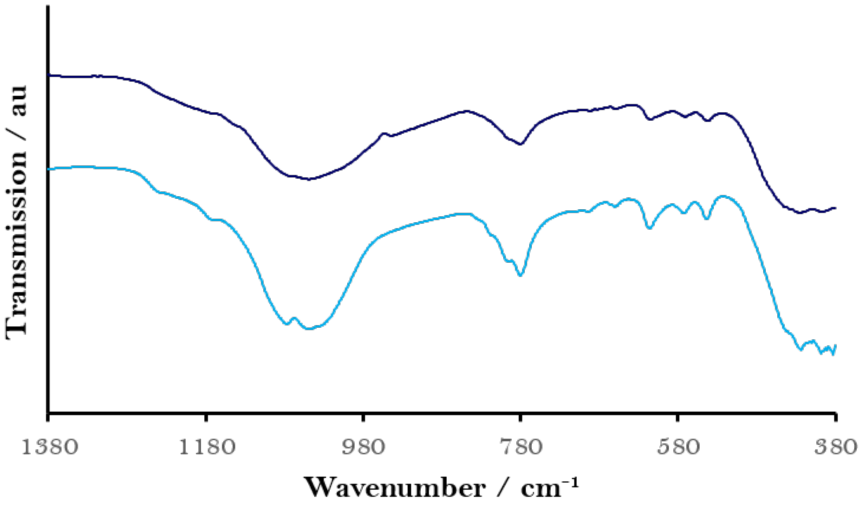

Figure 6.11: FTIR analysis of the 3-day hydrothermally treated 5 μl g^{-1} microemulsion-synthesised nanoquartz (light blue line) and the 3-day hydrothermally treated large droplet (1.25 wt.%) microemulsion-synthesised nanoquartz (dark blue line).

6.3.1.5 Conclusions

Larger ~5 nm α-quartz nanocrystals were successfully synthesised and extracted under ambient conditions by using SB microemulsions that contained a 50 μl g^{-1} dispersed phased concentration. Two SMS wt.% solution were used, 0.5 and 1.25 wt.%. Although TEM analysis confirmed the existence of ~5 nm particles for both SMS concentrations, the 1.25 wt%-derived nanoquartz exhibit less/more Q^3/Q^4 silica suggesting that it may contain larger particles.

These two wt.%-derived nanoquartz was used to seed hydrothermal treatments. After 3 days treatment, both samples of nanoquartz had a more perturbed structure than that of the 3 day treated 5 μl g^{-1} microemulsion-derived nanoquartz. Therefore, in order to recover the bulk α-quartz structure more than 7 days treatment time would most likely be needed, and therefore experiments were not taken further, as it is this chapters aim to reduce this time. The 1.25 wt.% nanoquartz does not show the quartz doublet emerging after 3 days. This could be due to the seeds containing minority phases of cristobalite and fumed silica as would be expected from a higher SMS wt.% concentration encapsulated within larger droplets.

Unfortunately, growing the microemulsion-derived nanoquartz to ~5 nm pre-hydrothermal treatment has not helped in reducing the treatment time needed to recover the bulk α-quartz structure.

6.3.2 Acidified Synthesis of Nanoquartz

The synthesis of large nm triangular shaped quartz nanocrystals has been previously demonstrated through acidifying SB microemulsions.[133] This acidic system is adapted here (Table 6.3) to promote the synthesis of large α-quartz nanocrystals suitable for hydrothermal treatment. In order to obtain sufficient material for extraction and analysis, large scale (420 g) microemulsions were made up. Firstly two independent 210 g microemulsions were formed: the first containing a 2.5 wt.% SMS solution 25 μl g^{-1} dispersed phase; the second containing a 2.2 M HCl 25 μl g^{-1} dispersed phase. These were then mixed to create the 420 g microemulsion and left for 14 days for nanoquartz synthesis and sedimentation. This created an overall dispersed phase concentration of 25 μl g^{-1} ("large droplet") that contained 1.25 SMS wt.%.

Table 6.3: Composition of the 1.25 wt.% SMS aqueous solution acidic SB microemulsions. Both the SMS and acid phases were formed independently before mixing to form the final acidified microemulsion.

	SMS Phase Mass / g	Acid Phase Mass / g	Total Mass / g
Heptane	120	120	240
Span®80	40	40	80
Brij®30	40	40	80
2.5 wt.% SMS Aqueous Solution	10	-	10
2.2 M HCl	-	10	10
Total	210	210	420

FTIR analysis (Figure 6.12) reveals a spectrum akin to that of the 5 μl g^{-1} microemulsion-derived nanoquartz.

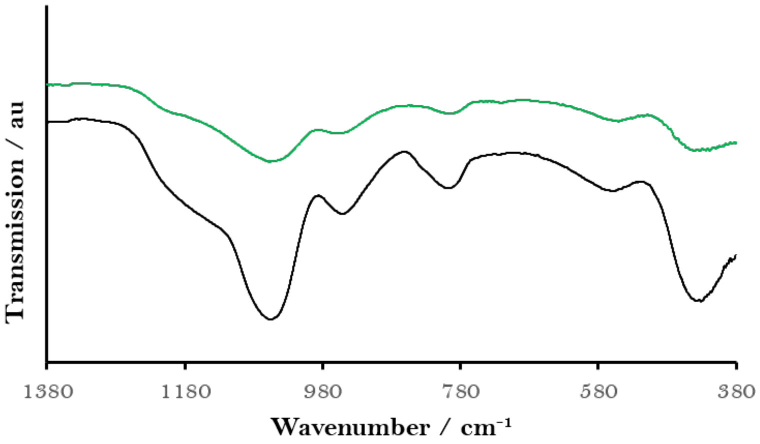

Figure 6.12: FTIR analysis of the microemulsion-synthesised nanoquartz (black line) and the large droplet (1.25 wt.%) acidified microemulsion-synthesised nanoquartz (green line).

However, ssNMR analysis indicates that the large droplet acidified microemulsion-derived nanoquartz does contain a different structure to that of the 5 μl g^{-1} microemulsion-derived nanoquartz (Figure 6.13). The Q^2, Q^3 and Q^4 peaks at -92, -101 and -110 ppm

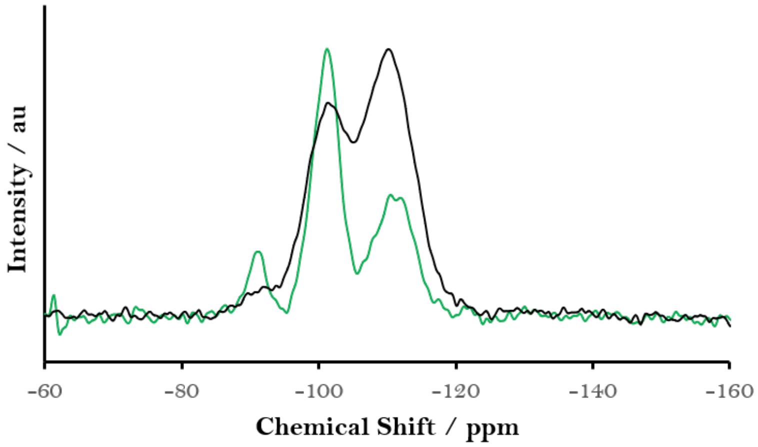

Figure 6.13: ssNMR analysis of the microemulsion-synthesised nanoquartz (black line) and the large droplet (1.25 wt.%) acidified microemulsion-synthesised nanoquartz (green line).

have significantly narrowed with the Q^4 beginning to split. This is akin to the early stages of the transformation seen in the hydrothermal treatment of the 5 μl g^{-1} microemulsion-derived nanoquartz.

TEM studies show no indication of any large triangular shaped nanoquartz ~400 nm in size. However, the nanocrystals are the greatest in size synthesised from any microemulsion method presented in this thesis with some larger than 20 nm. The mean size of the nanocrystals were 5.7 nm ± 3.9 nm, based on the sizing of 639 particles (Figure 6.14). These TEM studies on the large droplet acidified microemulsion-derived

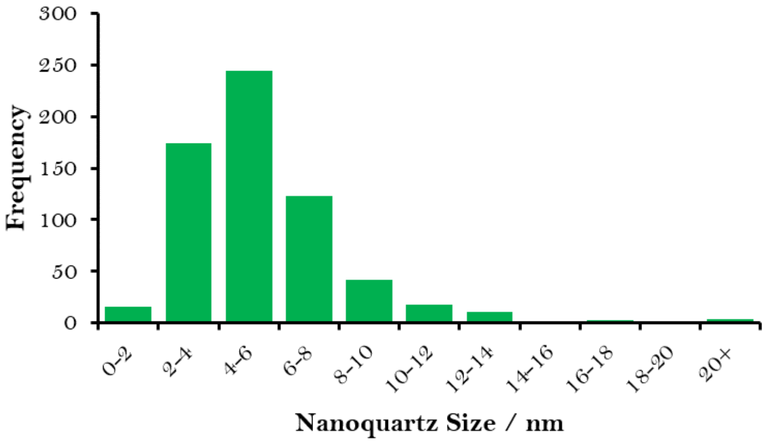

Figure 6.14: Histogram showing the particle size distribution for the large droplet acidified microemulsion-synthesised nanoquartz obtained by sizing 639 particles from TEM micrographs.

nanoquartz established the formation of α-quartz nanocrystals as the majority silica phase present once again (Figure 6.15). Diffraction rings are visible at spacings of 0.2 and 0.24 nm, attributed to $\{1\bar{2}0\}$ and $\{02\bar{1}\}$ α-quartz planes respectively.

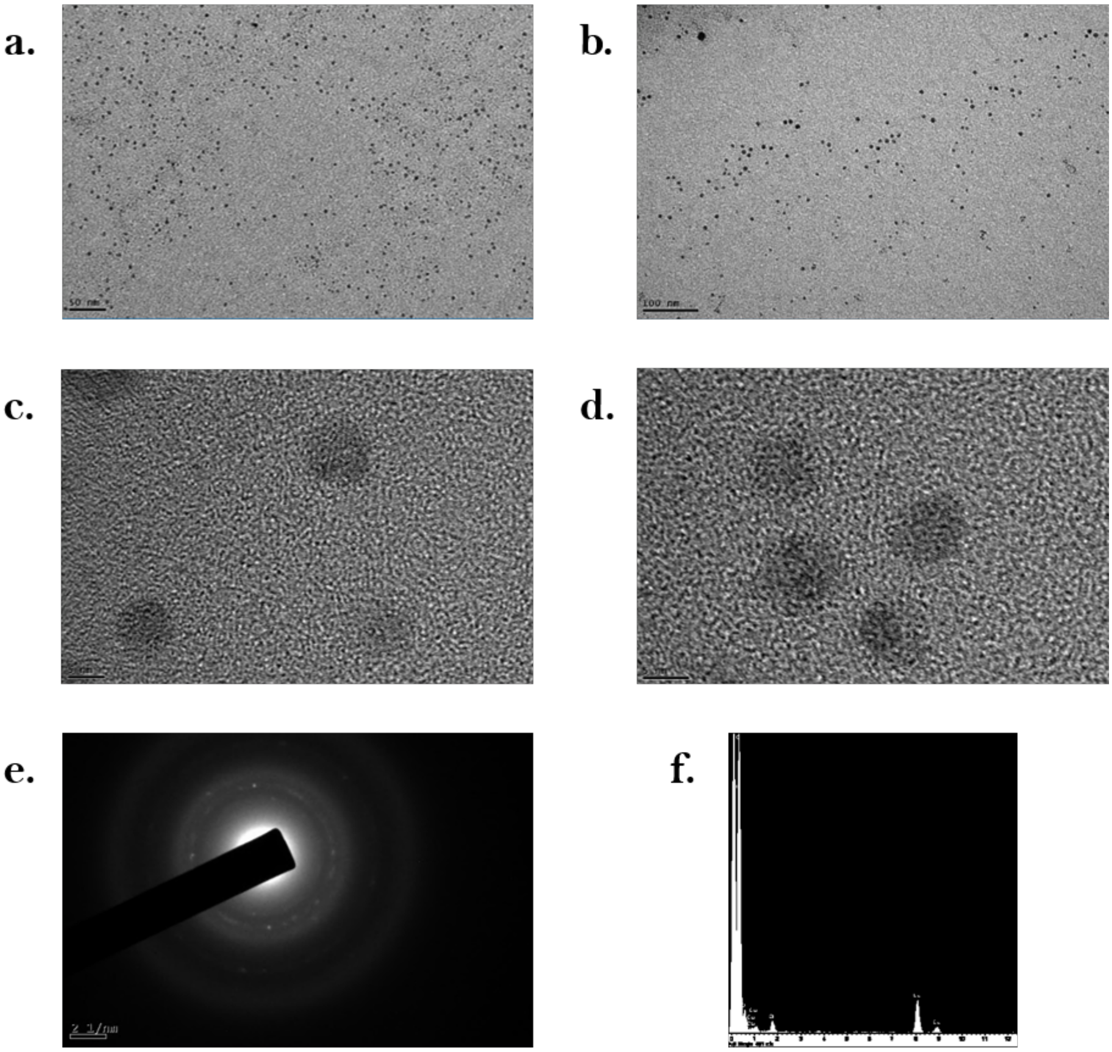

Figure 6.15: Representative TEM data of the nanoquartz synthesised from SB microemulsions using 25 μl g^{-1} of a 2.5 wt.% aqueous SMS solution and 25 μl g^{-1} of 2.2 M HCl. **a.**, **b.** Bright field images of ~5 nm acidified large droplet microemulsion-derived nanoquartz particles. **c.**, **d.** High resolution image (HREM) of ~5 nm nanoquartz particles. **e.** Electron diffraction pattern of the region shown in **a.** revealing diffraction spots attributed to α-quartz at spacings of 0.24 an 0.2 nm. Scale bars are 50 nm in **a.**, 100 nm in **b.**, 5 nm in **c.** and **d.**, and 2 nm^{-1} in **e.** **f.** Representative EDX spectra of the acidified large droplet microemulsion-synthesised nanoquartz TEM micrographs. There is no signal due to sodium (expected at 1.04 keV), showing that the silica phase present does not contain any sodium silicate.

6.3.2.1 Hydrothermal Studies

Again, these larger crystals yielded from the acidified large droplet microemulsions were used to seed hydrothermal syntheses under 175 ^{o}C and autogenic pressure. After 3 days of hydrothermal treatment, The FTIR spectrum of the acidified large droplet microemulsion-derived nanoquartz shows similarity to that of amorphous silica (Figure 6.16). There is

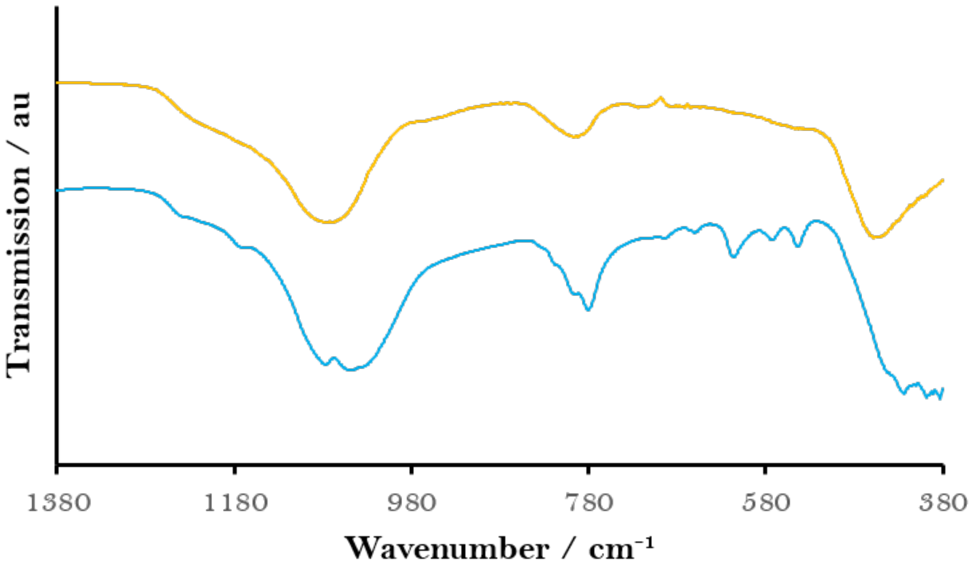

Figure 6.16: FTIR analysis of the 5 μl g^{-1} 3-day hydrothermally treated microemulsion-synthesised nanoquartz (light blue line) and the 3-day hydrothermally treated large droplet (2.5 wt.%) acidified microemulsion-synthesised nanoquartz (orange line).

no indication the characteristic quartz-doublet at 780 and 800 cm^{-1} as is expected after 3 days of hydrothermal treatment. As such, no further hydrothermal treatments were carried out as the bulk α-quartz structure would not be evident before 7 days.

6.3.2.2 Conclusions

Larger nanoquartz crystals were successfully synthesised with a mean size of 5.7 ± 3.9 nm, from larger drop acidified microemulsions. The structure of these crystals exhibited similarities to the early stage annealing of hydrothermally treated nanoquartz, as seen through the narrowing of ssNMR signals and the onset of the Q^4 splitting to reveal an emerging bulk α-quartz peak at -108 ppm. This indicates the potential for the use as effective seeds for subsequent hydrothermal treatments.

After three days hydrothermal treatment under mild conditions, the large droplet acidified microemulsion-derived nanoquartz showed no signs of improved crystal perfection as expected. As such, treatment times of over 7 days would be needed and again the nanocrystals would begin to aggregate. It is clear that increasing the seed crystal size does not shorten the hydrothermal treatment times needed for the nanocrystals to exhibit a bulk α-quartz structure. In this case, it is postulated that the residual acid groups that would be apparent on the seed particles was sufficient to lower the pH of the hydrothermal environment in order and increase the supersaturation, enabling amorphous silica to precipitate.

6.3.3 TEOS Shell Coating of Nanoquartz

A nanocrystal silica shell coating can be achieved through the use of tetraethyl orthosilicate (TEOS) TEOS. This has been previously used to coat metal nanoparticles, where the shell coating synthesis was performed as an additional step to the nanocrystal synthesis.[273] Here, this method is adapted to be included as part of the one-pot microemulsion synthesis (Table 6.4). Firstly, 420 g large droplet (1.25 wt.% SMS) microemulsions were made up as before. After 4 days, when α-quartz nanocrystals have formed but sedimentation is yet to occur, TEOS is added and the resultant microemulsion is left under stirring for an additional 10 days in order for the silica shell to form before the particles sediment.

Table 6.4: Composition of the 1.25 wt.% SMS aqueous solution large droplet SB microemulsions with added TEOS† for encapsulation. † TEOS was added directly to the microemulsion 4 days after formation.

	Mass / g
Heptane	240
Span®80	80
Brij®30	80
1.25 wt.% SMS Aqueous Solution	20
Total	420
TEOS	7.42

TEM studies on these particles establish the formation of monodisperse silica shells that are ~50 nm in size (Figure 6.17). Upon closer inspection of HREM micrographs, it is clear that the nanoquartz particles are encapsulated within the silica shells. Although some of the shell particles seemed to have aggregated, the particles within are isolated and dispersed.

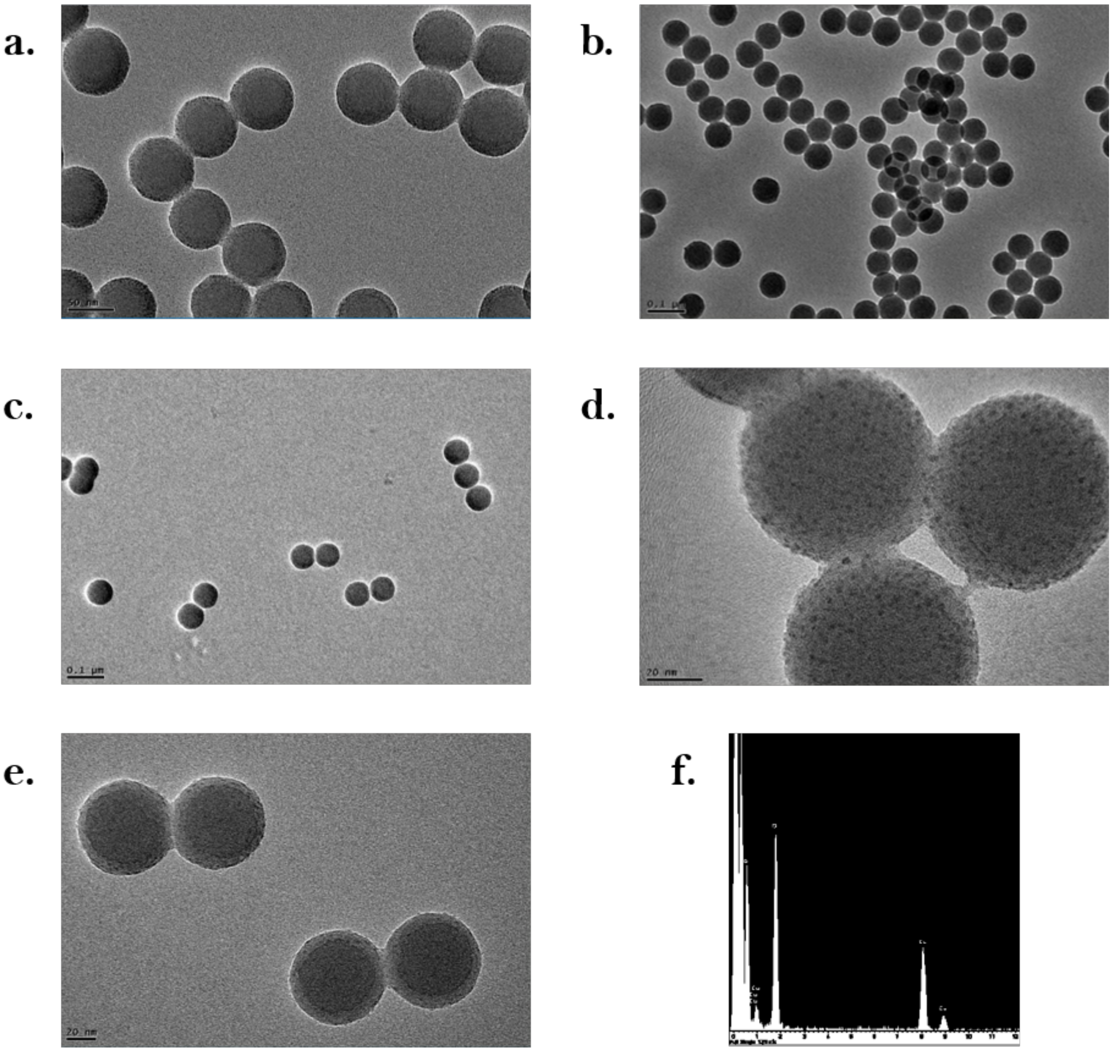

Figure 6.17: Representative TEM data of the nanoquartz synthesised from SB microemulsions using 50 μl g^{-1} of a 1.25 wt.% aqueous SMS solution with added TEOS. **a.**, **b.**, **c.** Bright field images of ~50 nm silica spheres. **d.**, **e.** High resolution image (HREM) of ~50 nm silica spheres encapsulating 1-5 nm nanoquartz particles. Scale bars are 50 nm in **a.**, 100 nm in **b.** and **c.**, and 20 nm in **d.** and **e.**. **f.** Representative EDX spectra of the large droplet microemulsion-synthesised encapsulated nanoquartz TEM micrographs. There is no signal due to sodium (expected at 1.04 keV), showing that the silica phase present does not contain any sodium silicate.

6.3.3.1 Hydrothermal Studies

These shell coated particles were used to seed hydrothermal treatments under the mild conditions used previously. After 3 days hydrothermal treatment, the FTIR spectrum of the hydrothermally treated shell coated nanoquartz exhibits peaks associated with defective bulk quartz and moganite, akin to the uncoated particles (Figure 6.18). However, the "quartz doublet" seen at 780 and 800 cm^{-1} is yet to emerge for the treated shell coated particles and remains as a broad peak with a shoulder.

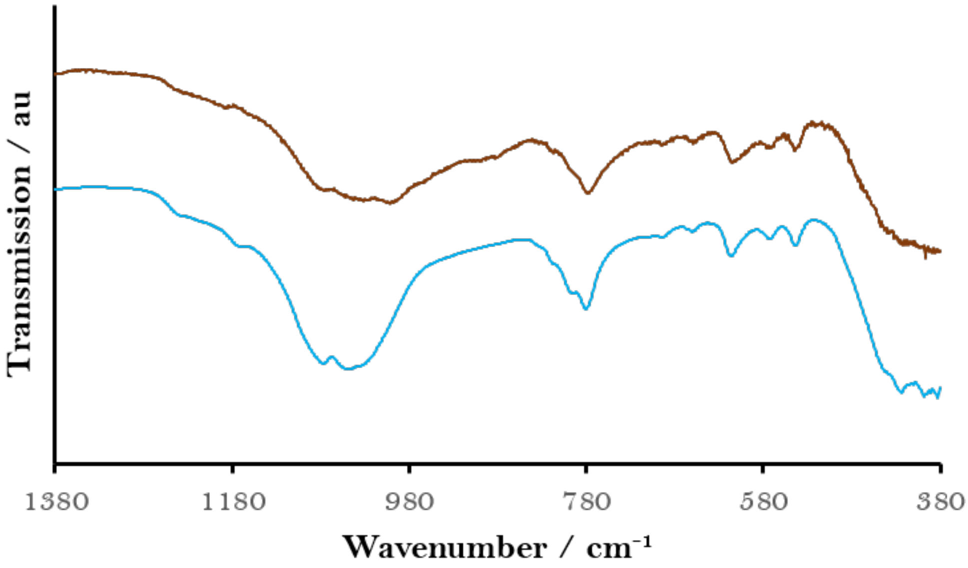

Figure 6.18: FTIR analysis of the 5 μl g^{-1} 3-day hydrothermally treated microemulsion-synthesised nanoquartz (light blue line) and the 3-day hydrothermally treated silica shell coated microemulsion-synthesised nanoquartz (brown line).

6.3.3.2 Conclusions

α-Quartz nanoparticles have successfully been synthesised and coated in a 50 nm silica shell by utilising TEOS. These coated particles are monodisperse in size, and although some aggregation has occurred, the nanocrystals contained within the shells remain isolated and dispersed. It was hoped that when these particles underwent hydrothermal treatment, that the shells would provide sufficient protection so that the nanocrystals could grow and perfect over 7 days without aggregating.

After undergoing 3 days of hydrothermal treatment under the usual mild conditions of 175 ^{o}C and autogenic pressure, the resulting nanoquartz contained a defected bulk quartz structure. In fact, this structural perfecting 'lags' behind what we see for the 5 μl g^{-1} microemulsion-derived nanoquartz after 3 days treatment. This is because the amorphous silica shell will also contribute to the FTIR data. Before nanoquartz growth and crystal perfecting under hydrothermal conditions can occur, firstly the silica shell must be dissolved. Hence, longer annealing times will be required to produce the perfected bulk α-quartz structure. Time constraints prevented these longer annealing time experiments from being performed and so this remains an area for future work.

6.4 Discussion

In the previous chapter, 1-5 nm α-quartz nanocrystals were synthesised and extracted from water-in-oil microemulsions under ambient conditions within 14 days. These nanocrystals seeded subsequent hydrothermal syntheses under mild conditions to enable nanoquartz of a defined size to be obtained. Although after 7 days hydrothermal treatment, the quartz crystals had grown and perfected, they had begun to aggregate into larger ~40 nm sized groups. This chapter explored 3 different synthesis methods with a view to restrict nanoparticle aggregation when hydrothermally treated to yield isolated, dispersed nanocrystals of a defined size and structure.

Firstly, microemulsions containing a dispersed phase concentration of 50 μl g^{-1} were used with a SMS wt.% solution of 0.5 and 1.25 wt.%. Both microemulsions successfully produced α-quartz nanocrystals as a predominant phase. These nanocrystals were of a greater size than those produced from 5 μl g^{-1} microemulsions. It was hoped that seeding hydrothermal syntheses with these larger 5 nm crystals would shorten the time needed for the bulk α-quartz to emerge and would reduce the aggregation seen previously. After 3 days treatment, both samples of nanoquartz had a more perturbed structure than that of the 3 day treated 5 μl g^{-1} microemulsion-derived nanoquartz. As a result, more than 7 days would be needed to recover the bulk α-quartz structure and aggregation would be unlikely to be reduced.

Secondly, acidified microemulsions containing HCl were used. These microemulsions contained a dispersed phase concentration of 50 μl g^{-1} and a SMS wt.% solution of 0.5 wt.%. Previous acidified microemulsion quartz syntheses produced large ~400 nm sized particles. Seeding hydrothermal syntheses with crystals of this size could be advantageous in reducing the treatment time. Using this method, larger nanoquartz crystals were successfully synthesised with a mean size of 5.7 ± 3.9 nm. Although, some larger >20 nm crystals were observed no 400 nm particles could be seen in TEM micrographs. Nevertheless, these acidified-derived particles were used to seed hydrothermal treatments of 3 days. After 3 days, the large droplet acidified microemulsion-derived nanoquartz showed no signs of improved crystal perfection as expected. Again, treatment times of over 7 days would therefore be needed and the nanocrystals would begin to aggregate. Here however, it is postulated that residual acid groups contained on the seed particles would be sufficient to lower the pH of the hydrothermal environment and raise the supersaturation. This would cause amorphous silica to precipitate out of solution and traditional nucleation and growth steps would proceed in an uncontrolled way.

As increasing seed particle size was ineffective at reducing hydrothermal treatment times, a method in which the seed crystals were coated with an amorphous silica shell was studied. These shells could prove effective at stopping hydrothermally treated nanoparticle aggregation by providing a physical barrier between them. α-Quartz nanoparticles were successfully synthesised and coated in a 50 nm silica shell by utilising TEOS. Although these amorphous silica shells were monodisperse in size (~50 nm), some aggregation of the shells was observed. The encapsulated nanocrystals, however, were isolated and dispersed throughout the shells. After 3 days hydrothermal treatment, the extracted nanoquartz exhibited a defected bulk quartz structure that was 'lagging' behind that of the 5 μl g^{-1} microemulsion-derived nanoquartz after 3 days treatment; FTIR analysis of the 5 μl g^{-1} microemulsion-derived nanoquartz after 3 days treatment showed structure more akin to that of bulk alpha quartz. It is postulated that silica shell dissolution and hydrothermal nanoquartz growth occur concurrently. As the silica shell dissolves, the supersaturation is raised, leading to immediate growth. It is this dissolving of amorphous silica that appears to cause the 'lag' in perfecting the nanocrystals structure. If hydrothermal experiments with longer annealing times could have been performed, it is thought that the shell would contain enough silica to fuel growth of the confined crystals whilst still creating a barrier to hinder particle aggregation.

Unfortunately none of the methods was successful in reducing the hydrothermal times required to perfect the nanoquartz, meaning that particle aggregation may still occur. It must be noted however, that the synthesis methods outlined in this chapter were successful in producing nanoquartz under ambient conditions of a larger ~5 nm size. Also the successful shell coating of these nanoparticles with an amorphous silica sphere was also successful. To avoid aggregation of the nanoparticle whilst undergoing hydrothermal treatment in the future, a hydrothermal unit that contains a stirring capability is suggested. Although systems under stirring typically induce aggregation of particles, here it is thought to aid the isolation of nanocrystals for the following reasons:

1. It is clear from TEM analysis (Figure 5.13) that the aggregated crystals have begun to coalesce with any grain boundaries annealed away. For this to occur the particles would have to be within close proximity of each other for a significant amount of time, as is thought to be the case here.

2. Under stirring, the particles would be under constant motion and therefore the

nanocrystals would not be able to maintain a close proximity for sufficient amounts of time. Thus, the particles would not be able coalesce and exhibit the same scattering behaviour as we see in the case of the hydrothermally treated nanoquartz.

Chapter 7

Conclusion

This thesis has presented novel, low temperature syntheses of nanographite and nanoquartz using bottom-up methods. This contradicts the high temperatures and pressures employed previously in the literature. To do this, lamellar and microemulsion surfactant phases were used to elicit 2-D and 3-D nanoconfinement respectively to gain thermodynamic control of crystallisation.

In chapter 4, a low temperature synthesis route of nanographite was presented. Lamellar surfactant phases were employed in order to confine sugar and sulphuric acid and produce nanographite in a controlled way. Though this method yielded much larger quantities of product than that seen in previous microemulsion syntheses, the loss of thermodynamic control by moving to a 2-D system had largely resulted in the formation of a furanic product. Increasing the total concentration of acid present in the aqueous channels shifted furanic production towards the formation of aromatic polycondensed benzene rings. This was done *via* two methods, using diluted fuming sulfuric acid and by increasing the mass ratio of acid to other aqueous components in the system. A further improvement to the product was seen after the samples were sulfuric acid treated. Sulfuric acid treatment at 250 °C for one hour has yielded a highly aromatic rich, few layer carbonaceous product with the sought after polycondensed sp^2 hybridised carbons and an inter layer spacing the same as graphite.

Chapter 5 detailed a microemulsion-mediated method for the synthesis and extraction of α-quartz nanocrystals for the first time. Here, the 3-D nanoconfinement seen in these microemulsion systems was sufficient to elicit thermodynamic control over the silica containing precursor (SMS) to produce nanoquartz crystals of 1-5nm in size. These nanocrystals were shown to have a perturbed bulk-quartz structure, but nonetheless had sufficient crystallinity to act as effective seeds for the hydrothermal synthesis of larger quartz nanocrystals under mild conditions of 175 °C and autogenic pressure. The nanocrystals grew and annealed over time, readily enabling nanoquartz of defined size and structure to be obtained exclusively by changing reaction times for the first time. The catalytic ability of these various nanocrystals on the yield of 4-(phenylamino)-pent-3-en-2-one performed as expected; better catalytic performance was seen from the shorter hydrothermally treated products whilst a strong catalytic inhibition was observed from the longer hydrothermally treated products. This microemulsion-hydrothermal strategy may provide a mechanism for studying other inorganic nanocatalytic systems.

Chapter 6 outlines three further microemulsion-mediated methods for the synthesis and extraction of α-quartz nanocrystals. Two methods utilised microemulsions with a dispersed phase concentration of 50 μl g^{-1}, in order to grow the crystals to $\sim$ 5 nm in size whilst still in the microemulsions. The second of these two also involved the addition of HCl. Although both systems successfully grew the nanoquartz crystals to a larger size than that seen in Chapter 5, both were ineffective at seeding hydrothermal syntheses where the treatment time took less than 7 days for the bulk quartz structure to appear. As a result, increasing the size of the seed particles in this way would be unlikely to stop the aggregation of the longer hydrothermally treated nanoquartz. Finally a method in which the seed crystals were coated with an amorphous silica shell was outlined. These shells, synthesised using TEOS, were hoped to prove effective at stopping hydrothermally treated nanoparticle aggregation by providing a physical barrier between them. Unfortunately this method, again, would need longer hydrothermal times in order to perfect the nanoquartz, and so may also ultimately prove ineffective at preventing aggregation. In order to stop this aggregation it is suggested that hydrothermal treatments under stirring should be studied further.

7.1 Further Work

The materials synthesised in this thesis may prove fruitful in various application spaces, however more work would need to be undertaken to study this.

The nanographitic material synthesised in chapter 4 could be of use in batteries/super capacitor applications. Graphite is heavily used as a material for anodes in lithium-ion batteries and it has been suggested that higher capacitance batteries would arise from anodes made of nanographitic material. Firstly, 80 keV TEM studies would have to be employed to probe the size and crystallinity of the nanographitic product further. Electrochemical studies would then need to be conducted to confirm any increased capacitance seen. At its most basic level, this could include cyclic voltammetry tests in which the current, I, is measured with changing voltage, V. The capacitance of the system, C, can then be calculated (Equation 7.1).

$$I(t) = C\frac{dV(t)}{dt} \tag{7.1}$$

Furthermore, this material could be used in applications of carbon quantum dots, where they could be used in medicine, bioimaging, chemical sensors, solar lights and LEDs. Simple studies of shining a blue laser through dispersions of the nanographite in 50:50 acetone:water corroborate this. The laser light changes colour to green upon entering the dispersion showing the photoluminescence effect.

The α-quartz nanocrystals synthesised in chapters 5 and 6 are free from growth modifiers or other contaminants. Furthermore, the tunable crystal size and degree of crystal perfection seen in the hydrothermal experiments make these particles ideal for studies aimed at elucidating the harmful role that silica crystallinity plays in inducing lung diseases such as silicosis. Biomedical experiments would be needed to study this further.

Appendix A

Acid Concentration Determination

Throughout this project, the concentration of sulfuric acid used in the nanographite synthesis has been varied. This has been done *via* two methods: the dilution of >95% H_2SO_4 with UHP water and the dilution of fuming H_2SO_4 with UHP water.

In order to study the affect acid concentration has on the syntheses, one must be able to calculate the overall acid concentration in the aqueous phase after the two initial lamellar phases have been mixed. This is given by

$$\text{\% Total Sulfuric Acid in Aqueous Phase} = \frac{100 \times F_A \times M_A}{M_A + (0.6 \times M_X)}, \tag{A.1}$$

where F_A is the overall mass % of H_2SO_4 in the acid aqueous solution, M_A is mass of the acid solution used in the synthesis and M_X is the mass of the aqueous xylose solution used in the synthesis. Note that in equation (A.1) the total mass of xylose solution is multiplied by 0.6 to account for mass contribution from the aqueous components only.

The dilution of fuming sulfuric acid is more complicated. Fuming H_2SO_4 (or oleum as it is also known) is a composition of sulphur trioxide in sulfuric acid. Before equation (A.1) can be used, one must first convert % oleum to % H_2SO_4:[274]

$$\text{\% Sulfuric Acid} = 100 + \frac{18 \times \text{\% Oleum}}{80}. \tag{A.2}$$

The % total sulfuric acid in the aqueous phase of the mixed lamellar system can then be calculated as before.

Appendix B

Scherrer Equation

When conducting powder X-ray diffraction techniques, a sample exhibiting crystallinity will produce sharp peaks in the pattern. If the sample is amorphous no peaks or broad humps will be evident. However line broadening can occur for crystalline nm-sized particles giving the impression that a material is amorphous when in fact it isn't. This phenomenon is described using the Scherrer equation (Equation B.1).[275]

$$B = \frac{K\lambda}{Lcos\theta} \tag{B.1}$$

Here, B is the mean size of the crystalline domains, K is a dimensionless shape factor, which is typically taken to be 0.9 but can vary with the crystal shape, λ is the X-ray wavelength, L is the line broadening at half the maximum intensity in radians after extracting the instrumental line broadening (typically instrumental line broadening is negligible) and θ is the Bragg angle.

One can use the Scherrer Equation to predict the size of a sample's crystalline domain when analysing powder XRD patterns.

Appendix C

A Note on pH

Note that pH is typically defined as a macroscopic property.[268] Therefore in Chapter 5, it has been chosen to refer to individual hydroxide and more rarely hydronium ions being confined within individual droplets rather than pH. In addition, there are studies that suggest an overall shift towards neutrality can occur in microemulsion droplets under ambient temperature and pressure conditions.[269,276,277] Please note, however, experiments carried out on microemulsions with added HCl concentrations between 0.3 M and 2.2 M still observe quartz nucleation under these ambient conditions for small droplet sizes in all cases.[133] Accordingly, it can be said with confidence that quartz nucleation can occur in microemulsions prepared from solutions covering a range of pH values and so it is not the critical factor for its occurrence, rather it is the 3-D nanoconfinement.

Appendix D

SMS Silica Source

The sodium metasilicate (SMS) used for nanoquartz formation was only 98.5 wt.% pure, and although the FTIR spectrum of the insoluble SMS residue indicated the impurities consisted mainly of calcium carbonate with a broad peak at 1435 cm^{-1} and sharper peak at 880 cm^{-1}, it is clearly vital to verify that the nanoquartz was not, in fact, a minority impurity in the SMS starting material. Accordingly, we also used SMS solutions made by dissolving fumed silica in aqueous sodium hydroxide to prepare our microemulsions. There was no detectable difference between the nanoquartz synthesized from these microemulsions and those obtained from using the 98.5 wt.% SMS silica source.

Bibliography

[1] M. Rosen, *Surfactants and Interfacial Phenomena*, John Wiley & Sons, Inc., 3rd edn., 2004.

[2] L. Schramm, E. Staiuk and M. D., *Annual Reports - Royal Society of Chemistry, Section C: Physical Chemistry*, 2003, **99**, 3–48.

[3] D. Myers, *Surfactant Science and Technology*, John Wiley & Sons, Inc., 3rd edn., 2006.

[4] R. Nagarajan, *Langmuir*, 2002, **18**, 31–38.

[5] J. Eastoe, *Surfactant Chemistry*, Unpublished, 2003.

[6] G. Jian, G. Wei and L. Jinghai, *Science in China Series B: Chemistry*, 2005, **48**, 470–475.

[7] J. Mitchell and B. Ninham, *J. Chem. Soc., Faraday Trans. 2*, 1981, **77**, 601–629.

[8] R. Nagarajan and E. Ruckenstein, *Langmuir*, 1991, **7**, 2934–2969.

[9] R. Alany, T. Rades, S. Agatonovic-Kustrin, N. Davies and I. Tucker, *International Journal of Pharmaceutics*, 2000, **196**, 141–145.

[10] C. Mendonca, Y. Silva, W. Böckel, E. Simo-Alfonso, G. Ramis-Ramos, C. Piatnicki and C. Bica, *Journal of Colloid and Interface Science*, 2009, **337**, 579–585.

[11] N. Pandit, J. Kanjia, K. Patel and D. Pontikes, *International Journal of Pharmaceuticals*, 1995, **122**, 27–33.

[12] J. Phillips, *Phillips, J. N. "The energetics of micelle formation." Transactions of the Faraday Society*, 1955, **51**, 561–569.

[13] S. Raghavan, H. Edlund and E. Kaler, *Langmuir*, 2002, **18**, 1056–1064.

[14] P. Mukherjee, S. Padhan, S. Dash, S. Patel and B. Mishr, *Advances in Colloid and Interface Science*, 2011, **162**, 59–79.

[15] C. Manohar, *Bulletin of Materials Science*, 1994, **17**, 1299–1306.

[16] S. Kumar, D. Sharma and K. Din, *Langmuir*, 2000, **16**, 6821–6824.

[17] A. Martin, I. Lopez, F. Monroy, A. Casielles, F. Ortega and F. Rubio, *Journal of Chemical Physics*, 1994, **101**, 6874–6879.

[18] J. Appell and G. Porte, *Journal de Physique*, 1983, **16**, 689–695.

[19] G. Warr, T. Zemb and M. Drifford, *The Journal of Physical Chemistry*, 1990, **94**, 3086–3092.

[20] G. Fritz, G. Scherf and O. Glatter, *Journal of Physical Chemistry B*, 2000, **104**, 3463–3470.

[21] J. Hanrahan, K. Ziegler, J. Glennon, D. Steytler, J. Eastoe, A. Dupont and J. Holmes, *Langmuir*, 2003, **19**, 3145–3150.

[22] C. Ablan, D. Sheppard, E. Beckman, M. Olmstead and M. Jessop, *Green Chemistry*, 2005, **7**, 590–594.

[23] W. Griffin, *Journal of Cosmetic Science*, 1949, **1**, 311–326.

[24] P. Kruglyakov, *Hydrophile - Lipophile Balance of Surfactants and Solid Particles*, Elsevier Science, 1st edn., 2000.

[25] W. Griffin, *Journal of Cosmetic Science*, 1954, **5**, 249–256.

[26] J. Davies and E. Rideal, *Interfacial phenomena*, New York: Academic Press, 2nd edn., 1963.

[27] C. Rodriguez-Abreu and M. Lazzari, *Current Opinion in Colloid & Interface Science*, 2008, **13**, 198–205.

[28] J. Sjoblom, *Encyclopedic Handbook of Emulsion Technology*, Marcel Dekker, 2001.

[29] P. Taylor, *Advances in Colloid and Interface Science*, 1998, **75**, 107–163.

[30] T. Cosgrove, *Colloid Science: Principles, Methods and Applications*, John Wiley & Sons, Inc., 2nd edn., 2010.

[31] P. Voorhees, *Journal of Statistical Physics*, 1985, **38**, 231–252.

[32] E. Dickinson and D. McClements, *Advances In Food Colloids*, Blackie Academic & Professional, 1st edn., 1995.

[33] J. Kuipers, *Mean-field description of the structure and tension of curved fluid interfaces*, Faculty of Science, Leiden University, 2009.

[34] T. Ngai and S. Bon, *Particle-stabilized emulsions and colloids*, Royal Society of Chemistry, 2014.

[35] A. Gupta, H. B. Eral, T. A. Hatton and P. S. Doyle, *Soft Matter*, 2016, **12**, 1452–1458.

[36] M. Kumar, A. Misra, A. Babbar, A. Mishra, P. Mishra and K. Pathak, *International journal of pharmaceutics*, 2008, **358**, 285–291.

[37] D. K. Sarker, *Current drug delivery*, 2005, **2**, 297–310.

[38] C. Lovelyn and A. A. Attama, *Journal of Biomaterials and Nanobiotechnology*, 2011, **2**, 626.

[39] N. Anton, J.-P. Benoit and P. Saulnier, *Journal of Controlled Release*, 2008, **128**, 185–199.

[40] K. Landfester, *Angewandte Chemie International Edition*, 2009, **48**, 4488–4507.

[41] O. Sonneville-Aubrun, J.-T. Simonnet and F. L'alloret, *Advances in colloid and interface science*, 2004, **108**, 145–149.

[42] H. B. Eral, M. O'Mahony, R. Shaw, B. L. Trout, A. S. Myerson and P. S. Doyle, *Chemistry of Materials*, 2014, **26**, 6213–6220.

[43] A. Z. M. Badruddoza, P. D. Godfrin, A. S. Myerson, B. L. Trout and P. S. Doyle, *Advanced healthcare materials*, 2016, **5**, 1960–1968.

[44] A. Gupta, H. B. Eral, T. A. Hatton and P. S. Doyle, *Soft matter*, 2016, **12**, 2826–2841.

[45] T. Delmas, H. Piraux, A.-C. Couffin, I. Texier, F. Vinet, P. Poulin, M. E. Cates and J. Bibette, *Langmuir*, 2011, **27**, 1683–1692.

[46] A. Gupta, V. Narsimhan, T. A. Hatton and P. S. Doyle, *Langmuir*, 2016, **32**, 11551–11559.

[47] J. N. Wilking and T. G. Mason, *Physical Review E*, 2007, **75**, 041407.

[48] K. Roger, B. Cabane and U. Olsson, *Langmuir*, 2010, **27**, 604–611.

[49] A. Forgiarini, J. Esquena, C. González and C. Solans, in *Trends in colloid and interface science XIV*, Springer, 2000, pp. 36–39.

[50] A. Forgiarini, J. Esquena, C. Gonzalez and C. Solans, *Langmuir*, 2001, **17**, 2076–2083.

[51] A. Forgiarini, J. Esquena, C. González and C. Solans, in *Trends in colloid and interface science XV*, Springer, 2001, pp. 184–189.

[52] A. Gupta, A. Z. M. Badruddoza and P. S. Doyle, *Langmuir*, 2017, **33**, 7118–7123.

[53] I. Danielsson and B. Lindman, *Colloids and Surfaces*, 1981, **3**, 391–392.

[54] J. Chai, Y. Gao, K. Zhao, G. Li and G. Zhang, *Chinese Chemical Letters*, 2005, **16**, 1263–1266.

[55] R. Strey, *Colloid and Polymer Science*, 1994, **272**, 1005–1019.

[56] S. Cooper, O. Cook and N. Loines, in *Crystallization-Science and Technology*, InTech, 2012.

[57] T. Tadros, *Emulsion Formation and Stability*, John Wiley & Sons, Inc., 2013.

[58] P. Winsor, *Transactions of the Faraday Society*, 1948, **44**, 376–398.

[59] A. K. Ganguli, A. Ganguly and S. Vaidya, *Chemical Society Reviews*, 2010, **39**, 474–485.

[60] M. Boutonnet, J. Kizling, P. Stenius and G. Maire, *Colloids and Surfaces*, 1982, **5**, 209–225.

[61] K. Naoe, C. Petit and M. Pileni, *Langmuir*, 2008, **24**, 2792–2798.

[62] C. Petit, P. Lixon and M. Pileni, *Journal of Physical Chemistry*, 1990, **94**, 1598–1603.

[63] J. Eastoe, M. J. Hollamby and L. Hudson, *Advances in colloid and interface science*, 2006, **128**, 5–15.

[64] A. K. Ganguli, T. Ahmad, S. Vaidya and J. Ahmed, *Pure and Applied Chemistry*, 2008, **80**, 2451–2477.

[65] S. Vaucher, M. Li and S. Mann, *Angewandte Chemie International Edition*, 2000, **39**, 1793–1796.

[66] A. K. Ganguli and T. Ahmad, *Journal of nanoscience and nanotechnology*, 2007, **7**, 2029–2035.

[67] R. Koole, M. M. van Schooneveld, J. Hilhorst, C. de Mello Donegá, D. C. t. Hart, A. van Blaaderen, D. Vanmaekelbergh and A. Meijerink, *Chemistry of Materials*, 2008, **20**, 2503–2512.

[68] Y. Yang, L. Jing, X. Yu, D. Yan and M. Gao, *Chemistry of materials*, 2007, **19**, 4123–4128.

[69] M. J. Lawrence and G. D. Rees, *Advanced drug delivery reviews*, 2012, **64**, 175–193.

[70] K. Shinoda and H. Saito, *Journal of Colloid and Interface Science*, 1969, **30**, 258–263.

[71] R. Laughlin, *The Aqueous Phase Behaviour of Surfactants*, London: Academic Press, 1996.

[72] D. Evans and H. Wennerström, *The Colloidal Domain: Where Physics, Chemistry, Biology, and Technology Meet*, New York: Wiley VCH, 2nd edn., 1999.

[73] I. Americas, *The HLB system: a time-saving guide to emulsifier selection*, ICI Americas, Incorporated, 1984.

[74] T. Tadros, *An Introduction to Surfactants*, Walter de Gruyter, 2014.

[75] G. Grosso and G. P. Parravicini, *Solid State Physics*, Academic Press, 2nd edn., 2014.

[76] J. W. Mullin, *Crystallization*, Butterworth Heinemann, 4th edn., 2001.

[77] W. Garner, *Discussions of the Faraday Society*, 1949, **5**, 7–10.

[78] H. Takiyama, *Advanced Powder Technology*, 2012, **23**, 273–278.

[79] G. Coquerel, *Chemical Society Reviews*, 2014, **43**, 2286–2300.

[80] A. Myerson, *Handbook of industrial crystallization*, Butterworth-Heinemann, 2002.

[81] D. Chirgadze, *University of Cambridge*, 2001.

[82] E. o. Berkeley, *The London, Edinburgh, and Dublin Philosophical Magazine and Journal of Science*, 1912, **24**, 254–268.

[83] S. Young, *Journal of the American Chemical Society*, 1911, **33**, 148–162.

[84] J. W. Gibbs, *The Collected Works of J. Willard Gibbs: pt. 1. Elementary principles in statistical mechanics.-pt. 2. Dynamics. Vector analysis and multiple algebra. Electromagnetic theory of light, etc*, Yale University Press, 1948, vol. 2.

[85] M. Volmer and A. Weber, *Z. phys. Chem*, 1926, **119**, 277–301.

[86] R. Becker and W. Döring, *Annalen der Physik*, 1935, **416**, 719–752.

[87] I. V. Markov, *Crystal growth for beginners: fundamentals of nucleation, crystal growth and epitaxy*, World scientific, 2003.

[88] S. Teychené and B. Biscans, *Crystal Growth and Design*, 2008, **8**, 1133–1139.

[89] R. P. Sear, *Journal of Physics: Condensed Matter*, 2007, **19**, 033101.

[90] C. B. Murray, C. Kagan and M. Bawendi, *Annual Review of Materials Science*, 2000, **30**, 545–610.

[91] P. R. ten Wolde and D. Frenkel, *Science*, 1997, **277**, 1975–1978.

[92] O. Gliko, N. Neumaier, W. Pan, I. Haase, M. Fischer, A. Bacher, S. Weinkauf and P. G. Vekilov, *Journal of the American Chemical Society*, 2005, **127**, 3433–3438.

[93] S. Karthika, T. Radhakrishnan and P. Kalaichelvi, *Crystal Growth & Design*, 2016, **16**, 6663–6681.

[94] P. G. Vekilov, *Crystal growth & design*, 2004, **4**, 671–685.

[95] H. Cölfen and M. Antonietti, *Angewandte Chemie International Edition*, 2005, **44**, 5576–5591.

[96] P. Cubillas and M. W. Anderson, *Zeolites and Catalysis: Synthesis, Reactions and Applications*, 2010, 1–55.

[97] V. Voronkov, in *Growth of Crystals*, Springer, 1976, pp. 1–17.

[98] G. R. Desiraju, J. J. Vittal and A. Ramanan, *Crystal engineering: a textbook*, World Scientific, 2011.

[99] M. Sleutel, D. Maes, L. Wyns and R. Willaert, *Crystal Growth and Design*, 2008, **8**, 4409–4414.

[100] D. Hull and D. J. Bacon, *Introduction to dislocations*, Butterworth-Heinemann, 2001.

[101] W.-K. Burton, N. Cabrera and F. Frank, *Phil. Trans. R. Soc. Lond. A*, 1951, **243**, 299–358.

[102] W. Burton, N. Cabrera and F. Frank, *Nature*, 1949, **163**, 398.

[103] H. Föll, *Faculty of Engineering, University of Kiel.© Prof. Dr. Helmut Föll. Launch Site*, 2005.

[104] A. R. Verma, *Nature*, 1951, **167**, 939.

[105] S. Aitipamula, R. Banerjee, A. K. Bansal, K. Biradha, M. L. Cheney, A. R. Choudhury, G. R. Desiraju, A. G. Dikundwar, R. Dubey, N. Duggirala *et al.*, *Crystal growth & design*, 2012, **12**, 2147–2152.

[106] J. Bernstein, *Journal of Physics D: Applied Physics*, 1993, **26**, B66.

[107] G. P. Stahly, *Crystal Growth & Design*, 2007, **7**, 1007–1026.

[108] Y.-n. Xu and W. Ching, *Physical Review B*, 1991, **44**, 11048.

[109] N. R. Keskar and J. R. Chelikowsky, *Physical Review B*, 1992, **46**, 1.

[110] M. L. Di Lorenzo, M. Cocca and M. Malinconico, *Thermochimica acta*, 2011, **522**, 110–117.

[111] M. L. Di Lorenzo, M. C. Righetti and B. Wunderlich, *Macromolecules*, 2009, **42**, 9312–9320.

[112] M. Cocca, M. L. Di Lorenzo, M. Malinconico and V. Frezza, *European Polymer Journal*, 2011, **47**, 1073–1080.

[113] A. Llinàs and J. M. Goodman, *Drug Discovery Today*, 2008, **13**, 198–210.

[114] A. V. Trask, N. Shan, W. S. Motherwell, W. Jones, S. Feng, R. B. Tan and K. J. Carpenter, *Chemical Communications*, 2005, 880–882.

[115] M. M. De Villiers, R. J. Terblanche, W. Liebenberg, E. Swanepoel, T. G. Dekker and M. Song, *Journal of pharmaceutical and biomedical analysis*, 2005, **38**, 435–441.

[116] S.-F. Chen, S.-H. Yu, J. Jiang, F. Li and Y. Liu, *Chemistry of materials*, 2006, **18**, 115–122.

[117] K. Chadwick, R. Davey, R. Mughal and I. Marziano, *Organic Process Research & Development*, 2009, **13**, 1284–1290.

[118] W. Beckmann, R. Boistelle and K. Sato, *Journal of Chemical and Engineering Data*, 1984, **29**, 211–214.

[119] W. Ostwald, *Z. phys. Chem*, 1897, **22**, 289–330.

[120] T. Threlfall, *Organic process research & development*, 2003, **7**, 1017–1027.

[121] S. R. Chemburkar, J. Bauer, K. Deming, H. Spiwek, K. Patel, J. Morris, R. Henry, S. Spanton, W. Dziki, W. Porter *et al.*, *Organic Process Research & Development*, 2000, **4**, 413–417.

[122] J. Bauer, S. Spanton, R. Henry, J. Quick, W. Dziki, W. Porter and J. Morris, *Pharmaceutical research*, 2001, **18**, 859–866.

[123] C. E. Nicholson, C. Chen, B. Mendis and S. J. Cooper, *Crystal Growth & Design*, 2011, **11**, 363–366.

[124] C. Chen, O. Cook, C. E. Nicholson and S. J. Cooper, *Crystal Growth & Design*, 2011, **11**, 2228–2237.

[125] C. E. Nicholson and S. J. Cooper, *Crystals*, 2011, **1**, 195–205.

[126] O. Glatter, *Journal of Applied Crystallography*, 1979, **12**, 166–175.

[127] J. Roberts, *Nuclear Magnetic Resonance: Applications to Organic Chemistry*, CaltechBOOK, 1959.

[128] J. Keeler, *Understanding NMR Spectroscopy*, John Wiley & Sons, Inc., 2006.

[129] D. Apperley, R. Harris and P. Hodgkinson, *Solid-state NMR: Basic Principles & Practice*, Momentum Press, 2012.

[130] W. Kolodziejski and J. Klinowsk, *Chemical Reviews*, 2002, **102**, 613–628.

[131] S. Hartmann and E. Hahn, *Physical Review Letters*, 1962, **128**, 2042–2053.

[132] R. Bertrand, W. Moniz and G. Garroway, A. amd Chingas, *Journal of the American Chemical Society*, 1978, **100**, 5227–5229.

[133] N. Hargreaves, *Ph.D. thesis*, Durham University, 2016.

[134] P. R. Griffiths and J. A. De Haseth, *Fourier transform infrared spectrometry*, John Wiley & Sons, 2007, vol. 171.

[135] P. Atkins and J. De Paula, *Elements of physical chemistry*, Oxford University Press, USA, 2013.

[136] Y. Yang, L. Teng and S. Seetharaman, *Metallurgical and Materials Transactions B*, 2012, **43**, .

[137] Perkinelmer.com, 2020.

[138] D. Chung, *Journal of Materials Science*, 2002, **37**, 1475–1489.

[139] J. Robertson, *Materials Science and Engineering Reports*, 2002, **37**, 129–281.

[140] Y. Xu, X. Li and J. Dong, *Nanotechnology*, 2010, **21**, 065711.

[141] M. Koshino, *Physical Review B*, 2010, **81**, 125304.

[142] J. J Hass, W. de Heer and E. Conrad, *Journal of Physics: Condensed Matter*, 2008, **20**, 323202.

[143] X. Chen, F. Tian, C. Persson, W. Wenhui Duan and N. Chen, *Scientific Reports*, 2013, **3**, 3046.

[144] J. Bernal, *Proceedings of the Royal Society of London*, 1924, **106**, 749–773.

[145] J. Charlier, X. Gonze and J. Michenaud, *Europhysics Letters*, 1994, **28**, 403–408.

[146] S. Peng, X. Fan, S. Li and J. Zhang, *Journal of the Chilean Chemical Society*, 2013, **58**, 2213–2217.

[147] T. Blanton and D. Majumdar, *Powder Diffraction*, 2012, **27**, 104–107.

[148] P. Avouris and C. Dimitrakopoulos, *Materials Today*, 2012, **15**, 86–97.

[149] C. Lee, X. Wei, J. Kysar and J. Hone, *Science*, 2008, **321**, 385–388.

[150] J. Bunch, S. Verbridge, J. Alden, A. van der Zande, J. Parpia, H. Craighead and P. McEuen, *Nano Letters*, 2008, **8**, 2458–2462.

[151] A. Balandin, S. Ghosh, W. Bao, I. Calizo, D. Teweldebrhan, F. Miao and C. Lau, *Nano Letters*, 2008, **8**, 902–907.

[152] C. Lau, W. Bao and J. Velasco, *Materials Today*, 2012, **15**, 238–245.

[153] R. Nair, P. Blake, A. Grigorenko, K. Novoselov, T. Booth, T. Stauber, N. Peres and A. Geim, *Science*, 2008, **320**, 1308.

[154] A. Castro Neto, F. Guinea, N. Peres, K. Novoselov, and A. Geim, *Review of Modern Pysics*, 2009, **81**, 109.

[155] Fkf.mpg.de, 2016.

[156] K. Bolotina, K. Sikes, Z. Jiang, M. Klima, G. Fudenberg, J. Hone, P. Kim and H. Stormer, *Solid State Communications*, 2008, **146**, 351–355.

[157] A. Geim, *Science*, 2009, **324**, 1530–1534.

[158] A. Geim and K. Novoselov, *Nature Materials*, 2007, **6**, 183–191.

[159] R. Edwards and K. Coleman, *Nanoscale*, 2013, **5**, 38–51.

[160] P. Sutter, *Nature Materials*, 2009, **8**, 171–172.

[161] K. Emtsev, A. Bostwick, K. Horn, J. Jobst, G. Kellogg, L. Ley, J. McChesney, T. Ohta, S. Reshanov, J. Röhrl, E. Rotenberg, A. Schmid, D. Waldmann, H. Weber and T. Seyller, *Nature Materials*, 2009, **8**, 203–207.

[162] C. Virojanadara, M. Syväjarvi, R. Yakimova, L. Johansson, A. Zakharov and T. Balasubramanian, *Physical Review B*, 2008, **78**, 245403.

[163] R. Tromp and J. Hannon, *Physical Review Letters*, 2009, **102**, 106104.

[164] Z. Juang, C. Wu, C. Lo, W. Chen, C. Huang, J. Hwang, F. Chen, K. Leou and C. Tsai, *Carbon*, 2009, **47**, 2026–2031.

[165] A. Woodworth and C. Stinespring, *Carbon*, 2010, **48**, 1999–2003.

[166] T. Yoneda, M. Shibuya, K. Mitsuhara, A. Visikovskiy, Y. Hoshino and Y. Kido, *Surface Science*, 2010, **604**, 1509–1515.

[167] C. Kang, L. Fan, S. Chen, Z. Liu, P. Xu and C. Zou, *Applied Physics Letters*, 2012, **100**, 251604.

[168] J. Caldwell, T. Anderson, J. Culbertson, G. Jernigan, K. Hobart, F. Kub, M. Tadjer, J. Tedesco, J. Hite, M. Mastro, R. Myers-Ward, C. EddyJr., P. Campbell and D. Gaskill, *ACS Nano*, 2010, **4**, 1108–1114.

[169] S. Unarunotai, Y. Murata, C. Chialvo, H. Kim, S. MacLaren, N. Mason, I. Petrov and J. Rogers, *Applied Physics Letters*, 2009, **95**, 202101.

[170] X. Li, W. Cai, J. An, S. Kim, J. Nah, D. Yang, R. Piner, A. Velamakanni, I. Jung, E. Tutuc, S. Banerjee, L. Colombo and R. Ruoff, *Science*, 2009, **324**, 1312–1314.

[171] X. Li, C. Magnuson, A. Venugopal, J. An, J. Suk, B. Han, M. Borysiak, W. Cai, A. Velamakanni, Y. Zhu, L. Fu, E. Vogel, E. Voelkl, L. Colombo and R. Ruoff, *Nano Letters*, 2010, **10**, 4328–4334.

[172] C. Mattevi, H. Kim and M. Chhowalla, *Journal of Materials Chemistry*, 2011, **21**, 3324–3334.

[173] J. Wintterlina and M. Bocquet, *Surface Science*, 2009, **603**, 1841–1852.

[174] M. Batzill, *Surface Science Reports*, 2012, **67**, 83–115.

[175] A. Dato, V. Radmilovic, Z. Lee, J. Phillips and M. Frenklach, *Nano Letters*, 2008, **8**, 2012–2016.

[176] A. Dato and M. Frenklach, *New Journal of Physics*, 2010, **12**, 125013.

[177] C. Herron, K. Coleman, R. Edwards, and B. Mendis, *Journal of Materials Chemistry*, 2011, **21**, 3378–3383.

[178] K. Novoselov, A. Geim, S. Morozov, D. Jiang, Y. Zhang, S. Dubonos, I. Grigorieva and A. Firsov, *Science*, 2004, **306**, 666–669.

[179] C. Su, A. Lu, Y. Xu, F. Chen, A. Khlobystov and L. Li, *ACS Nano*, 2011, **5**, 2332–2339.

[180] G. Wang, B. Wang, J. Park, Y. Wang, B. Sun and J. Yao, *Carbon*, 2009, **47**, 3242–3246.

[181] P. Blake, P. Brimicombe, R. Nair, T. Booth, D. Jiang, F. Schedin, L. Ponomarenko, S. Morozov, H. Gleeson, E. Hill, A. Geim and K. Novoselov, *Nano Letters*, 2008, **8**, 1704–1708.

[182] Y. Hernandez, V. Nicolosi, M. Lotya, F. Blighe, Z. Sun, S. De, I. McGovern, B. Holland, M. Byrne, Y. Gun'Ko, J. Boland, P. Niraj, G. Duesberg, S. Krishnamurthy, R. Goodhue, J. Hutchison, V. Scardaci, A. Ferrari and J. Coleman, *Nature Nanotechnology*, 2008, **3**, 563–568.

[183] Y. Hernandez, M. Lotya, D. Rickard, S. Bergin and J. Coleman, *Langmuir*, 2010, **26**, 3208–3213.

[184] U. Khan, A. O'Neill, M. Lotya, S. De and J. Coleman, *Small*, 2010, **6**, 864–871.

[185] U. Khan, H. Porwal, A. O'Neill, K. Nawaz, P. May and J. Coleman, *Langmuir*, 2011, **27**, 9077–9082.

[186] C. Lee, H. Lim, W. Chee, A. Pandikumar and N. Huang, *Graphene*, 2014, **2**, 1–7.

[187] M. Lotya, Y. Hernandez, P. King, R. Smith, V. Nicolosi, L. Karlsson, F. Blighe, S. De, Z. Wang, I. McGovern, G. Duesberg and J. Coleman, *Journal of the American Chemical Society*, 2009, **131**, 3611–3620.

[188] M. Lotya, P. King, U. Khan, S. De, and J. Coleman, *ACS Nano*, 2010, **4**, 3155–3162.

[189] H. Huang, Y. Xia, X. Tao, J. Du, J. Fang, Y. Gan and W. Zhang, *Journal of Materials Chemistry*, 2012, **22**, 10452–10456.

[190] L. Viculis, J. Mack, O. Mayer, H. Hahn and R. Kaner, *Journal of Materials Chemistry*, 2005, **15**, 974–978.

[191] N. Pu, C. Wang, Y. Sung, Y. Liua and M. Ger, *Materials Letters*, 2009, **63**, 1987–1989.

[192] Y. Gao, W. Wen Shi, W. Wang, Y. Wang, Y. Zhao, Z. Lei, and R. Miao, *Industrial & Engineering Chemistry Research*, 2014, **53**, 2839–2845.

[193] T. Wei, Z. Fan, G. Luo, C. Zheng and D. Xie, *Carbon*, 2009, **47**, 337–339.

[194] D. Chung, *Journal of Materials Science*, 1987, **22**, 4190–4198.

[195] W. Hummers and R. Offeman, *Journal of the American Chemical Society*, 1958, **80**, 1339–1339.

[196] M. Allen, V. Tung and R. Kaner, *Chemical Reviews*, 2010, **110**, 132–145.

[197] E. Schmidt, *Hydrazine and Its Derivatives*, John Wiley & Sons, Inc., 2nd edn., 2001, vol. 1.

[198] D. Dreyer, S. Park, C. Bielawski and R. Ruoff, *Chemical Society Reviews*, 2010, **39**, 228–240.

[199] H. Schniepp, J. Li, M. McAllister, H. Sai, M. Herrera-Alonso, D. Adamson, R. Prud'homme, R. Car, D. Saville and I. Aksay, *Journal of Physical Chemistry B*, 2006, **110**, 8535–5839.

[200] M. Choucair, P. Thordarson and J. Stride, *Nature Nanotechnology*, 2009, **4**, 30–33.

[201] Z. Xu, H. Li, W. Li, G. Cao, Q. Zhang, K. Li, Q. Fu and J. Wang, *Chemical Communications*, 2010, **47**, 1166–1168.

[202] N. Hargreaves and S. Cooper, *Crystal Growth & Design*, 2016, **16**, 3133–3142.

[203] X. Huang, X. Qi, F. Boey and H. Zhang, *Chemical Society Reviews*, 2012, **41**, 666–686.

[204] E. Burzuri, J. Island, R. Diaz-Torres, A. Fursina, A. Gonzalez-Campo, O. Roubeau, S. Teat, N. Aliaga-Alcalde, E. Ruiz and H. van der Zant, *ACS Nano*, 2016, **10**, 2521–2527.

[205] X. Wang, L. Zhi and K. Müllen, *Nano Letters*, 2008, **8**, 323–327.

[206] F. Schwierz, *Nature Nanotechnology*, 2010, **5**, 487–496.

[207] L. Huang, Y. Huang, J. Liang, X. Wan and Y. Chen, *Nano Research*, 2011, **4**, 675–684.

[208] M. Liang and L. Zhi, *Journal of Materials Chemistry*, 2009, **19**, 5871–5878.

[209] Y. Huang, J. Liang and Y. Chen, *Small*, 2012, **8**, 1805–1834.

[210] Y. Lin, A. Valdes-Garcia, S. Han, D. Farmer, I. Meric, Y. Sun, Y. Wu, C. Dimitrakopoulos, A. Grill, P. Avouris and K. Jenkins, *Science*, 2011, **332**, 1294–1297.

[211] H. Hibino, S. Tanabe, S. Mizuno and H. Kageshima, *Journal of Physics D: Applied Physics*, 2012, **45**, 154008.

[212] Y. Lin, C. Dimitrakopoulos, K. Jenkins, D. Farmer, H. Chiu, A. Grill and P. , *Science*, 2010, **327**, 662.

[213] W. Choi, I. Lahiri, R. Seelaboyina and Y. Kang, *Critical Reviews in Solid State and Materials Sciences*, 2010, **35**, 52–71.

[214] O. Compton and S. Nguyen, *Small*, 2010, **6**, 711–723.

[215] C. Moreau, A. Finiels and L. Vanoye, *Journal of Molecular Catalysis A: Chemical*, 2006, **253**, 165–169.

[216] M. Brasholz, K. von Känel, C. Hornung, S. Saubern and J. Tsanaktsidis, *Green Chemistry*, 2011, **13**, 1114–1117.

[217] A. Dias, M. Pillinger and A. Valente, *Journal of Catalysis*, 2005, **229**, 414–423.

[218] M. Antunes, S. Lima, A. Fernandes, M. Pillinger, M. Ribeiro and A. Valente, *Applied Catalysis A: General*, 2012, **417**, 243–252.

[219] K. Enslow and A. Bell, *RSC Advances*, 2012, **2**, 10028.

[220] B. Temelso, T. Phan and G. Shields, *The Journal of Physical Chemistry A*, 2012, **116**, 9745–9758.

[221] X. Hu, R. Westerhof, D. Dong, L. Wu and C. Li, *ACS Sustainable Chemistry & Engineering*, 2014, **2**, 2562–2575.

[222] www.sigmaaldrich.com, 2019.

[223] Y. Hong, Z. Wang and X. Jin, *Scientific Reports*, 2013, **3**, 3439.

[224] J. Anderson, R. Johnson, K. Schmidt-Rohr and B. Shanks, *Carbon*, 2014, **74**, 333–345.

[225] www.fishersci.co.uk, 2016.

[226] http://www.solvay.us/, 2016.

[227] B. Wu, T. Liu, Q. Xia and X. Wu, *Journal of the Electrochemical Society*, 2013, **160**, A1720.

[228] X. Sun and Y. Lei, *TrAC Trends in Analytical Chemistry*, 2017, **89**, 163–180.

[229] L. W. Hobbs and X. Yuan, in *Defects in SiO2 and Related Dielectrics: Science and Technology*, Springer, 2000, pp. 37–71.

[230] D. J. Belton, O. Deschaume and C. C. Perry, *The FEBS journal*, 2012, **279**, 1710–1720.

[231] M. Lider and H. Yurtseven, *3D Research*, 2014, **5**, 28.

[232] J. D. H. Donnay, *Crystal data: determinative tables*, National Bureau of Standards, 1978, vol. 3.

[233] J. F. Bertone, J. Cizeron, R. K. Wahi, J. K. Bosworth and V. L. Colvin, *Nano Letters*, 2003, **3**, 655–659.

[234] X. Jiang, Y.-B. Jiang and C. J. Brinker, *Chemical Communications*, 2011, **47**, 7524–7526.

[235] L. M. Sochalski-Kolbus, H.-W. Wang, A. J. Rondinone, L. M. Anovitz, D. J. Wesolowski and P. S. Whitfield, *Crystal Growth & Design*, 2015, **15**, 5327–5331.

[236] M. Cargnello, T. R. Gordon and C. B. Murray, *Chemical reviews*, 2014, **114**, 9319–9345.

[237] I. A. Rahman and V. Padavettan, *Journal of Nanomaterials*, 2012, **2012**, 8.

[238] A. Carretero-Genevrier, M. Gich, L. Picas, J. Gazquez, G. Drisko, C. Boissiere, D. Grosso, J. Rodriguez-Carvajal and C. Sanchez, *Science*, 2013, **340**, 827–831.

[239] T. Matsuno, Y. Kuroda, M. Kitahara, A. Shimojima, H. Wada and K. Kuroda, *Angewandte Chemie International Edition*, 2016, **55**, 6008–6012.

[240] V. Bansal, A. Ahmad and M. Sastry, *Journal of the American Chemical Society*, 2006, **128**, 14059–14066.

[241] F. T. Mackenzie and R. Gees, *Science*, 1971, **173**, 533–535.

[242] W. Stöber, A. Fink and E. Bohn, *Journal of colloid and interface science*, 1968, **26**, 62–69.

[243] X.-D. Wang, Z.-X. Shen, T. Sang, X.-B. Cheng, M.-F. Li, L.-Y. Chen and Z.-S. Wang, *Journal of colloid and interface science*, 2010, **341**, 23–29.

[244] D. Napierska, L. C. Thomassen, D. Lison, J. A. Martens and P. H. Hoet, *Particle and fibre toxicology*, 2010, **7**, 39.

[245] G. Calvert, F. Rice, J. Boiano, J. Sheehy and W. Sanderson, *Occupational and Environmental Medicine*, 2003, **60**, 122–129.

[246] F. Turci, C. Pavan, R. Leinardi, M. Tomatis, L. Pastero, D. Garry, S. Anguissola, D. Lison and B. Fubini, *Particle and fibre toxicology*, 2015, **13**, 32.

[247] R. L. Bunde, E. J. Jarvi and J. J. Rosentreter, *Talanta*, 1998, **46**, 1223–1236.

[248] P. Alivisatos, *Nature biotechnology*, 2004, **22**, 47.

[249] C.-C. Chen, A. B. Herhold, C. S. Johnson and A. P. Alivisatos, *Science*, 1997, **276**, 398–401.

[250] S. Rıos, E. Salje and S. Redfern, *The European Physical Journal B-Condensed Matter and Complex Systems*, 2001, **20**, 75–83.

[251] C. Chen, C. E. Nicholson, H. E. Ramsey and S. J. Cooper, *Crystal Growth & Design*, 2015, **15**, 1060–1066.

[252] P. Buckley, N. Hargreaves and S. Cooper, *Communications Chemistry*, 2018, **1**, 49.

[253] J. Brunner-Popela and O. Glatter, *Journal of Applied Crystallography*, 1997, **30**, 431–442.

[254] J. Pitts and A. Czanderna, *Nuclear Instruments and Methods in Physics Research Section B: Beam Interactions with Materials and Atoms*, 1986, **13**, 245–249.

[255] J. D. Kubicki, J. O. Sofo, A. A. Skelton and A. V. Bandura, *The Journal of Physical Chemistry C*, 2012, **116**, 17479–17491.

[256] G. Miehe, H. Graetsch *et al.*, *European Journal of Mineralogy*, 1992, **4**, 693–706.

[257] O. Schäf, H. Ghobarkar, A. Garnier, C. Vagner, J. Lindner, J. Hanss and A. Reller, *Solid State Sciences*, 2006, **8**, 625–633.

[258] M. Zhang and T. Moxon, *American Mineralogist*, 2014, **99**, 671–680.

[259] H. Graetsch, I. Topalovic and H. Gies, *European Journal of Mineralogy*, 1994, **6**, 459–464.

[260] H. Alinezhad, M. Tajbakhsh, M. N. Sarkati and M. Zare, *Monatshefte für Chemie-Chemical Monthly*, 2016, **147**, 1591–1596.

[261] A. R. Gholap, N. S. Chakor, T. Daniel, R. J. Lahoti and K. V. Srinivasan, *Journal of Molecular Catalysis A: Chemical*, 2006, **245**, 37–46.

[262] J. D. Rimer, R. F. Lobo and D. G. Vlachos, *Langmuir*, 2005, **21**, 8960–8971.

[263] C. C. Carcouët, M. W. Van De Put, B. Mezari, P. C. Magusin, J. Laven, P. H. Bomans, H. Friedrich, A. C. C. Esteves, N. A. Sommerdijk, R. A. Van Benthem *et al.*, *Nano letters*, 2014, **14**, 1433–1438.

[264] J. M. Fedeyko, D. G. Vlachos and R. F. Lobo, *Langmuir*, 2005, **21**, 5197–5206.

[265] H. Lindgreen, V. Drits, A. Salyn, F. Jakobsen and N. Springer, *Clay Minerals*, 2011, **46**, 525–537.

[266] V. A. Drits, J. Skibsted, O. V. Dorzhieva, A. E. Fallick and H. Lindgreen, *American Mineralogist: Journal of Earth and Planetary Materials*, 2017, **102**, 1402–1417.

[267] D. C. Crans, A. M. Trujillo, S. Bonetti, C. D. Rithner, B. Baruah and N. E. Levinger, *The Journal of organic chemistry*, 2008, **73**, 9633–9640.

[268] D. C. Crans and N. E. Levinger, *Accounts of chemical research*, 2012, **45**, 1637–1645.

[269] B. Baruah, D. C. Crans and N. E. Levinger, *Langmuir*, 2007, **23**, 6510–6518.

[270] K. Esumi and M. Ueno, *Structure-performance relationships in surfactants*, CRC Press, 2003, vol. 112.

[271] A. Yaghmur, A. Aserin, I. Tiunova and N. Garti, *Journal of thermal analysis and calorimetry*, 2002, **69**, 163–177.

[272] R. Zhang, Y. Wang, L. Tan, H. Zhang and M. Yang, *Journal of chromatographic science*, 2012, **50**, 598–607.

[273] C. R. Vestal and Z. J. Zhang, *Nano Letters*, 2003, **3**, 1739–1743.

[274] http://www.rsc.org, 2016.

[275] A. Patterson, *Physical review*, 1939, **56**, 978.

[276] B. Baruah, J. M. Roden, M. Sedgwick, N. M. Correa, D. C. Crans and N. E. Levinger, *Journal of the American Chemical Society*, 2006, **128**, 12758–12765.

[277] N. E. Levinger, L. C. Rubenstrunk, B. Baruah and D. C. Crans, *Journal of the American Chemical Society*, 2011, **133**, 7205–7214.